Department of Architecture
and Built Environment



The University of Nottingham

UNITED KINGDOM · CHINA · MALAYSIA

SIMULATION OF THE THERMAL AND ELECTRICAL PERFORMANCE OF A NOVEL PVT-PCM SYSTEM

Tianyu Chen

BEng (Hons)

Thesis submitted to the University of Nottingham for the degree of Doctor of Philosophy

September 2017

ABSTRACT

This study provides an insight into the fundamentals of PV performance enhancement under different environmental conditions. The study also presents a new concept of PCM integrated PVT system which has a better performance from both electrical and thermal perspectives.

The study employs both analytical and computational techniques to investigate the PV performance under the effect of different parameters such as wind speed, solar radiation level, ambient temperature and additional cooling condition. A parametric analysis of the PCM is also carried out under different solar radiation level, water inlet temperature and flow speed. Additional analysis regarding to the effects of PCM's thermal physical properties against its thermal performance is also presented. A validation analysis is carried out prior to the parametric analysis to ascertain the reliability of the CFD models used, the prediction result of the CFD model is compared with analytical calculations as well as data from literature.

The study found that the active water cooling is the best solution which can provide guaranteed performance enhancement regardless effects of ambient conditions.

The novel PVT-PCM system is found to have a noticeable electrical performance enhancement over conventional PV

panel as well as having the ability to store a significant amount of thermal energy. It is found that the PVT-PCM system has much lower PV cell temperature (maximum temperature reduction of 36.5℃ and 38.3℃ respectively) compared to conventional PV systems when used in both Nottingham and Shanghai area, hence provide up to 5.4kWh (5.7kWh in Shanghai) more energy per unit module. The stored thermal energy could be utilized to provide moderate heating to air and/or water. The air preheated by PVT-PCM system could satisfy space heating requirement during April to October in Nottingham without any additional energy consumption. On the other hand, the preheated water could reduce boiler heating energy from up to 20% and 41% respectively for Nottingham and Shanghai climate. The overall performance benefits of the proposed PVT-PCM system could be greater if used in hotter climates. Finally, a cost analysis was carried to prove the whole system is financially feasible for use in both climates of Nottingham and Shanghai with a discounted payback period of 10.67 and 12.83 years respectively.

ACKNOWLEDGEMENTS

This work could not have been completed without the support and help from the Department of Architecture and Built Environment.

I would like to express my deepest thanks to my main supervisor Dr. Guohui Gan, who offered his valuable guidance and support throughout the work; Dr. Jie Zhu, my second supervisor for the inspiration and valuable inputs.

My sincere gratitude also goes to Dr. Yuehong Su, who has shown his great support and kept me on track with lots of constructive comments during his busy time.

I also wish to thank my friend Dr. Weiguang Su for his support on the basics of CFD during the early stage of my work; Dr. Jiawei Yao for the frequent progress discussions. I would also like to thank Dr. Dengfeng Du for his valuable suggestions which helped settle my future career.

I would also like to show my gratefulness to my parents, who supported me with love and care in the past 26 years. I cannot go this far without all of your sacrifices.

Finally, I would like to thank my partner Rong Qu, for understanding, tolerating and accompanying a final year Ph.D.

TABLE OF CONTENTS

Abstract I

Acknowledgements III

List of Figures IX

List of Tables XX

Nomenclature XXIII

Chapter 1. Introduction 1

1.1 Introduction 1

1.2 Problem Statement 5

1.3 The proposed PVT-PCM system 6

1.4 Aims and Objectives 8

1.5 Thesis Structure 9

Chapter 2. Literature review 11

2.1 Introduction 11

2.2 Photovoltaic system 11

2.2.1 PV module type 13
2.2.2 Effect of cell temperature 15
2.2.3 Other parameters relating to PV efficiency 19

2.3 Thermal management of PV panel 21

2.3.1 Passive cooling and active cooling 21
2.3.2 Air cooling 23
2.3.3 Water cooling 25

2.4 PVT and BIPVT system 28

2.4.1 Air based PVT 31
2.4.2 Water based PVT 35
2.4.3 PVT optimization 39

2.5 Phase Change Material 42

2.5.1 Types of PCM 45
2.5.2 Applications of PCM 47
2.5.3 Improving thermal performance of PCM 51

2.6 Numerical studies on PVT and PCM performance 55

2.6.1 Numerical studies on PVT performance 55
2.6.2 Numerical studies on PCM performance 57

2.7 PVT-PCM Application 60
2.8 Summary 65
Chapter 3 Analytical and CFD methodology 66
3.1 Analytical models for PVT-PCM system 66
3.1.1 Energy model of back cooled flat plate PV panel 66
3.1.2 Energy models of heat transfer 77
3.1.3 Model of PV panel electrical performance 80
3.1.4 Thermal Model of Phase Change Material 81
3.2 Computational Fluid dynamics methodology 83
3.2.1 Governing equations 83
3.2.2 Turbulence models 85
3.2.3 Near wall treatments 87
3.2.4 Enthalpy-porosity approach 89
3.2.5 Solver 90
3.2.6 Spatial discretization 91
3.2.7 Under-relaxation factors 91
3.3 Summary 92
Chapter 4. Validation of CFD approach 94
4.1 Introduction 94
4.2 Validation Analysis for PV-temperature 94
4.2.1 Geometry, mesh, and materials 95
4.2.2 Boundary and Initial conditions 96
4.2.3 Results and discussion 97
4.3 Validation Analysis for heat transfer in water pipe . 100
4.3.1. Model setup 100
4.3.2 Mesh, material and boundary conditions 101
4.3.3 Results and discussion 102
4.4 Validation Analysis for PCM 104
4.4.1 CFD Validation of solidification and melting approach against Solid (specified heat capacity) approach 104
4.4.2 CFD Validation of PCM using solid only method against data from literature 114
4.5 Summary 123
Chapter 5. Study on thermal performance of Salt Hydrate PCM 125

5.1 Introduction 125
5.2 Model setup 125
5.3 Comparison between PCM and water 126
5.4 Thermal performance of PCM-HS22P 128
5.5 Effects of PCM thermal properties 134
5.5.1 The effect of thermal capacity 137
5.5.2 The effect of fusion heat 138
5.5.3 Effect of phase change temperature 139
5.5.4 The effect of thermal conductivity (k) 140
5.5.5 The effect of temperature related thermal conductivity 142
5.6 Summary 147
Chapter 6. Analysis of the PVT-PCM system components ... 148
6.1 Introduction 148
6.2 Proposed design of the novel PVT-PCM system 148
6.2.1 System components 149
6.2.2 System working principles 152
6.2.3 Latent heat utilization 153
6.3 Analysis of system components 154
6.3.1 Pump power calculation 154
6.3.2 Parametric analysis on PV side 157
6.3.3 Parametric analysis on PCM side 167
6.3.4 Fin analysis for PCM storage system 178
6.4 Summary 194
Chapter 7. PVT-PCM optimization for UK weather. 196
7.1 Introduction 196
7.2 Performance evaluation for PV only system 198
7.2.1 Summer design day 200
7.2.2 Winter design day 202
7.3 PVT-PCM system design and optimization 203
7.3.1 PCM storage panel sizing 203
7.3.2 System specification 204
7.4 System performance evaluation and optimization . 205
7.4.1 PV performance under maximum loads 206
7.4.2 PCM performance under maximum load 209
7.4.3 Additional fin design 210

7.4.4 PVT-PCM pump sizing 216
7.4.5 Hourly analysis – daytime 216
7.4.6 Ability of PCM self-heat dissipation 223
7.5 Performance comparison 226
7.5.1 PV panel thermal management 227
7.5.2 PV electrical performance 232
7.6 Energy saving potential of PVT system 236
7.7 Cost analysis 238
7.8 Summary 242
Chapter 8. Potential heat utilization – Case study 244
8.1 Introduction 244
8.2 PCM melting condition prediction 247
8.3 Air preheating 248
8.3.1 System description 248
8.3.2 Case model setup 249
8.3.3 Results and discussion 251
8.4 Water preheating 257
8.4.1 System description 257
8.4.2 Case model setup 258
8.4.3 Results and discussion 259
8.5 Summary 261
Chapter 9. PVT-PCM system in Subtropical climate 262
9.1 Introduction 262
9.2 Thermal Performance analysis 263
9.2.1 Summer design day 264
9.2.2 Winter design day 267
9.3 Electrical performance analysis 270
9.3.1 Summer design day 270
9.3.2 Winter design day 271
9.4 Energy saving potential 273
9.5 Cost analysis 275
9.6 Latent heat utilization 276
9.7 Performance comparison under two climate conditions 278
9.8 Summary 279

Chapter 10. Conclusion and Recommendations 280
10.1 Introduction 280
10.2 Achievements and Findings 281
10.3 Limitations 284
10.4 Future work 284
Bibliography 285
Appendix 302

LIST OF FIGURES

Figure 1.1 Energy consumption structure outlook 2
Figure 1.2 Low carbon electricity's share of generation 3
Figure 1.3 Percentage sector shares of UK energy consumption in 2015.....3
Figure 1.4 Layout of the proposed PVT-PCM system 7
Figure 2.1 PN junctions inside a typical PV cell 12
Figure 2.2 Global annual PV production from 1991-2010 13
Figure 2.3 Cell efficiency regard to temperature. 16
Figure 2.4 Relationship between PV cell temperature against voltage drop under different solar insolation levels.....17
Figure 2.5 IV Curve of Mono-Si PV cell under different temperature.....18
Figure 2.6 Mono-Si Panel output power against voltage under various temperatures. 18
Figure 2.7 PV cell power output wattage against dust thickness recorded by Mailuha et al.....19
Figure 2.8 An example of typical air cooling solutions for PV panel 25
Figure 2.9 The converging channel cooling proposed by Baloch et al.....26
Figure 2.10 Schematic diagram of different solar systems...28
Figure 2.11 Layers of components of a water based PVT system designed by Rockendorf et al. 29
Figure 2.12 A typical roof top BIPVT system.....30
Figure 2.13 Schematic diagram of the air based PVT built with HRV 32
Figure 2.14 Ventilated PV glazing facade.....33

Figure 2.15 Sample configurations of single and double-pass air based PVT systems 34
Figure 2.16 Double-pass BIPVT facade. 35
Figure 2.17 Sample configurations of water based PVT system 36
Figure 2.18. Different absorber flow designs studied by Ibrahim 38
Figure 2.19 Schematic diagram of the hybrid PVT system. .. 42
Figure 2.20 PCM temperature change during the discharging period 43
Figure 2.21 A typical PVT-PCM configuration..... 48
Figure 2.22 PVT-PCM system with metal fins used in Huang et al.’s study 53
Figure 2.23 Cross section view of the aluminium foil TES system 53
Figure 2.24 Schematic diagram of PVT-dPCM system..... 54
Figure 2.26 Model of heat exchange tube with wire used in Koller et al.’s study 59
Figure 2.27 Modular LTS unit from Meng and Zhang’s work. 60
Figure 2.25 PV-PCM configuration 61
Figure 2.26 PVT-MEPCM system..... 63
Figure 2.27 Water based PVT without PCM (top) and with PCM (bottom) 64
Figure 2.28 Wetted PVT collector with added PCM 65
Figure 3.1 Main paths of energy transfer from and to the PV panel 67
Figure 4.1 PV validation model geometry and dimension..... 95
Figure 4.2 Boundary conditions of the CFD model 1 97
Figure 4.3 Steady state temperature of PV cell against wind speed for CFD model..... 98

Figure 4.4 Steady state temperature of PV cell against solar radiation level for CFD model 99
Figure 4.5 Steady state temperature of PV cell against ambient air temperature for CFD model 100
Figure 4.6 Average surface heat transfer coefficient against flow velocity (Turbulent) 103
Figure 4.7 Average surface heat transfer coefficient against flow velocity (Laminar) 103
Figure 4.8 Geometry dimension and structured mesh of the validation model 106
Figure 4.9 PCM temperature against different timestep size in charging process 110
Figure 4.10 PCM temperature against different timestep size in discharging process 110
Figure 4.11 Temperature Profile comparison of PCM-HS22P during Charging process 112
Figure 4.12 Temperature Profile comparison of PCM-HS22P during Discharging process 113
Figure 4.13 3D geometry recreated for Iten et al.'s model 114
Figure 4.14 2D cross-sectional view of the PCM panel in the air duct 115
Figure 4.15 Mesh and boundaries for the PCM-RT25 validation model 116
Figure 4.16 Temperature related Specific Heat of PCM-RT25 read from Iten et al.'s measurements..... 117
Figure 4.17 Temperature contours of the PCM RT-25 from CFD model during charging process from t= 0 (a) with 30min interval..... 119

Figure 4.18 Charging process PCM temperature contours from Iten et al.’s work from t= 0 (a) with 30min interval 119
Figure 4.19 Minimum PCM temperature profile comparison during charging process 120
Figure 4.20 Temperature contours of the PCM RT-25 from CFD model during discharging process from t= 0 (a) with 30min interval..... 121
Figure 4.21 Discharging process PCM temperature contours from Iten et al.’s work from t= 0 (a) with 30min interval .. 121
Figure 4.22 Maximum PCM temperature profile comparison during discharging process..... 122
Figure 5.1 Comparison of average Temperature of Water vs PCM (Charging period) 127
Figure 5.2 Comparison of average Temperature of Water vs PCM (Discharging period) 128
Figure 5.3 PCM temperature contour during charging process 129
Figure 5.4 PCM liquid fraction contour during charging process 129
Figure 5.5 PCM temperature contour during discharging process 130
Figure 5.6 PCM liquid fraction contour during discharging process 131
Figure 5.7 Average Temperature and Liquid Fraction of PCM-HS22P during charging process 132
Figure 5.8 Average Temperature and Liquid Fraction of PCM-HS22P during discharging process 133
Figure 5.9 Temperature profile of PCM-HS22P in charging and discharging process using solid and liquid state thermal properties. 136

Figure 5.10 PCM temperature profile against time at different heat capacity values..... 137
Figure 5.11 PCM temperature profile against time at different heat of fusion values. 139
Figure 5.12 Temperature profiles of modified PCM with different phase change temperature..... 140
Figure 5.13 Temperature profile of modified PCM-HS22P in discharging process with different thermal conductivities .. 141
Figure 5.14 Comparison of time needed for completing discharging process for PCM with different thermal conductivities 142
Figure 5.15 Temperature profiles of modified PCM sets A,B,C,D,E against time 143
Figure 5.16 Discharging time comparison between constant thermal conductivity against temperature related thermal conductivity 145
Figure 5.17 Time required for charging process against different solid phase thermal conductivity values. 146
Figure 6.1 3D illustration of a sample configuration of the PVT-PCM system..... 150
Figure 6.2 Daytime operation schematic diagram of the PVT-PCM system 152
Figure 6.3 Schematic illustration of water preheating configuration..... 154
Figure 6.4 Schematic illustration of air preheating configuration..... 154
Figure 6.5 Pump energy requirement against flow speed .. 157
Figure 6.6 3D geometry of the PV model 158
Figure 6.7 Temperature monitor line on PV panel surface.. 160

Figure 6.8 X-Y Plot of PV cell temperature against X position in different flow velocity 161
Figure 6.9 Average temperature of Panel and water outlet against flow velocity..... 161
Figure 6.10 Water inlet and outlet temperature difference against flow velocity..... 162
Figure 6.11 X-Y Plot of PV cell temperature against X position in different solar radiation conditions (Φ, W/m^2) at flow velocity of 0.05m/s 164
Figure 6.12 Average temperature of panel and outlet water in different solar radiation conditions (Φ, W/m^2) at flow velocity of 0.05m/s..... 164
Figure 6.13 X-Y Plot of PV cell temperature rise against X position in different water inlet temperatures 165
Figure 6.14 Outlet and inlet temperature difference under different ambient temperatures 166
Figure 6.15 Temperature contour comparison of parallel and counter flow. 167
Figure 6.16 3D geometry and 2D slice of the PCM model .. 168
Figure 6.17 Schematic diagram and boundaries of the PCM model 169
Figure 6.18 PCM temperature contour of the charging process at flow velocity of 0.05m/s..... 170
Figure 6.19 Average PCM temperature against time during charging period under different inlet water velocities..... 171
Figure 6.20 PCM liquid fraction against time of different flow velocities. 172
Figure 6.21 Total charging and discharging time required against different flow velocities..... 172

Figure 6.22 Average water outlet temperature against time during under different inlet water velocities..... 173
Figure 6.23 Average PCM temperature against time under different inlet water temperatures..... 175
Figure 6.24 PCM liquid fraction against flow time during discharging process under different inlet water temperatures 175
Figure 6.25 Total charging and discharging time required against different inlet temperature..... 176
Figure 6.26 Average water outlet temperature against time under different inlet water temperature 177
Figure 6.27 Common designs of longitudinal fins 178
Figure 6.28 model geometry used for interval analysis (not to scale)..... 180
Figure 6.29 Comparison of time-related PCM temperature contour between case with 25mm fin interval and reference case in charging process..... 181
Figure 6.30 Average PCM temperature against flow time for various fin intervals in charging process 182
Figure 6.31 Average PCM temperature against flow time for various fin intervals in discharging process 183
Figure 6.32 Charging and discharging time requirement of fins with different length/interval ratio..... 184
Figure 6.33 Geometries of the Fin length analysis models . 186
Figure 6.34 Temperature and liquid fraction contour of the fin length analysis models at time of 1hr, 2hr, 3hr and 4hr during charging process 187
Figure 6.35 Temperature and liquid fraction contour of the fin length analysis models at time of 1hr, 2hr, 3hr and 4hr during discharging process 188

Figure 6.36 Fin temperature drop against times during charging process 189
Figure 6.37 Fin temperature drop against times during discharging process 189
Figure 6.38 PCM liquid fraction against time during charging process 190
Figure 6.39 PCM liquid fraction against time during discharging process 190
Figure 6.40 Average PCM temperature against time for charging process 191
Figure 6.41 PCM melt fraction contour at stage A(top left), B(top right), C(bottom) 192
Figure 6.42 Average PCM temperature against time for discharging process 193
Figure 7.1 Sample illustration of additional PCM enclosure with dampers and a simple damper contol algroism 198
Figure 7.2 Hourly PV temperature profile in windy condition (Summer Design day) 200
Figure 7.3 Hourly PV temperature profile in calm condition (Summer Design day) 201
Figure 7.4 Hourly PV temperature profile in winter design day for both calm and windy conditions 203
Figure 7.5 Cross sectional view of the PV and PCM parts ... 205
Figure 7.6 Meshing of the sliced PV absorber unit 207
Figure 7.7 Temperature contour of the PV surface on the heatsink 207
Figure 7.8 Average temperature of PV panel and outlet water 208
Figure 7.9 Temperature contour at the outlet end of PCM storage tank 210

Figure 7.10 Dimension and placement of the added fin..... 211
Figure 7.11 Temperature contour at the outlet end of PCM storage tank with added fin..... 212
Figure 7.12 Temperature contour of added fins..... 213
Figure 7.13 Comparison of melt fraction contour of the cross-sectional area of the PCM panel at time = 18000s..... 213
Figure 7.14 PCM melt faction contour comparison between two different inlet velocity settings..... 214
Figure 7.15 Comparison of average PCM temperature and water outlet temperature between model with fins and model without fins..... 215
Figure 7.16 Flow chart of the hourly simulation process.... 218
Figure 7.17 PCM outlet water temperature under different inlet temperature settings..... 218
Figure 7.18 Daily maximum temperature contour of PV temperature at 12:00 (summer)..... 219
Figure 7.19 Hourly liquid fraction contour of the vertical and horizontal cross-sectional area of the PCM storage panel (summer) 220
Figure 7.20 Hourly average temperature profile of PCM and the outlet water (summer)..... 221
Figure 7.21 Daily maximum temperature contour of PV temperature at 16:00 (winter) 222
Figure 7.22 Hourly average temperature profile of PCM and the outlet water (Winter) 223
Figure 7.23 Hourly liquid fraction contour of the cross-sectional area of the PCM storage panel during summer night time..... 225
Figure 7.24 PCM temperature comparison of the two working modes with/without latent heat utilization..... 225

Figure 7.25 Summer time hourly average PV temperature comparison (Windy day) 228
Figure 7.26 Summer time hourly average PV temperature comparison (Calm day) 229
Figure 7.27 Winter time hourly average PV temperature comparison (Windy day) 231
Figure 7.28 Winter time hourly average PV temperature comparison (Calm day) 231
Figure 7.29 Summer time hourly PV electricity output comparison (Windy day) 232
Figure 7.30 Summer time hourly PV electricity output comparison (Calm day) 233
Figure 7.31 Winter time hourly PV electricity output comparison (Windy day) 235
Figure 7.32 Winter time hourly PV electricity output comparison (Calm day) 235
Figure 8.1 A sample configuration of PVT-PCM system used for the case study 245
Figure 8.2 Sample configurations of PCM modules (stacked modular panel, 4 x 5 modular panel and 4 x 5 combined panel) 246
Figure 8.3 Detailed vie of PCM panel inside the ventilation channel 246
Figure 8.4 Schematic diagram of the designed air preheating system 249
Figure 8.5 Cross sectional view of the ventilation channel. 249
Figure 8.6 Geometry and dimension of air pre-heating model 250
Figure 8.7 Room air temperature contours with 2℃ inlet temperature 252

Figure 8.8 Room air velocity vectors with 2℃ inlet temperature..... 252
Figure 8.9 Temperature and velocity at different inlet temperature..... 253
Figure 8.10 Correlation between room temperature and inlet temperature..... 254
Figure 8.11 Room temperature under different PCM storage surface temperature..... 255
Figure 8.12 Correlation between room temperature and PCM storage surface temperature 255
Figure 8.13 Monthly comparison between ambient temperature and predicted preheated room temperature .. 256
Figure 8.14 Schematic diagram of the water preheating configuration..... 258
Figure 8.15 Geometry of the water preheating model..... 258
Figure 8.16 Liquid fraction contour of PCM panel cross-section after 1 hour..... 259
Figure 8.17 Temperature profile of pre-heated water and PCM against time..... 260
Figure 9.1 Summer design day PV panel temperature comparison of PVT-PCM and PV only setup in windy condition. 265
Figure 9.2 Summer design day PV panel temperature comparison of PVT-PCM and PV only setup in calm condition. 265
Figure 9.3 Melt fraction contour of PCM-S32..... 266
Figure 9.4 Temperature profile comparison of PCM, PCM outlet and PV outlet (Summer). 267

Figure 9.5 Winter design day PV panel temperature comparison of PVT-PCM and PV only setup in windy condition. 268
Figure 9.6 Winter design day PV panel temperature comparison of PVT-PCM and PV only setup in calm condition. 268
Figure 9.7 Temperature profile comparison of PCM, PCM outlet and PV outlet (Winter)..... 269
Figure 9.8 Summer time hourly electricity output comparison (Windy condition) 271
Figure 9.9 Summer time hourly electricity output comparison (Calm condition)..... 271
Figure 9.10 Winter time hourly electricity output comparison (Windy condition) 272
Figure 9.11 Winter time hourly electricity output comparison (Calm condition)..... 273
Figure 9.12 Temperature profile of PCM and pre-heated water temperature..... 277

LIST OF TABLES

Table 2.1 Comparison of different basic cell types under various factors. 13
Table 2.2 Comparison between paraffin and salt hydrate PCMs 46
Table 3.1 Properties of the PV panel components 69
Table 3.2 PV panel equivalent thermal physical properties... 70
Table 3.3 Under Relaxation Factors used in FLUENT..... 92

Table 4.1 Mesh element counts and RMS error for CFD model 1 95
Table 4.2 Mesh element counts and RMS error of heat transfer validation model 102
Table 4.3 Mesh element counts and RMS error for liquid approach model 106
Table 4.4 Mesh element counts and RMS error for PCM-RT25 validation model 116
Table 4.5 Thermal physical properties of PCM-RT25 116
Table 5.1 Input data of PCM-HS22P thermal properties 135
Table 6.1 Properties from BP-275L manufacturer datasheet 150
Table 6.2 Properties from PCM-HS22P manufacturer datasheet 151
Table 6.3 Mesh element and RMS error of the PV analysis model 158
Table 6.4 Parameter sets of the PV side analysis 159
Table 6.5 Mesh element and RMS error of the PCM parametrical analysis model 168
Table 6.6 Parameter sets of the PCM side analysis 169
Table 7.1 Hourly ambient temperature and solar radiation of summer and winter design days of Nottingham, UK 196
Table 7.2 Sizing of required PCM material 204
Table 7.3 Energy saving potentials of the PVT-PCM system compared with PV only system 237
Table 7.4 Overall daily electrical and thermal efficiency 237
Table 7.5 Material cost of PCM 238
Table 7.6 Material cost of Copper plate and pipe 239
Table 7.7 Material cost of aluminium pipe and sheet 239
Table 7.8 Material cost of water pump 240

Table 7.9 Total additional material cost of PVT-PCM (apart from PV)..... 240
Table 7.10 Yearly saving estimation..... 241
Table 7.11 Discounted payback period calculation 241
Table 8.1 Monthly PCM melting ability estimation 248
Table 9.1 Hourly ambient temperature and solar radiation of summer and winter design days of Shanghai, China..... 262
Table 9.2 PlusICE PCM-S32 properties. 263
Table 9.3 Sizing of required PCM material 263
Table 9.4 Energy saving potentials of the PVT-PCM system 274
Table 9.5 Overall daily electrical and thermal efficiency..... 274
Table 9.6 Adjusted additional cost of PVT-PCM..... 275
Table 9.7 Yearly saving estimation for Shanghai 275
Table 9.8 Discounted payback period calculation for Shanghai 276
Table 9.9 Comparison of some key factors under two climates 279

NOMENCLATURE

C	Heat Capacity (J/kg.K)		ε	Emissivity
T	Temperature (K)		η	Efficiency
t	Time (s)		Φ	Incident irradiance (W/m^2)
h	Heat transfer coefficient (W/m^{2}K)		k	Thermal conductivity (W/(m.K))
Q	Energy (W/m^2)		v	Kinematic Viscosity (m/s^2)
q	Net energy (W)		μ	Dynamic viscosity (Pa-s)
A	Area (m^2)		σ	Stefan-Boltzmann constant
W	Width (m)		Pr	Prandtl number
H	Height (m)		Nu	Nusselt Number
u	Velocity (m/s)		Re	Reynolds number
L_x	Long wave irradiance (W/m^2)		Ra	Rayleigh number
F_{xy}	View factor		Gr	Grashof number
ρ	Density (kg/m^3)		f	Friction factor
m	Mass (kg)		$\bar{\bar{T}}$	Stress tensor
$\dot{m}$	Mass flow rate (kg/s)		$\vec{F}$	External body Force
d	Thickness (m)		$\vec{J_J}$	Diffusion flux of species J(mol/m^{2}s)
α	Absorbance		$\bar{\bar{t}}$	Shear stress (Pa)
S	Heat Source (W)			

CHAPTER 1. INTRODUCTION

1.1 Introduction

At present, the rapid increase of global energy consumption has become a major concern. According to the international energy outlook (IEO) 2016, the world energy consumption increases from 524 quadrillion Btu in 2010 to 630 quadrillion Btu in 2020 and 820 quadrillion Btu in 2030, and most of the growth will be made by the developing countries (EIA, 2016). The transformation and adjustments of energy consumption structure are urgently needed to prevent global energy crisis. Thus, the development of new energy and renewable energy is becoming more and more important. Figure 1.1 below shows the energy structure outlook from 2012 – 2040, by the year of 2040, there will be 25% - 30% percent energy produced by renewable technologies. Compare with the current renewable market, there is a huge developing potential.

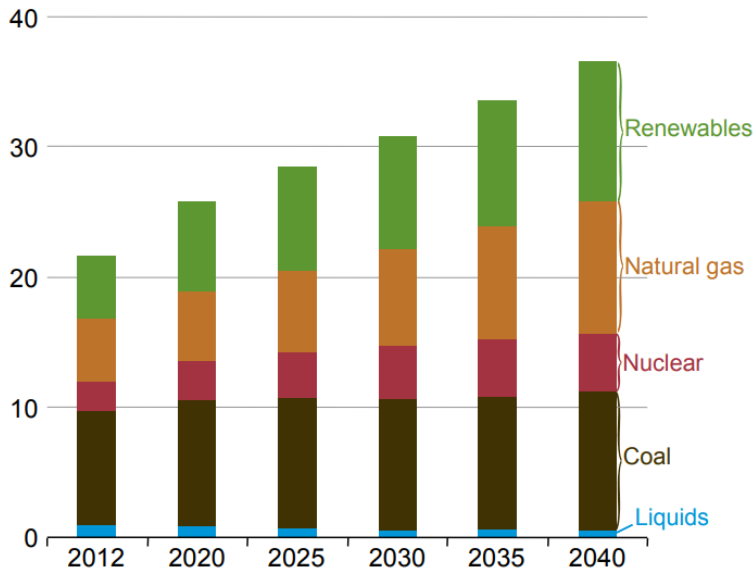


Figure 1.1 Energy consumption structure outlook (EIA, 2016)

Today more than 50% of the electricity in the UK is generated by low carbon energy resources as shown in Figure 1.2 below, which includes clean energy sources like wind, solar, hydro and biomass as well as nuclear power. The percentage of low carbon generation in Scotland is even greater, at 77%. The percentage of electricity generated from coal-fired power plants has dropped from 34% in 2006 to less than 2% in Q3 2016. In the next decade, the percentage of low carbon electricity generation will continue to rise, and another 25GW of new electricity generation is likely to be needed by the UK in the year 2025 (DBEIS, 2016).

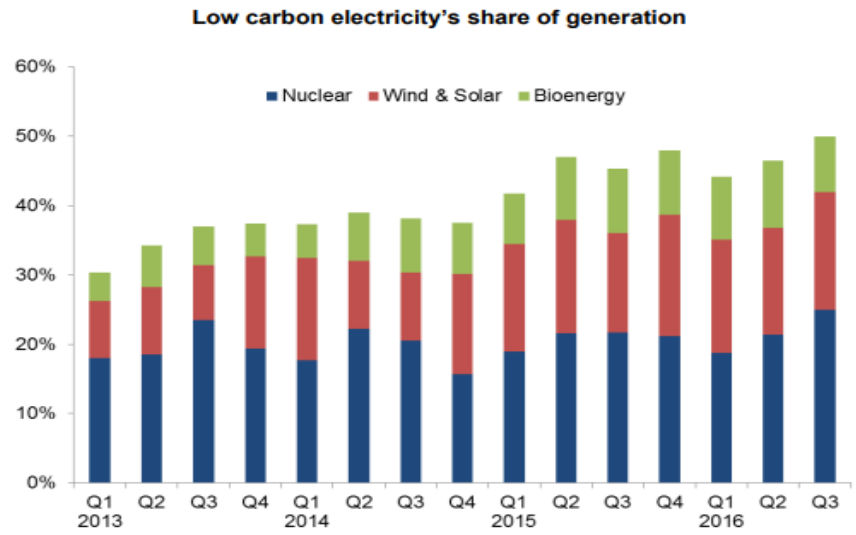


Figure 1.2 Low carbon electricity's share of generation (DBEIS, 2016)

Figure 1.3 shows the percentage sector shares of UK energy consumption in the year 2015. It can be seen from the figure that the domestic sector comprises the most important energy consumer. In recent decades, small scale household renewable energy technologies have been used to reduce energy demand from the national grid as well as reducing carbon footprint. Among them, technologies that utilize solar energy to provide heat and electricity has become the most popular choices in the UK for average householders.

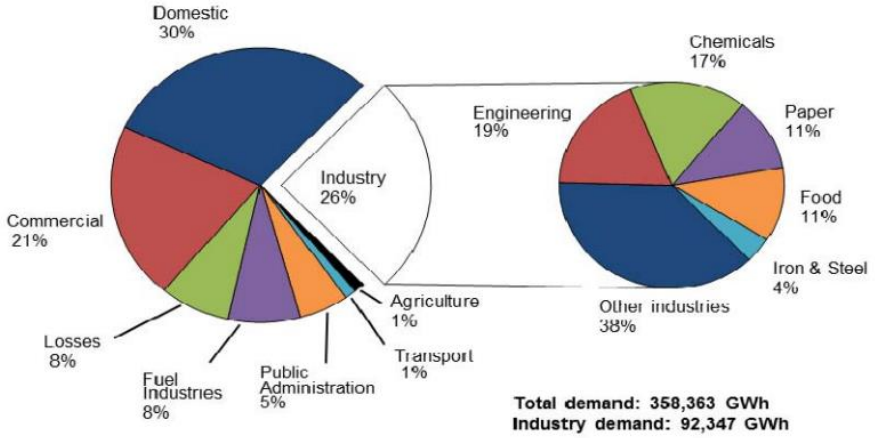


Figure 1.3 Percentage sector shares of UK energy consumption in 2015 (DBEIS, 2016)

As a major renewable energy source with the most noticeable characteristics of inexhaustibility and environmental friendliness, solar energy has great research values and broad application prospects. The solar energy technology and its applications have developed significantly over the recent years. Among them, two widely used systems have been developed to utilize solar energy: solar thermal system which converts solar energy into thermal energy, and photovoltaic (PV) system which converts solar energy into electrical energy. These two systems are ideally suitable for buildings as they can provide heating as well as the electricity to fulfil partial or even the whole amount of building energy requirement.

The first photovoltaic application used for buildings appears during the early 1970s. It was framed by aluminium and mounted on the roof to provide electricity for off-grid houses. After several decades of development, building integrated photovoltaic (BIPV) system, which is the PV system specially designed to replace the conventional building envelope, has been commercially available. BIPV has many advantages over the conventional wall or roof mounted flat plate PV systems. The biggest advantage is that the initial cost of BIPV can be reduced by replacing the normal building envelope during the building design process, hence material and labour cost for the replaced building envelope could be saved. As a matter of fact, the BIPV has become one of the fast-growing applications of the PV industry. However, in 2011, the U.S. National Renewable Energy Laboratory mentioned that the overall cost of the BIPV applications is still less economical compared with other types of PV applications at the moment, as there are still

many technological challenges which might need to be solved before having the actual financial feasibility.

1.2 Problem Statement

With the vast advancement of global PV market, the overheating of PV cells under intense sunlight becomes a major concern. The excess amount of heat accumulated on the PV panel surface will not only reduce the photovoltaic efficiency but also reduce the life span of the PV cells. In some extreme conditions, the overheated surface temperature could reach to such a high temperature that may become a fire hazard to the surroundings. For combined PV Thermal (PVT) applications, although higher fraction of solar energy can be utilized compared with PV applications, the photovoltaic efficiency is still greatly affected by the thermal collecting part of the system.

Moreover, most PVT systems nowadays are either air based or water based, and both types have their limitations. The air based PVT system could not effectively cool down the surface panel during hot days, and the thermal energy utilized is significantly less compared with water based PVT systems. On the other hand, the water based PVT systems often have bulky water storage tanks in order to store that amount of thermal energy.

During recent years, phase change materials (PCMs) have been used by some researchers as an alternative solution to regulate PV cell temperature. At the moment, almost all PCM based PVT

systems share a similar design which consists a flat plate PV panel with an added PCM layer sticks to its backplate. While results prove that PCM could effectively reduce the peak cell temperature, due to PCMs' low thermal conductivity properties, the enhancement is still restricted by the back mounted design. Moreover, most studies of PVT-PCM applications are more focused on the temperature regulating potentials; the related latent heat utilization is sometimes not considered.

Thus, it is imperative to have a PVT-PCM system that has enhanced photovoltaic thermal performance, in a relatively small sized footprint.

1.3 The proposed PVT-PCM system

Instead of using common back mounted design, the novel PVT-PCM system proposed in this study has a separate design to allow much flexible configuration. Instead of adding the PCM directly to the PV panel, the proposed design uses recirculated water to achieve better heat transfer between PV and PCM. The 3D layout of the system is shown in Figure 1.4. During the daytime, unwanted thermal energy is stored in the PCM as latent heat via recirculated water, and the stored latent heat can be utilized by demand. More detailed description of the system is presented in Chapter 7.

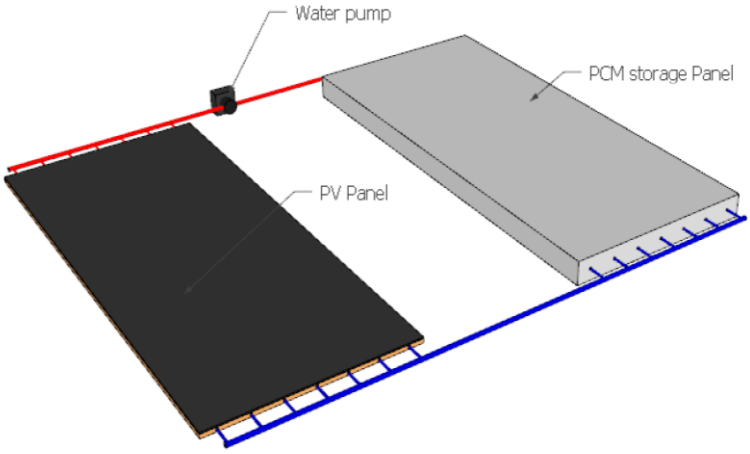


Figure 1.4 Layout of the proposed PVT-PCM system

The novel PVT-PCM system has superior electrical performance over conventional air/water based PVT systems and back mounted PVT-PCM systems, without sacrificing thermal performance. Meanwhile, under the same system performance, the size of PCM storage is significantly smaller compared to the conventional water based storage solutions. Moreover, the PCM storage could also be integrated into the building structure such as floor or ceiling which doubles as an additional insulation layer. By doing so, the required space for the proposed PVT-PCM system could be further reduced, while at the same time, the unwanted fabric heat loss/gain could be better controlled due to the additional PCM insulation layer.

At the moment, there are no other studies sharing the similar design of the proposed PVT-PCM system. Thus, this work is conducted to investigate the practicality of this design as well as its relevant performance potentials.

1.4 Aims and Objectives

The aim of this research is to evaluate the energy and economic performance of the proposed novel PVT-PCM system. The following objectives need to be accomplished for this study:

1) To evaluate the performance of conventional PV panel in different environmental conditions as a reference;

2) To design a novel PVT-PCM system which has better overall performance without sacrificing other parameters such as compactness or cost;

3) To develop analytical and numerical models for the components of proposed PVT-PCM system;

4) To conduct parametric analysis for each of the system components;

5) To evaluate the performance of the proposed PVT-PCM system in transient environmental conditions;

6) To optimize the proposed PVT-PCM system for real environmental uses.

7) To discover the feasibility of PVT-PCM's latent thermal energy utilization via a case study;

1.5 Thesis Structure

The thesis consists of 11 chapters. Below is the brief description of the contents of each chapter.

- Chapter 1 – Introduction chapter that provides background information for the research, the problem and motivations of the study, as well as the objectives that need to be accomplished during the study.

- Chapter 2 – Literature review that provides the framework of the current knowledge about PV/PVT and PVT-PCM applications which is critical to this study. Literature is organized and presented in different system classifications.

- Chapter 3 –The analytical models used for evaluating the thermal and electrical performance of the system are presented. Principle and methodology of the computational fluid dynamics (CFD) are discussed. The governing equations are presented. The parameter selection of turbulence model as well as solver setup are presented and discussed.

- Chapter 4 – The analytical calculations and the CFD models are validated with each other along with results from the literature. The CFD model is proved to be valid for further analysis.

- Chapter 5 – The study of the characteristics of PCM-HS22P is presented. The effect of each thermal physical properties against the overall thermal performance is analysed and discussed.

- Chapter 6 – The proposed design of the novel PVT-PCM system is presented in this chapter. The parametric analysis of system components is presented. The final results are used to size the PVT-PCM system for real climate situations.

- Chapter 7 – The performance of the PVT-PCM system is evaluated under the real climate conditions of Nottingham, UK. The thermal and electrical performance is compared with conventional PV only configuration. The energy and economic performance are also presented and discussed.

- Chapter 8 – The potential performance of two proposed latent heat utilization methods under UK weather are presented and evaluated via a case study.

- Chapter 9 – The system's energy and economic performance if used in Shanghai, China is evaluated using the same methodology presented in chapter 8 and 9, and is compared against UK condition.

- Chapter 10 – Conclusion and recommendations conclude the thesis with a brief summary of the results and achievements made during the study, as well as pointing out further research directions.

CHAPTER 2. LITERATURE REVIEW

2.1 Introduction

This chapter provides an extensive review of the literature covering major aspects of PV, PVT and PCM related applications. The review starts with basic principles of PV system. The effects of temperature on PV efficiency are discussed and corresponding thermal management techniques are summarised. After that, various design and optimization studies of PVT and BIPVT system are presented. The basic principles of PCM are also introduced as well as recent studies of PVT-PCM integration. In addition, some numerical studies are also reviewed, which are helpful for the design, evaluation, and optimization of the novel PVT-PCM system studied in this work.

2.2 Photovoltaic system

Photovoltaic (PV) system is currently a mature technology to generate and supply electric energy by converting a portion of solar energy. The photovoltaic effect was first discovered by Edmund Becquerel in 1839, and the first silicon solar cell was made later by Daryl Chaplin, Calvin Fuller and Gerald Pearson in 1954 (Chaplin et al., 1954). The core design of the PV cell at

that time is not changed by much compared with modern PV panels. A typical PV system consists of multiple arrays of photovoltaic cells (solar cells), which is a semiconductor incorporated with PN junction to develop photo voltage when exposed to the light (Goetzberger, 2003). Figure 2.1 below illustrates the construction of a typical PV cell.

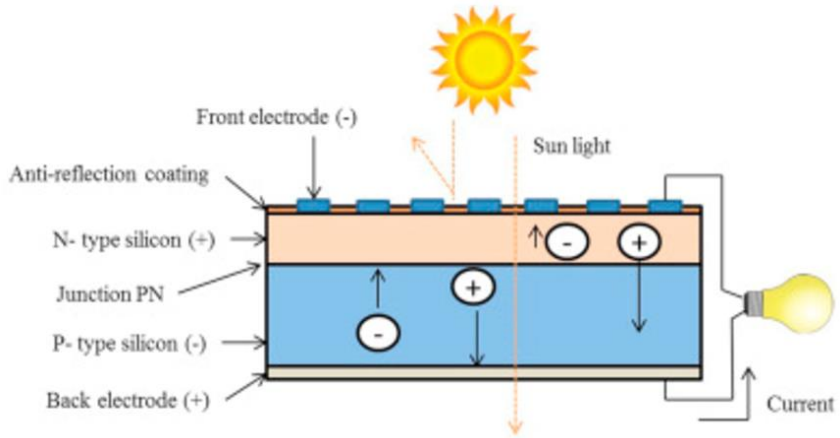


Figure 2.1 PN junctions inside a typical PV cell (Goetzberger, 2003)

Despite of the great energy saving potential, during early years, PV panel is often considered to have very poor economic performance due to its high manufacturing cost. However, with the improvement of manufacturing techniques and the expanding of global PV market in recent decades, the cost of PV panel has dropped significantly. Figure 2.2 below shows the annual production growth of the PV module. It can be seen that the annual power produced by PV has increased by almost 1000 times, and the relative annual growth was also growing steadily. Although PV installation at the moment only takes about 0.1% of the global electricity generation, a market review indicated that there will be a 40% annual growth on this potential market (Zhang et al., 2012). With the development

of the PV market, the manufacturing cost of the panel will continue to drop, and PV is becoming a competitive mean of electrical generation by the public.

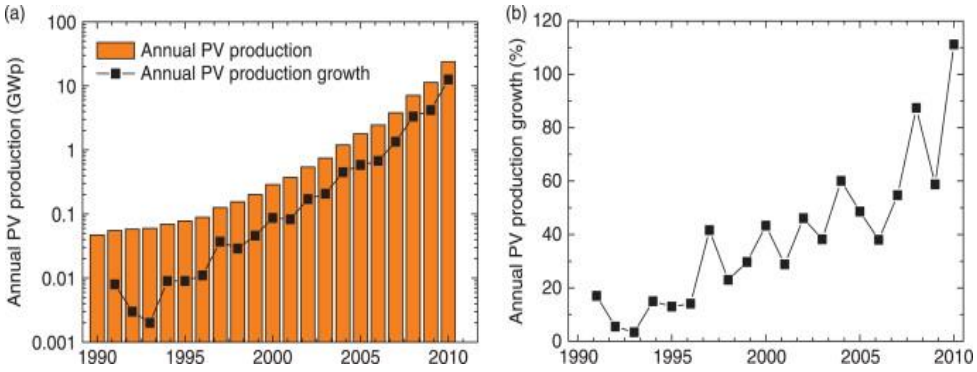


Figure 2.2 Global annual PV production from 1991-2010 (Zhang ET AL., 2012)

2.2.1 PV module type

The PV module types used in common PV applications could be divided mainly into three categories; Monocrystalline Silicon module, Polycrystalline Silicon module and thin-film module. Table 2.1 shows the comparison of three module type based on other's literature (Sendy 2017; NEF 2017).

Table 2.1 Comparison of different basic cell types under various factors.

	Mono-Si	**Poly-Si**	**Thin film**
Higher efficiency	✓✓	✓	
Lower cost		✓	✓✓
Better durability	✓✓	✓	
Compactness		✓	✓✓
Better at hot climate	✓		✓✓

Lower performance degradation	✓✓	✓	
Better economic efficiency		✓	✓✓
Note: ✓✓ = best, ✓ = average, no ✓ = worst			

The Monocrystalline Silicon module is generally the most efficient type of PV module that is commercially available at the moment. The average efficiency of Monocrystalline Silicon modules is around 15%. The manufacturing cost of Monocrystalline Silicon modules is the highest compared to Polycrystalline Silicon modules or thin film modules due to its complicated manufacturing technique.

The Polycrystalline Silicon module uses a simpler and more efficient manufacturing technique. The Polycrystalline Silicon module is cheaper but with a slightly less photovoltaic efficiency around 12%. With the rapid expansion of residential solar panel market, Polycrystalline Silicon modules are the dominant type used for residential applications (Sendy, 2017).

Thin film modules use a technology which is different from monocrystalline silicon and polycrystalline silicon modules. Instead of slicing from a silicon ingot, the photovoltaic substance is deposited on a thin solid surface. The photovoltaic substance commonly used are Amorphous Silicon, Cadmium Telluride (CdTe), Copper Indium Gallium Selenide (CGIS) and Dye-sensitized solar cell(DSC) (NEF, 2017). The thin film modules are the cheapest, but the photovoltaic efficiency is also the lowest (around 6%) compared to Monocrystalline and

Polycrystalline Silicon modules. However, with the rapid advancement of technology, thin film modules have the greatest potential to become the most economical type of PV module.

2.2.2 Effect of cell temperature

As there are more and more extensive studies based on PV panels, the decrease of PV cell efficiency under high solar insolation conditions has been noticed and studied during recent years. When cell temperature rises, the rule of thumb is that the conversion efficiency of crystalline silicon module drops by around 0.5% per ℃ (as shown in Figure 2.3). The conversion efficiency drop of thin film modules, on the other hand, is lower around 0.21% - 0.36% per ℃ depending on the material that made the module (Kumar & Rosen, 2011). Considering the fact that under intense sunlight, un-cooled PV cell temperature could rise significantly, it is hence necessary to consider the degree of surface temperature of PV modules while designing any PV applications as temperature rise can significantly reduce the photovoltaic efficiency.

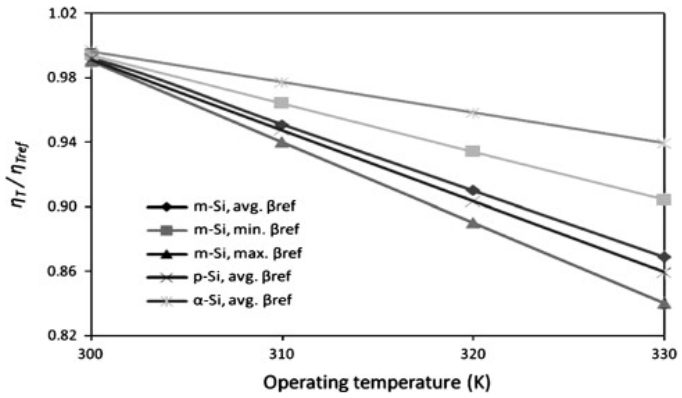


Figure 2.3 Cell efficiency regard to temperature (Kumar & Rosen, 2011).

In general, commercial PV cells only convert around 4% - 17% of total solar insolation into electricity, and more than 50% of solar energy is absorbed as thermal energy (Chandrasekar et al., 2013). As a result, the temperature of PV panel increases rapidly when exposed to direct sunlight. The high temperature of PV panel causes the modules to suffer from both short-term and long-term losses. The short-term loss is the decrease of PV cell's photovoltaic efficiency when the surface temperature is too high. The long-term damage will occur as high temperature causes thermal degradation of the module, and this damage is permanent and irreversible.

The main reason for the reduced efficiency is the decrease of semiconductor's band gap with increased temperature. As a result, the open circuit voltage drops significantly with increased temperature. The decrease of open circuit voltage under high temperature was studied by Huang et al. (2011) by measuring the junction PV cell temperature using an indirect non-destructive method. It is found that voltage drops with

increased cell junction temperature in all solar radiation levels. The correlation of voltage drop against cell junction temperature under difference solar radiation levels is shown in Figure 2.4 below. The drop rate of the voltage is consistent and is independent of solar radiation levels. The estimated drop rate is considered to be around 0.0021V/℃.

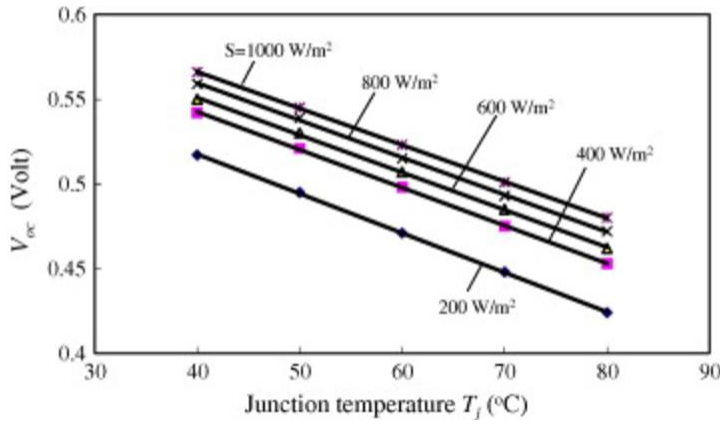


Figure 2.4 Relationship between PV cell temperature against voltage drop under different solar insolation levels (Huang, et al., 2011)

On the other hand, as temperature rises, the decreased band gap of the semiconductor also means a higher short circuit current as the energy carried from valence band to conduction band is increased (Singh et al., 2008). As a result, PV panel with higher temperature will have higher short circuit current. Figure 2.5 shows the difference of the short circuit current (I_{SC}) and open circuit voltage (V_{OC}) under different cell temperatures. It can be seen that the increase of short circuit current is insignificant compared to the drop of open circuit voltage, which leads to an overall efficiency drop. The temperature related overall efficiency is studied by Radziemska (2003). In his experimental study, monocrystalline silicon cells were

tested under different temperatures from 28℃ to 80℃. The results are shown in Figure 2.6. It was found that the cell output power is decreased by 0.65%/ ℃ with increased temperature.

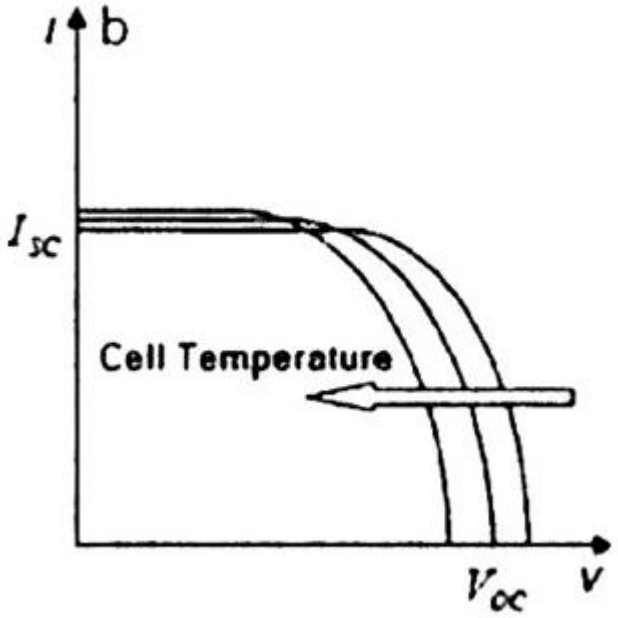


Figure 2.5 IV Curve of Mono-Si PV cell under different temperature (Kalogirou, 2009)

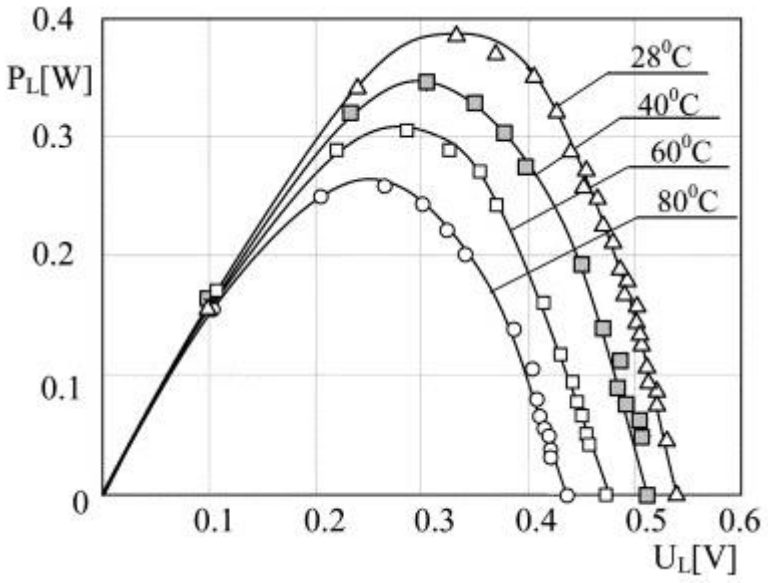


Figure 2.6 Mono-Si Panel output power against voltage under various temperatures (Radziemska, 2003).

2.2.3 Other parameters relating to PV efficiency

One of other reasons of the performance degradation of outdoor PV system is the airborne particles such as dust. The accumulated dust on the surface of PV panel could block incoming solar insolation. Maliuha et al. (1994) studied the effect of dust concentration on the PV cell performance. The results are shown in Figure 2.7. It can be seen from the result that the performance degradation of PV cell is present with high dust concentration on the panel surface, the effect is more significant in conditions with low solar insolation level. A later case study by Radziemska (2015) shows that in northern Poland, the module efficiency degradation due to accumulated dust layer could be as high as 3% per year. It is highly suggested that PV panels should be cleaned regularly in order to maintain its optimum efficiency.

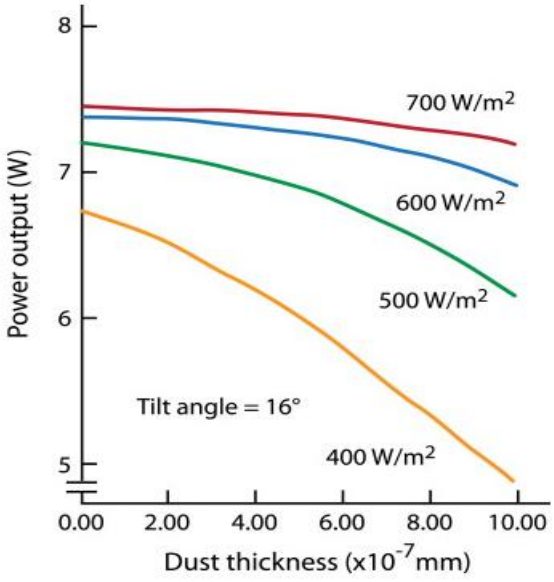


Figure 2.7 PV cell power output wattage against dust thickness recorded by Mailuha et al., (1994).

Karatepe et al. (2007) studied the effect of shadow (non-uniform solar irradiation) on the PV panel regarding to its electrical output. A group of PV modules were arranged into different array configurations. The numerical model was built and simulated at a normal working condition. A later study by Wang et al. (2014) continues to investigate the effect of frame shadow on its electrical performance. The conclusion from the simulation is that area of the shadow will significantly affect the electrical output of PV module even the shaded area is relatively small. There can be as much as 31.6% and 39.3% output reduction on series and parallel circuit, respectively, if part of the PV module is shaded by frame. The suggestion is that the PV cells must be placed without the shaded area at all times, not only shading caused by surround objects but also the shading from its frame.

Another key factor that will affect PV cell efficiency is the tilting angle. Kacira et al. (2004) investigated the effect of collector tilting angle on maximizing solar irradiance on PV panel in Turkey. It was found that the optimum tilting angle was 30 - 50° from Jan to Mar, 0 – 20° from April to Aug and 40 -60° from Sep to Dec. The results indicate that higher tilting angle is recommended during winter time while lower tilting angle is recommended during summer time.

Vasel and lakovidis (2017) studied the effect of wind direction on the PV cell performance. It was found that in northern hemisphere, fixed tilt PV panels generate more electricity under

southerly winds. It was hence suggested that the PV panel should be located on areas with strong and frequent winds from south. On the other hand, in southern hemisphere, the PV panel should be placed at locations with strong northerly wind.

2.3 Thermal management of PV panel

As mentioned above, excessive PV cell temperature could result in both short-term and long-term performance degradation; it is hence necessary to extract the extra amount of energy which is not converted to electrical energy. During recent decades, extensive efforts have been made to the techniques of PV panel thermal management.

2.3.1 Passive cooling and active cooling

There are many approaches that can be employed to provide cooling for PV panels. However, a valid and effective PV thermal management design could not be generalized and is highly dependent on various factors such as the size and geometry of the PV array, the geographical location of the system, and the macro and micro climate conditions where the system locates.

Based on the review of various literature regarding to the PV thermal management techniques, those techniques could fall into two categories: passive cooling and active cooling. Passive cooling does not require additional energy, which usually can

be achieved by utilizing either natural convection or evaporation. Most of the passive cooling enhancement is achieved by adding fins as an extended surface for greater heat exchange rate (Theodore, 2011). More complicated passive cooling techniques include the use of phase change material(PCM) to reduce peak panel temperature or using heat pipes to extract heat from PV panels through condensation and vaporization process.

The limitation of passive cooling techniques, however, is that the effectiveness of the technique is heavily dependent on the local climate conditions. As an example, the passive cooling technique will generally work better in areas with cold and dry climate rather than areas with hot and humid climate. Moreover, the effectiveness of passive cooling technique will also be greatly affected by transient ambient conditions such as ambient temperature and the presence of wind. For example, the passive cooling will have significantly reduced effects when there is little wind.

On the other hand, the active cooling techniques often achieve better cooling performance compared to the passive cooling techniques by using blower fan or water pump to force the air or water to circulate through the heat exchange area. As a result, the effectiveness of the active cooling system is less sensitive to environmental factors such as the wind. One fact needs to be considered is that the active cooling technique consumes additional energy, however, compared to the

increased electrical performance resulted from active cooling, the amount of additional energy consumption is generally considered to be relatively small.

2.3.2 Air cooling

So far, many researches have been conducted to study the effectiveness and performance enhancement of various passive and active cooling designs. Krauter et al. (1999) did experimental studies on the performance comparison of different cooling systems used on a vertical PV facade. The types of cooling system studied are air based natural/forced convection, active water cooling system with additional insulation. It was then compared to the baseline model which has no cooling system with/without additional insulation. The results indicated that the ventilated types have up to 8% increase in electrical power output than conventional PV facades, the electrical power output of the insulation only type is reduced by 9.3% due to the high temperature of the PV module. Moreover, the hybrid system with water cooling system shows an increased 9% electrical power output, and the amount of heat can be utilized by demands.

Gokmen et al. (2016) investigated the effect of wind speed on PV panel cooling in windy conditions. The study shows that the variation of wind speed could significantly affect PV cell temperature. Moreover, the tilting angle will also affect the wind flow especially during summer seasons. It is suggested

the added wind cooling effects could lead to an average increase of 3.5% of the predicted annual electricity output without considering the effect of wind.

Teo et al. (2012) designed an air based active cooling system for PV panels by adding an air duct underneath the back plate of the panel (as illustrated in Figure 2.8). Several manifold designs were presented and discussed in order to ensure the air flow inside the duct is evenly distributed. The system is actively cooled by blower fans. Results show that the cell temperature could drop from 68℃ to 38℃ after using the active cooling, which increased the photovoltaic efficiency from 8.6% to 12.5%. A later parametric study of the same system was done by Farshchimonfared et al. (2015) regarding to the effect of duct depth, air flow speed, air distribution duct diameter against panels with different length/with ratio. It is found that the optimum duct depth is associated with the length and width ratio of the solar panel. It is also noticed that the additional energy required for the fan is accounted at 23.5% of the total energy, which is considered not cost-efficient. In general, compared to the electrical performance gain of active water cooling system, the active air cooling system shows less efficiency due to the less heat extraction ability of air (Xu et al., 2012).

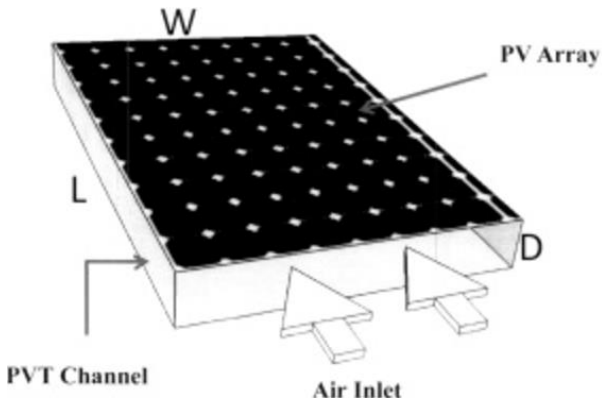


Figure 2.8 An example of typical air cooling solutions for PV panel

2.3.3 Water cooling

Krauter (2004) developed a water cooling and cleaning system that uses water films flow from the top to the bottom of the front panel. The water is pumped to the top and spread on the surface panel by a line of nozzles, and then be collected at the bottom for recirculation. The results show that there is up to 22℃ decrease compared with the panel without cooling, and the daily electricity yield is increased by 10.3%.

Bahaidarah et al. (2013) developed a back surface water cooling system that can be attached on the back side of the PV panel in order to reduce the surface temperature of the PV module. The results show that the temperature has dropped by 20% and the electrical efficiency has therefore increased by 9%. However, the size of their design is relatively large, and the additional energy needed to operate the water pump is not considered in the study.

Baloch et al. (2015) studied the performance of a converging water channel used for cooling PV panel. The schematic of the system is shown in Figure 2.9 below. The result shows that by using the water cooling channel, the maximum cell temperature drops from 71.2℃ to 31.4℃ during the tested period. It is also found that the optimum converging angle ∅ is 2 degree, which has slightly better performance compared to the conventional parallel setup. The cooling effectiveness will drop significantly if the angle ∅ is greater than 2 degree angle due to the low uniformity of the flow. Moreover, from economy's perspective, the cooled setup has 19.5% reduction of LCE(levelized cost of energy), which makes it economically feasible when used in extreme climate conditions.

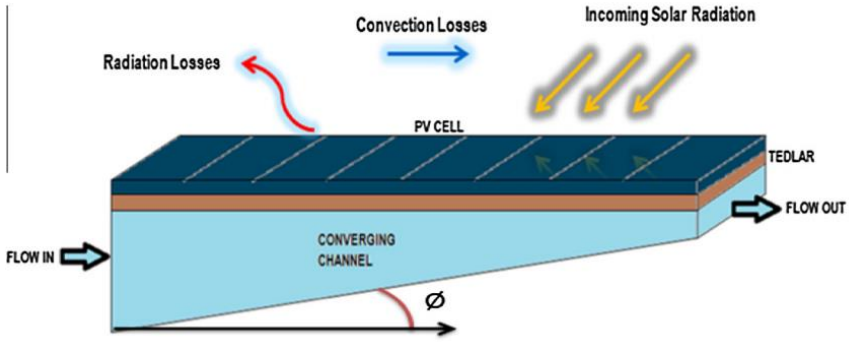


Figure 2.9 The converging channel cooling proposed by Baloch et al. (Baloch et al., 2015)

Alami (2014) has introduced an evaporative cooling system using wet clay pad, and the results show a 19.1% enhancement in output power. However, as stated in his article, an automated water feeding system is needed, which means additional source of energy may be required to provide cooling. The technique is later adjusted by Ebrahimi et al. (2015) by

directly spreading water onto the panel surface. The effect of vapor flow rate, vapor temperature and vapor distribution against solar cell temperature were discussed. It is found that these three parameters are independent of each other, and all has an effect on the cooling performance of PV panel. Among them, vapor temperature is the most important factor that could affect the cell temperature. A similar approach has been used in Schiro et al. (2017)'s work with additional water spreading system installed on the PV panel surface. In order to achieve a uniform water film, 9 spreading nozzles were used, and the total water flow rate was 0.09l/s per m^2 of surface area. The results show that by spreading water on to the surface of the PV panel, the cell temperature could be effectively reduced. The reduction of cell temperature is more significant when in high temperature, no wind, and high solar radiation conditions.

Chandrasekar and Senthilkumar (2015) developed an experimental setup using cotton wick strips to provide cooling for solar panels. The cotton strips are fixed on an aluminum heat spreader located on the back of the PV panel, and both ends are connected with water header. Results show that there is a 5.9℃ peak PV cell temperature drop (from 49.2℃ to 43.3℃) by using the cotton wick cooling, which results in a 1.4% photovoltaic performance increase.

2.4 PVT and BIPVT system

It is discussed in section 2.3 that by adopting proper thermal management solution, PV cell temperature could be greatly reduced under the same load. In order to further improve the efficiency of the PV module and make more use of solar energy, it is desirable to extract the extra amount of heat from the PV module and use as an energy source. PVT and BIPVT are technologies that aim to extract heat from the PV panel, which combines conventional PV panels together with heat extraction components. This kind of system allows cooling of PV panels in order to get higher electrical converting efficiency and at the same time utilizing the extracted heat for heating or other purposes. By doing so, the overall efficiency of the system is dramatically increased, and it is a better way to utilize solar energy. The concept of (BI)PVT system represents an alternative direction for sustainable power generation and heating. Figure 2.10 below indicates the relationship between different existing solar conversion technologies.

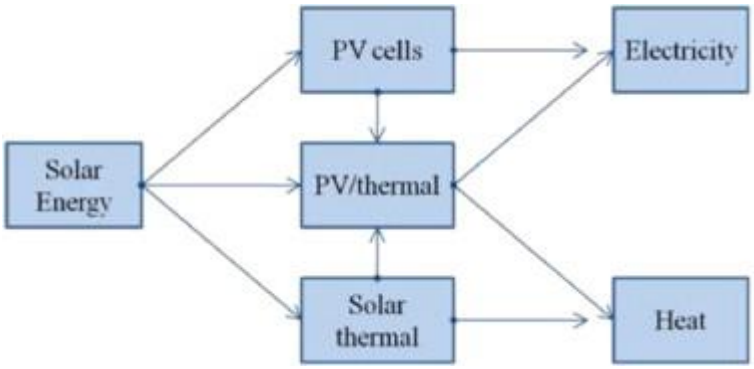


Figure 2.10 Schematic diagram of different solar systems (Zhang et al., 2012)

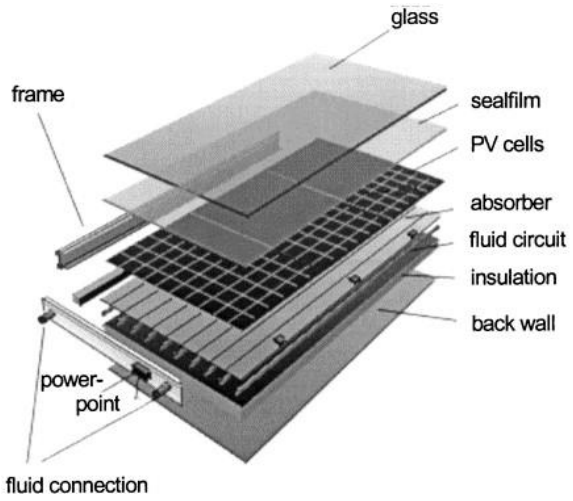


Figure 2.11 Layers of components of a water based PVT system designed by Rockendorf et al. (1999)

A typical PVT system is a sandwiched structure that consists of several layers, the most important layer is the photovoltaic module and the heat extracting components, and the heat extracting components also can be regarded as the active cooling system served for the PV modules. The cooling media (or working fluid) can vary by design. There is usually a thermal insulation layer at the bottom of the PVT panel to provide a near adiabatic boundary. Some of the design will add a glaze layer on top of the PV panel in order to increase the thermal efficiency of the whole system. The efficiency of a PVT system can be regarded as the sum of the photovoltaic efficiency and thermal efficiency. A typical water based PVT collector designed by Rockendorf et al. (1999) is shown in Figure 2.11. The system was later studied and improved by many researchers.

At the same time, with the rapid advancement of building technology and PV manufacturing techniques, PV panels are

showing great potential to substitute part of building exterior components such as roof and vertical façade. Such PV systems are called building integrated photovoltaic (BIPV) systems. The first BIPV system was installed in 1991 (Hao, et al., 2007), after then, the demand for modules for building integration grew rapidly. Most BIPVT systems are designed to be used in the building envelope. The design principle of BIPVT system is more or less the same as the conventional PVT system; however, the BIPVT system is more compact and should be regarded as part of the building façade. Figure 2.12 shows a typical roof top BIPVT system. The BIPVT must be designed not only to optimize conversion of solar energy but also to provide wind and snow load as part of the structural elements. Moreover, other things such as thermal expansion coefficient should also be considered as the BIPVT is built within the building envelope thus damage to either PV panels or the structural substrate may occur as the temperature fluctuates.

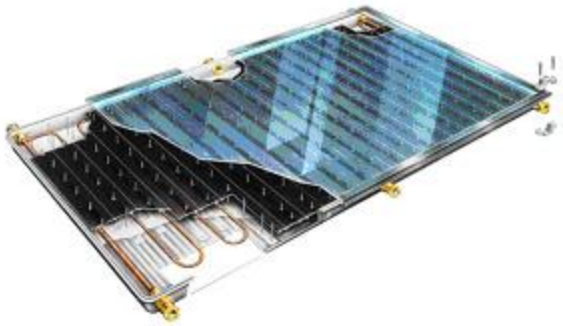


Figure 2.12 A typical roof top BIPVT system

Similar to the thermal management solutions of PV panel, the working principle of PVT and BIPVT system could mainly be divided into two major parts: air based (BI)PVT system and water based (BI)PVT system. The difference between two

systems is the utilization of different cooling media (air and water). Most (BI)PVT systems found in literature uses active cooling techniques to achieve better overall performance.

2.4.1 Air based PVT

The simplest air based PVT system is the single-pass air based PVT system, which has an air duct located on the back of the PV panel. The thermal efficiency of the single-pass PVT system is generally very low at around 10% - 20% (Affolter, et al., 2006). Many researches have been carried out to improve the efficiency of this single-pass PVT system. Mojumder et al. (2016) conducted an experimental investigation on the performance of the single-pass air based PVT system with integrated fins. The result shows that both electrical and thermal performance was enhanced after fins were added. The mass flow rate of air affects the PV performance significantly. At solar radiation level of 700W/m^2, the thermal efficiency difference before and after adding fins is measured to be 19%.

Kim et al. (2014) did an experimental study on the efficiency of a single-pass air based PVT system with aluminium slats inserted in the air duct. It is found that the electrical and thermal efficiencies are measured at 15% and 22% respectively.

Kasaeian et al. (2017) studied the effects of forced convection on the performance of the single-pass air based PVT system. It is found that by variating air duct depth from 0.15 to 0.05m, the overall efficiency is reduced by 20%. On the other hand, by increasing the air mass flow rate from 0.018kg/s to 0.06kg/s, the thermal and electrical performance is increased by 15% - 31% and 12% - 24% respectively.

Ahn et al. (2015) designed a single-pass air based PVT system built into the heat recovery ventilation system. The schematic diagram of the system is shown in Figure 2.13 below. The heat recovery system has an overall heat recovery efficiency of 80%, The added PVT system provides additional fresh air preheating. The result shows that the system is capable of increasing fresh air temperature from 0℃ to 15℃ during the midday of wither period. The heat recovery efficiency was improved by 20% with air preheating using PVT system, and the performance of the PVT system is measured at 38%.

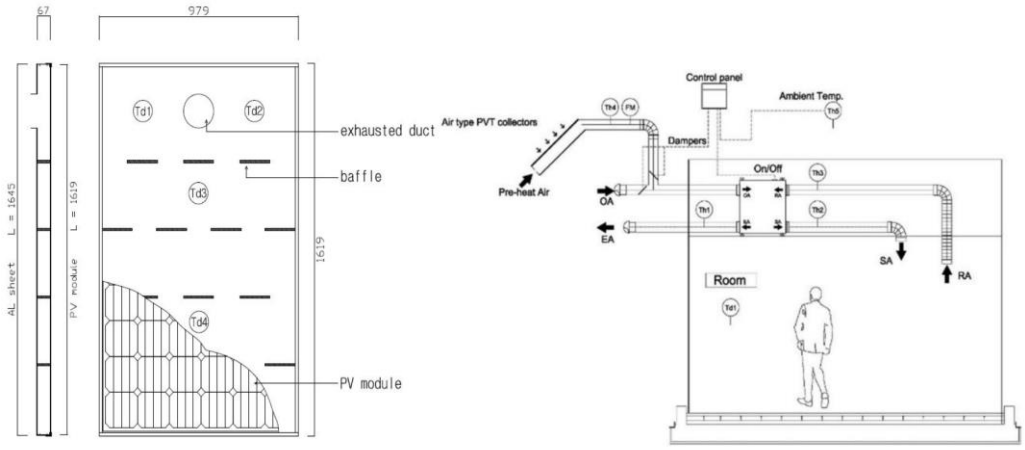


Figure 2.13 Schematic diagram of the air based PVT built with HRV (Ahn et al., 2015)

Agrawai and Tiwari (2010) studied the influence of connection types of a series of single-pass air based BIPVT modules regarding to its performance in cold climatic conditions. In their experimental study, a series of 6 individual BIPVT modules were connected in three different types; the parallel connection, the series connection, and the mixed connection. The connection type only refers to the thermal side but not the photovoltaic side. The result shows that the series connection is more suitable for thermal energy utilization with the highest efficiency of 53.7% when fitted at roof top.

Chow et al. (2007) designed a vertical ventilated PV glazing façade using similar designs of the single-pass air duct. The system is shown in Figure 2.14 below. A later performance study by Chow (2010) shows that this PVT façade could effectively reduce direct solar gain and glare during summer period compared to the normal double-glazing façade. The air conditioning power consumption could be reduced by up to 82%.

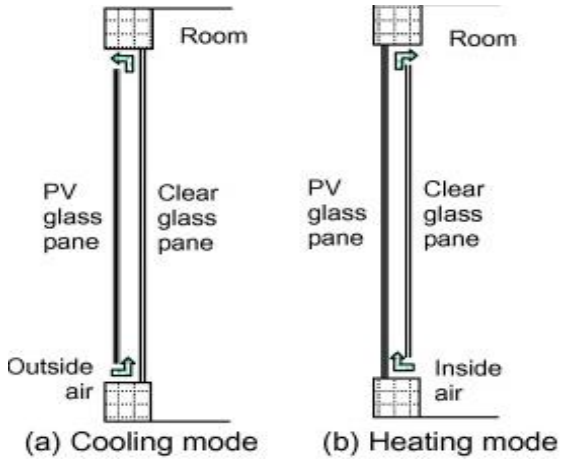


Figure 2.14 Ventilated PV glazing façade (Chow et al., 2010).

Sopian et al. (1996) designed a double-pass air based PVT system and is compared with conventional single-pass air based PVT system. The system adds an additional air duct at the front of the panel while conventional single-pass systems have only one air duct on the bottom of the PV cell. The difference between single and double-pass air based PVT system is shown in Figure 2.15. The obtained result shows that the double-pass system has improved photovoltaic efficiency over the single-pass system, at the same time, the outlet air temperature is higher which represents higher thermal efficiency. The design was later modified by many researchers (Alfegi et al., 2008) (Srinivas & Jayaraj, 2013) (Elsafi & Gandhidasan, 2015) by adding various fin design to improve the overall performance further.

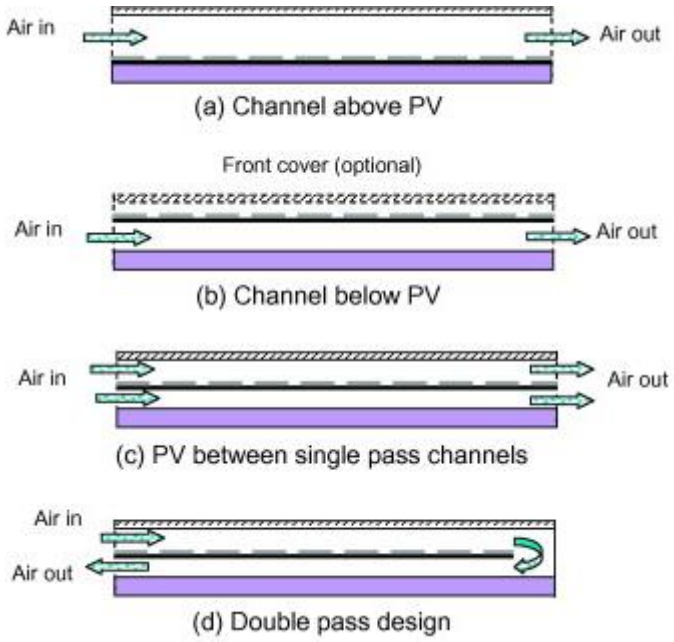


Figure 2.15 Sample configurations of single and double-pass air based PVT systems (Chow, 2010)

Kamthania et al. (2011) designed a BIPVT façade using the same double pass design (shown in Figure 2.16) and evaluated the system performance. The results show that the system could potentially provide a total amount of 1729.84kWh thermal and electrical energy each year. The heated air by the BIPVT system shows a 5-6℃ increase during winter days. It is also suggested that using semi-transparent PV module could have better electrical performance compared with the opaque module due to the much lower module temperature. However, the thermal performance of the system will be reduced accordingly.

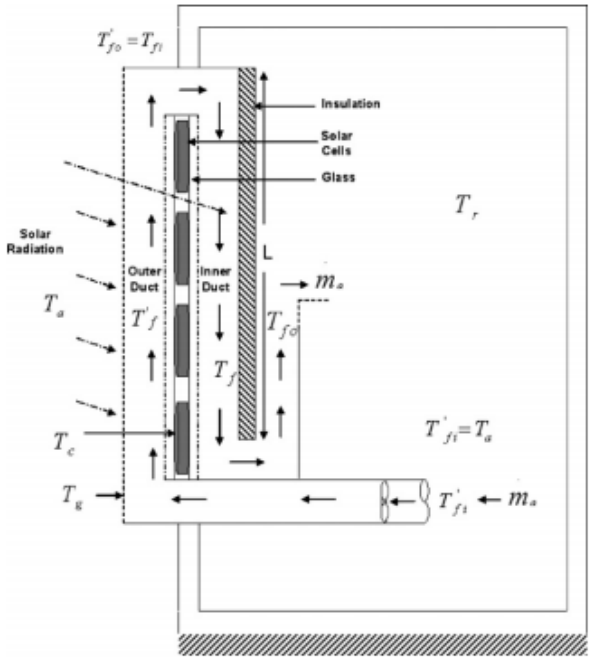


Figure 2.16 Double-pass BIPVT façade (Kamthania et al., 2011).

2.4.2 Water based PVT

The basic water based PVT collector was studied by Florschuetz in 1979 (Kalogirou, 2009). The working principle of a water based PVT or BIPVT system is to use circulated water as cooling media to extract heat from PV panels for water/space heating. A typical sheet and tube water based PVT configuration is shown in Figure 2.17 (a). The water based system is generally more efficient than air based PVT and BIPVT system (Daghigh et al,, 2011). Different water flow patterns could greatly affect the overall performance of the system; hence, researchers are mainly focused on studies to investigate the effectiveness of different water flow patterns. Among them, the most common design is sheet-and-tube design which consists of a flat sheet absorber and several water tubes. Another design is box channel design which consists of many rectangular flow channels below the PV panel. Figure 2.17 illustrates the sample configurations of two different water channel design.

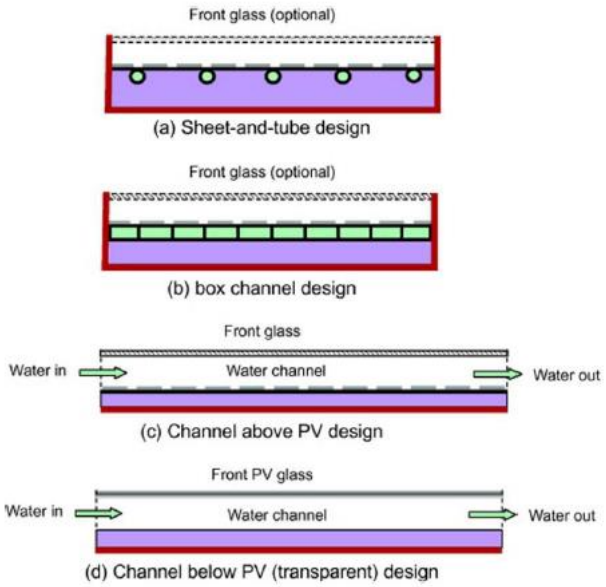


Figure 2.17 Sample configurations of water based PVT system (Chow, 2010)

Huang et al. (2001) did an experimental performance evaluation of a water based solar PVT with parallel flow back plate absorber. The performance of the system is compared with a conventional solar hot water collector. Results show that the PVT system can achieve up to 76% of thermal efficiency of the solar hot water collector. Moreover, at a constant evaporating temperature, the increase of solar intensity will cause the increase of overall PVT efficiency but the decrease of Photovoltaic efficiency. At a constant solar intensity, the rise of evaporating temperature will lead to a decrease of both overall and photovoltaic efficiency. The same system was later improved and retested by Shan et al. (2014) using R410A as the working fluid.

Chow et al. (2008) did an energy and exergy analysis of flat plate water based PVT collector with and without glass cover. The result shows that the energetic efficiency of the glazed collector is always better than the unglazed collector in all cases examined. However, it is suggested that in specific situations, i.e., the electricity output takes the priority, the unglazed collector can be chosen with proper design.

Ibrahim (2009) studied the theoretical performance of various different absorber designs (shown in Figure 2.18). The results show that under water flow rate of 0.01kg/s, the spiral flow design (f) has the highest thermal and electrical efficiencies of 50.12% and 11.98% respectively. The spiral design was later experimentally studied by Fundholi et al. (2014). The result

shows that system has achieved 13% - 13.8% electrical efficiency and 45% – 55% thermal efficiency. However, it is considered that in reality, spiral flow absorbers are generally much more expensive to make, and has more flow resistance hence requires much more pumping power.

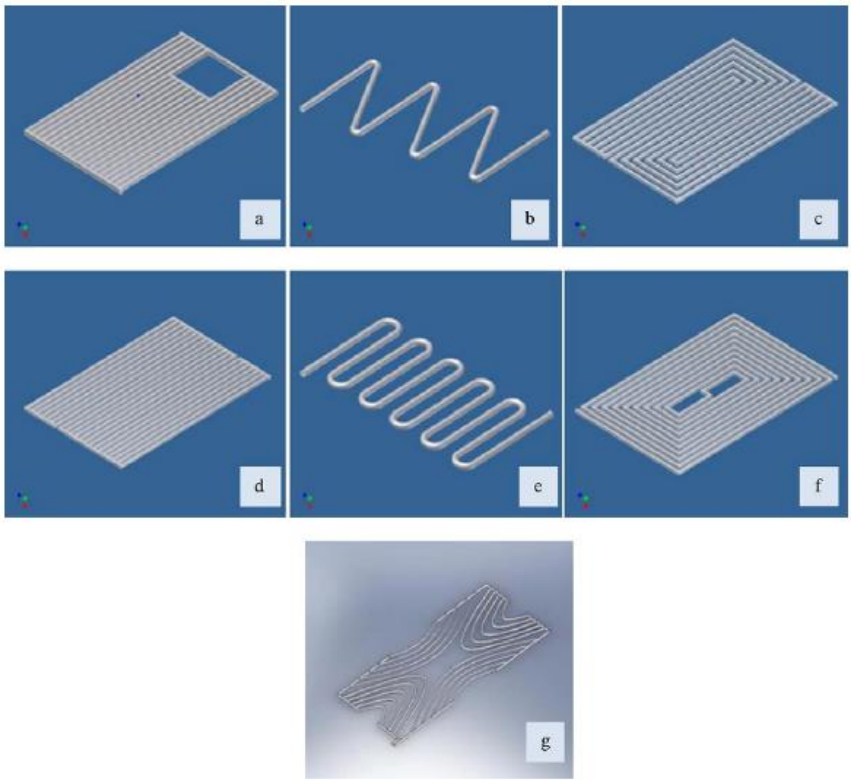


Figure 2.18. Different absorber flow designs studied by Ibrahim (Ibrahim , 2009)

Haurant et al. (2014) did a full-scale experimental study on a water based PVT hybrid system for domestic hot water applications. This system connected a conventional flat plate PVT system to a water tank fitted with heat exchanger to provide domestic hot water. The system was tested in real climate, and the overall system efficiency reached 44.5%. A similar test was also done in South Korea by Kim et al. (2014), the results give the thermal and electrical efficiencies of 30%

and 17% respectively. When the thermal system works together with photovoltaic system, there is an increase of electrical efficiency of 6%. In addition, the BIPVT system can provide hot water for up to 40℃ which can be used as an alternative heat source and hence lower overall heating cost.

2.4.3 PVT optimization

The thermal and electrical performance of PVT system could vary significantly within a year. As an example, a real-time performance assessment done in India by Aaditya et al. (2013) indicates that maximum efficiency was recorded in February, while the minimum efficiency was recorded in July. During recent years, researchers have done enormous work on optimizing PVT system efficiency from different perspectives.

Tripanagnostopoulos et al. (2002) researched the performance difference of four types of hybrid PVT system using either water or air as heat extraction fluid. The four systems are water cooled PVT system, Air cooled PVT system, Water cooled PVT system with glaze on top, and the air cooled PVT system with glaze on top. For all four systems, the cooling mechanisms are located behind the panel and are thermal insulated. The results show that compared with the air cooled system, the water cooled system can achieve much higher efficiency compared with the air cooled system, and the additional glaze will increase the thermal output by up to 45% and up to 100%

respectively to the system using water and air. However, the additional glaze will reduce the electricity output by 16%.

Zakharchenko et al. (2004) studied the influence of the area ratio of the PV modules and the thermal collector on a flat plate water based hybrid PVT system. The experiment was carried out and proved that the optimal design of the system needs the PV module to be essentially smaller than the collector layer. Moreover, it is better to place the PV modules near the cold water inlet as the thermal conductivity of the PV panel is usually poor. They also suggested that the poor thermal conductivity can be improved by adding a metallic substrate covered with an insulation layer.

Anderson et al. (2009) did a parametric analysis to maximize the performance of a water based BIPVT collector. The result indicates that the change of inlet water velocity, pipe diameter, and wind speed will affect the overall exergy efficiency. A similar study was also done by Sobhnamayan et al. (2014). It is found that the material that made the collector base made little difference to the thermal efficiency, which means low-cost material could be used with proper consideration to the balance between the thermal and electrical efficiency. The study also indicated that a good thermal contact between the PV cells and the absorber should be made; this can be achieved by using high conductive adhesives. Moreover, any modifications that can improve the absorption of long wave radiation should be

added as this will increase the thermal efficiency greatly without reducing too much electrical efficiency.

Vats et al. (2012) studied the effect of packing factor (PV cell area against total module area) on the performance of a rooftop air based semi transparent BIPVT system. Different packing factors (0.42, 0.62 and 0.83) and types of PV modules (mono crystalline silicon (m-Si), poly crystalline silicon (p-Si), amorphous silicon (a-Si), cadmium telluride (CdTe), copper indium gallium diselenide (CIGS), and heterojunction with thin layer (HIT)) were chosen. The results show that the PV module temperature is increased by 10℃ when changing the factor from 0.42 to 0.83, and the outlet air temperature is also increased. It is also found that the packing factor of 0.62 has the best balance between the electrical and thermal efficiency (2212kWh annual thermal energy output by HIT module with 0.62 packing factor versus 2129kW with 0.83 packing factor).

Su et al. (2016) carried out a dynamic performance analysis of a dual channel PVT system using different combinations of water and air. The result shows that the water-water combination can achieve best electrical performance while air-air combination has the least electrical performance. The study suggests that using water as cooling solutions will have better performance from both electrical and thermal perspective. It is also found that increasing the water flow speed or increasing the water pipe diameter can further enhance the photovoltaic efficiency.

Othman et al. (2016) carried out a performance analysis of a PVT system using both water and air. The system uses solar collector plate to heat up water while use air to cool the transparent PV panel. The schematic diagram is shown in Figure 2.19 below. The calculations are made from Hottel-Whillier-Bliss equation. The result shows that under solar radiation level of 800W/m^2, the maximum photovoltaic efficiency can be as high as 17%, while the corresponding thermal efficiency is predicted to be 4 times greater.

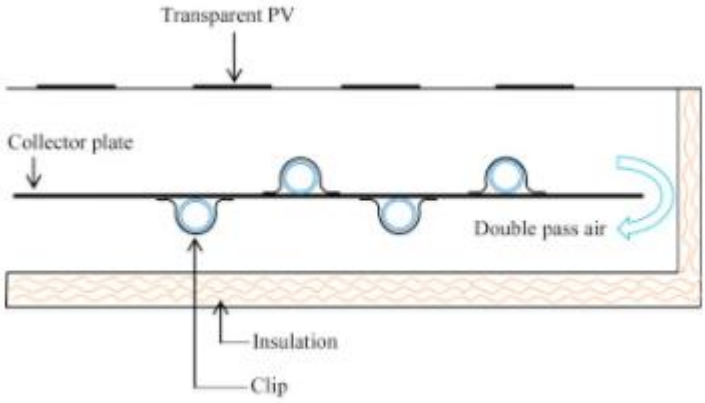


Figure 2.19 Schematic diagram of the hybrid PVT system (Othman, et al., 2016).

2.5 Phase Change Material

Phase change material (PCM) is generally referred to the substance which will melt and solidify within a certain temperature range. The phase change process normally absorbs/releases a large amount of fusion heat. It has the capability to store and release a large amount of latent heat during its phase change. In general, the thermal energy is

stored either by changing the internal energy (sensible heat) of the material, or by changing the phase (latent heat) of the material. Compared with conventional thermal energy storage techniques, PCMs have much higher energy storage density together with an isothermal storage process. However, the disadvantage of the PCM is that they usually have poor thermal conductivities. Figure 2.20 shows the temperature change process during a typical discharging progress. Phase change material normally stores or releases a large amount of thermal energy at a certain phase change temperature during its fusion, melting and solidifying process. In that case, heat is stored as the material changes its phase from solid to liquid and vice versa without changing its temperature.

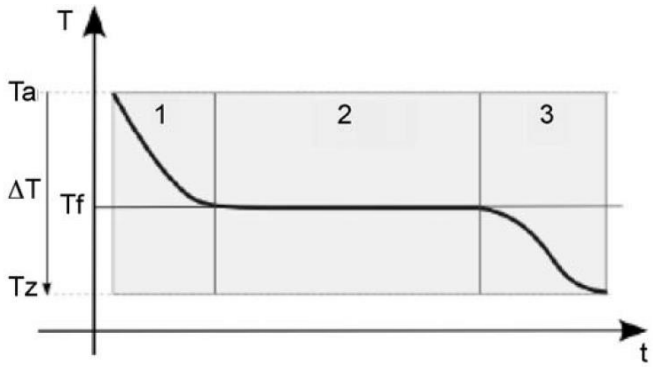


Figure 2.20 PCM temperature change during the discharging period

The working principle of a typical PCM latent heat storage system basically consists of two operation modes:

- Charging process: The thermal energy is transferred into the heat storage system by heat transfer fluid or other media. PCM absorbs the heat by changing its phase from solid to liquid at a certain constant temperature.

- Discharging process: latent heat stored in PCM is discharged from the heat storage system for utilization. During the discharging period, PCM continuously releases heat by changing its phase from liquid to solid at a certain constant temperature.

The criteria below should be considered when selecting proper materials for latent heat storage (Pasupathy et al., 2008).

Thermodynamic properties

- Melting temperature in the desired operating temperature range
- High latent heat of fusion per unit volume
- High specific heat, high density, and high thermal conductivity
- Small volume changes on phase transformation and small vapor pressure at operating temperatures to reduce the containment problem
- Congruent melting

Kinetic properties

- High nucleation rate to avoid super cooling of the liquid phase
- High rate of crystal growth, so that the system can meet demands of heat recovery from the storage system

Chemical properties

- Chemical stability
- Low volume expansion
- Complete reversible freeze/melt cycle
- No degradation after thousands of freeze/melt cycle
- Non-corrosiveness, non-toxic, non-flammable and non-explosive materials

Economic properties

- Low cost
- Large-scale availabilities

2.5.1 Types of PCM

According to Sharma et al. (2009), PCMs can be classified as organic PCMs, inorganic PCMs, eutectics, and hygroscopic materials.

The most commonly studied organic PCMs are paraffins (C_nH_{2n+2}). Other non-paraffin organic PCMs include materials such as some fatty acids and carbohydrates. Those non-paraffin PCMs have various thermal physical properties based on its own composition, unlike paraffin PCMs which have similar properties across the range (Sharma et al., 2009).

The inorganic PCMs are mostly salt-hydrates ($AB \cdot nH_2O$) and some metals with low melting temperature. The salt hydrate

PCMs dehydrate and release water molecules at certain temperature, which is similar to the melting process of paraffin. The most extensive review regarding to the commercially available salt hydrate PCMs was done by Kenisarin and Mahkamov (2016). The review includes 18 salt hydrates including the calcium chloride hexahydrate, which is the basic components of PCM-HS22P used in this study. It is found that although the calcium chloride hexahydrate has been investigated by number of researchers, most of them were done 60 – 70 years ago, and the thermal phase change diagrams were mostly inaccurate (Kenisarin and Mahkamov, 2016). Meanwhile, thermal physical properties such as density, specific heat, thermal conductivity, thermal diffusivity and viscosity are not sufficiently studied for most of the salt hydrate PCMs. It is also found that none of the thermal performance and stability data published by the PCM manufacture was certified by relevant authorities.

Paraffins are the most commonly used PCM regarding to thermal management applications of PV panel, while salt hydrates are mainly used for other large capacity thermal storage solutions. The comparison of paraffin and salt hydrates in terms of various factors is clearly shown in Table 2.2 below.

Table 2.2 Comparison between paraffin and salt hydrate PCMs

	Paraffin	**Salt Hydrate**
Higher volumetric latent heat capacity		✓
Non-flammable		✓
Non-reactive	✓	
High heat of fusion	✓	✓

Smaller volumetric change	✓	
Less segregation	✓	
Sharper melting point		✓
Sharper solidification point	✓	
Higher thermal conductivity		✓
Self-nucleating	✓	
Lower cost		✓

The Eutectics are combinations of two or more PCMs, organic or inorganic. Eutectic PCMs are relatively new, which reduces the amount of segregation by the nature of mixed crystals. Hygroscopic materials are porous materials that can absorb and release water via condensation and vaporization. Hygroscopic materials are commonly found in building industry such as wool insulation, concrete, and clay. The detailed properties of eutectics and hygroscopic materials are not presented here as they are out of the scope of this study.

2.5.2 Applications of PCM

The application of PCM is a relatively new field which is showing great potential. Many studies use PCM as thermal management solution in small scale applications like electronic components (Ling et al. 2014; Wu et al. 2016; Sahoo et al. 2016). At the same time, studies also found that PCM could effectively be used in building industries to reduce heat or cooling load and improve comfort level (Lin et al. 2004; Biswas et al. 2014; Li et al. 2015; Lee et al. 2015). As for PV related applications, PCM is often directly attached to the panel to reduce the peak

PV temperature and improve electrical efficiency. This section mainly focuses on the recent studies of PVT-PCM applications. Figure 2.21 shows a typical back mounted PVT-PCM system which is commonly studied in various literature.

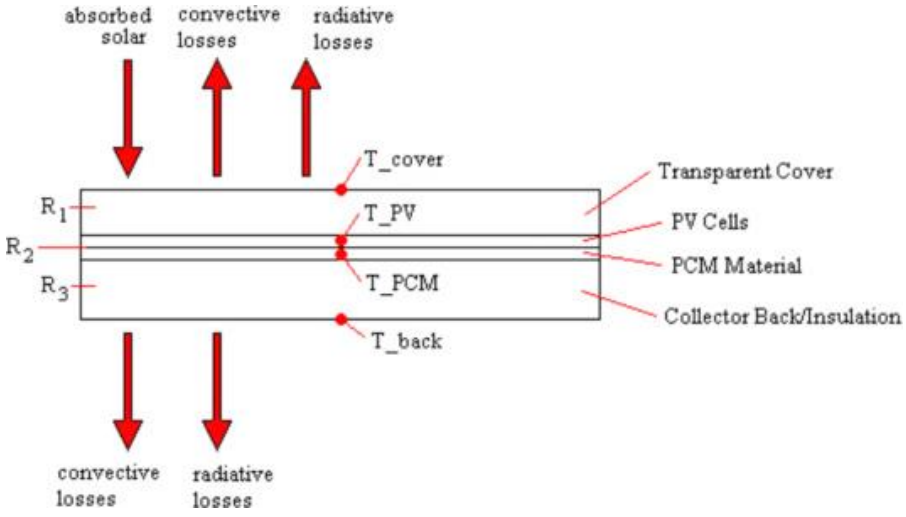


Figure 2.21 A typical PVT-PCM configuration (Stropnik and Stritih, 2016)

Ho et al. (2012) studied the thermal and electrical performance of a BIPV integrated with a microencapsulated phase change material layer. The results shows that the minimum efficiency is increased by 0.13% and 0.42% respectively in summer and winter condition. It is also found that during the summer operation cycle, a portion of PCM stays in the liquid phase throughout the entire cycle.

Aelenei et al. (2014) designed a hybrid BIPV-PCM system and studied its performance. The PCM storage layer is located on the wall and there was an air gap designed between the PV panel and the PCM layer. The numerical model is then compared with the real climatic measurement and shows a

fairly good prediction. The result shows that there is about 10% increase in both thermal and electrical efficiency.

Elarga et al. (2016) studied the photovoltaic and thermal performance of a building integrated(BI) PV-PCM system in double skin facades. The result shows that the cooling energy demand is reduced by 20% - 30% while the heating energy demand is not affected in general. It is also found that the proper ventilation between the PV-PCM and the building facades is a key factor that will significantly affect the performance of the BIPV-PCM system.

Stropnik and stritih (2016) carried out an experimental study of a PCM based PV panel setup using PCM-RT28HC. Based on the experimental result, the maximum PV cell temperature is reduced up to 35.6℃ in October 2013. The model is then simulated in TRNSYS software, and the predicted annual electrical power output is increased by 7.3% compared to the same panel without PCM base.

Kosny et al. (2012) studied the performance of a naturally ventilated photovoltaic solar roof with PCM heat sink. The PCM is packed on the back side of the PV panel, and the natural ventilated air gap is located between the PV panel and the original asphalt roof. The result shows that with the installation of PV-PCM solar roof, in winter there is about 30% reduction of winter heating load and in summer there is about 55% reduction of cooling load. In addition, the peak daytime roof

heat flux is reduced by about 90% after the installation of the PV-PCM solar roof.

Khanna et al. (2017) carried out a performance analysis of tilted PV system with back mounted PCM under various operating conditions. Results show that the PV temperature could be reduced by up to 19℃ with added PCM layer. Another finding is that by increasing the tilt angle of the PV panel, the rate of heat extraction of PCM is enhanced. It was also found that PCM with lower melting temperatures could maintain PV at lower temperatures, which can further enhance electrical performance.

Hasan et al. (2017) studied the yearly energy performance of a PCM based PV system in a hot climate. The result shows that by adding PCM layer, the average peak PV cell temperature is reduced by 10.5℃ on a yearly basis. The annual electricity generation is increased by 5.9%. It is also found that by choosing the right type of PCM, it is economically feasible for the PV-PCM system to be used in such hot climates.

Chandel and Agarwal (2017) did an extensive review of the current PCM based PV cooling solutions. The review shows that the PCM is currently not the most preferred way for cooling PV panels as its poor thermal conductivity and lack of configurability. It is also pointed out that the PCM used in building integrated designs are more economically suitable as the reuse of PCM latent heat is possible. However, the current

literature is more about the organic PCM; there is some literature pointing out that salt-hydrates are more suitable for PV cooling applications. However, the literature studying the salt hydrate is limited.

2.5.3 Improving thermal performance of PCM

It is found by numerous studies that due to the low overall thermal conductivity of PCM, the thermal performance of PCM is often limited. In order to remedy this, various heat transfer enhancement approaches have been suggested, such as fins, metal grids, dispersed highly conductive particles and microencapsulation (Shatikian et al., 2008).

Jegadheeswaran and Pohekar (2009) did a review on performance enhancement techniques in latent heat storage systems. They conclude the current enhancement techniques into four categories: (1) Using extended surface, (2) Employing multiple PCM, (3) Thermal conductivity enhancement, (4) Microencapsulation of PCM. The features and limitation of each method have been concluded. This literature is highly referable when designing a PCM thermal storage system.

Fu et al. (2000) used high conductivity carbon fibres to improve the thermal conductivity of PCM. Two types of techniques were presented in the study; one is using randomly oriented carbon fibres; the other one is using a carbon fibre brush. The result

shows that both of the enhancement techniques are effective in increasing thermal conductivity. The carbon fibre brush has more significant effect on the thermal conductivity along its direction. Meanwhile, the study indicated that the choice between the two techniques also depends on other parameters, i.e., the structure of the energy storage equipment and the cost.

Shatikian et al. (2008) conducted a numerical investigation of the effect of added internal fins into PCM latent heat storage system. The numerical model has been built to have constant heat flux, both horizontally and vertically. The result shows a fairly good generalization of predicting melt fractions and Nusselt numbers, however, the fin efficiency could not be generalized using this constant heat flux model. Suggestions are made to taking account of additional width effect by Rayleigh number. Similar studies were later carried out experimentally by Huang et al. (2011). The fin used in the study is shown in Figure 2.22 below. It is found that by adding metal fins instead of the flat aluminium plate, the PV cell temperature could be reduced, however, on the other hand, adding fins also shorten the temperature regulation period. It is also noticed that solidification shrinkage which occurs during the phase change process will further affect the melting process.

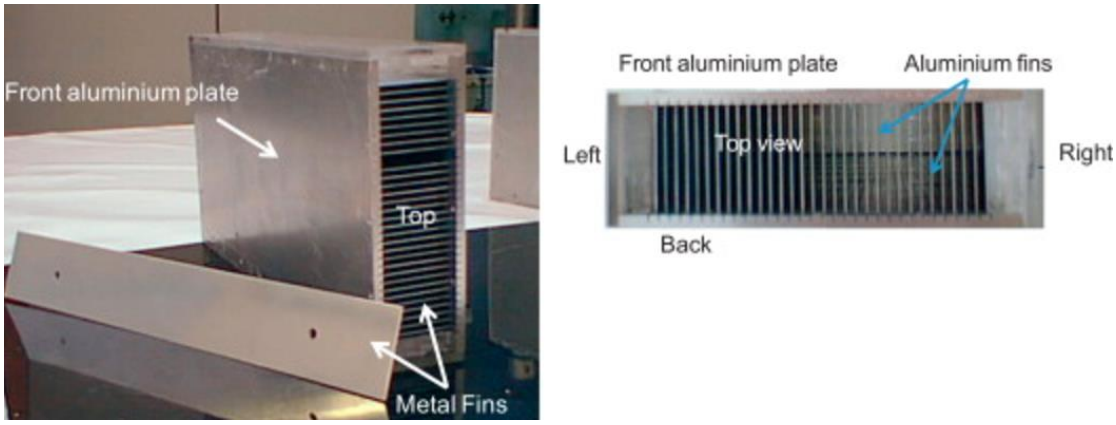


Figure 2.22 PVT-PCM system with metal fins used in Huang et al.'s study (2011)

Guo and Zhang (2008) used several layers of aluminium foils to enhance the heat transfer rate from the steam pipe to the PCM cells (see Figure 2.23). The model was simulated by Fluent 6.2 software and was compared to the same model without foils. The result shows that the charging period is significantly accelerated by adding aluminium foils. Meanwhile, the parametric analysis of the geometry of the aluminium foil, the tube radius, boundary conditions and thermal conductivity of PCM was also done, and the relative equations were given.

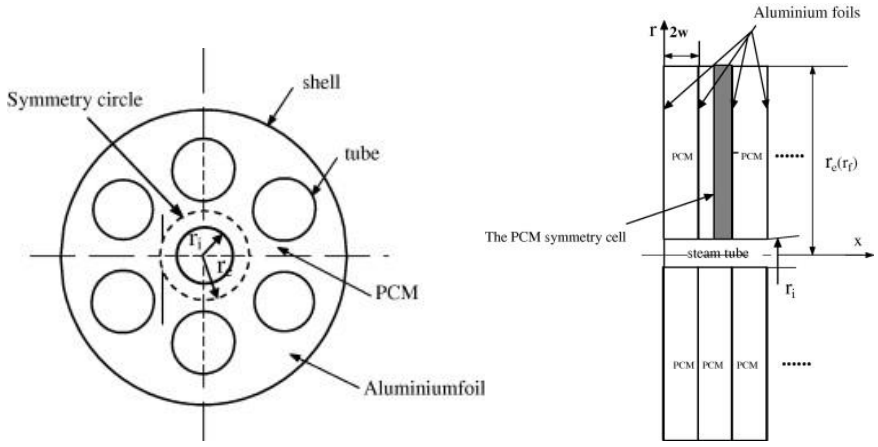


Figure 2.23 Cross section view of the aluminium foil TES system (Guo & Zhang, 2008)

Huang (2011) studied the effect of using two different types of PCMs to regulate the PV temperature (Figure 2.24). The 2D CFD model of the system is built and simulated under solar insolation of 1000W/m^2 and ambient temperature of 20℃. For different types of PCM were used, with melting temperature ranging from 21℃ - 60℃. The results show that the two PCMs could effectively regulate PV cell temperature at around 25℃ which is close to their operating temperature. By using two different PCMs with triangular metal cells, the volume expansion of the PCM is reduced.

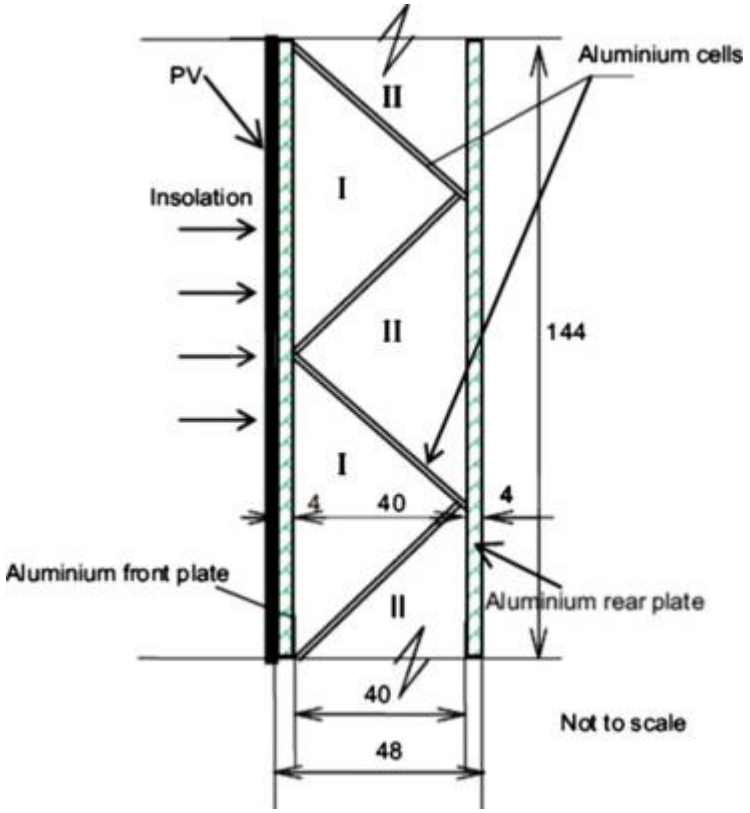


Figure 2.24 Schematic diagram of PVT-dPCM system (Huang, 2011)

Nithyanandam et al. (2014) analyzed a latent thermocline storage system with encapsulated PCMs for concentrating solar power. The system used a cylinder storage tank filled with

spherical PCM capsules. The computational model was built, and the effects of nondimensional variables on the steady and dynamic performance of the system were analyzed. The result shows that the smaller radius capsules can achieve higher latent heat utilization and higher mass flow rate of heat transfer liquid will decrease the system performance due to the expansion of heat exchange zone. The melting point of PCM has a non-monotonic effect on system utilization, which means in order to achieve high latent heat utilization, the melting point should either greater than the discharge cut-off temperature or lesser than the charge cut-off temperature.

2.6 Numerical studies on PVT and PCM performance

In order to predict or estimate the overall performance of a PVT or PCM system, various numerical models have been developed during past decades. For PVT system performance, analytical approaches has shown great accuracy based on the researches reviewed in section 2.6.1; For PCM system performance, CFD software is often used which has also shown its reliability. Researches about CFD approach is reviewed in section 2.6.2.

2.6.1 Numerical studies on PVT performance

Duffie and Beckman (1991) developed numerical models of both flat plate solar collector and concentrated solar collector. They took the vast majority of parameters into consideration and thus resulted in a very realistic approach. The two models

were lately being used by many researchers as fundamentals to estimate the thermal and electrical performance of these two systems (Costello, 2015).

Bergene and Lovvik (1995) developed a mathematical model of a water based flat plate solar PVT collector. The model was created, validated compared with several experimental measurements done by previous researchers. The model turns out to be fairly well in predicting both thermal and electrical system efficiency (about 60% - 80% of overall efficiency). A similar model was used and improved by Hazi et al. (2014) and José et al. (2014), in their mathematical models, the system parameters can be varied and compared with clear trade-offs. These models can be used for making quantitative and qualitative predictions regarding the system performance.

Garg and Adhikari (1999) developed a numerical study of the performance of an air based flat plate PVT collector with various coated absorber. The results indicated that the thermal performance of collectors with selective coated absorbers are better than the black painted absorber; The thermal performance of the collectors without PV modules are better than the collectors covered with PV modules for all kinds of absorbers. This behaviour is concluded as the portion of the solar energy is converted into electrical energy.

Xu et al. (2014) developed an optimized numerical model for PV cells explicit equations; the model is much simple but

accurate compared with the PV cell manufacturer's original model. The *I-V* curves generated according to the model is highly acceptable. The maximum relative error was around 1% at the ideal temperature of 25℃. However, and imprecise value of ideality factor may affect the accuracy in low light condition.

Brideau and Collins (2014) developed and validated a numerical model of a hybrid air based PVT collector with impinging jets. The result shows a good agreement between numerical model and experimental results; however, the time step size in the numerical model may need to be adjusted if the thermal mass is changed.

Brinkworth (2006) established a numerical method to calculate optimal depth of PV cooling air ducts. The suggestion is that the optimal duct depth is in relationship with PV panel length and air flow Reynolds number. The first order theoretical correlation can be expressed as: $(L/D)_{opt} = 2Re_D{}^{0.24}$ (7000 < Re <20000).

2.6.2 Numerical studies on PCM performance

Jmal and Baccar (2015) did a numerical study about the effect of natural convection during solidification process of a paraffin wax PCM in a finned tube. The results show that although adding fins could reduce the discharging process of PCM, adding too many fins will have little enhancement of the

discharging process due to the blockage of solid phase PCM reducing the thermal-convective flow. It is shown in the work that the natural convection takes a significant role in enhancing discharging performance. However, the kinetic viscosity value used in their study seems to be incorrect ($1.5 \times 10^{-6} m^2/s$), which for paraffin wax PCM the kinetic viscosity should be within 10^{-3} range.

For studying the melting and solidification process of PCM, due to the high viscosity of PCM, many researches use constant density for PCM instead of temperature dependent density while studying the melting & solidification process (Sebti et al., 2013), (Sattari et al., 2017). An alternative practice when studying the buoyancy effect with PCM domain is to use VOF (volume of fluid) model with an additional layer of air (Darzi et al., 2015), (Dhaidan, 2017), (Puertas et al., 2017).

Koller et al. (2016) studied the solidification and melting process of a sodium nitrate ($NaNO_3$) using wired matrix (as shown in Figure 2.26). A transient numerical investigation has been conducted in order to study whether conduction or natural convection is the dominant heat transfer mechanism within the PCM domain. The result shows that the effect of natural convection is more obvious in charging process than the discharging process, while in both processes, conduction heat transfer takes the dominant effect over convection heat transfer. It is also found that the wired matrix could be an alternative to longitudinal fins used to as heat transfer enhancement

technique, assuming the wire has perfect connection with the tube surface. However, in real situations, the thermal performance will be less due to the thermal resistance of the wire and the connection between each part.

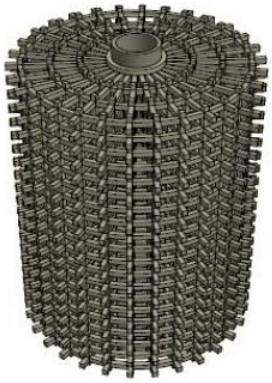


Figure 2.26 Model of heat exchange tube with wire used in Koller et al. (2016)'s study

Vikas et al. (2017) used Ansys FLUENT for simulating the melting process of paraffin wax PCM by a vertical heated wall. It is found that the melting process could be enhanced by PCM's natural convection. It is also suggested that proper meshing and time step size should be carefully set prior to the simulation when using Ansys FLUENT. Otherwise the results will become diverged during the calculation process.

Meng and Zhang (2017) designed and simulated a novel U shaped tube-in-tank latent thermal storage (LTS) unit (shown in Figure 2.27). The concept of this PCM storage system is to use water as heat transfer media, and flows through U shaped copper pipes inserted into the PCM. The results show that the

good heat transfer performance could be achieved with the design. It is also found that higher inlet temperature and flow speed could shorten the charging process of the LTS system. The system is fully modular and could be combined in large numbers, and the performance would be the same, which is similar to the PVT-PCM designs of this study.

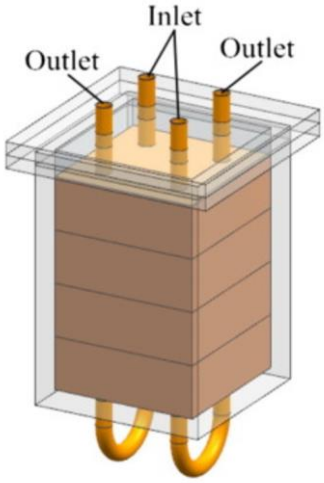


Figure 2.27 Modular LTS unit from Meng and Zhang (2017)'s work

2.7 PVT-PCM Application

During recent years, PVT-PCM related applications has drawn increasing interests. Huang et al. (2004) studied the performance of a BIPV panel with added PCM layer (Figure 2.25). It was the first numerical study related to PV-PCM performance and was successfully validated with experiments. A follow-up study (Huang, 2006) used a small scale 3-D model to compare with a validated 2-D model, results show that the 2D model can make good enough predictions of the results using the 3D model. Another study (Huang et al., 2011) presented a performance evaluation of PCM pack panel fitted below PV module, The CFD model was built and simulated, and

at the same time, the experimental test was also conducted. The result shows that the PV panel could remain cool during the first several hours due to the existence of PCM. However, due to the limit of space and the conduction area, the cooling capacity of this PCM back panel is restricted.

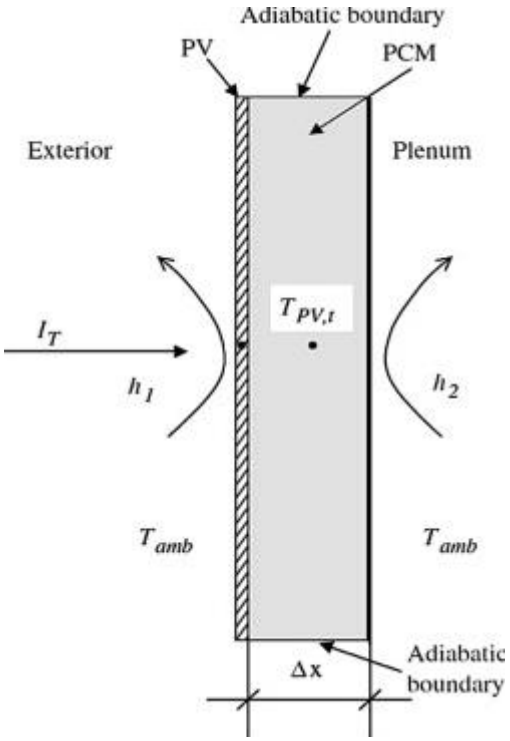


Figure 2.25 PV-PCM configuration (Huang et al., 2004)

Ciulla et al. (2012) built a finite difference model of a PV system with PCM backpack storage. The model is then simulated and compared with the real climatic condition. The results show that the proposed model is valid and it can also be used to calculate the thermal behaviour of the multilayer wall which contains PCM. The only thing different to the realistic measurement is the night time temperature which means there may be an error in estimating the radiative heat exchange during the night.

Qiu et al. (2016) carried out an experimental investigation of the energy performance of a novel Micro encapsulated PCM (MEPCM) slurry based PVT system. The idea is to use MEPCM based slurry instead of water in a conventional water based PVT system. It is found that by using MEPCM slurry of 10% concentration and 3000 Reynolds number, the system could achieve overall solar efficiency of 80.0 – 83.9%.

Kant et al. (2016) built a CFD model to study the heat transfer of PV panels with added PCM layer on the bottom. The melting and solidification process of PCM during the working cycle has been simulated. Results show that while considering the convective heat transfer within the PCM, the maximum PV cell temperature is reduced by 3℃, compared to the conduction only model. It is also found that the increase of tilting angle from the horizontal surface will slightly reduce the maximum PV cell temperature. However, the difference is within 1℃.

Ho et al. (2013) designed an innovative BIPVT-PCM system which uses micro encapsulated PCM (MEPCM) instead of normal back plated PCM block. The layout of the system can be seen in Figure 2.26. It is found that the melting of MEPCM is evenly distributed along the panel, and the simulated performance gain is recorded as 1.8℃ reduction in cell temperature and 2.1% improvement in electrical efficiency.

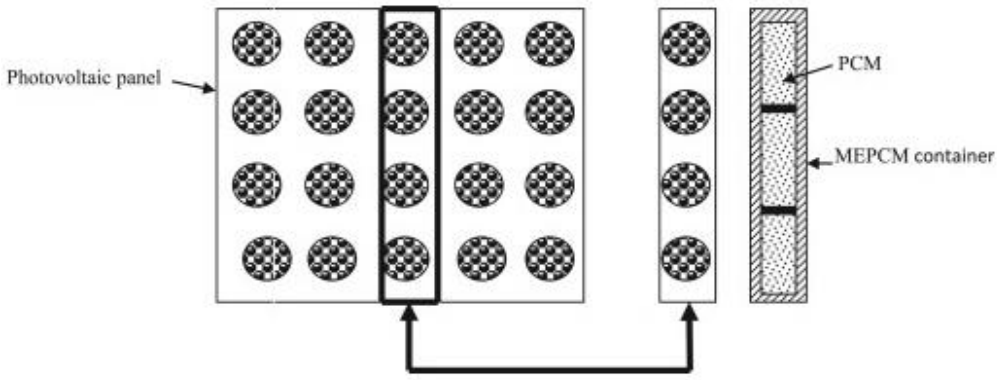


Figure 2.26 PVT-MEPCM system (Ho et al., 2013)

Iten et al. (2017) studied the level of agreements between experimental results and CFD simulation results. A commercial paraffin type PCM-RT25 has been tested through DSC (Differential scanning calorimetry) analysis for both charging and discharging process. The result is then compared with CFD simulation predictions. It is suggested that it is important to use correct thermal physical properties while using CFD simulations, in order to increase the precision. The most important thermal physical properties for simulating PCM performance is the temperature related specific heat.

Preet et al. (2017) carried out an experimental investigation of a water based PVT system with and without PCM. The layout of the two system is shown in Figure 2.27 below. Results found that the PV cell temperature of the system without or with PCM is reduced by 47% and 53% respectively compared to conventional flat plate PV panel. It is also noticed that the overall daily electrical efficiency at water flow rate of

0.0031kg/s is increased by 230% without PCM and 300% with PCM when compared to conventional panels.

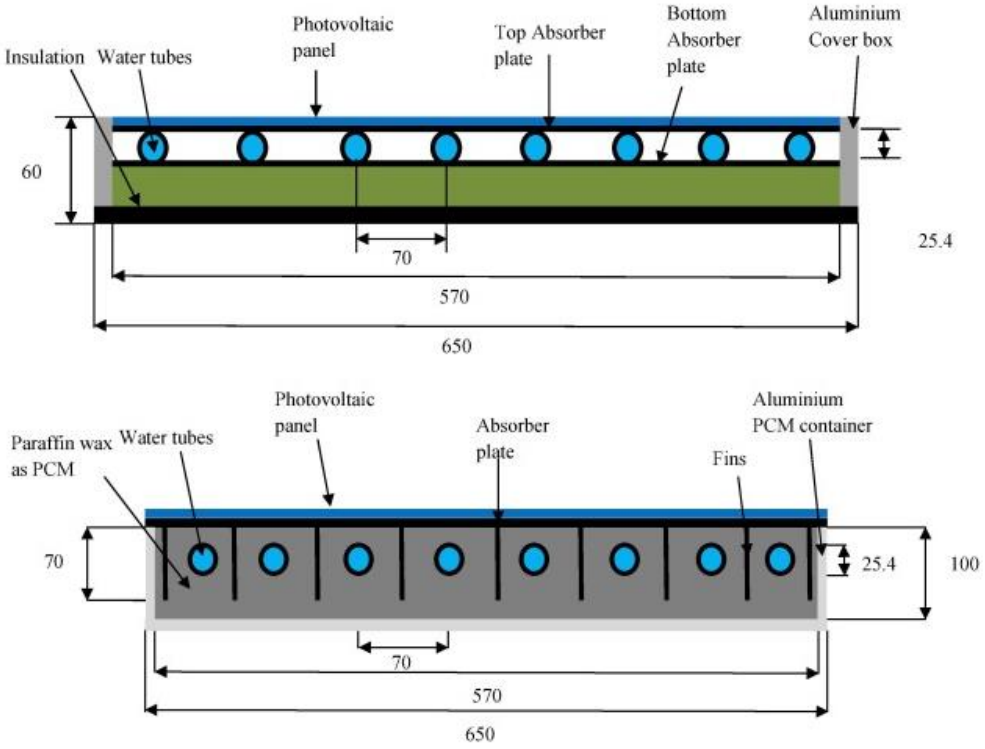


Figure 2.27 Water based PVT without PCM (top) and with PCM (bottom) (Preet et al., 2017)

Gaur et al. (2017) did a numerical study on the thermal and electrical performance of a wetted PVT collector with added PCM storage medium. The layout of the system is shown in Figure 2.28. The PCM acts as heat source for collector water during night-time. The performance of the system is compared numerically with the same system without PCM, and is found that PCM maximizes both electrical and thermal efficiency, with around 9% increase in electrical output and 51% increase in thermal output compared with the same system without PCM.

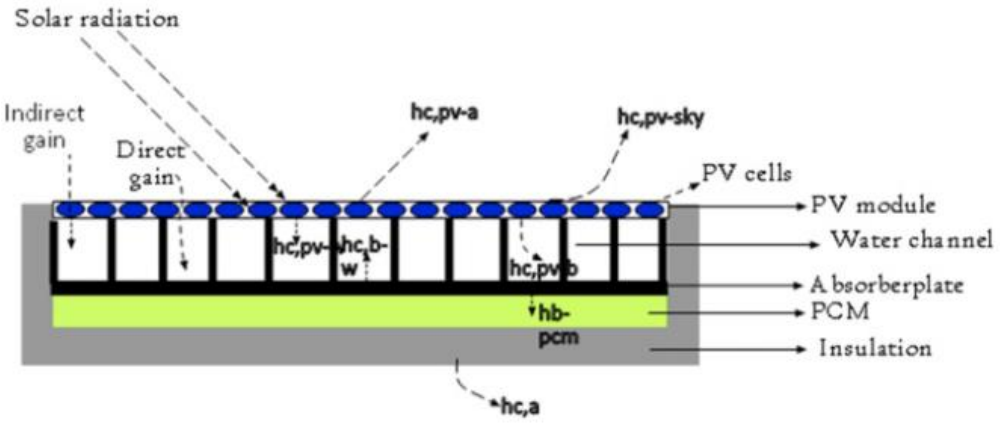


Figure 2.28 Wetted PVT collector with added PCM (Gaur et al., 2017)

2.8 Summary

This chapter presents an extensive literature review about the basics and the recent developments of PV, PVT and PCM applications. It is found that there is limited literature available to help accurately predict the thermal performance of PCMs especially salt hydrate PCMs. Meanwhile, literature on numerical studies and performance optimization is also reviewed to help evaluate and optimize system performance of the proposed PVT-PCM system. At the current stage, most of the PCM based PVT systems are air based systems that only has limited size back-mounted PCM storage, hence the benefits of added PCM is restricted. In most recent researches, water based PVT-PCM systems were introduced. Although the overall performance of system is further improved, the PCM is still back mounted and hence restricted in size. At the moment, very limited literature is available regarding both thermal and electrical performance of the PCM based PVT system.

CHAPTER 3 ANALYTICAL AND CFD METHODOLOGY

3.1 Analytical models for PVT-PCM system

This section presents a comprehensive series of analytical models for all components in the proposed PVT-PCM system, including the PV panel, the cooling solution, and the latent heat storage system regarding their thermal and electrical performance. These numerical models are calculated using explicit method by Excel Spreadsheet. The results of the models are used during the system design and component selection process as they provide the baseline data and reflect basic requirements for specified system components. The results will also be used to gauge and validate the CFD simulation predictions to prove its reliability.

3.1.1 Energy model of back cooled flat plate PV panel

3.1.1.1 Energy model of PV

The working principle of a PV panel is to absorb irradiance from the ambient environment and generate heat as well as electrical power. Main paths of energy transfer are illustrated in Figure 4.1 below. Thermal energy is transferred from and to

the module via three modes, conduction, convection, and radiation, while other energy is taken from the module in the form of electrical energy. The main energy exchange happens on the front and the back surface of the PV panel, while the energy loss/gain from the framework is considered negligible due to the relatively small exposed area for convection or small contact surface for conduction heat transfer with building structures.

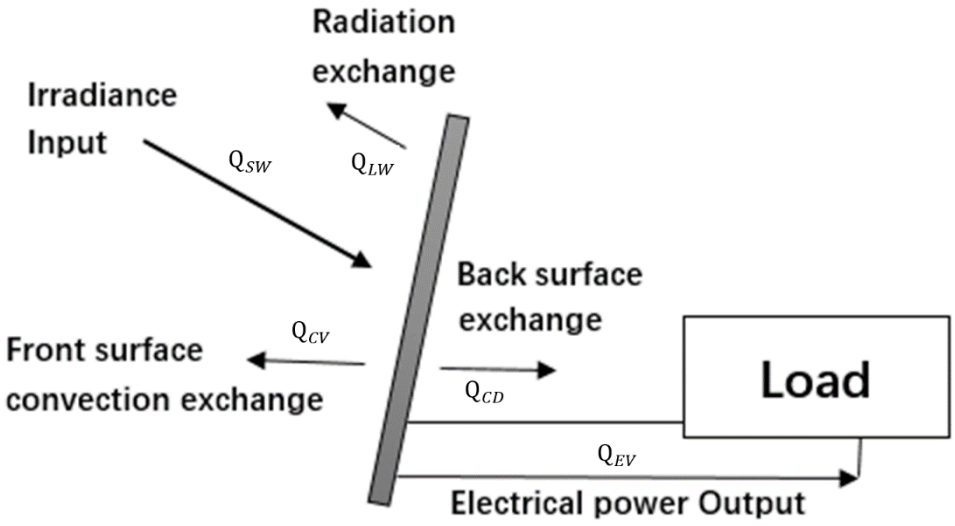


Figure 3.1 Main paths of energy transfer from and to the PV panel

The energy balance equation of the working PV panel at steady state is as follows:

$$Q_{CV} + Q_{CD} + Q_{SW} + Q_{LW} + Q_{EV} = 0 \qquad \textbf{3.1}$$

Where Q_{CV} corresponds to the convective heat transfer(W) either by natural and/or forced convection, Q_{CD} corresponds to the conduction heat transfer to the back plate absorber, Q_{SW} and Q_{LW} correspond to the short wave and long wave radiation heat transfer respectively. And Q_{EV} corresponds to electrical energy generated by the photovoltaic cells.

The module temperature is sensitive to the ambient conditions and will keep changing throughout a day.

The module temperature change over a certain amount of time could be expressed by equations below:

$$C_P m_p \frac{\Delta T}{t} = q_{cv} + q_{cd} + q_{lw} + q_{sw} - q_{ev} \quad \textbf{3.2}$$

Where C_P corresponds to the specific heat of the PV module (J/kg), m_p corresponds to the mass of the module (kg), T corresponds to the temperature and t is the time(s).

Rearranging the above equation gives the expression of cell temperature $T_{(t)}$ by knowing the time period t and the initial cell temperature $T_{(t\prime)}$.

$$T_{(t)} = \frac{q_{cv}+q_{lw}+q_{sw}}{C_P m_p} \times \Delta t + T_{(t\prime)} \quad \textbf{3.3}$$

3.1.1.2 Module heat capacity

A typical flat plate PV module normally consists of three layers, on top is a toughened glass cover, on the bottom is a tri-laminated polyester and a thin layer of PV cell array is in between. The panel used in this research consists of a 3mm thick toughened glass cover, a 0.5mm thick monocrystalline

silicon PV cell module, and a 0.5mm thick tri-laminated polyester (BP Solar, 2001). The surface dimension of the panel is 1183mm x 525mm. The characteristic properties of each material are listed in Table 4.1 below. Due to the lack of data in manufacturer data sheet, it is impossible to determine the exact properties of the material used in the PV panel. Thus the values are chosen based on known values of the same type.

Table 3.1 Properties of the PV panel components

Material	ρ_m	C_m	d_m
	(kg/m^3)	(J/kgK)	(m)
Toughened Glass	3000	500	0.003
Monocrystalline silicon cell	2330	677	0.0005
Tri-laminated Polyester	1200	1250	0.0005

The equivalent thermal capacity of the panel could be calculated from knowing its volume, density and specific heat capacity of each layer. The equation is shown in below.

$$Cp = \sum_1^m \frac{M_m}{M_t} \cdot C_m \qquad \textbf{3.4}$$

Where M_m corresponds to the weight of individual material layer (kg), M_t corresponds to total weight of the panel (kg), and C_m corresponds to the specific heat of each material (J/kgK).

By knowing the individual properties of each component, it is then possible to determine the properties of the whole PV module. The table 4.2 below shows the heat capacity, weight

and thermal conductivity of three layers and the whole panel. (The surface area of PV panel is 0.621 m^2). The total heat capacity of the module is calculated to be 560.96 J/kgK and the density is 2691.25 kg/m^3. The panel total thermal conductivity k_t with m individual layer could be calculated using equation below:

$$k_t = \frac{d_t}{\sum_1^m \frac{d_m}{k_m}} \qquad \textbf{3.5}$$

Where d_t corresponds to the total thickness of the panel (m) and k_m corresponds to thermal conductivity of each layer (W/mK).

Table 3.2 PV panel equivalent thermal physical properties

Layer	**Heat Capacity**	**Weight**	**Thermal conductivity**
	(J/kgK)	(Kg)	(W/mK)
Toughened Glass	500	5.59	0.8
Monocrystalline silicon cell	677	0.72	148
Tri-laminated Polyester	1250	0.37	0.17
Total	560.96	6.69	0.59

3.1.1.3 Short wave radiation heat transfer

The short-wave radiation reaches the front surface of the solar panel can be determined by knowing the solar radiation intensity and the absorptivity of the PV cell face. The short wave heat transfer can be expressed as:

$$q_{sw} = \alpha \cdot \Phi \cdot A \quad \textbf{3.6}$$

Where α corresponds to the absorptivity of the panel (%), Φ corresponds to the radiation level (W/m^2), and A is the panel area(m^2)

The total absorptivity can be determined by knowing the individual absorptivity of each layer. It can be expressed by equation below.

$$\alpha = \alpha_1 \cdot \alpha_2 \cdots \alpha_n \quad \textbf{3.7}$$

The thermal absorptivity for monocrystalline silicon cells is considered to be around 77% (Merrigan, 1982). According to the manufacturer data sheet, a toughened glass cover has been added above the silicon cells which has a light transmission ratio of 92%. Thus, the total absorptivity of the whole panel can be determined as 71%.

3.1.1.4 Long wave radiation heat transfer

The Long wave radiation heat transfer, q_{lw}, per unit area at surface temperature, T, can be expressed by the Stefan-Boltzmann equation below:

$$q_{lw} = \sigma \cdot \varepsilon \cdot T^4 \quad \textbf{3.8}$$

Where ε corresponds to emissivity (%)

Due to the fact that long wave radiation could reflect between different surfaces, it is important to determine the net long wave radiation between two different surfaces. In particular, the net long wave radiation between the front PV panel to other surrounding surfaces. The back side of the panel is covered with cooling plates, and the side surfaces have relatively small surface area, the effect of the long wave radiation heat transfer from other surfaces of the panel is relatively small and could be neglected. The net long wave radiation between surface x and y can be determined by the equation below.

$$q_{lw} = A_x \cdot F_{xy} \cdot \left(L_x - L_y\right) = A_y \cdot F_{xy} \cdot (L_y - L_x) \qquad \textbf{3.9}$$

If the module has a tilted surface at angle β from the horizontal axis, it can be calculated that the two viewing angle of sky and ground are (1+cos β)/2 and (1-cos β)/2 respectively. By considering the tilting angle, the net long wave radiation of the front surface could be expressed as equation below (Liu & Jordan, 1963).

$$q_{lw} = A \cdot \sigma\left(\frac{(1+cos\beta)}{2}\varepsilon_s \cdot {T_s}^4 + \frac{(1-cos\beta)}{2}\varepsilon_g \cdot {T_g}^4 - \varepsilon_P \cdot {T_P}^4\right) \qquad \textbf{3.10}$$

Where σ corresponds to Stefan-Boltzmann constant which is 5.669×10^{-8} W/m^{2}K^4, ε_s corresponds to the sky emissivity, it is considered to take 0.95 for clear sky conditions and 1.0 for overcast conditions (Liu & Jordan, 1963), ε_g corresponds to the ground emissivity and is considered to be 0.95 (Liu &

Jordan, 1963), ε_P corresponds to the emissivity of the panel front surface, which is considered to be 0.9 (Liu & Jordan, 1963), T_g corresponds to the ground temperature(K), T_s corresponds to the sky radiation temperature(K) and T_a corresponds to the ambient temperature of the surrounding environment(K). It is considered that for clear sky conditions, $T_s = (T_a - 20K)$, for overcast conditions, $T_s = T_a$ (Schott, 1985).

3.1.1.5 Convection heat loss

The convection heat transfer, q_{cv}, can be expressed by equation below:

$$q_{cv} = -h_{cv} \cdot \mathrm{A} \cdot (T_p - T_a) \qquad \textbf{3.11}$$

Where q_{cv} corresponds to the convection heat transfer (W), h_{cv} corresponds to the convective heat transfer coefficient(W/m^{2}K), A corresponds to the surface area(m^2), T_p and T_a stands for PV panel and ambient temperature ($\mathbb{C}$) respectively.

The convection heat transfer can be divided into 2 ways; the free convection, and the forced convection. The free convection is caused due to the temperature difference of the fluid which will affect density, and thus affect the relative buoyancy. Inside the fluid region, due to the presence of the gravitational field,

the less dense part will rise while the denser part will fall, thus cause bulk fluid movement. On the other hand, forced convection occurs due to the presence of external forces, in this case, wind. It accelerates the rate of heat exchange.

Free convection coefficient

The free convection heat coefficient can be determined by the equation below:

$$h_{free} = \frac{\overline{Nu_{free}} k_{air}}{L'} \quad \textbf{3.12}$$

The characteristic length L' of a flat plate PV panel can be calculated as follows, Where L and W is the length and width of the PV module.

$$L' = \frac{LW}{2(L+W)} \quad \textbf{3.13}$$

The $\overline{Nu_{free}}$ is the Nusselt number for free convection, according to Incropera (2007)'s work, the empirical correlation is defined as:

$$\overline{Nu_{free}} = 0.68 + 0.67(Ra_L \Psi)^{\frac{1}{4}} \quad \textbf{3.14}$$

Where Rayleigh number Ra_L ($0 < Ra_L < 10^9$) , and Ψ are defined as:

$$Ra_L = Gr_L Pr = \frac{9.81\beta|T_p - T_a|L'^3}{{v_{air}}^2} Pr \quad \textbf{3.15}$$

and

$$\Psi = \left(1 + \left(\frac{0.492}{Pr}\right)^{\frac{9}{16}}\right)^{-\frac{16}{9}} \quad \textbf{3.16}$$

Where Gr corresponds to the Grashof number, Pr corresponds to Prantl number, β corresponds to the volumetric thermal expansion coefficient, T_p corresponds to the panel temperature (℃), T_{air} corresponds to air temperature(℃), v_{air} corresponds to air kinetic viscosity(m^2/s) and L' corresponds to the characteristic length of the panel(m).

For the PV panel with tilted angle θ , the $\overline{Nu_{free}}$ can also be calculated as (Bejan, 2003):

$$\overline{Nu_{free}} = 0.14\left[(GrPr)^{1/3} - (Gr_{cr}Pr)^{1/3}\right] + 0.56(Gr_{cr}Prcos\theta)^{1/4} \quad \textbf{3.17}$$

Where the equation is suitable for $15° < \theta < 75°$. The Gr_{cr} is given as $5x10^9$, $2x10^9$,10^8 and 10^6 for θ of 15°, 30°, 60°, 70° respectively.

Forced convection coefficient

Sparrow and Tian (1977) proposed an empirical correlation of the forced heat transfer coefficient, h_{force}, as:

$$h_{force} = \frac{0.931\rho_{air}v_{air}C_{pair}Re^{\frac{1}{2}}}{L'} \quad \textbf{3.18}$$

and

$$Re = \frac{L'}{\rho_{air}\mu_{air}}v_w \quad \textbf{3.19}$$

where v_w corresponds to the local wind speed(m/s), ρ_{air} corresponds to the density of air(kg/m^3), μ_{air} corresponds to the dynamic viscosity of air(Pa-s), C_{air} corresponds to the specific heat of air(J/kgK), Re corresponds to the Reynolds number, and L' corresponds to the characteristic length of panel.

The Nusselt number of forced convection heat transfer, Nu_{force}, could then be calculated as:

$$\overline{Nu_{force}} = \frac{h_{force}L'}{k_{air}} \quad \textbf{3.20}$$

Where h_{force} corresponds to the forced heat transfer coefficient(W/m^{2}K), L' corresponds to the characteristic length of panel and k_{air} is the air thermal conductivity(W/mK).

An approximation (Incropera, 2007) showed the relationship of combined convection heat transfer coefficient against free and forced convection heat transfer coefficient which is:

$$h_{cv} = \frac{\overline{Nu_{cv}}k_{air}}{L'} \quad \textbf{3.21}$$

and

$$\overline{Nu_{cv}}^3 = \overline{Nu_{free}}^3 + \overline{Nu_{force}}^3 \quad \textbf{3.22}$$

Where h_{cv} corresponds to the convective heat transfer coefficient(W/m^{2}K), Nu_{cv} , Nu_{free} , Nu_{force} correspond to the total Nusselt number, free convection Nusselt number and forced convection Nusselt number respectively, k_{air} corresponds to the thermal conductivity of air(W/mK), L' corresponds to the characteristic length of the panel(m).

3.1.1.6 Conduction heat transfer

The conduction heat transfer from the back surface of the PV panel to heat absorber can be expressed as:

$$q_{cd} = -Q_{HT} \cdot \eta \qquad \textbf{3.23}$$

Where Q_{HT} equals the total heat transfer rate of the heat transfer solution(W), η corresponds to the adjustment factor based on how heat absorber attached to the PV back panel.

3.1.2 Energy models of heat transfer

3.1.2.1 Conduction heat transfer

The conduction heat transfer, q_{cd}, from the back surface of the PV panel to heat sink can also be expressed as:

$$q_{cd} = A \cdot \frac{k}{d} \Delta T \quad \textbf{3.24}$$

Where A equals the contacting surface area(m^2), d corresponds to the thickness of the heat sink(m), k corresponds to the solid thermal conductivity(W/mK) and ΔT corresponds to the temperature difference between two materials (℃).

3.1.2.2 Water cooling system

The equation describing heat transfer from back surface panel to copper water tube can be expressed as:

$$q_{cd} = \dot{m} C_{p(water)} (T_{out} - T_{in}) = h_{pipe} A_{pipe} (T_{wall} - T_{film}) \quad \textbf{3.25}$$

Where $\dot{m}$ corresponds to the mass flow rate of water(kg/s), $C_{p(water)}$ corresponds to the specific heat of water(J/kgK) ,T_{out} and T_{in} correspond to water outlet and inlet temperature respectively, T_{wall} and T_{film} correspond to temperature of copper tube wall and the temperature of bulk fluid (mean temperature of the inlet and outlet temperature) respectively, h_{pipe} corresponds to the convective heat transfer coefficient of pipe(W/m^2K), A_{pipe} corresponds to the surface area of the pipe(m^2).

The convective heat transfer coefficient of the pipe can be defined as:

$$h_{pipe} = \frac{Nu_D k}{D} \quad \textbf{3.26}$$

Where Nu_D corresponds to the Nusselt number of water, k corresponds to the thermal conductivity of water(W/mK), D corresponds to the internal diameter of pipe(m).

The Nusselt number of water, Nu_{water} in turbulent flow, can be determined by the Dittus-Boelter equation shown as:

$$Nu_D = 0.023 Re^{0.8} Pr^{0.4} \ (\frac{L}{D} > 10 \ and \ 0.6 \leq Pr \leq 160) \quad \textbf{3.27}$$

The Nusselt number of water in turbulent flow could also be determined by Gnielinski correlation which can be expressed as:

$$Nu_D = \frac{(f/8)(Re-1000)Pr}{1+12.7\left(\frac{f}{8}\right)^{\frac{1}{2}}(Pr^{\frac{2}{3}}-1)} \ (0.5 < Pr < 2000 \ and \ Re \geq 3000) \quad \textbf{3.28}$$

Where f is the Darcy friction factor in the Moody chart.

The Nusselt number of water, Nu_{water}, in laminar flow condition, can be determined by the below correlation according to Edward et al. (1970) as:

$$Nu_{water} = 3.66 + \frac{0.065 RePr\frac{D}{L}}{1+0.04(RePr\frac{D}{L})^{2/3}} \quad \textbf{3.29}$$

Where the Re and Pr correspond to Reynolds number and Prandtl number of water respectively, and can be calculated by:

$$Re = \frac{u\rho D}{\mu} \quad \textbf{3.30}$$

$$Pr = \frac{C_p \mu}{k} \quad \textbf{3.31}$$

Where C_p corresponds to the specific heat of water(J/kgK), D and L corresponds to the diameter and length(m) of the pipe respectively, ρ corresponds to water density(kg/m^3), u and μ correspond to the velocity (m/s) and dynamic viscosity(Pa.s) of water respectively, and k corresponds to thermal conductivity of water (W/mK).

3.1.3 Model of PV panel electrical performance

The electrical efficiency of PV module is determined by equation below (Chow et al., 2007),

$$\eta_c = \eta_r[1 - \beta(T_c - T_r)] + \gamma log G_r \quad \textbf{3.32}$$

Where η_r is the standard panel efficiency at PV cell temperature T_r of 25 °C and at solar irradiance G_r on the module equals to 1000 W/m^2; T_c is the average module temperature; β and γ are the temperature and the solar irradiance coefficients of the PV panel respectively.

Generally, the parameters (T_r, η_r, γ and β) are given by the photovoltaic manufacturer, and γ and β depend on the material used for the PV module. In most studies, γ is equal to 0.
Thus, the electrical output can be expressed as

$$q_{ev} = G_r \cdot \eta_r[1 - \beta(T_c - T_r)] \quad \textbf{3.33}$$

3.1.4 Thermal Model of Phase Change Material

The heat transferred to the PCM material can be divided into three parts, one part of the heat is used to increase the solid phase temperature, one part of the heat is used to complete the phase changing process, and the rest of the part is used to increase the liquid phase temperature. Among those three parts of heat transfer process, the most amount of heat is stored during phase change progress as latent heat; this unique characteristic makes PCM a superior solution for latent heat storage.

The instantaneous heat balance equation is given by,

$$\delta Q = m_s C_{p,s} \frac{\partial T_s}{\partial t} + m_l C_{p,l} \frac{\partial T_l}{\partial t} + \Delta h \frac{dm}{dt} \quad \textbf{3.34}$$

For a certain charging process, the initial temperature of the PCM is T_1, then the PCM is heated to its melting temperature T_m, after the phase change process, the liquid phased PCM continues to be heated up until the temperature reaches T_2 . In order to express the amount of heat absorbed by the PCM, the above equation can be rewritten by,

$$Q = mC_{p,s}(T_m - T_1) + mC_{p,l}(T_2 - T_m) + m\Delta h \quad \textbf{3.35}$$

For transient calculation of PCM thermal performance, Poirier and Salcudean (1988) developed the effective heat capacity method. The method uses an approach to increase sensible heat capacity to account for the latent phase change progress. The equations are shown as below.

$$\frac{\partial}{\partial t}\left(\rho C_{eff}\right) = k\nabla T \quad \textbf{3.36}$$

Where C_{eff} corresponds to the effective heat capacity and is given by

$$C_{eff} = \int_{T_s}^{T_l} \rho C_p dT \quad \textbf{3.37}$$

and

$$C_p = C_{p,s}\ if\ T < T_s \quad \textbf{3.38}$$

$$C_p = (1 - f_l)C_{p,s} + f_l C_{p,l} + \frac{L}{T_l - T_s}\ if\ T_s < T < T_l \quad \textbf{3.39}$$

$$C_p = C_{p,l}\ if\ T > T_l \quad \textbf{3.40}$$

Where $C_{p,s}$ and $C_{p,l}$ are the specific heat of solid phase and liquid phase respectively(J/kgK), f_l is the liquid fraction. T_s and T_l are solid and liquid temperature(K).

3.2 Computational Fluid dynamics methodology

Computational fluid dynamics (CFD) is a very powerful technique that has been used widely among industrial and non-industrial areas. The CFD technique is first introduced in the 1960s, after that, many from aerospace industry have started using CFD for the product design and R&D of aircraft and jet engines. CFD software can analyse a wide variety of fluid systems including fluid flow, heat transfer and other associated phenomena (Versteeg & Malalasekera, 1995).

3.2.1 Governing equations

The concept of CFD model is to discretise a complex flow domain into individual cells which has a finite volume. Sequential dissipative calculations are used to transform the cell into equations that can be solved to predict results for unknown variables in terms of continuity, momentum, and energy perspective. These equations were first introduced by Claude-Louis Navier and George Gabriel Stokes (NASA, 2015), known as Navier-Stokes equations.

These equation set are widely used in scientific and engineering fields for predicting various flow types. The Navier-Stokes equation set can be described in Equation below.

Momentum equation:

$$\frac{\partial}{\partial t}(\rho\vec{v}) + \nabla(\rho\vec{v}) = \nabla\left[\bar{\bar{T}}\right] - \nabla p + \rho\vec{g} + \vec{F} \qquad \textbf{3.41}$$

Where t corresponds to time(s), $\bar{\bar{T}}$ corresponds to the stress tensor, ρ corresponds to density(Kg/m^3), $\vec{v}$ corresponds to the velocity(m/s), p corresponds to the static pressure(Pa), and $\rho\vec{g}$ is the gravitational body force. $\vec{F}$ is external force which also contains other source terms such as porous media or user defined sources.

The terms on the left side of the momentum equation represent the variation of total forces with time, the first term on the right side represents the total viscous forces, the second term represents the total pressure forces, the third term represents the gravitational force. and the fourth term represents the amount of external forces applied to the fluid.

Continuity equation:

$$\frac{\partial \rho}{\partial t} + \nabla(\rho\vec{v}) = 0 \qquad \textbf{3.42}$$

The continuity equation indicates the fact that the mass is conserved.

Energy balance equations:

$$\frac{\partial}{\partial t}(\rho E) + \nabla[\vec{v}(\rho E + p)] = \nabla\left[k\nabla T - \sum_j h_j\overrightarrow{J_j} + \left(\bar{\bar{t}}\vec{v}\right)\right] + S \qquad \textbf{3.43}$$

Where E corresponds to energy(J), k corresponds to thermal conductivity(W/m℃), T corresponds to temperature(℃), $\overrightarrow{J_j}$ corresponds to the diffusion flux of species J(mol/m^{2}s), $\bar{\bar{t}}$ corresponds to the shear stress(Pa) and S is the heat source(W).

The first term on the left side of the energy balance equation represents the energy stored during the specified time t; the second term represents the amount of energy change within the system, the first term on the right side represents the conduction heat transfer, heat diffusion, and viscous heat dissipation respectively. The second term represents the other amount of energy generated within the domain, i.e., by reaction.

3.2.2 Turbulence models

There are several turbulence models available in Ansys Fluent: RANS (Reynolds-Averaged Navier-Stokes) based models, Detached Eddy Simulation, and Large Eddy Simulation. The RANS based models consists of Spalart-Allmaras model, $k-\varepsilon$ models, $k-\omega$ models and Reynolds stress model (Ansys, 2013).

The Spalart-Allmaras model is a low-cost one equation RANS model which is still relatively new, its reliability is still not be proved to all types of complex engineering flows (Ansys, 2013). The $k-\varepsilon$ models are the most widely used engineering turbulence model in industrial applications, while the $k-\omega$ models are also gaining its popularity despite of the fact that it requires more computational cost per iteration. The Detached and Large Eddy Simulation, on the other hand, is mainly adopted in high-end applications where RANS models could not

meet the needs (e.g. Combustion, Mixing, External Aerodynamics), and the computational cost is significantly higher when compared to RANS models.

The $k-\varepsilon$ model i is proposed by Launder and Spalding in 1972 (Launder & Spalding, 1972). The standard $k-\varepsilon$ model is a two-equation model, allowing two extra transport equations to represent the turbulent properties of the flow, hence account for the history effects like convection and diffusion turbulent energy. The first transport k determines the turbulent kinetic energy, and the second transport ε determines the scale of turbulence. The RNG $k-\varepsilon$ model and Realizable $k-\varepsilon$ model are both variations of the standard $k-\varepsilon$ model, The RNG model is derived from Navier -Stokes equation by using renormalization group (RNG) methods (Ansys, 2013). Compared to the standard $k-\varepsilon$ model, the RNG $k-\varepsilon$ model is able to account for the effects of smaller scales of motion, which makes it more accurate for many flow conditions such as low Reynolds number flow and rapidly strained flow (Ansys, 2013).

The Realizable $k-\varepsilon$ model is proposed by Shih et al. in 1995, by adding an alternative formulation for turbulence viscosity, which is more accurate in certain situations than standard and RNG $k-\varepsilon$ model where mathematical constraints exist on the physics of turbulent flow. (Jean, 2013).

It is considered that both RNG $k-\varepsilon$ model and realizable $k-\varepsilon$ model have shown substantial improvements over the standard $k-\varepsilon$ model in certain types of flow with strong streamlined

curvature, vortices and rotation (Ansys, 2013). Many researches indicated that in normal flow conditions, the difference between RNG and realizable $k-\varepsilon$ model is minimal.

In this research work, the RNG $k-\varepsilon$ model is used for turbulent flow domains. The equation of RNG $k-\varepsilon$ model is shown as below:

$$\frac{\partial}{\partial t}(\rho k)+\frac{\partial}{\partial x_i}(\rho k u_i)=\frac{\partial}{\partial x_j}\left(\alpha_k \mu_{eff}\frac{\partial k}{\partial x_j}\right)+G_k+G_b-\rho\epsilon-Y_M+S_k \qquad \textbf{3.44}$$

and

$$\frac{\partial}{\partial t}(\rho \epsilon)+\frac{\partial}{\partial x_i}(\rho \epsilon u_i)=\frac{\partial}{\partial x_j}\left(\alpha_\epsilon \mu_{eff}\frac{\partial \epsilon}{\partial x_j}\right)+C_{1\epsilon}\frac{\epsilon}{k}(G_k+C_{3\epsilon}G_b)-C_{2\epsilon}\rho\frac{\epsilon^2}{k}-R_\epsilon+S_\epsilon \qquad \textbf{3.45}$$

Where G_k corresponds to the generation of turbulence kinetic energy due to velocity gradients, G_b corresponds to the generation of turbulence kinetic energy due to buoyancy. Y_M is the fluctuating dilatation in compressible turbulence to the overall dissipation rate. α_k and α_ϵ are the inverse effective Prandtl numbers for k and ε respectively. S_k and S_ϵ corresponds to additional user defined source terms.

3.2.3 Near wall treatments

The turbulence flow conditions near stationary non-slip walls are very different from the flow conditions at the centre of the

flow domain. Due to the presence of shear stress and viscosity, the local velocity of fluid contacting the walls has to be zero. This causes a steep velocity gradient within a relatively small area near the walls, which is defined as 'near wall regions' in FLUENT 18.0 (Ansys, 2013). The $k-\varepsilon$ model cannot give proper predictions of near wall flow as the model is only suitable for fully turbulent flow, where in near wall regions, the flow is not fully turbulent and is greatly affected by fluid viscosity. In order to accurately predict the near wall flow conditions, proper adjustments are made to the turbulent models by adding a viscosity-affected region between the wall and the fully turbulent region. There are two common choices available in FLUENT 18.0 for calculating near wall conditions, which is the Standard wall function and the Enhanced wall function.

The standard wall function is the default settings in FLUNET 18.0, which is based on the proposal of Launder and Spalding (Launder & Spalding, 1972). The standard wall function works reasonably well for a wide range of wall-bounded flows, and is commonly used for industrial flows. However, the predictions may be affected in situations like when severe pressure gradient exist at near wall region, or the flow is in strong non-equilibrium condition (Ansys, 2013).

The enhanced wall function, on the other hand, performs similarly to standard wall functions while the mesh at near wall regions is fine enough. However, in cases with more coarse meshing, the Enhanced wall function can provide more accurate predictions compared to the Standard wall function,

hence greatly reduces computational requirement. Thus, it is considered that the Enhanced wall function has better all-round performance compared to the Standard wall function.

In this work, the enhanced wall function will be used in all situations with turbulent flow domains.

3.2.4 Enthalpy-porosity approach

In FLUENT 18.0, enthalpy-porosity approach is used to predict the solidification & melting process. The approach uses a mushy zone instead of explicitly tracking the liquid-solid front. The mushy zone is treated as a porous zone, and the porosity equals the liquid-fraction. The mushy zone constant is set to 10^5 as recommended by FLUENT user manual (Ansys, 2013) The energy equations of the enthalpy-porosity approach is shown as:

$$\frac{\partial(\rho H)}{\partial t} + \nabla(\rho \vec{v} H) = \nabla(k \nabla T) + S \qquad \textbf{3.46}$$

Where ρ corresponds to the density (kg), t corresponds to the time (s), v corresponds to the fluid velocity (m/s) and S is the source term. H is the enthalpy (J) and can be calculated as the sum of sensible and latent heat:

$$H = h + \Delta H \qquad \textbf{3.47}$$

Where h is the sensible heat (J) and ΔH is the latent heat (J). The h and ΔH is calculated as:

$$h = h_{ref} + \int_{T_{ref}}^{T} C_p dT \quad \textbf{3.48}$$

and

$$\Delta H = \beta L \quad \textbf{3.49}$$

Where h_{ref} corresponds to the reference enthalpy (J/kg), T_{ref} is the reference temperature (℃) and C_p corresponds to the specific heat (J/kg.K). β is the liquid fraction and L is the latent heat of fusion(J/kg). The definition of liquid fraction β can be expressed as:

$$\beta = 0 \quad if\ T < T_s \quad \textbf{3.50}$$

$$\beta = 1 \quad if\ T > T_m \quad \textbf{3.51}$$

$$\beta = \frac{T - T_s}{T_m - T_s} \quad if\ T_s < T < T_m \quad \textbf{3.52}$$

Where T_s and T_m are solidification and melting temperatures (℃) respectively.

3.2.5 Solver

The pressure based solver will be used in this work as it is capable of predicting a wide range of flow regimes from low-speed incompressible flow to high-speed compressible flow.

3.2.6 Spatial discretization

As FLUENT 18.0 uses finite volume method, the flow domain is divided into individual mesh elements. Flow parameters are resolved around the mesh nodes, and is interpolated to the mesh faces. In order to interpolate field variables stored at the cell centre to the faces of control volumes, FLUENT 18.0 provides several schemes for momentum, turbulent kinetic energy, turbulent dissipation rate and energy: First-Order Upwind, Second-Order Upwind, Power Law, MUSCL and QUICK. There are also four algorithms available in FLUENT 18.0 for pressure-velocity coupling: SIMPLE, PISO, SIMPLEC and Coupled.

The discretization scheme used in this work is as follows: SIMPLE for pressure-velocity coupling, PRESTO for pressure interpolation, Second order upwind for momentum and energy, and First order upwind for turbulent kinetic energy and turbulent dissipation rate.

3.2.7 Under-relaxation factors

The default setting of under-relaxation factors is used for all models in this work (see Table 3.3). For models with converging issue with the default setting, the relevant adjustments will be made in the first few initial steps (up to 0.5 for Pressure and down to 0.6 for Momentum) to stabilize the calculation, and is set back to default afterward to ensure sufficient accuracy.

Table 3.3 Under Relaxation Factors used in FLUENT

Under Relaxation Factors	**Value**
Pressure	0.3 (0.5)
Density	1
Body Forces	1
Momentum	0.7 (0.6)
Turbulent Kinetic Energy	0.8
Specific Dissipation Rate	0.8
Turbulent Viscosity	1
Energy	1

3.3 Summary

In this chapter, a series of models have been presented for the PVT-PCM system. The complex problem of predicting and evaluating the working performance of a cooled PV panel and its latent energy storage solution is made possible by inputting boundary conditions such as ambient temperature, solar irradiance level, etc. It is also possible to make optimizations to the system by tweaking individual parameters of the system. Moreover, the results are also helpful to have better initial guess during the CFD simulation, as well as validate the predicted results.

Moreover, the governing equations of the FLUENT 18.0 used in this work have also been presented in this chapter. After comparing the different specialization and limitation of each setup parameters, it is suggested that the RNG $k-\varepsilon$

turbulence model with enhanced wall treatment will be used for air and water flows during this study. The other used setup parameters such as discretization and under relaxation factor are also present.

CHAPTER 4. VALIDATION OF CFD APPROACH

4.1 Introduction

This chapter presents the validations of several CFD models which will be used later for parametric and whole system analysis. Due to the fact that CFD is based fundamentally on combinations of governing equations, it is important to set up base line models and validate with other sources of results before proceeding for further analysis. In this chapter, three base line models (PV, water cooling section and PCM) will be established, which covers the main components of the proposed PVT-PCM systems. The predicted results of those base line models will be compared with either numerical calculations and / or other literature to prove the reliability of CFD modelling. The validated CFD models can then be used for different analysis requirements.

4.2 Validation Analysis for PV-temperature

The aim of the PV Validation model is to simulate the temperature performance of the BP-275L flat plate solar panel by considering the convection and radiation heat transfer to and from the panel. The predicted PV panel temperature of this CFD model will be compared and validated with analytical

results under different wind speed, solar radiation level, and ambient temperature conditions.

4.2.1 Geometry, mesh, and materials

The PV validation model is a rectangular shaped panel with dimensions of 1183mm x 525mm x 4mm. The case uses three-dimensional geometry for a better overall accuracy.

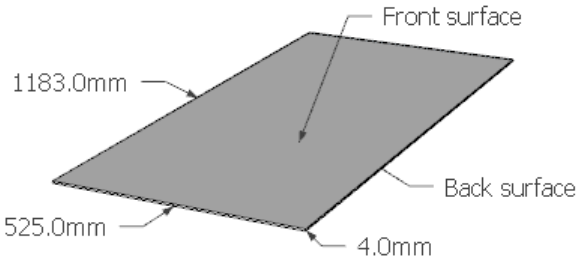


Figure 4.1 PV validation model geometry and dimension

The adapted mesh has a total amount of 38776 elements. The mesh has been adapted twice to show its independency, so that the influence of mesh size against final results has been minimized. The values of maximum and minimum PV temperature calculated by each mesh are compared with the original mesh using RMS (Root Mean Square) error method, and is shown in Table 4.1 below. The equivalent properties of PV panel have been calculated and presented in Section 3.1.1. The properties are implemented into FLUENT 18.0 with user defined material function.

Table 4.1 Mesh element counts and RMS error for CFD model 1

Mesh Case	Element count	RMS Error
Original	38776	

1st Adaption	49768	0.04%
2nd Adaption	68950	0.01%

4.2.2 Boundary and Initial conditions

Figure 4.2 below shows the boundary condition set up. The surrounding edges of the PV panel have been set to adiabatic conditions due to the relatively small exposure area. The front facing surface has been set to have convection heat transfer with free stream fluid, which needs input parameter of convection heat transfer coefficient and free stream fluid temperature. The back surface has been set to have heat flux input, as in real situations the layer that absorbs heat is placed beneath the transparent tempered glass cover. The simulation solver has been set to steady state, and initial conditions other than the varying parameter are set as follows: Solar radiation level = 450W/m^2, Ambient air temperature = 20 ℃, the convective heat transfer coefficient = 20.9W/m^{2}K at wind speed = 5m/s. The correlated convective heat transfer coefficient is calculated using Equation 3.20 and 3.21. The effective surface heat flux absorbed by the PV panel can be calculated by the equation below.

$$Q_E = \alpha \cdot \Phi \qquad \textbf{5.1}$$

While Q_E corresponds to the effective surface heat flux (W/m^2), Φ corresponds to the solar incident irradiance (W/m^2), and α is the panel absorbance.

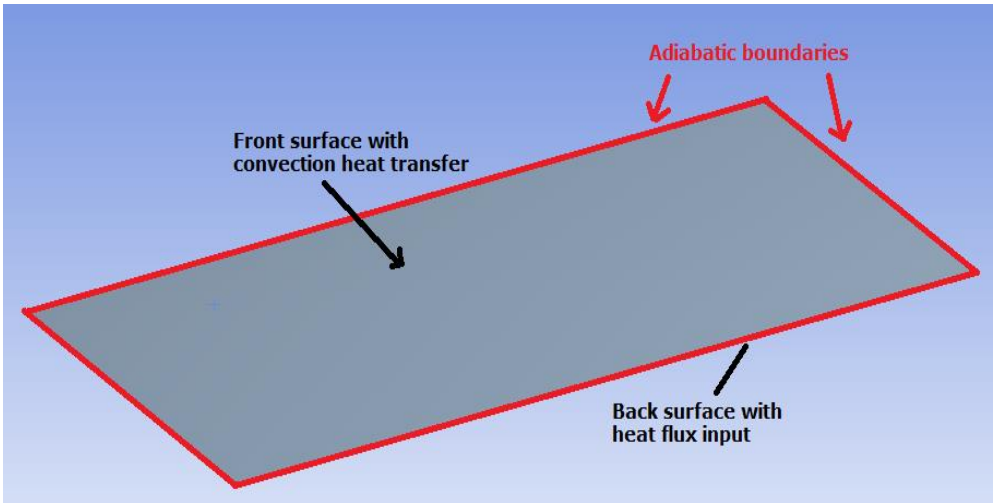


Figure 4.2 Boundary conditions of the CFD model 1

4.2.3 Results and discussion

The results calculated by FLUENT 18.0 are compared with analytical calculations. The analytical calculations are done by using explicit method using Excel with a set time step of 1s. The comparison has been made by changing one of the initial conditions, hence extensively examine the degree of agreement of the PV CFD validation model with the analytical model.

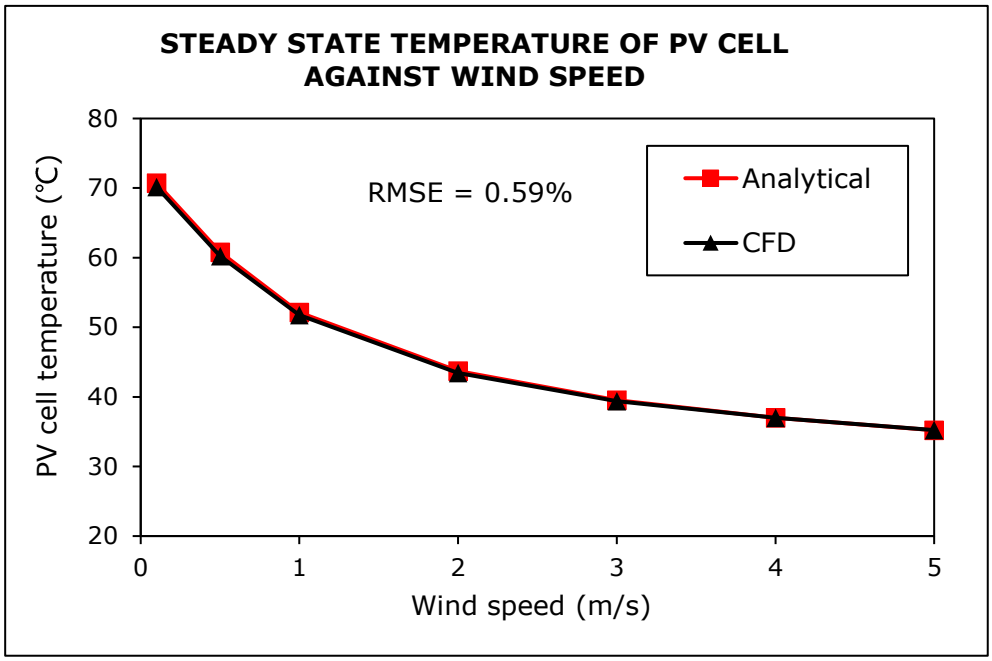


Figure 4.3 Steady state temperature of PV cell against wind speed for CFD model

Figure 4.3 shows the steady state cell temperature variation with increased local wind speed. The temperature monitored in CFD is the average front surface temperature of the PV panel in order to be comparable to analytical results. It is also noted as the PV panel's thickness is only 0.004m, there is no notable temperature difference between front and back surface of the panel. The two methods have a very good agreement with each other, with an RMS (Root Mean Square) error of 0.59%. It can be seen from the figure that the cell temperature drops from 70℃ to 35℃ as wind speed increased from 0.1m/s to 5m/s.

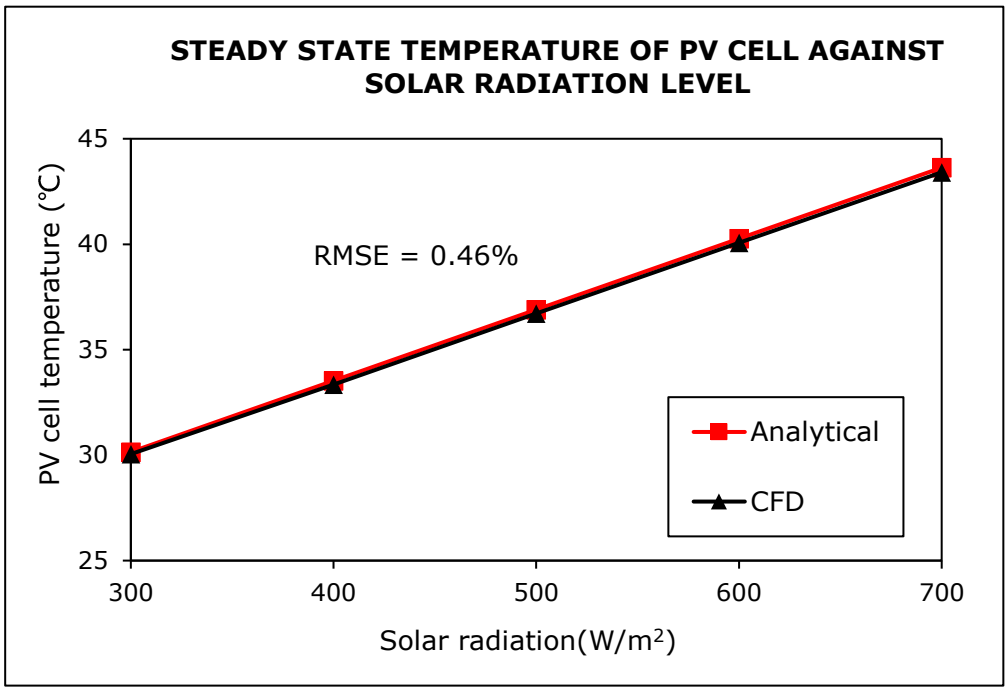


Figure 4.4 Steady state temperature of PV cell against solar radiation level for CFD model

Figure 4.4 shows the steady state cell temperature variation with increased solar radiation. The two methods have a very good agreement with each other, with an RMS error of 0.46%. The temperature rise has a linear relationship with the increase of solar radiation, with an increased rate of 4.3℃/100W/m^2 in steady condition.

It is also noticed that the two methods have better agreements at low solar radiation levels while PV cell temperature is relatively low. On the other hand, at solar radiation level = 700W/m^2, the difference of PV cell temperature predicted by the CFD model and analytical model is most significant (at 43.41 ℃ and 43.63 ℃ respectively). However, it is still considered to be accurate enough with percentage difference value of 0.5%.

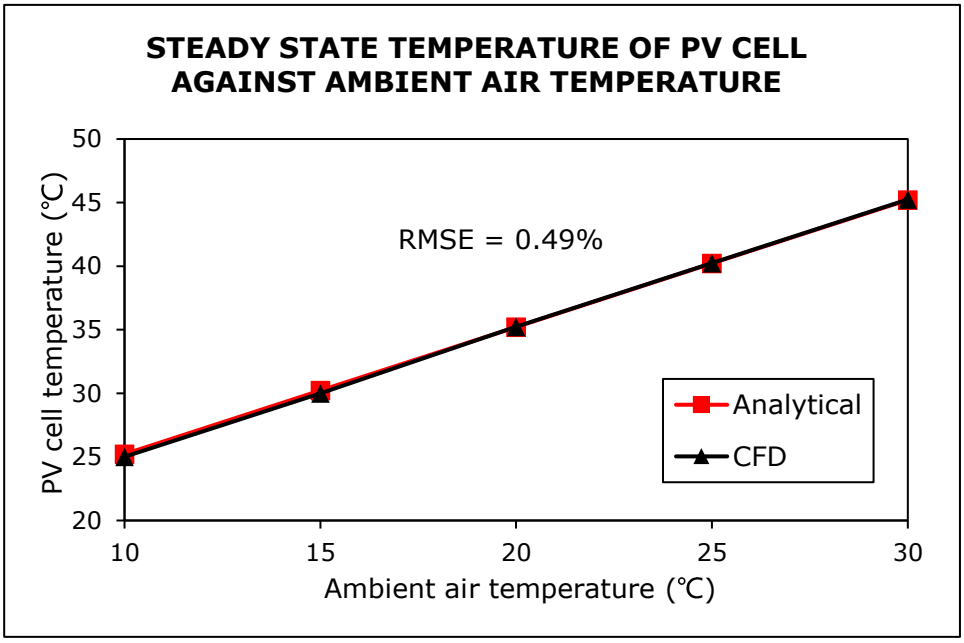


Figure 4.5 Steady state temperature of PV cell against ambient air temperature for CFD model

Figure 4.5 shows the steady state cell temperature variation with increased ambient air temperature. The two methods have a very good agreement with each other, with an RMS error of 0.49%. The cell temperature rise has a linear relationship with the increase of ambient temperature, with an increased rate of 1℃ per 1℃ ambient temperature rise in steady condition.

4.3 Validation Analysis for heat transfer in water pipe

4.3.1. Model setup

In order to validate the CFD's prediction results of convective heat transfer, a 3d geometry of water pipe with a diameter of 6mm and a length of 1183mm has been used for the simulation,

which is the same size of the water pipes used in proposed PVT system for panel cooling. Empirical correlations are used to calculate the average surface heat transfer coefficient, and the calculated data is then compared with CFD predicted results. Equation 4.28 is used to calculate the Nusselt number for laminar conditions, which is suitable for predicting the Nusselt number of water flow inside tubes with Reynolds number < 2200. The critical point of Reynolds number when transition flow occurs is different in different flow geometry, for flow in a pipe, the critical Reynolds number is generally considered to be around 2100 – 2300 (Warhaft, 1997). For Reynolds number > 4000, the flow is considered to be turbulent, in which case the Nusselt number could be calculated using Dittus-Boelter equation (equation 4.26) or Gnielinski correlation (equation 4.27).

4.3.2 Mesh, material and boundary conditions

The total mesh element count for this 3D geometry is 698650. The mesh has been adapted twice in order to show independency. Table 4.2 below shows the element count of two adapted mesh and their RMS error against original one. The material used in this case is water liquid, which has its properties stored in FLUENT 18.0 database. The inlet water has been set to a constant temperature of 20℃, with velocity variation from 0.35m/s to 0.65m/s for turbulent flow, and from 0.004m/s to 0.1m/s for laminar flow. The outlet has been set

to pressure outlet. The pipe surface has been set to have a constant temperature of 30℃.

Table 4.2 Mesh element counts and RMS error of heat transfer validation model

Mesh Case	Element count	RMS Error
Original	698650	
1st Adaption	1272908	0.63%
2nd Adaption	1360013	0.22%

4.3.3 Results and discussion

Figure 4.6 below presents the comparison of the average surface heat transfer coefficient against different flow velocity for both CFD and analytical calculations in turbulent flow conditions. It can be seen from the figure that both analytical approaches have good agreements with CFD predictions with maximum RMS error less than 10 percent. In low Reynolds number regions ($3000 < Re < 10000$), The Gnielinski correlation is considered to be more accurate than the Dittus-Boelter equation which is often used in flow conditions with Reynolds number greater than 10000. The CFD numerical prediction has better agreement with Gnielinski correlations with the RMS error of 3.25%. At the same time, the numerical prediction also shows a similar increasing trend with the Dittus-Boelter equation, with a slightly larger RMS error of 8.52%.

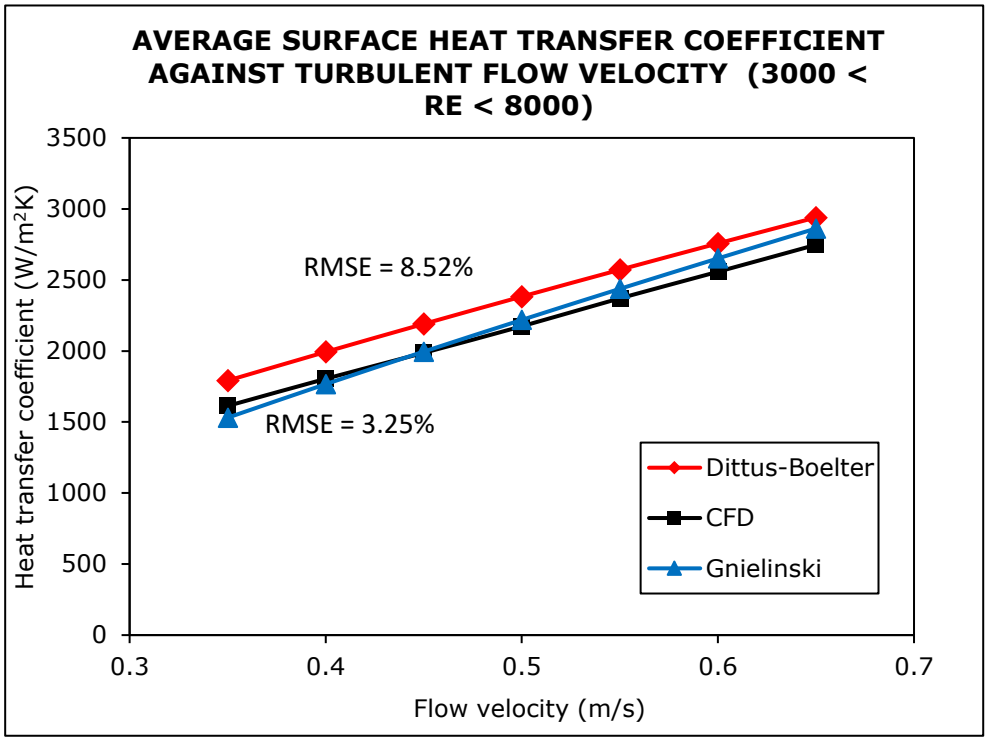


Figure 4.6 Average surface heat transfer coefficient against flow velocity (Turbulent)

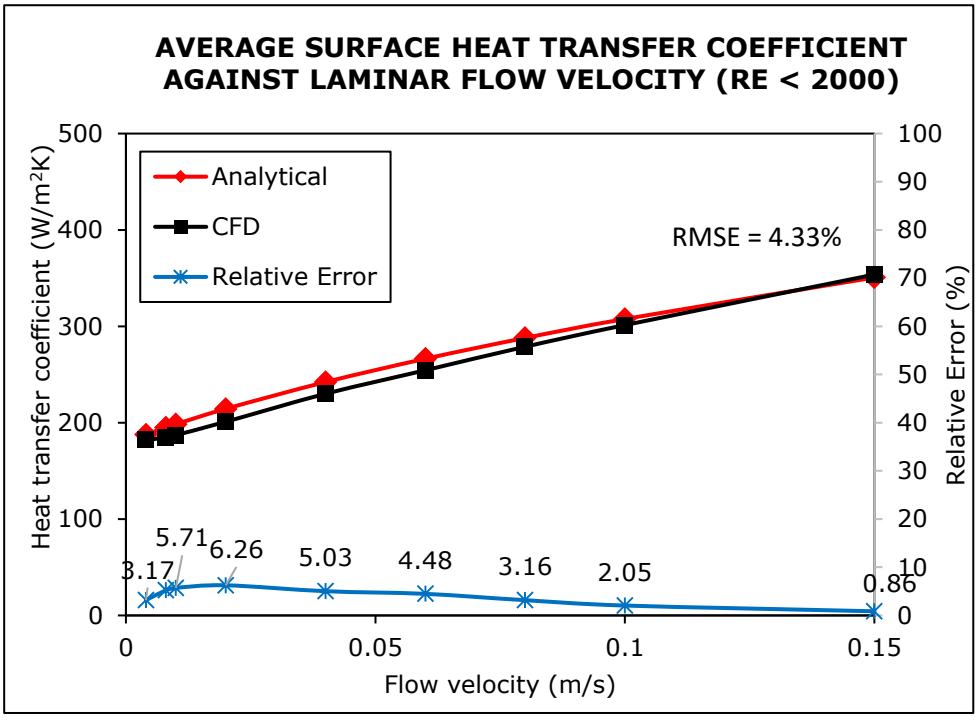


Figure 4.7 Average surface heat transfer coefficient against flow velocity (Laminar)

Figure 4.7 above presents the comparison of the average surface heat transfer coefficient against different flow velocity for both CFD numerical prediction and analytical calculation for laminar flow conditions. It can be seen from the figure that the two methods had a good agreement, with an overall RMS error of 4.33%. The Reynolds number varies from 48 to 1800 while flow velocity is increased from 0.004m/s to 0.14m/s, at flow velocity of 0.16m/s, the flow will become transition flow as Reynolds number exceeds the critical point. Both methods show a nearly linear relationship between the flow velocity and heat transfer coefficient. The maximum percentage difference occurs at flow velocity of 0.02m/s with a value of 6.26%.

In summary, the CFD predicted results are comparable to the data from analytical models in both laminar and turbulent flow conditions. The proposed heat transfer model can be considered valid to use in further analysis.

4.4 Validation Analysis for PCM

4.4.1 CFD Validation of solidification and melting approach against Solid (specified heat capacity) approach

The purpose of this validation model is to compare two different approaches available in FLUENT 18.0 for numerically modelling

PCM performance. The name 'solidification and melting approach' represents that the PCM is set to be fluid, while the corresponding temperature related thermal physical properties are set through solidification and melting option in FLUENT 18.0. On the other hand, 'Solid approach' represents that the PCM is set to be solid (set PCM to fluid generates same results as there's no flow inside the domain), with its thermal physical properties set within the material property configuration panel. The numerical predictions of the two results will be compared first, and then in section 4.4.2, the numerical prediction will be compared to external literature for further validation.

Geometry, mesh, and materials

The aim of the model is to study the surrounding PCM thermal performance while heated or cooled by a water pipe. For the purpose of studying PCM thermal performance, assuming the temperature gradient across the flow direction of the water pipe is negligible, the model could be simplified by using two-dimensional geometry of the cross-sectional area. Figure 4.8 below shows the geometry and its boundaries. This geometry represents the cross-sectional area of a 6mm diameter circular water pipe, surrounded by a 2.5mm thick layer of PCM. The thickness of pipe wall is neglected because its conductivity is much higher than the thermal conductivity of PCM.

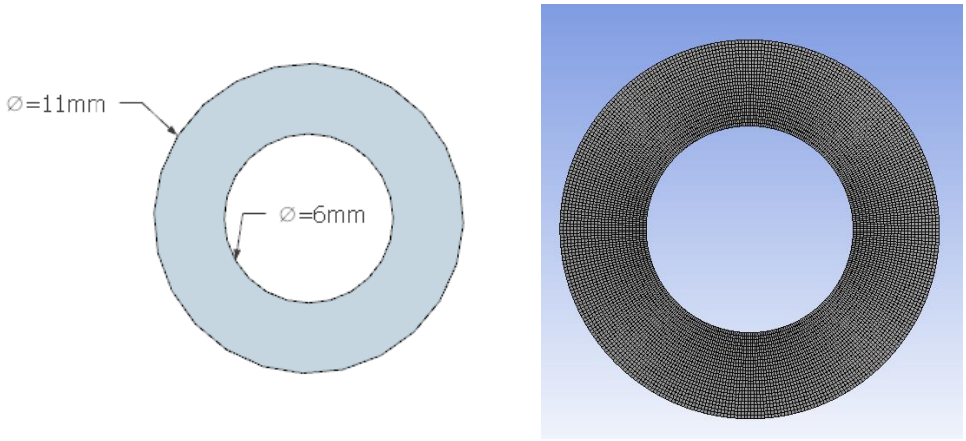


Figure 4.8 Geometry dimension and structured mesh of the validation model

The mesh has a total count of 8700 elements, and has been adapted twice to validate its independency, which means the effect of mesh element size against final results could be minimized. In order to compare results against three different meshes, average PCM temperature was recorded every 1800s, and RMSE method is used to calculate the error percentage. The element size and RMSE compared to the original mesh of two adapted mesh is shown in Table 4.3 below.

Table 4.3 Mesh element counts and RMS error for liquid approach model

Mesh Case	Element count	RMS Error
Original	8700	
1st Adaption	15776	0.33%
2nd Adaption	24678	0.16%

The material used in this simulation case is PCM-HS22P which is later discussed and chosen for the PVT-PCM system in Nottingham. The specific properties of PCM-HS22P are given by its manufacturer data sheet (savENRG, 2015). Due to the fact that PCM has some temperature related properties, those temperature related properties are implemented into FLUENT

18.0 using piecewise-polynomial (for temperature related specific heat capacity) or piecewise-linear (for temperature related conductivity) function.

Considering the fact that the internal buoyancy effect of PCM is minimal while being used in the proposed PVT-PCM application due to the nature of high viscosity and low temperature difference in heat transfer process, thus the density of the PCM is set to a constant value depending on the initial solid or liquid state.

The specific viscosity property of PCM-HS22P is not provided in the manufacturer data sheet, and is not found in other works related to this particular PCM. The closest viscosity property available for $\mathrm{CaCl_2 \cdot 6H_2O}$ salt hydrate is 11.8 mm^2/s at temperature of 50℃ (OXY, 2016).

While solidification & melting model is enabled, the melting latent heat could be directly set through the configuration panel. However, with solidification & melting model disabled, there is no such option available. In order to account for the latent heat, the latent heat is converted to the specific heat during melting temperatures by the equation below:

$$C_p = \frac{LH}{\Delta T} \qquad \textbf{4.1}$$

Where C_p is the specific heat during melting process, LH is the total amount of latent heat, and ΔT is the temperature difference between the start and the end of melting process.

The converted C_p is then implemented into FLUENT 18.0

For comparing different timestep sizes, the solid PCM approach is used. For solid only and solidification & melting approach comparison, the PCM is set both as solid and as fluid (with solidification and melting on) for each specific approach.

Boundary and Initial conditions

Overall, the two-dimensional geometry has 2 boundary types: PCM panel wall and heated surface. The panel wall has been set to adiabatic condition, and the heated surface has been set to a constant temperature of 25℃ during the charging period and 20℃ during discharging period. At t=0, the PCM initial temperature is set to be 20℃ in charging process and 25℃ during the discharging process. The solution control is left as default, however, during simulations with timestep size less than 1s, the energy under-relaxation factor was set to 0.9 for the first 100 timesteps in order to achieve convergence. The under-relaxation factor was set back to default after the solution stabilizes.

Results and discussion

- *The effect of timestep size against final results*

The timestep size used during numerical simulation could affect the final results significantly. Hence it is necessary to validate the timestep size before conducting any numerical simulation. A common practice for PCM related simulation is using timestep start with 0.05s – 0.1s (Koller et al. 2016; Wang et al. 2016; Vikas et al. 2017). Figure 4.9 below shows the comparison between different timestep size against average PCM temperature along the time during the charging process. It can be seen that The PCM finished it's melting process at around 27.5 minutes after the heating process, and reaches the maximum temperature at around 30 minutes. It is noticed that despite all temperature profile under different timestep settings show similar trends during the charging process, the 0.05s timestep size has the longest charging time, which is 1.5 minutes more compared to the rest of timestep settings. Considering the total time, the percentage difference regarding of the charging time is 5.45%. There is minimal difference between timestep sizes of 0.1s, 1s, and 10s.

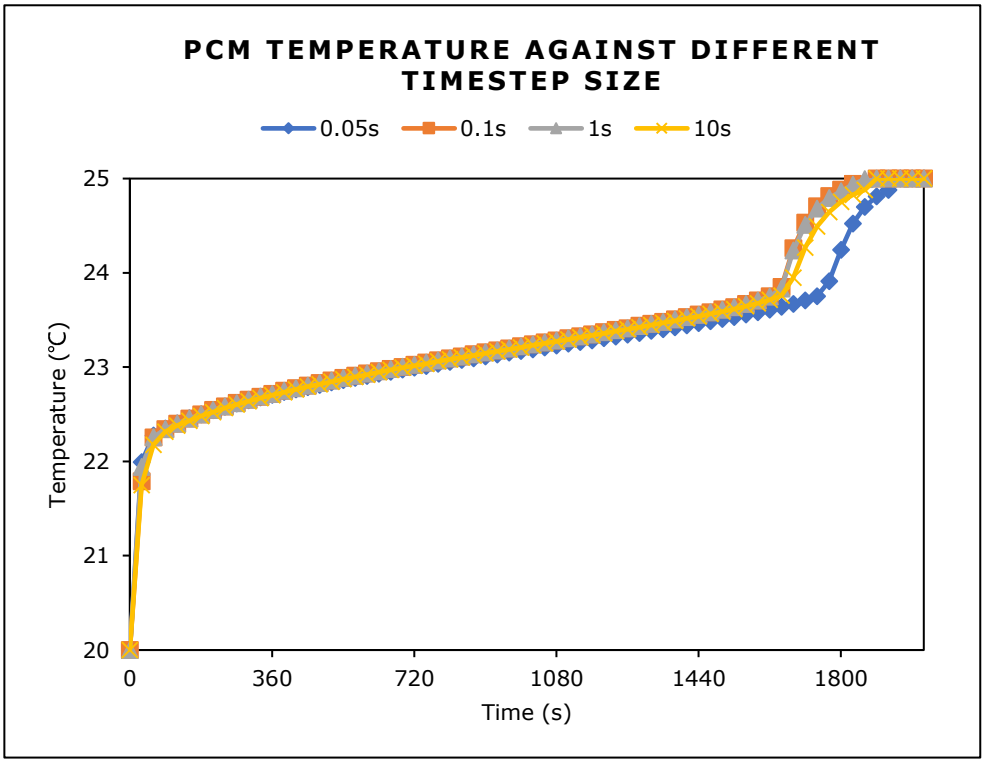


Figure 4.9 PCM temperature against different timestep size in charging process

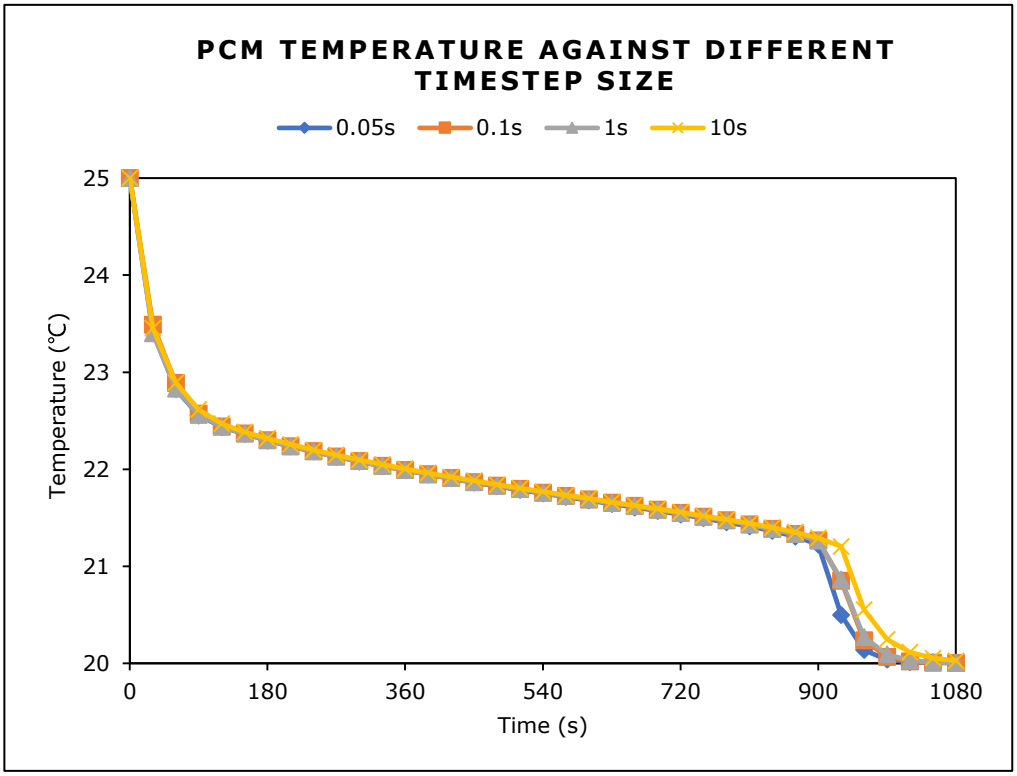


Figure 4.10 PCM temperature against different timestep size in discharging process

Figure 4.10 shows the comparison between different timestep size against average PCM temperature along the time during the discharging process. It can be seen that the PCM is fully solidified after 15 minutes, and is fully discharged after around 17 minutes. It is also noticed that the difference of temperature profile between each timestep size is smaller compared to temperature profile difference in charging process.

Considering the fact that using timestep smaller than 0.05s will require significant amount of extra calculation time with limited computational resource, in order to optimize the simulation process without affecting the final results, initial timestep of 0.05s will be used in all cases for this study. For models with large mesh elements and high complexity, after the temperature change rate is stabilized (PCM entering phase change state), the timestep is gradually increased so that the simulation time is significantly reduced without affecting accuracy.

- *Comparison between S&M and solid approaches*

Figure 4.11 below shows the comparison of the average temperature profile of PCM-HS22P in the PCM panel during charging process between solid only and solidification & melting approach. The results show that the two different approaches, despite having different material property and phase change consideration, have a very good agreement regarding to the prediction of PCM charging temperature profile. The PCM-HS22P starts to melt soon after the heating starts, and is able to stay in relatively low temperature until around 30 minutes of heating (from 22.2℃-23.5℃). The PCM

temperature then starts to rise at a faster speed due to the fact that the phase change process for the most part of PCM is finished. The fully liquefied PCM reached 25℃ which is the temperature limit of the heating surface after another 150 seconds (32.5 minutes in total for charging process). There is a slight time difference of the finishing time of the melting process between two approaches. However, the difference is considered to be relevantly small (less than 1%) compared to the total time frame of the charging process.

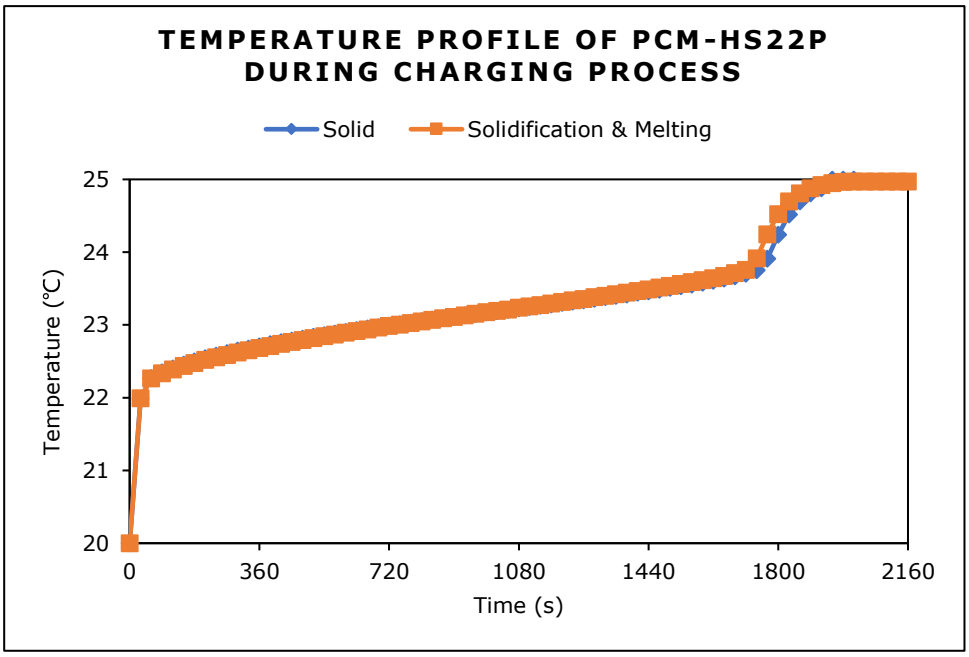


Figure 4.11 Temperature Profile comparison of PCM-HS22P during Charging process

Figure 4.12 below shows the comparison of the average temperature profile of PCM-HS22P in the PCM panel during discharging process between solid and liquid approach. The results show that the two different approaches have a very good agreement. The PCM-HS22P starts to solidify at around 90 seconds after the start of discharging process, and is slowly releasing its latent heat. After around 15 minutes, the

discharging process is finished, and the solid phase PCM is continued to be cooled to 20℃ which is the temperature limit of the cooled surface. There is also a slight time difference between two approaches regarding to the solidification time, however, the temperature difference is relatively small (less than 1%) compared to the total timeframe.

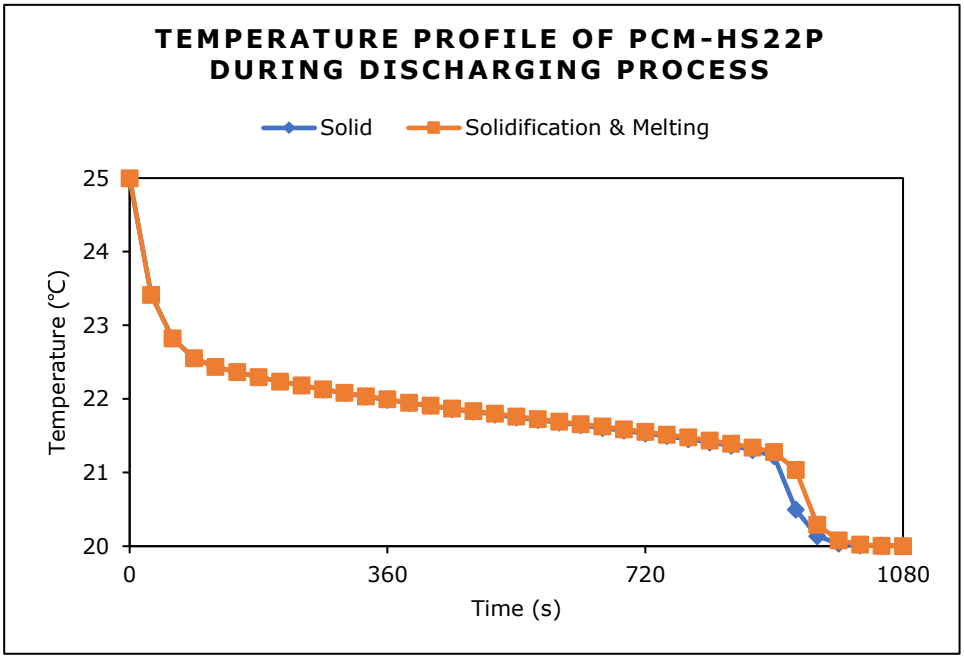


Figure 4.12 Temperature Profile comparison of PCM-HS22P during Discharging process

In summary, the predicted results of PCM temperature in both charging and discharging process from the solid only and solidification & melting approaches are comparable with minimal differences. Both methods could be used for numerical modeling for PCM thermal performance for this research work if either of the two approaches is valid. Section 4.4.2 below will present the validation of a recreated CFD model from Iten et al.'s work using solid only approach.

4.4.2 CFD Validation of PCM using solid only method against data from literature

The purpose of this validation model is to replicate the PCM-CFD model proposed by Iten et al. with the aim of comparing and justifying the setup parameters of the CFD model which can then be used in further analysis of this study.

Geometry, mesh, and materials

This simulation setup mainly represents three rectangular storage panels filled with PCM. The PCM panels were placed evenly inside an air channel. This simulation used two-dimensional geometry of the cross-sectional area. The geometry and dimensions of the model is shown in Figure 4.13 and Figure 4.14 below.

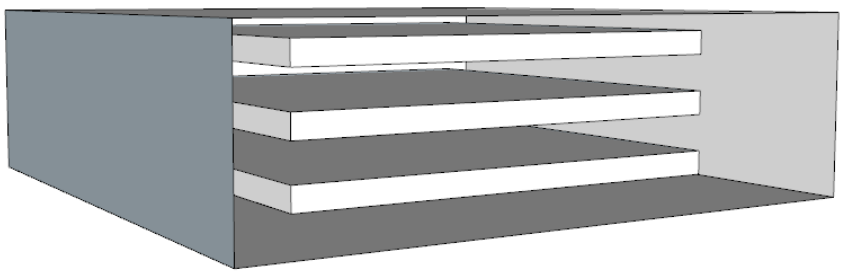


Figure 4.13 3D geometry recreated for Iten et al. (2017)'s model

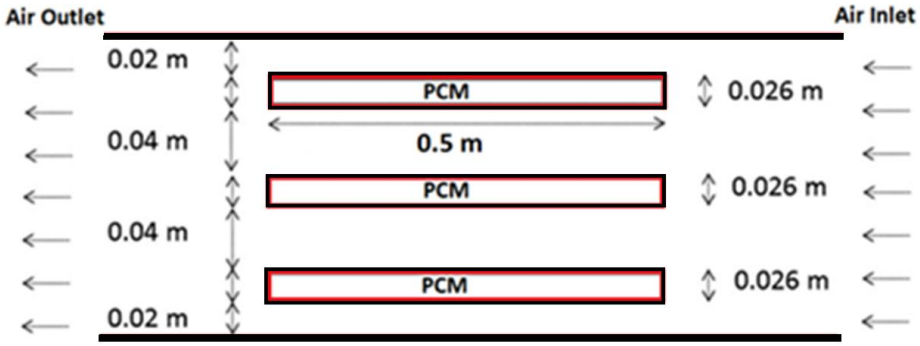


Figure 4.14 2D cross-sectional view of the PCM panel in the air duct (Iten et al., 2017)

The adapted mesh has a total count of 43202 elements and has been implemented near wall refinement to better suits complex fluid structure and heat transfer process near boundaries (as illustrated in Figure 4.15). The mesh was adapted twice to show its independency, which in that case the effect of mesh element size against final results could be minimized. In order to compare results calculated using three different meshes, average PCM temperature for every 1800s was recorded and compared using RMSE method. The element size and RMSE of two adapted mesh against original mesh are shown in Table 4.4 below. The materials used in this simulation case are air and PCM-RT25. The properties of air can be acquired from the fluent database, and some of the properties of PCM-RT25 can be obtained from manufacturer data sheet (RubiTherm, 2017). The temperature related specific heat values of PCM-RT25 is taken from experimental measurements done by Iten et al. (2017), and is implemented into FLUENT 18.0 using piecewise – linear function. It should be noted that due to the fact that there's no exact data of the temperature related specific heat value of PCM-RT25, numbers were estimated from the graph at best effort, as shown in Table 4.5

below. The PCM-RT25 is set to be solid phase as the initial state in both charging period and discharging period.

Table 4.4 Mesh element counts and RMS error for PCM-RT25 validation model

Mesh Case	Element count	RMS Error
Original	43202	
1st Adaption	69586	0.75%
2nd Adaption	173824	0.67%

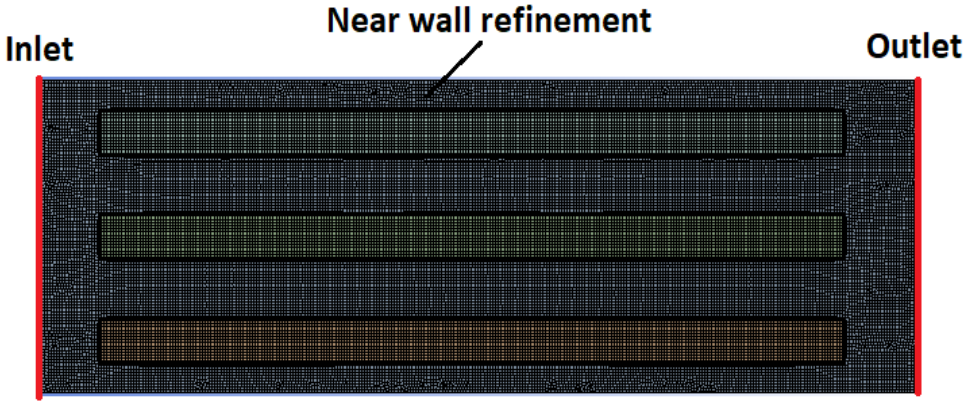


Figure 4.15 Mesh and boundaries for the PCM-RT25 validation model

Table 4.5 Thermal physical properties of PCM-RT25 (Iten et al., 2017)

Property	Unit	Value
Density	Kg/m^3	880
Thermal conductivity	W/mK	0.2
Dynamic viscosity	m^2/s	0.0072
Specific heat	kJ/kgK	See Figure 4.16

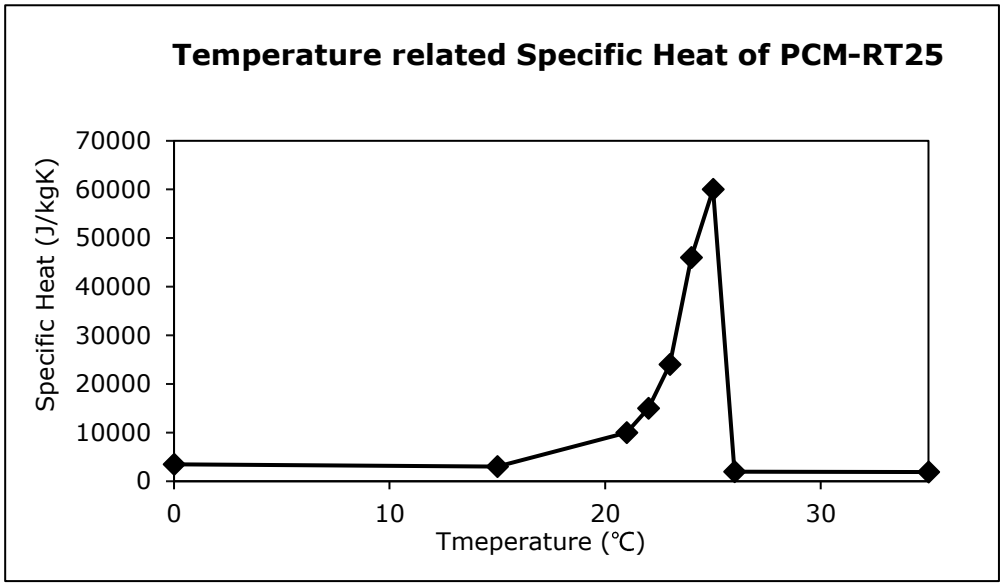


Figure 4.16 Temperature related Specific Heat of PCM-RT25 read from Iten et al. (2017)'s measurements.

Boundary and Initial conditions

The boundary conditions of the model have been set as follows: The walls of air duct have been set to have a convective heat transfer coefficient of 10W/m^2 with free stream bulk temperature of 19℃, while the PCM panel walls have been set as heat transfer interface between PCM and air. The inlet of air temperature has a constant velocity of 2.5m/s with temperatures of 38 ℃ in charging process and 12 ℃ in discharging process. At t=0, the PCM in charging process is set to have an initial temperature of 16℃, while the PCM in discharging process is set to have an initial temperature of 30℃. All boundary and initial conditions are identical with Iten et al.'s work.

Results and discussion

Figure 4.17 and Figure 4.18 show comparison of transient results between Iten et al. (2017)'s and the finished results of CFD replication model. The two figures show the hourly Temperature profile of PCM-RT25 during charging process for 4 hours. The contour temperature range is set from 16℃ to 25℃ in order to show clear and comparable temperature variation, which means the part of PCM will not show in the contour if the temperature of that part is below 16℃ or above 25℃.By comparing both temperature contours, it is found that the CFD model produces similar results as Iten et al.'s work, which is validated experimentally. It can be seen from two figures that the PCM has almost finished the charging process at around 2 hours, where temperature of the majority of PCM-RT25 is above 25℃. The PCM temperature rises soon after the charging process started, to a point when outer layers of PCM start melting. The melting process is not uniform along the panel due to the fact that the hot air is cooled when in contact with PCM panel. Air moves from right side to the left, and is cooled down along the channel, causing the Melting speed of the left side of PCM slower than the right side.

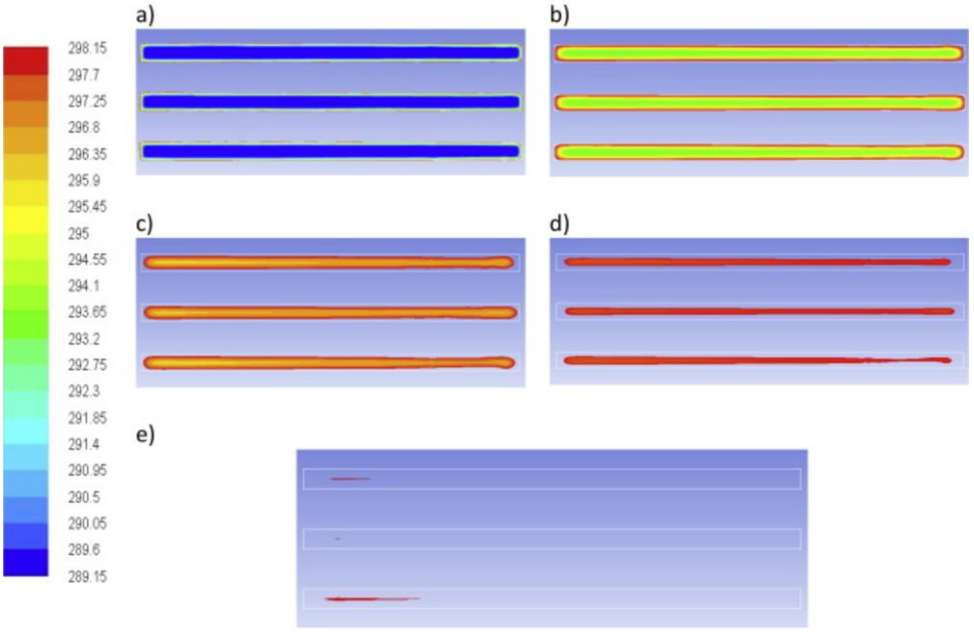


Figure 4.17 Temperature contours of the PCM RT-25 from CFD model during charging process from t= 0 (a) with 30min interval

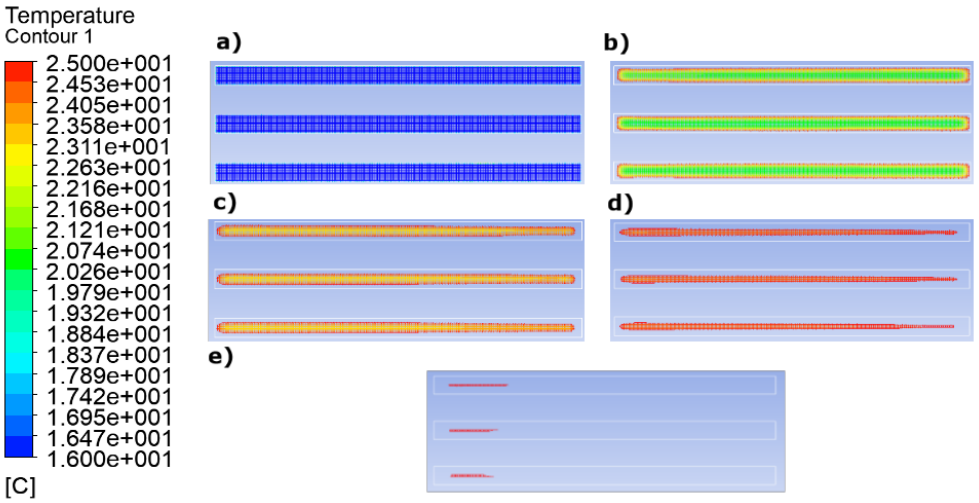


Figure 4.18 Charging process PCM temperature contours from Iten et al. (2017)'s work from t= 0 (a) with 30min interval

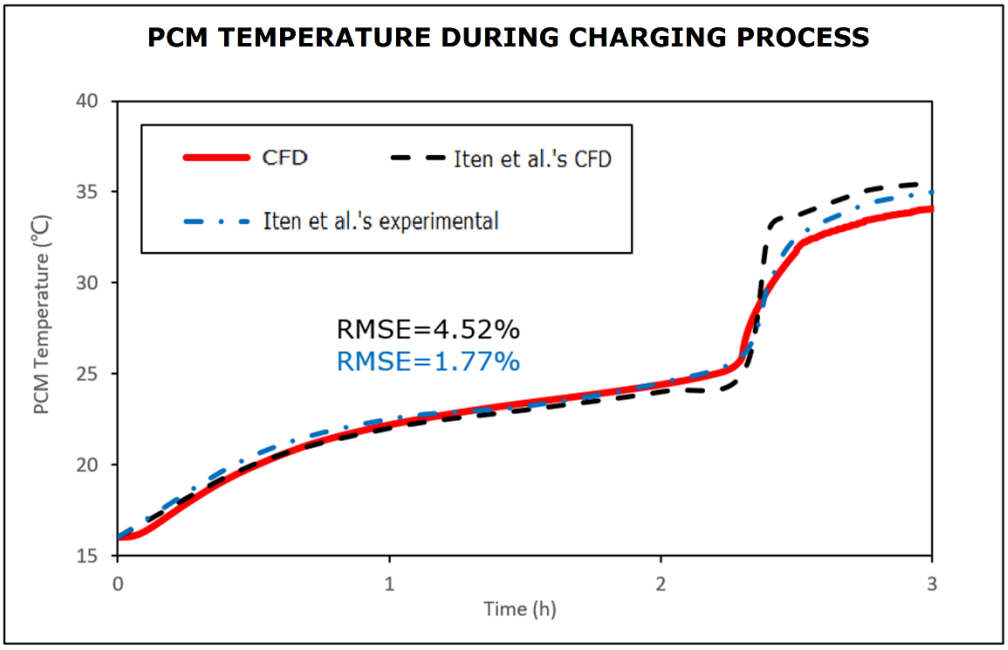


Figure 4.19 Minimum PCM temperature profile comparison during charging process

Figure 4.19 shows the minimum temperature of PCM-RT25 inside the panel during the charging process. It can be seen from the figure that the CFD results show a good agreement with Iten et al.'s CFD and experimental results, with an RMS error of 4.52% and 1.77% respectively. The temperature profile of CFD results matches to Iten et al. (2017)'s experimental results better; possible reasons are the finer mesh (43202 vs. 12160) with refined boundaries and more realistic specific heat input at higher temperatures when using the piecewise-linear function. It can be seen from the figure that the PCM finished charging process completely at around 2:15 hours, and is then heated up in the pure liquid state where the rise of temperature becomes significant.

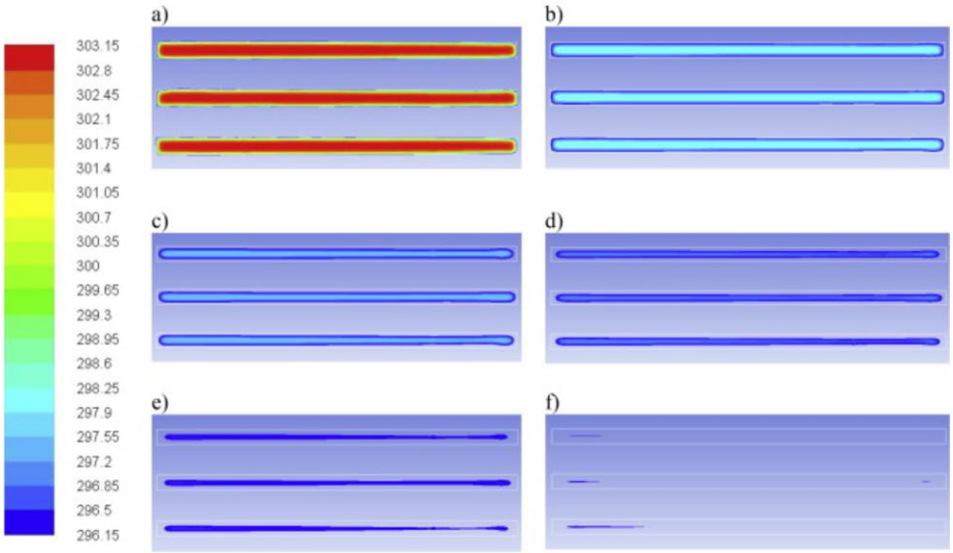


Figure 4.20 Temperature contours of the PCM RT-25 from CFD model during discharging process from t= 0 (a) with 30min interval

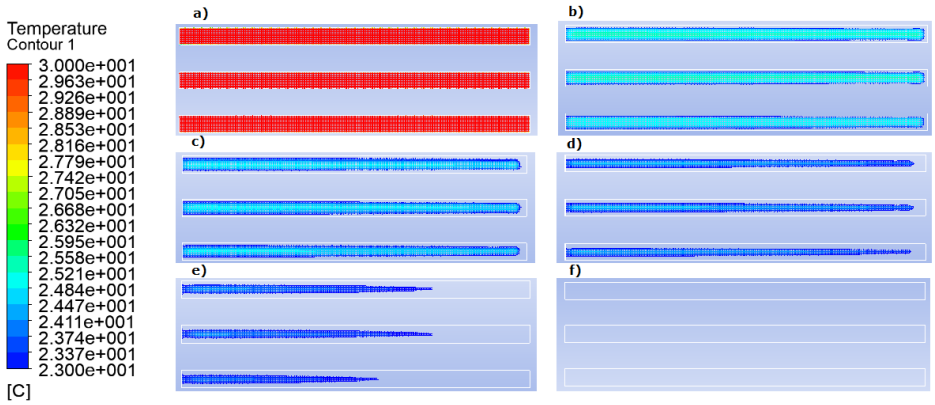


Figure 4.21 Discharging process PCM temperature contours from Iten et al. (2017)'s work from t= 0 (a) with 30min interval

Figure 4.20 and Figure 4.21 show comparison of transient results between Iten et al.'s work and the finished results of replication CFD model for the discharging process. The two figures show the temperature profile of PCM-RT25 during the discharging process at every 30 minutes for a total amount of 2 hours. The contour temperature range is set from 23℃ to 30℃, which means the part of PCM will not show in the contour if the temperature of that part is below 23℃. Results show that

the proposed CFD simulation produces similar results compared to Iten et al.'s work, with a slight variation towards the end of discharging process, where the temperature from the CFD model drops slightly faster. It can be seen from two figures that in both cases the PCM finished the discharging process after 2 hours. The bulk PCM temperature decreases after the cooling started to a point when solidification starts around outer layers. The solidification process is not uniform along the panel due to same reason in charging period, and same temperature variation pattern applies to both charging and discharging process.

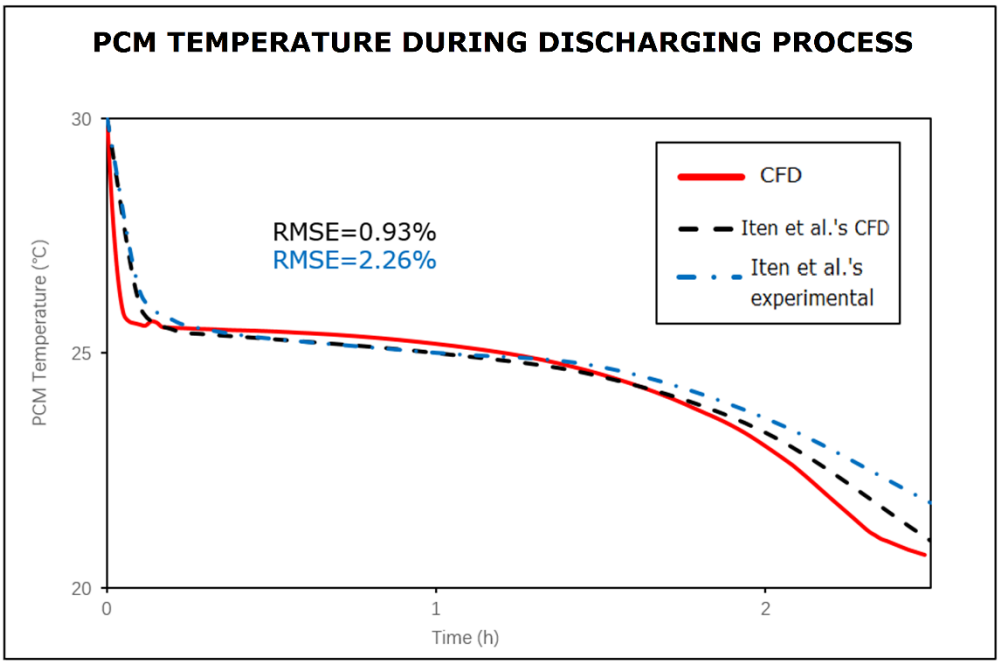


Figure 4.22 Maximum PCM temperature profile comparison during discharging process

Figure 4.22 shows the minimum temperature of PCM-RT25 inside the panel during the charging process. It can be seen from the figure that the CFD results show a good agreement with Iten et al.'s CFD and experimental results, with an RMS error of 0.93% and 2.26% respectively. The temperature

profile of the CFD model shows a slight offset compared to Iten et al.'s work towards the end of discharging process. One possible reason is that the input specific heat of PCM when the temperature drops below 23℃ is lower than actual value. It can be seen from the figure that the PCM finished its discharging process completely at around 2 hours, and is then continually cooled in solid state where the gradient of temperature decrease becomes steeper.

4.5 Summary

For PV cell temperature validation, the CFD model has a very good agreement with analytical calculations for different variables of wind speed, solar radiation level, and ambient temperature.

For water heat transfer validation, the CFD model and numerical calculations have very good agreement in both laminar and turbulent flow conditions. It is considered that in turbulent flow conditions, the Gnielinski shows better agreement with CFD predictions rather than the Dittus-Boelter equation.

For PCM validation, two CFD models have been built with different PCM property settings. The first PCM model is used to compare the solid only and solidification & melting approach, the result shows that both solidification & melting method and solid only method can accurately predict the PCM phase change process, while the only difference is that by using solidification

& melting method, the exact value of liquid fraction of PCM could be known, while using solid only method, the phase change situation can only be deduced by the temperature of the PCM. On the other hand, the charging and discharging of PCM-RT25 predicted by CFD models are compared with Iten et al. (2017)'s work. The results show that the replication of Iten et al.'s model generates comparable results as the original work.

CHAPTER 5. STUDY ON THERMAL PERFORMANCEE OF SALT HYDRATE PCM

5.1 Introduction

In this chapter, the thermal performance of a typical salt-hydrate PCM (PCM-HS22P, which is later used in the proposed PVT-PCM system) will be investigated and compared with most commonly used heat storage media - water. Despite of the fact that PCM-HS22P is commercially available and is often claimed to have better thermal performance than organic paraffin wax PCMs, there is currently no complete study available on its thermal performance as well as its thermal properties. Hence the chapter also presents parametric studies regarding to some thermal physical properties such as heat capacity, fusion heat and thermal conductivities for better understanding the effect of each property against overall thermal performance. By studying the characteristics of PCM-HS22P, a general idea could be given to predict the performance of other similar types of salt hydrate PCM.

5.2 Model setup

Geometry, mesh, and materials

The geometry and mesh profile of the model used is the same to the PCM validation model used for in section 4.4.1. The

materials used in this simulation case are PCM-HS22P and water. The properties of water can be found in the database of FLUENT 18.0, while the specific properties of PCM-HS22P can't be found. Thus the properties are acquired by its manufacturer data sheet (savENRG, 2015). Due to the fact that PCM has some temperature related properties, those temperature related properties are implemented into FLUENT 18.0 using the piecewise-polynomial function.

Boundary and Initial conditions

Overall, the two-dimensional geometry has 2 boundary conditions: PCM outer wall and Heated surface. The Outer wall has been set to adiabatic condition, and the heated surface has been set to a constant temperature of 25℃ during the charging period and 20℃ during discharging period. At t=0, the PCM initial temperature is set to be 20℃ in charging process and 25℃ during the discharging process, on the other hand, in order to have a direct comparison, the initial water temperature at t=0 is set to be the same as PCM-HS22P in both situations.

5.3 Comparison between PCM and water

Figure 5.1 and 5.2 show the temperature comparison of PCM-HS22P and water during charging and discharging process respectively. It can be seen from the figures that the PCM has much slower temperature changing rate compared to the common heat storage solution used in PVT researches. The

water reaches the maximum temperature in only 3.5 minutes during the charging process, while PCM can still maintain a low increase rate for up to 39 minutes. The discharging process shows similar trends; the water reaches the minimum temperature in 3.5 minutes while PCM uses 17 minutes.

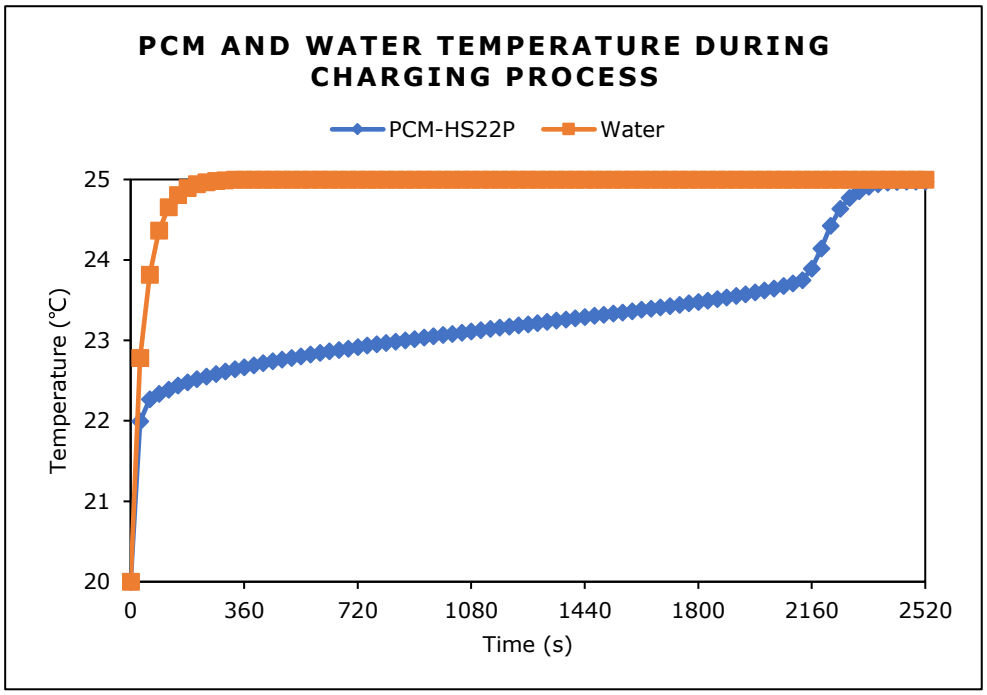


Figure 5.1 Comparison of average Temperature of Water vs PCM (Charging period)

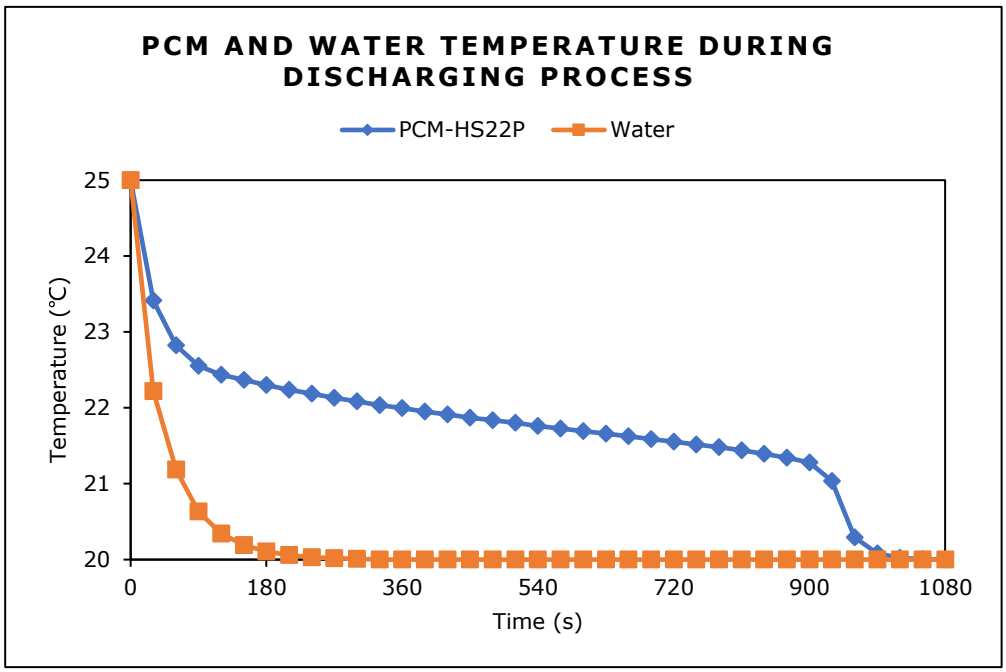


Figure 5.2 Comparison of average Temperature of Water vs PCM (Discharging period)

From the above comparison, it is clear that PCM has superior thermal performance over water, which means it is capable of providing long time cooling for PV during daytime as well as long time heating if moderate heating is required during night time. By using PCM over conventional water as thermal storage solution, the size of storage tank could be reduced significantly (by up to 17 times).

5.4 Thermal performance of PCM-HS22P

Figure 5.3 shows the temperature contour of the PCM around the heated pipe wall during the charging process. It can be seen from the result that the PCM near pipe wall has reached the maximum temperature of 25℃ soon after the start of the charging process, but the temperature diffusion towards the

outside is relatively slow. The PCM is fully melted after 25 to 30 minutes, while the temperature change becomes large during the 5-minute time interval compared to other contours. All part of PCM temperature reaches 25℃ soon after 30 minutes of charging, which means that the charging process is fully completed.

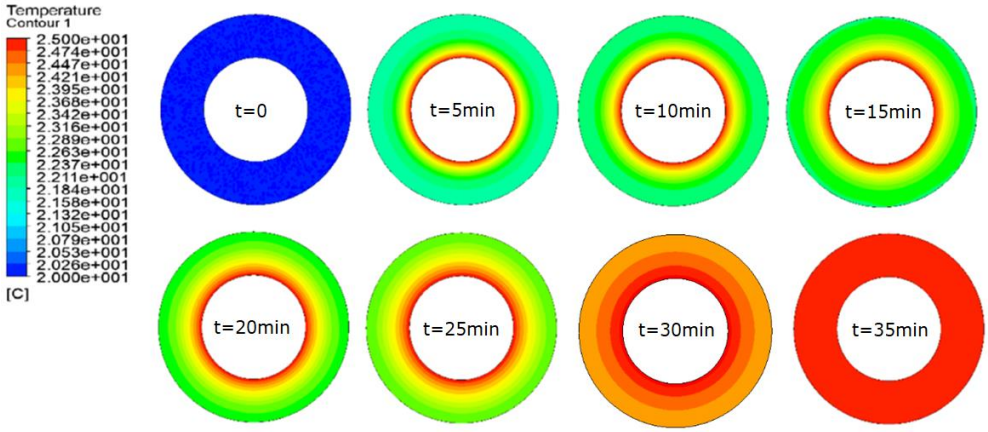


Figure 5.3 PCM temperature contour during charging process

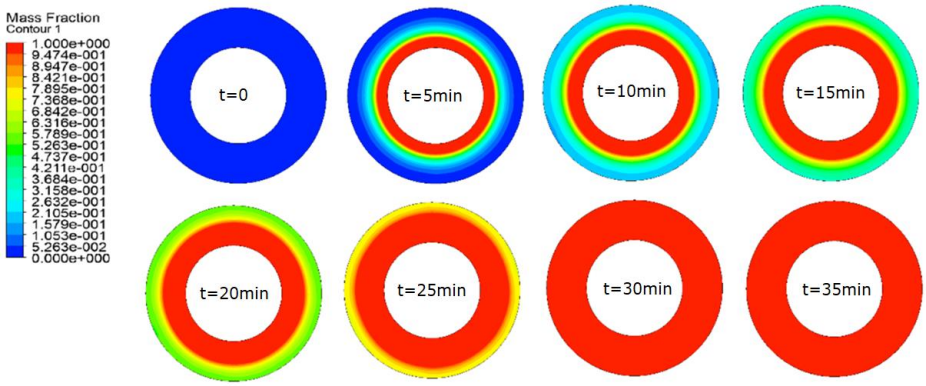


Figure 5.4 PCM liquid fraction contour during charging process

Figure 5.4 shows the liquid fraction contour of the PCM during the charging process. It can be seen from the figure that the PCM started to melt from the centre and slowly spreading outward. All PCM is melt after 25 – 30 minutes of heating, which explains the significant change of the corresponding

temperature contours. By comparing with Figure 5.1, it can be seen that the melted portion of PCM is always more than the fully charged PCM at a certain time, this layer of 'melted but not fully charged' PCM is a result of the low thermal conductivity properties of PCM.

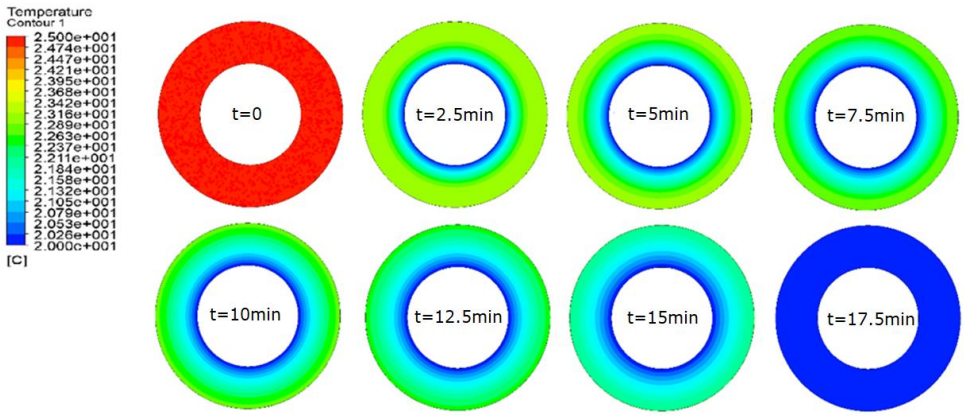


Figure 5.5 PCM temperature contour during discharging process

Figure 5.5 shows the temperature contour of PCM during the discharging process. It can be seen that the discharging process takes less time when compared to the charging process, which is the same found by Iten et al.'s case (2017). The PCM is fully discharged after 17.5 minutes of cooling.

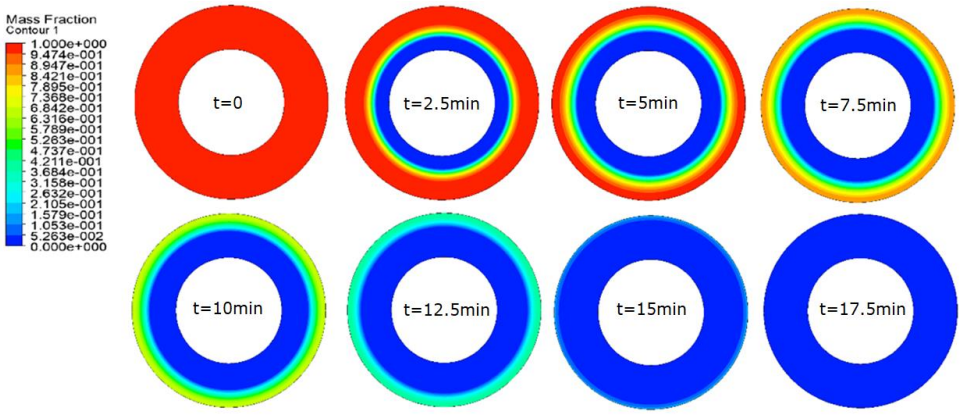


Figure 5.6 PCM liquid fraction contour during discharging process

Figure 5.6 shows the liquid fraction contour of PCM-HS22P during the discharge process. It can be seen that compared to Figure 5.10, the spreading speed of solidified PCM is faster than the melting process. The solidification is completely finished slightly after 15 minutes of cooling (there is still a very thin layer of mussy PCM at t =15min). Another observation after comparing the liquid fraction and temperature contour is that the liquid fraction contour could be replaced by the temperature contour with temperature range set to the phase change temperature (i.e., 22℃-23℃ for PCM-HS22P). By utilizing this method, liquid fractions could also be known even if the model is simulated in solid only approach.

Figure 5.7 below shows the average temperature profile of PCM-HS22P in the panel and its liquid fraction against time during the charging process. It can be seen from the figure that the liquid fraction has a near polynomial growth with increasing time. The average temperature rises rapidly while the liquid fraction is near 0 at the beginning, and then starts to increase gradually. The increase rate of temperature keeps steady until around 36 minutes, and is increasing rapidly again when the liquid fraction reaches 1, which means the PCM is fully melted at that time. The PCM is then heated up to the maximum temperature in 3 more minutes, and the total charging process is finished after 39 minutes. It is also noticed that the rate of first rapid PCM temperature increase is higher than the second

rapid increase, which can be explained by the fact that the specific heat capacity of liquid phase of PCM-HS22P is higher than the specific heat capacity of solid phase (3040J/kgK in liquid phase compared to 2200J/kgK in solid phase), while at the same time the temperature difference between PCM and heated surface (ΔT) is larger at the start of the charging process, which further enhances heat transfer.

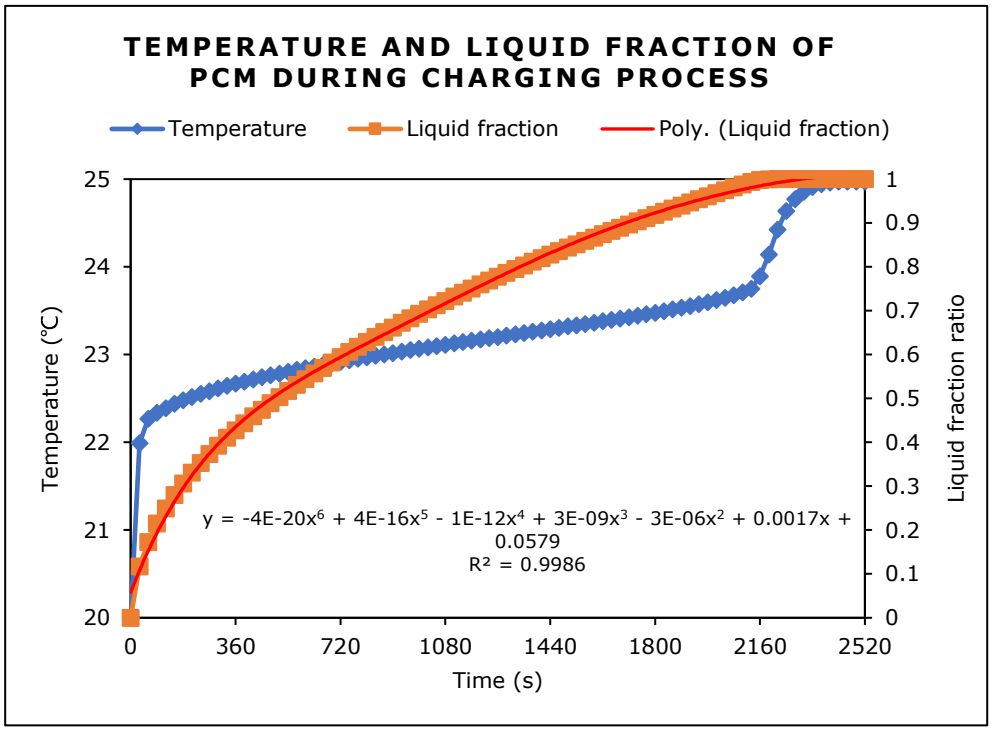


Figure 5.7 Average Temperature and Liquid Fraction of PCM-HS22P during charging process

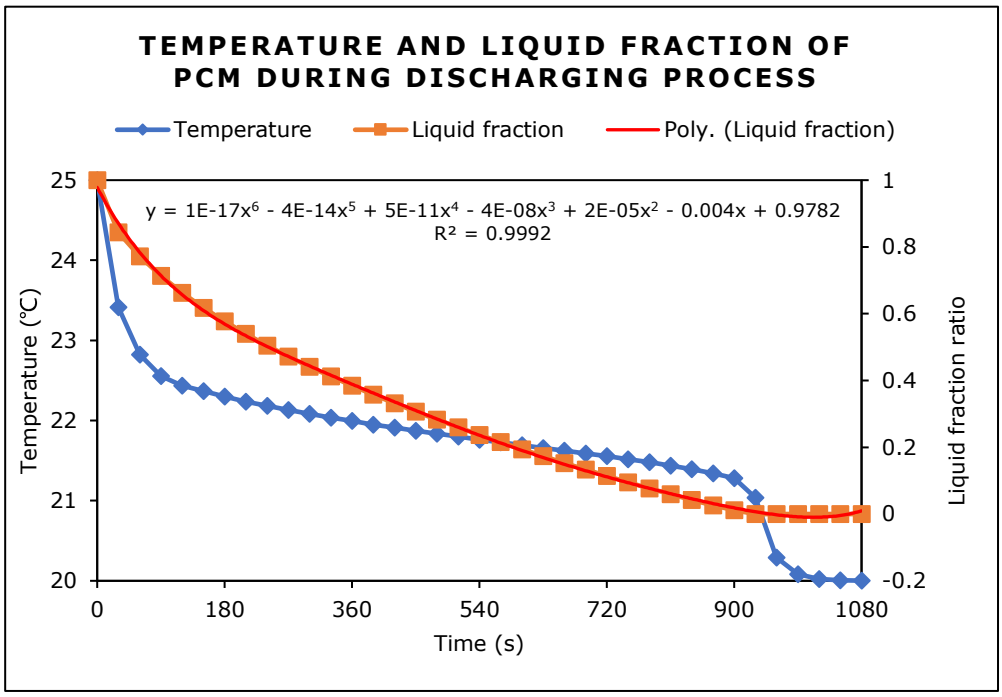


Figure 5.8 Average Temperature and Liquid Fraction of PCM-HS22P during discharging process

Figure 5.8 shows the average temperature profile of PCM-HS22P in the panel and its liquid fraction against time during discharging process. It can be seen from the figure that the liquid fraction also has a polynomial decrease along with increased time. The average temperature decreases at a very fast rate while the liquid fraction is near 1, after that the temperature starts to decrease gradually. The decrease rate of temperature keeps steady until around 15 minutes, and the second rapid temperature decrease appears where The PCM is fully solidified (liquid fraction = 0). The discharge process is completed at t = 17 minutes with the average PCM temperature reaches 20℃. It is noticed that the rate difference between first and second rapid PCM temperature decrease is not significant. This can be explained by the fact that although the specific heat capacity of PCM in the liquid phase is larger than the solid

phase, the greater initial temperature difference between PCM and cooling surface (ΔT) enhances the initial heat transfer, hence minimize the effect of heat capacity difference.

It can also be found by comparing Figure 5.5 and Figure 5.6 that the discharging process takes shorter time compared to the charging process, while the temperature difference in both cases is set to be same (initial temperature of 25℃ for 23℃ melting temperature in charging process and initial temperature of 20℃ for 22℃ solidification temperature in discharging process). This is due to the thermal conductivity difference between liquid and solid phase of PCM (0.56W/mK against 1.13W/mK respectively). During the second half of charging process (temperature from 22.5℃ to 25℃), the spreading of PCM melting is significantly restricted by all factors of lower thermal conductivity, higher heat capacity and lower ΔT, on the other hand, during discharge process, despite of the same lower ΔT, the spreading of PCM solidification is relatively faster due to the higher thermal conductivity and lower heat capacity value. The effect of thermal conductivity and heat capacity against PCM's charging and discharging performance will be detailly discussed in section 5.5 below.

5.5 Effects of PCM thermal properties

There is a wide arrange of PCM currently on the market with individual characteristics, in thermal performance perspective, the related properties are heat capacity, heat of fusion, phase change temperature and thermal conductivities. As stated in

Kenisarin and Mahakamov (2016)'s review, after extensive research, there is no clear information about the impact of each of PCM's thermal properties on the overall thermal performance. Hence, in this section, the effect of each thermal properties will be briefly investigated. The table of thermal properties used in the study is shown as below.

Table 5.1 Input data of PCM-HS22P thermal properties

	Heat capacity Cp (kJ/kgK)	**Heat of fusion LH (kJ/kg)**	**Thermal conductivity k (W/mK)**	**Phase change temperature T (Ts, Tm)**
Solid (Set 1)	2.2	185	1.13	22,23
Liquid (Set 2)	3.04	185	0.56	22,23
Property Variations				
Cp	**LH**	**k**	**Ts**	**Tm**
1.6	160	0.50	21	22
1.7	170	0.70	22	23
1.8	180	0.90	23	24
1.9	190	1.10		
2.0	200	1.30		

In order to study the effect of temperature related PCM thermal properties against the charging and discharging performance, the PCM-HS22P is first assumed to have constant thermal properties regardless of temperature and phase change. Figure 5.9 below shows the temperature profile comparison of PCM-HS22P in charging and discharging process using two different thermal property sets. The set 1 uses thermal properties of solid phase PCM-HS22P, which has heat capacity of 2200 J/kgK and thermal conductivity of 1.13 W/mK, and set 2 uses thermal

properties of liquid phase PCM-HS22P, which has heat capacity of 3040 J/kgK and thermal conductivity of 0.56 W/mK. Results show that although the heat of fusion is the same, the charging and discharging time of PCM with different thermal properties can vary significantly. The PCM with liquid phase thermal properties has significantly longer charging and discharging time compared to the PCM with solid phase thermal properties. There is a 13-minute charging and discharging time difference between PCM with two sets of thermal properties. It is also noted that by eliminating the time-related thermal properties, the temperature profile, as well as time required for both charging and discharging of the PCM, is the same.

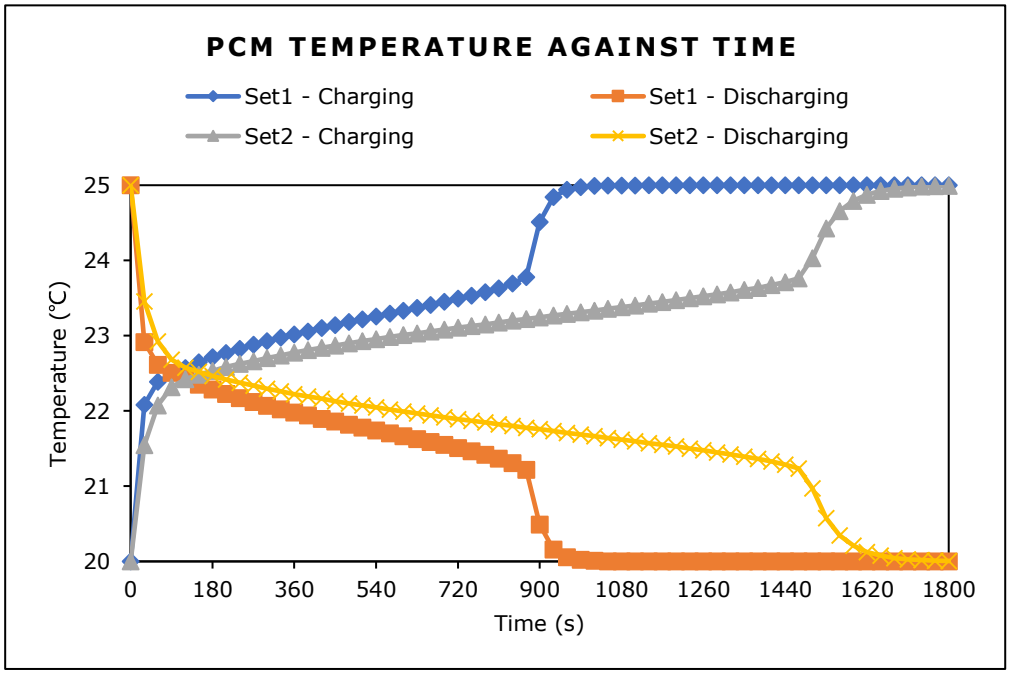


Figure 5.9 Temperature profile of PCM-HS22P in charging and discharging process using solid and liquid state thermal properties.

5.5.1 The effect of thermal capacity

In order to study the effect of different PCM heat capacity against its thermal performance, the PCM-HS22P with thermal property set1 is modified to have different heat capacity values of 2200 J/kgK, 2400 J/kgK, 2600 J/kgK, 2800 J/kgK and 3000J/kgK. The results in the same charging conditions are shown in Figure 5.10 below. It can be seen from figure that the changing value of heat capacity of PCM has very little effects on the overall charging time, due to the fact that most heat stored in the PCM during charging process is in the form of latent heat, there is only very little amount of sensible heat which could be affected by the varying heat capacity. Overall it is considered that the effect of heat capacity is minimal and could be neglected due to the significantly larger amount of fusion heat.

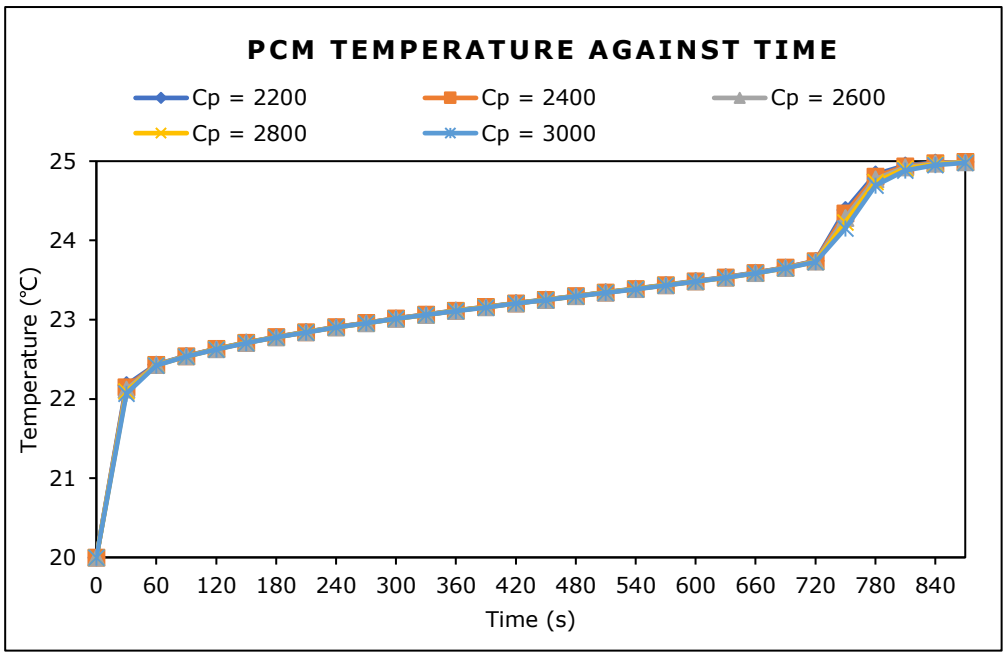


Figure 5.10 PCM temperature profile against time at different heat capacity values.

5.5.2 The effect of fusion heat

The heat of fusion is one of the unique characteristics of PCM, which makes it capable of storing/releasing a large amount of energy by completing phase change process with very small temperature change. In order to study the effect of fusion heat on the PCM's thermal performance, the PCM-HS22P with thermal property set1 is modified to have different fusion heat values of 160kJ/kg, 170 kJ/kg, 180 kJ/kg, 190 kJ/kg and 200 kJ/kg. All modified PCMs have been put under the same charging process. Figure 5.11 below shows the comparison of the temperature profile of all cases against time. The result shows that by increasing fusion heat from 160kJ/kg to 200kJ/kg, the charging time needed is increased from 12.5 to 24.5 minutes. There is a 30s difference of charging time with every 10 kJ/kg fusion heat increase. The main reason for the time difference is the temperature increase rate during phase change, while PCM has higher fusion heat will need more energy and hence longer time to complete phase change. On the other hand, the thermal performance of discharging process is identical to that of charging process with a reversed temperature profile. In general, The PCM with higher fusion heat is capable of providing a steady temperature for a longer time while the heat/cool input is the same, hence stores more latent energy.

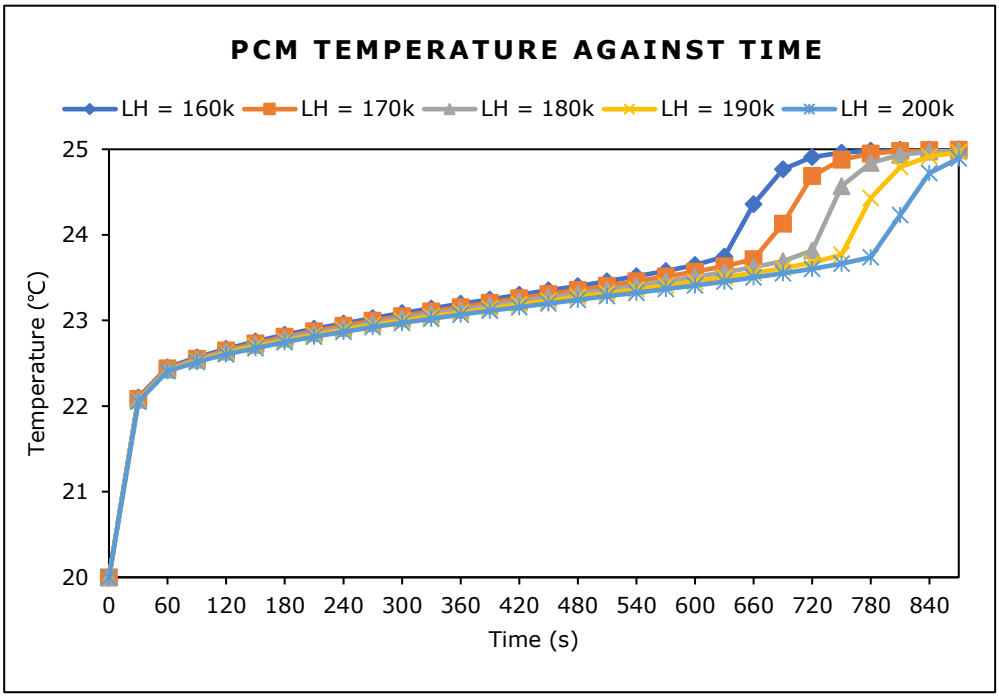


Figure 5.11 PCM temperature profile against time at different heat of fusion values.

5.5.3 Effect of phase change temperature

In order to study the effect of the phase change temperature against its thermal performance at given charging and discharging temperature, the PCM-HS22P with thermal property set1 is modified to have three different phase change temperature ranges (21℃-22℃, 22℃-23℃, 23℃-24℃). The results are shown in Figure 5.12 below. From the figure, it can be seen that the PCM with phase change temperature of 21℃-22℃ performs the best during the charging process, while on the other hand, PCM with phase change temperature of 23℃-24 ℃ has the best performance. The closer the target temperature is to the solidification temperature (melting temperature) during discharging (charging) process, the less performance the PCM will have. Thus, for more efficient PV

panel cooling, it is desired to have PCM melting temperature as low as possible for a given source temperature.

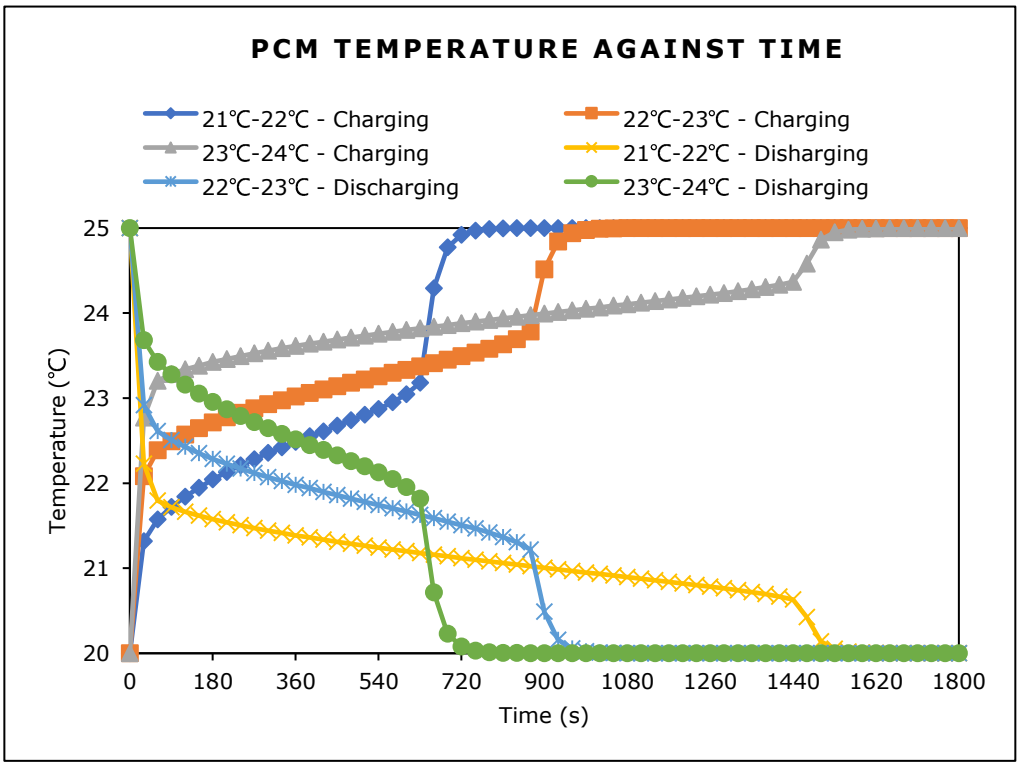


Figure 5.12 Temperature profiles of modified PCM with different phase change temperature

5.5.4 The effect of thermal conductivity (k)

In order to study the effect of thermal conductivity on PCM's thermal performance, the PCM-HS22P with thermal property set1 is firstly modified to have different thermal conductivity values of 0.5 W/mK, 0.7 W/mK, 0.9 W/mK, 1.1 W/mK and 1.3 W/mK. The chosen thermal conductivity values filled the gap between PCM-HS22P's solid and liquid phase thermal conductivity values. The results of discharging time difference

of modified PCM with different thermal conductivities are shown in Figure 5.13. Note that the figure only illustrates the temperature profile of discharging process, as the thermal performance in charging process is identical with a reversed temperature profile. From the figure, it can be seen that the time needed for discharging process with different thermal conductivity values are significantly different. The PCM with 0.5 W/mK thermal conductivity value needs 30.5 minutes to finish discharging, while the PCM with 1.3 W/mK thermal conductivity value only needs 12.5 minutes. The main cause of the time difference is the different temperature drop rate during phase change process. The PCM with higher thermal conductivity can achieve higher heat transfer rate during phase change, hence needs less amount of time needed for completing the phase change process.

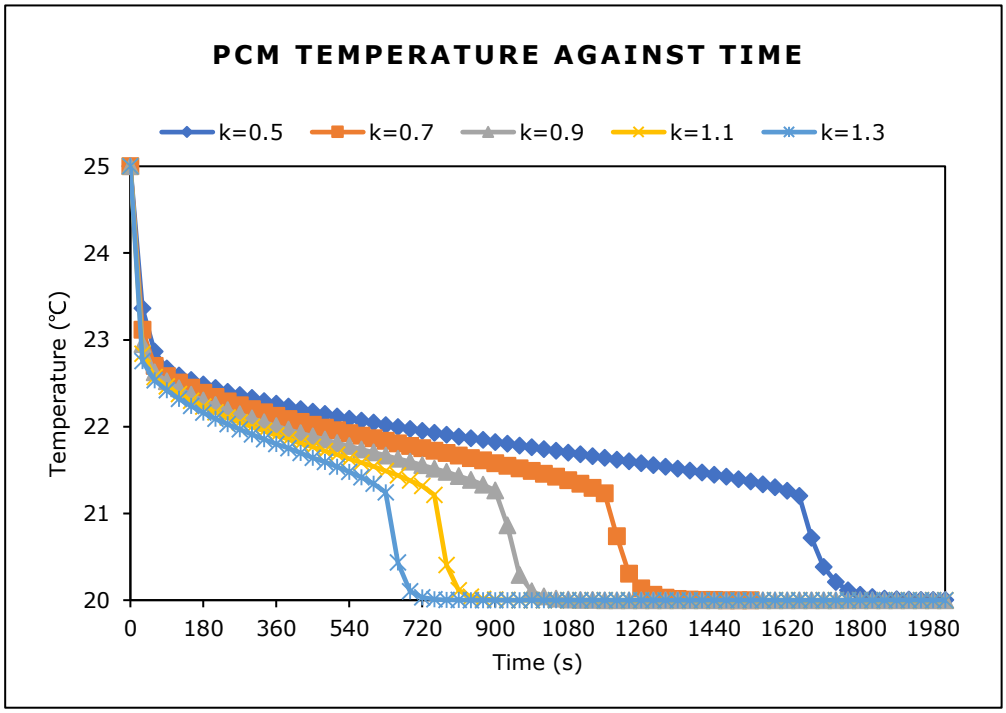


Figure 5.13 Temperature profile of modified PCM-HS22P in discharging process with different thermal conductivities

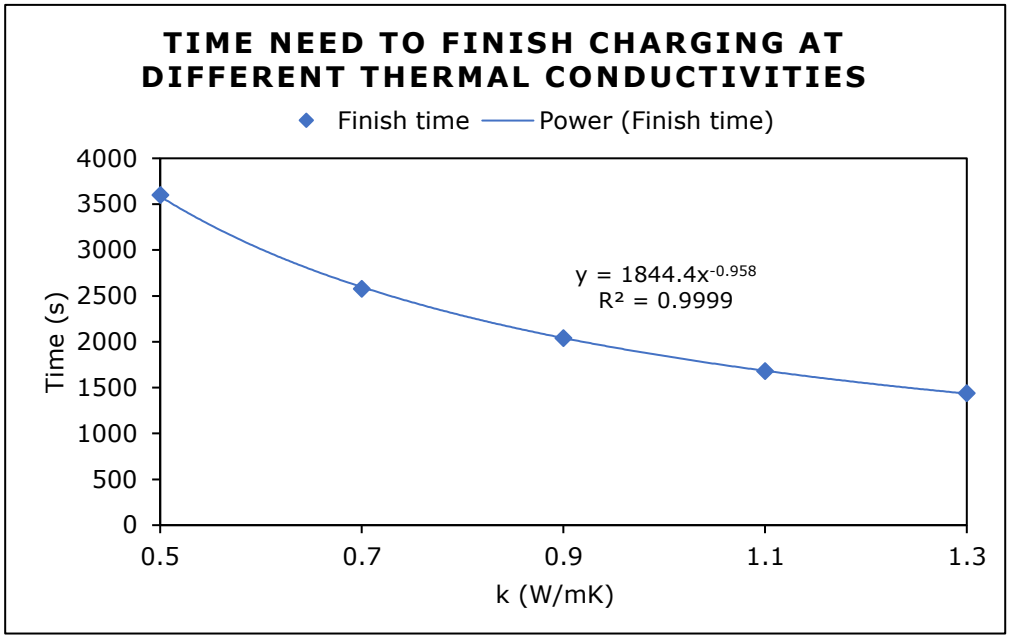


Figure 5.14 Comparison of time needed for completing discharging process for PCM with different thermal conductivities

Figure 5.14 above shows the comparison of time needed for completing discharging process for PCM with different thermal conductivities. It can be seen that the time needed against thermal conductivity could be represented by a power law trendline. Normally, Salt hydrate PCMs has higher thermal conductivity values compared to organic PCMs such as paraffin wax, which has a typical thermal conductivity value of 0.25W/mK, and is often considered to be more thermally efficient and is more desirable in most PCM applications.

5.5.5 The effect of temperature related thermal conductivity

Due to the nature that PCM needs to be either melted or solidified in order to store or release latent heat, the

temperature related thermal properties will cause PCM to perform differently during charging and discharging process. In order to study the effects of temperature related thermal conductivity against overall PCM thermal performance, the PCM-HS22P with the thermal property set 1 is further modified into 5 sets (A,B,C,D,E). Each set has constant heat capacity but with different temperature related thermal conductivity. All sets has the same liquid phase thermal conductivity of 0.5 W/mK, while the solid phase thermal conductivity is set to 0.5 W/mK, 0.7 W/mK, 0.9 W/mK, 1.1 W/mK and 1.3 W/mK for set A,B,C,D,E respectively. All 5 sets are put into same charging and discharging conditions so that the amount of time needed to complete the process could be compared against each other. Figure 5.15 below shows the temperature profiles for both charging and discharging processes of all 5 sets.

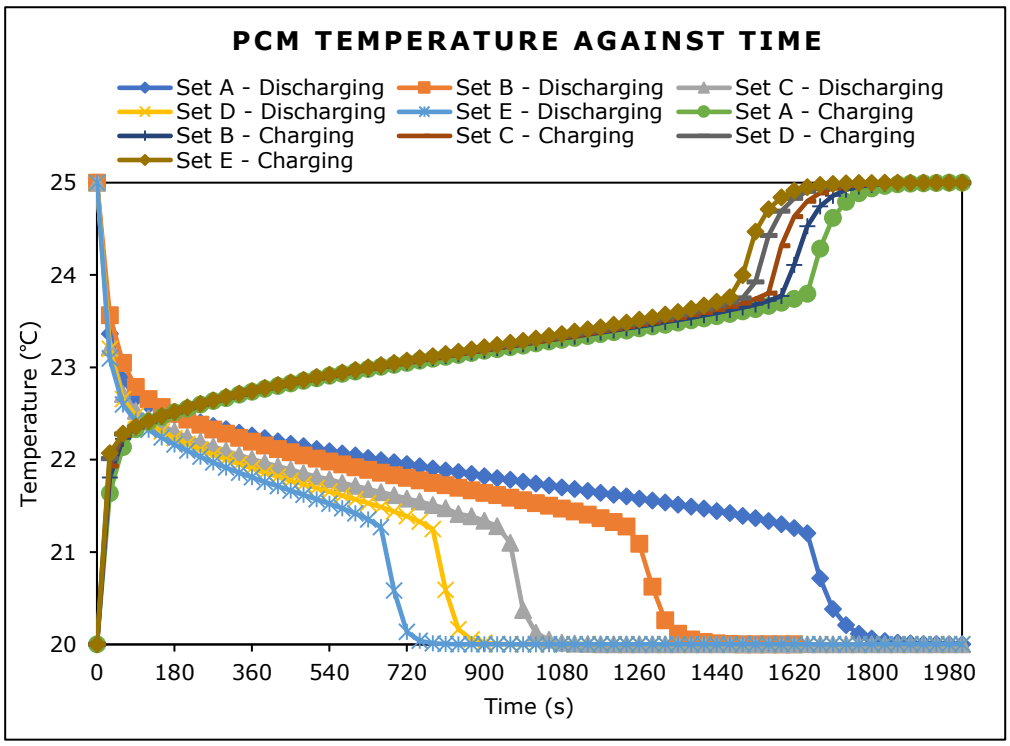


Figure 5.15 Temperature profiles of modified PCM sets A,B,C,D,E against time

It can be seen from the figure that the PCM thermal performance of charging and discharging process starts to show differences when only solid phase thermal conductivity is changed. By increasing solid phase thermal conductivity from 0.5W/mK to 1.3 W/mK, the amount of time needed for discharging process has reduced from 30.5 minutes to 12.5 minutes, while the time required for charging process is only reduced from 30.5 minutes to 28.5 minutes. The smaller difference of charging time across all sets indicates that the heat transfer is restricted by the low liquid phase thermal conductivity, which slows the spreading of melting process. On the other hand, the time required to complete discharging process is also affected by the low liquid phase thermal conductivity (see Figure 5.22 below), but at a significantly smaller scale.

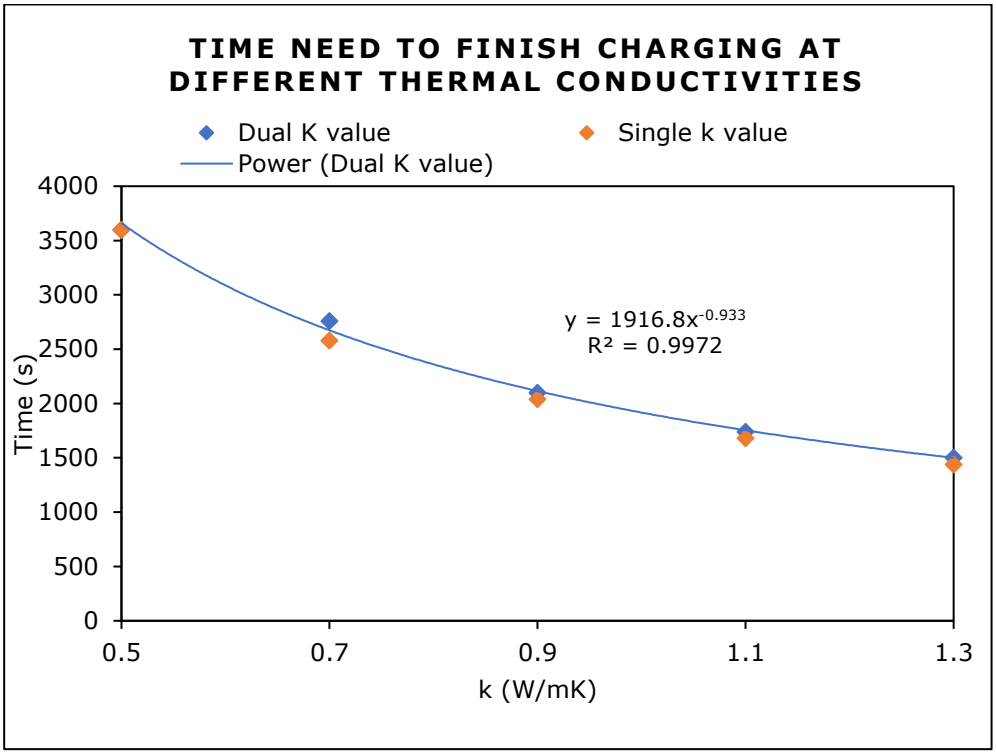


Figure 5.16 Discharging time comparison between constant thermal conductivity (Single k value) against temperature related thermal conductivity (Dual k value)

Figure 5.16 above shows the discharging time comparison between constant thermal conductivity (0.5 - 1.3 W/mK for both solid and liquid phase) against temperature related thermal conductivity (0.5 - 1.3 W/mK for solid phase and 0.5W/mK constant for liquid phase). It can be seen that the time needed against solid phase thermal conductivity for the dual k models could also be represented by the power law trendline.

It is also noticed that the amount of time difference is decreases with increasing solid phase thermal conductivity. This is due to the fact that the negative impact of low liquid phase thermal conductivity is reduced by the larger temperature difference between solid and liquid phase PCM at the phase change boundary.

On the other hand, the charging time affected by the changing solid phase conductivity is much smaller (shown in Figure 5.17 below) due to the restriction of the low liquid phase thermal conductivity. The time required for charging process against different solid phase thermal conductivity values could be represented by linear correlation.

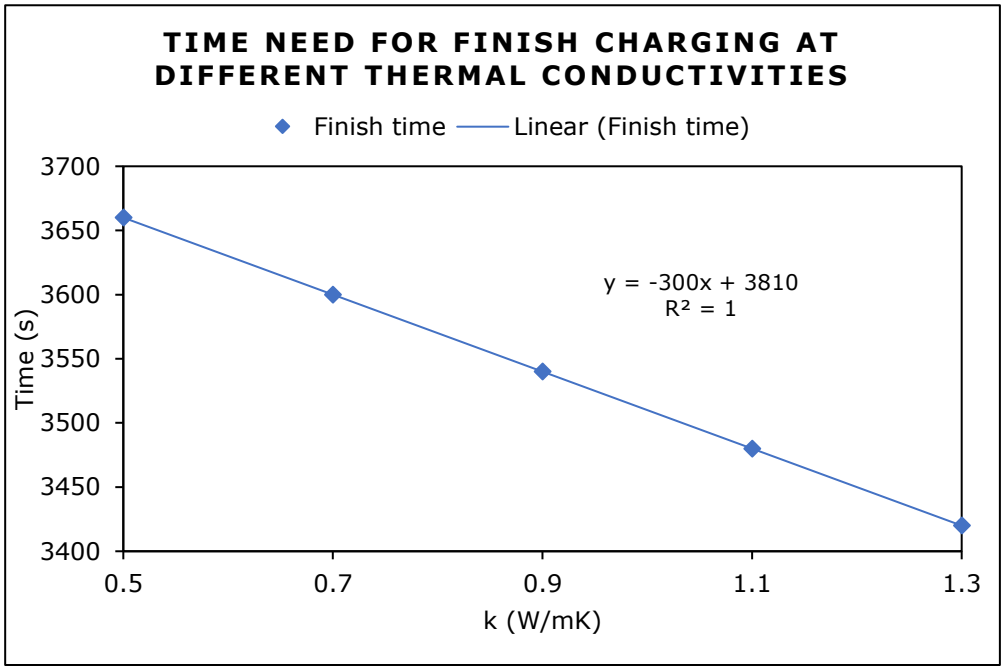


Figure 5.17 Time required for charging process against different solid phase thermal conductivity values.

In addition, the change of liquid phase thermal conductivity has identical but inverted effects on the PCM thermal performance. In other words, charging time is mainly affected by the liquid phase thermal conductivity, while the discharging time is mainly determined by the solid phase thermal conductivity. For thermal storage system used in the proposed PVT-PCM system, faster discharging rate is desirable due to the heat dissipation requirement during night time while the temperature difference

is much smaller compared to the daytime charging temperature.

5.6 Summary

In this chapter, the thermal performance of PCM-HS22P is studied, at the same time, the effects of heat capacity, fusion heat, phase change temperature and thermal conductivity on the PCM's thermal performance are also discussed. It is found that the heat capacity has very little effect on the total charging and discharging time, while PCM with larger fusion heat has longer charging and discharging time. Additionally, PCM with lower melting (higher solidification) temperature has better charging (discharging) performance. Another finding is that the temperature related thermal conductivity has different performance impact on charging and discharging process. The PCM with higher solid phase thermal conductivity has a significant reduction in discharging time while the reduction of charging time is relatively small.

CHAPTER 6. ANALYSIS OF THE PVT-PCM SYSTEM COMPONENTS

6.1 Introduction

In this chapter, the proposed design and components selection of the PVT-PCM system is presented. The system can be separated into two parts: a water-cooled PV panel and a water heated PCM storage panel. A series of parametric analysis will be carried out, the impact of different parameters such as ambient temperature, flow speed, solar radiation levels against PV and PCM performance will be analysed and discussed. The investigation was carried out for each parameter individually while other parameters were set to be constant. By examining the effects of each parameter, the correlation between the parameter and whole system behaviour could be revealed. Hence design optimization could be made. In addition, a fin analysis is also conducted in order to enhance heat transfer between circulated water and PCM.

6.2 Proposed design of the novel PVT-PCM system

The concept of the proposed PVT-PCM system is to combine conventional flat plate PV panels with custom designed PCM latent heat storage system. The system can achieve better electrical performance compared to conventional PV panels, as

well as have the ability to store the extra amount of thermal energy without affecting the photovoltaic efficiency. Unlike back-mounted PVT-PCM system used in many recent studies, in this study the PCM is designed to be separated from the PV panel. As a result, the thickness and weight of PV module is greatly reduced, while the heavy PCM storage panel could be placed elsewhere as long as they are connected with PV module. The modular and highly flexible design allows the proposed PVT-PCM to suit for different configuration requirements. This chapter will introduce the detailed design and components of the proposed PVT system as well as its various working modes.

6.2.1 System components

The PVT-PCM system mainly consists of a flat plate PV panel, a rectangular sized storage panel, as well as a small water pump for water circulation. A sample configuration of the system is illustrated in Figure 6.1 below. Note that PCM storage tank is placed beside PV panel just for illustration purpose, it could be placed anywhere by demand.

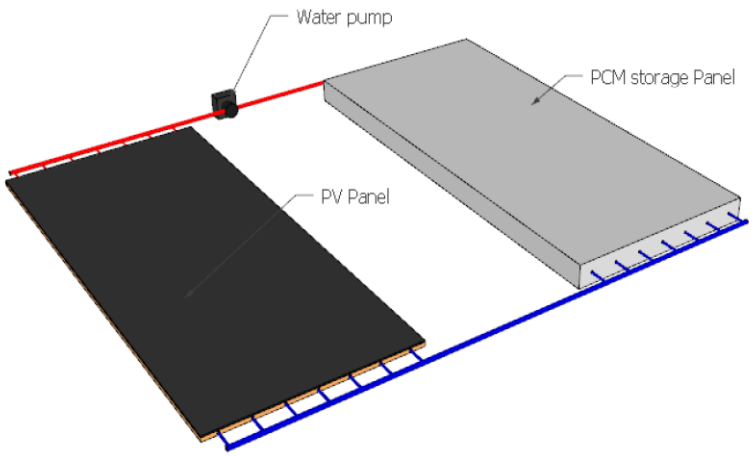


Figure 6.1 3D illustration of a sample configuration of the PVT-PCM system

■ *Selection of PV panel*

There are different makes of PV panels available on the market at the moment; the most used is the crystalline silicon module. In this study, the PV panel used is the BP-275L, which is a 75W monocrystalline silicon module manufactured by BP solar. The manufacturingr data is presented in Table 6.1 below (BP Solar, 2015).

Table 6.1 Properties from BP-275L manufacturer datasheet

Electrical data	
Maximum power (P_{max})@STC	75W
Open-circuit voltage (V_{oc}) @STC	21.4V
Short-circuit current (I_{sc}) @STC	4.75A
Voltage at point of maximum power (V_{mpp}) @STC	17V
Current at point of maximum power (I_{mpp}) @STC	4.45A
Nominal efficiency (η_r) @STC	11.9%
Fill Factor	73.8%
Nominal Cell Operating Temperature (NOCT)	47°C
Dimension (A_0)	1183.0 × 525.0 × 4mm

Effective surface area (A_1)	1125mm x 500mm
Weight	7.5kg
Temperature Coefficient of I_{sc}	0.065 %/ºC
Temperature Coefficient of V_{oc}	-0.38 %/ºC
Temperature Coefficient of P_{mp}	-0.50 %/ºC
***STC: Standard Test Condition: Irradiance = 1000W/m^2, Air mass = 1.5, Cell temperature = 25 ºC**	

■ *PCM material selection*

There are mainly 2 types of PCM available on the market, namely organic PCMs and inorganic PCMs. Generally speaking, the inorganic salt hydrate PCM has better thermal conductivity performance compared to organic ones. In this study, inorganic salt hydrate PCM-HS22P is chosen to be the heat storage solution in order to effectively control PV cell temperature. The manufacturer datasheet is shown in Table 6.2 below (savENRG, 2015).

Table 6.2 Properties from PCM-HS22P manufacturer datasheet

PCM-HS22P	
Property	Value
Melting Temperature (℃)	22
Freezing Temperature (℃)	23
Liquid Density (kg/m3)	1540
Solid Density (kg/m3)	1840
Latent Heat (kJ/kg)	185
Specific Heat – Liquid (kJ/kg.K)	3.04
Specific Heat – Solid (kJ/kg.K)	2.2
Thermal Conductivity – Liquid (W/m.K)	0.56
Thermal Conductivity – Solid (W/m.K)	1.13
Max. Operating Temperature (℃)	~80

6.2.2 System working principles

Daytime working cycle

The daytime working cycle of the PVT-PCM system is shown in Figure 6.2 below. The flat plate PV panel is located at a place on a building envelope. The back side of PV panel is attached to a copper heat absorber, and the absorber is cooled by recirculated water via multiple 6mm diameter copper pipes. The water-cooled PV panel is separate from the PCM latent heat storage panel and connected by additional pipework according to different installation demands.

During the daytime, the PV panel gets cooled down by the recirculating water; the water is then pumped through PCM panel to charge the PCM. The cooled outlet water is then recirculated back to the panel for cooling. The only active component of this system is the small water pump, which is used to circulate water within the closed loop system and can be fully powered by PV panel.

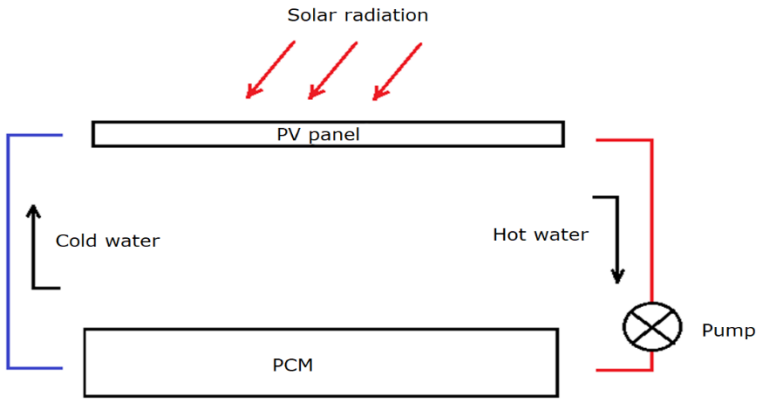


Figure 6.2 Daytime operation schematic diagram of the PVT-PCM system

Night time working cycle

During night time, the pump used for cooling PV is not used as there's no cooling requirement. The stored latent heat inside PCM could either be utilized or be dissipated using night time natural ventilation. By using either of the methods mentioned above, the PCM could be cooled back to the solid state to perform another daytime cycle.

6.2.3 Latent heat utilization

The energy stored in the PCM during the daytime needs to be released effectively in order to prevent overheating of the whole system. There are many ways to utilize the latent heat; the proposed design features two different approaches. Figure 6.3 and 6.4 below illustrate the two ways of utilizing latent thermal energy. As the fully charged PCM temperature is only 23℃, it is not efficient to directly provide water or space heating. Thus, the concept of the heat utilization is to reduce water and space heating energy consumption by providing a moderate degree of preheating.

In water preheating configuration, the PCM can be used to preheat water from supply water mains in order to reduce the hot water heating load, or can be used directly to increase comfort level. In air preheating configuration, the PCM panel modules could be put together inside a specially designed air

duct, hence preheating cold air to a moderate temperature during cold days.

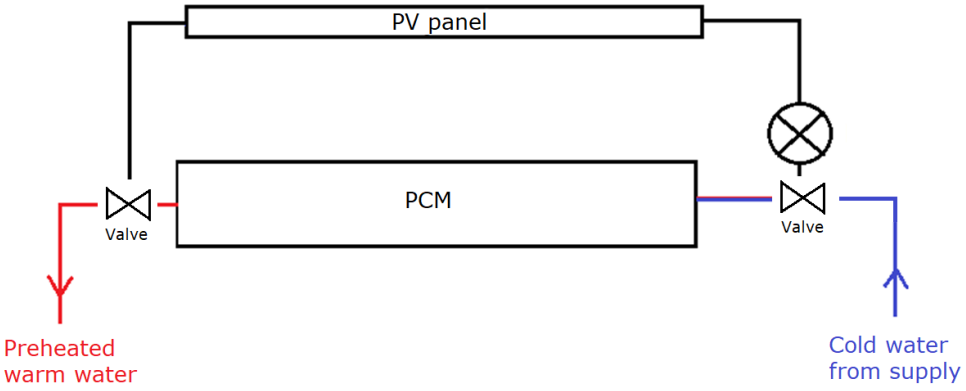


Figure 6.3 Schematic illustration of water preheating configuration

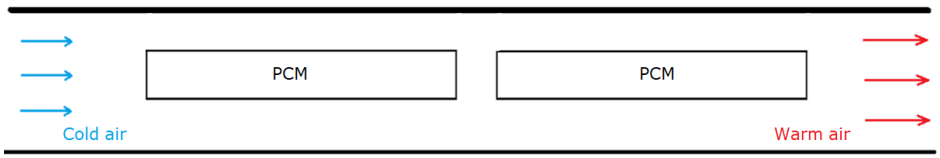


Figure 6.4 Schematic illustration of air preheating configuration

6.3 Analysis of system components

6.3.1 Pump power calculation

Due to the separated design, the amount of pipework needed can vary from case to case. Hence it is impossible to accurately predict the power requirement of water pump. However, the minimal pump power required could be known by eliminating all additional pipework.

The Pump power could be calculated by equation below,

$$P = \frac{Q \times H \times g \times \rho}{pump\ efficiency} \quad \textbf{6.1}$$

Where P is the pump power(W), Q is the volume flow rate (m^3/s), g is the gravitational acceleration (m/s^2), ρ is water density and H is the total head, which equals to the sum of static head (H_S) and dynamic head (H_D):

$$H = H_S + H_D \quad \textbf{6.2}$$

The proposed system is a closed loop system, thus $H_S = 0$. The dynamic head could be calculated using equation below:

$$H_D = \frac{Kv^2}{2g} \quad \textbf{6.3}$$

Where v is the flow velocity and K is the total loss coefficient, which is the sum of the loss coefficient of fittings ($K_{fitting}$) used and the loss coefficient of pipe (K_{pipe}).

Assuming the PVT-PCM system is looped with 180° bends ($K_{fitting}$ = 0.2) (The Engineering Tool Box, 2016) on each side of the pipe, the total $K_{fitting}$ is equal to 2.8.

The loss coefficient of pipe, on the other hand, can be calculated using the equation below:

$$K_{pipe} = \frac{fL}{D} \quad \textbf{6.4}$$

Where L is the pipe length (m), and d is the pipe diameter (m). the friction factor (f) in smooth pipe could be determined by:

$f = \frac{64}{Re}$ for laminar flow, and $f = \frac{0.316}{Re^{1/4}}$ for turbulent flow (Smooth pipe only with Re<10000) (Kiijarvi, 2011).

6.5

Where Re is the Reynolds number. Alternatively, f could also be found in moody chart.

As an example, for flow speed = 0.05m/s, with total effective pipe length of 16.56m the K_{pipe} of the PVT-PCM system is calculated to be 774.22.

By using equation 6.1 – 6.5, assuming 80% pump efficiency (centrifugal pumps normally offer efficiency between 75% - 93% (Evans, 2012)), the minimum pump power needed is calculated as 0.002W.

Figure 6.5 shows the pump energy consumption against different flow speeds. It can be seen that increasing the flow speed will require a lot more pumping power due to the increased dynamic head. In this case, without considering the additional resistance from pipework, the pump energy difference is neglectable. However, in real situations, with system configuration with lots of pipework, the difference will become more significant.

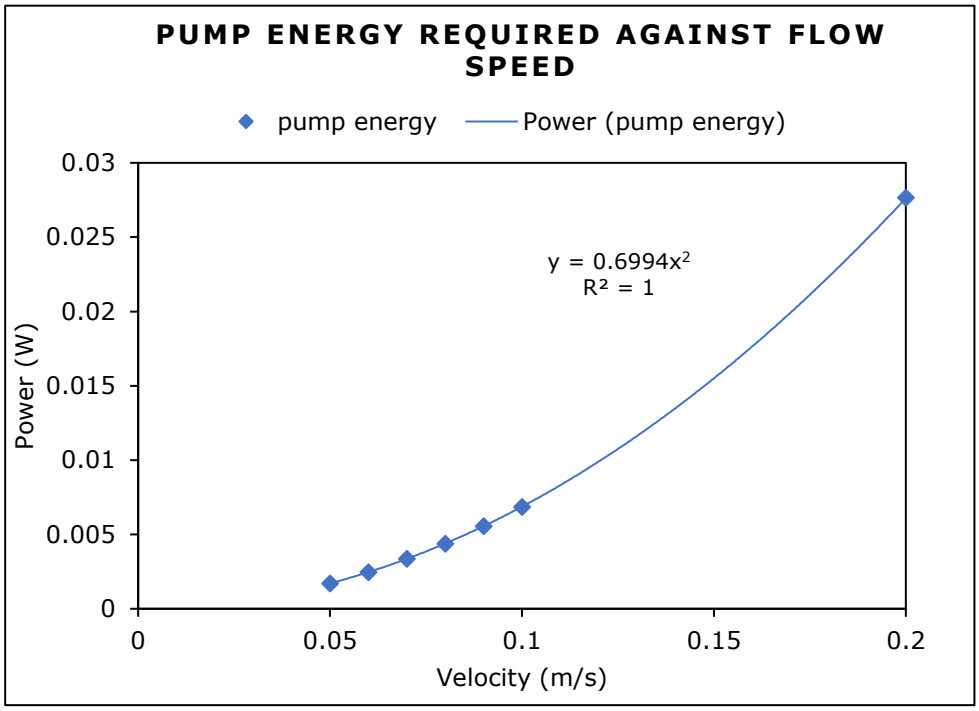


Figure 6.5 Pump energy requirement against flow speed

In general, the required amount of pumping energy for low speed closed loop water circulation is relatively small, however, the pumping energy is greatly dependent on the actual system configuration and pipework layout. The further the PCM storage tank is located away from the PV panel, the more the pumping power it will need to compensate for the additional friction loss.

6.3.2 Parametric analysis on PV side

Geometry, mesh, and materials

This model has a 3D geometry of one of seven identical sections sliced from the whole panel geometry (as shown in Figure 6.6). It is considered that the thermal performance of the whole PV panel is equal to the thermal performance of the sliced section. The meshing profile contains 1264718 mesh

elements along with two adapted meshes. Results generated by all three mesh are compared to ensure the results are independent of element size level. The mesh element counts and the relative RMS errors of each mesh profile is shown in Table 6.3 below. The materials used in this case are liquid water, copper, and PV, the properties of water and copper can be found in FLUENT 18.0 database, and the properties of PV are calculated previously.

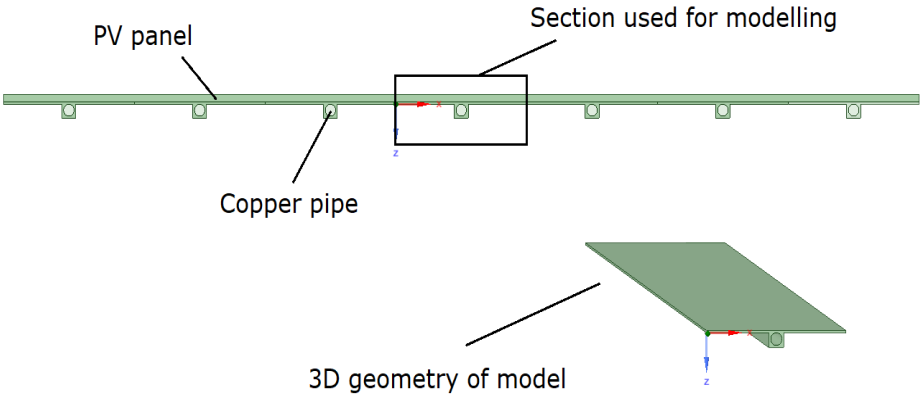


Figure 6.6 3D geometry of the PV model

Table 6.3 Mesh element and RMS error of the PV analysis model

Mesh Case	Element count	RMS Error
Original	1264718	
1st Adaption	1517661	0.23%
2nd Adaption	1770605	0.15%

Boundary and Initial conditions

There are 4 specified boundary types, namely water inlet, water outlet, PV panel surface and bottom surface. The inlet is set as velocity inlet with given velocity and temperature value, and the outlet is set to pressure outlet. The bottom surface of the heat sink is set to adiabatic condition along with all other walls in order to have better-controlled value for parametric

analysis. The PV panel surface has been set to have a constant heat flux with 4mm thick PV layer. The conversion of solar radiation ($\emptyset$, W/m^2) to heat flux (Q, W/m^2) can be done using below equation.

$$Q = PV\ absorption\ ratio \times \emptyset \quad \textbf{6.6}$$

Parametric analysis setups

The model has been simulated with different parameter adjustments. The effect of velocity, ambient temperature as well as solar radiation level on the PV thermal performance has been studied. Each simulation has been set to have only 1 modifying parameters at a time with other parameters set to initial condition values. Table 6.4 below shows the parameter sets used in the analysis.

Table 6.4 Parameter sets of the PV side analysis

	Solar radiation Φ (W/m²)	**Inlet water temperature Ti (℃)**	**Flow speed v (m/s)**
Set parameter	900	23	0.05
Parameter Variations			
	Φ	**Ti**	**v**
	400	23	0.005
	500	25	0.01
	600	27	0.03
	700	29	0.05
	800	31	0.07
			0.09
			0.11
			0.2

The base conditions other than the varying parameter are set with inlet velocity of 0.05m/s, inlet water temperature of 23℃ and solar radiation of 900W/m^2. A monitor line is used to generate X-Y plots of PV cell temperature, the line is located at the centre of the panel surface, and the direction is parallel to flow direction (as illustrated in Figure 6.7).

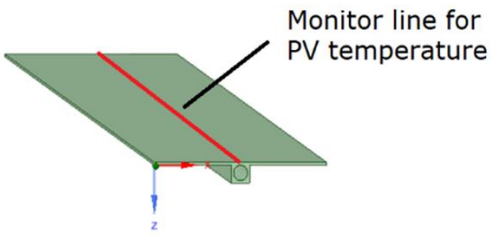


Figure 6.7 Temperature monitor line on PV panel surface

Results and discussion

- *Effect of Velocity*

Figure 6.8 shows the X-Y plot of PV cell temperature variations along the panel with different water inlet velocities. It can be seen from the figure that the PV cell temperature rises when the distance of the cell is far from the water inlet. The water temperature rises as water gets heated up from inlet to outlet. It is also noticed that the cell temperature change along the flow direction is relatively small while the flow speed is reduced from 0.2m/s to 0.05m/s, however, when changing flow speed from 0.005m/s to 0.001m/s, the cell temperature rises significantly.

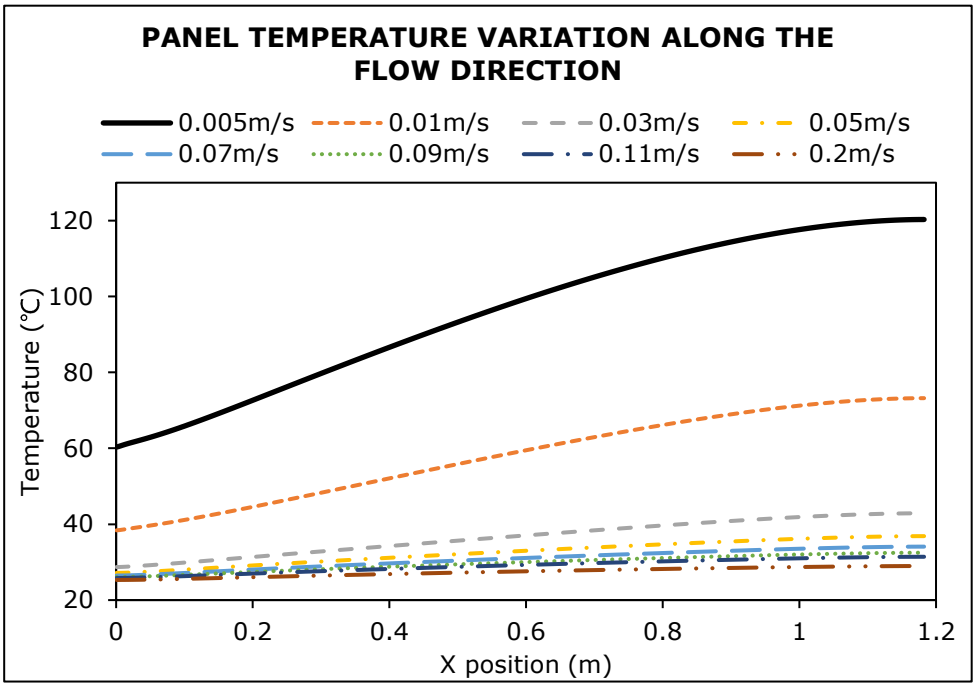


Figure 6.8 X-Y Plot of PV cell temperature against X position in different flow velocity

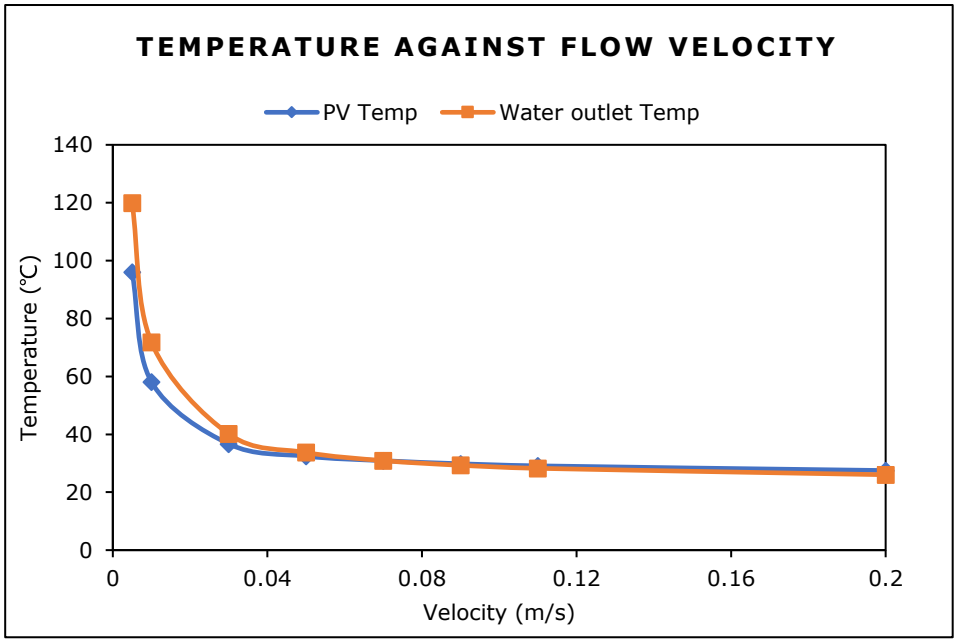


Figure 6.9 Average temperature of Panel and water outlet against flow velocity

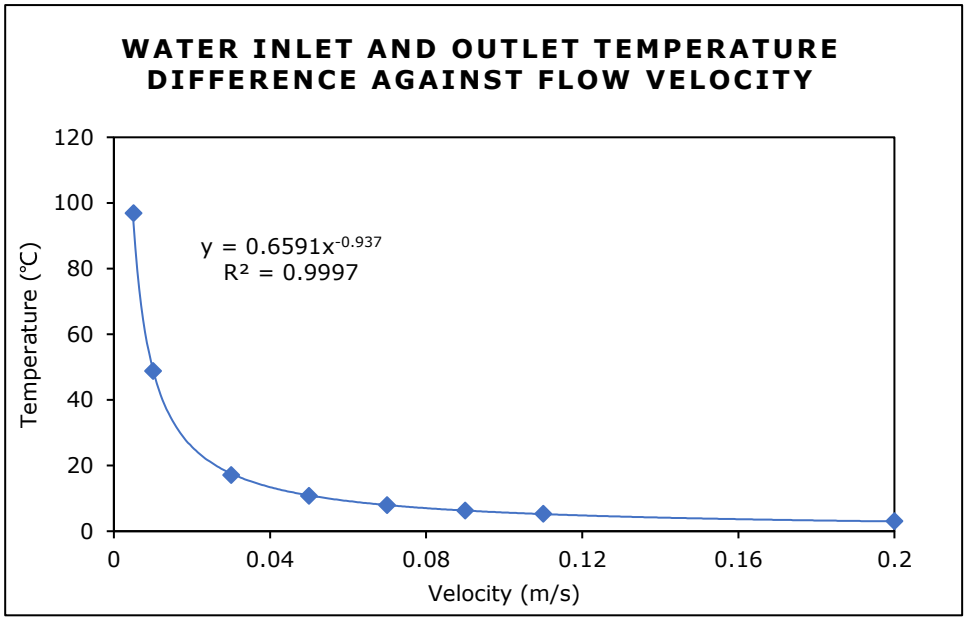


Figure 6.10 Water inlet and outlet temperature difference against flow velocity

Figure 6.9 shows the average panel and water outlet temperature against different flow velocities. It can be seen that the outlet water temperature at velocity of 0.001m/s reaches a maximum temperature of 120 ℃ while its corresponding panel temperature also reaches 71.81℃. This indicates the fact that the bulk water is heated up to the same cell temperature before reaching the outlet, which leads to the loss of overall cooling capability. As flow speed increases, the difference of water outlet temperature and panel temperature reduces. There is not much temperature change for both outlet water and PV panel once the velocity is higher than 0.05m/s. At velocity higher than 0.1m/s, the outlet water temperature starts to drop below average panel temperature, which indicates that the bulk water fluid is still at cooler temperature. Figure 6.10 shows the trendline of water temperature rise between inlet and outlet at different

flow velocity. The temperature difference diminishes as flow velocity increases.

Additionally, in order to sufficiently utilize the connected PCM panel, it is desirable to have outlet temperature higher than the melting temperature of PCM which is 23℃, in order to initiate the phase change process which would be achieved after recirculating water in the system.

- *Effect of solar radiation*

Figure 6.11 and 6.12 present the PV cell temperature variation along the X position with different solar radiation levels, at flow velocity of 0.05m/s. The panel temperature near water inlet has the lowest temperature, and increased gradually along the panel towards water outlet. The increasing rate changes as water is heated up during the cooling process. The result shows that the increasing solar radiation level will lead to a relatively small rise of the overall cell temperature, at an average rate about 1.2℃ per 100W/m^2 increased solar radiation (as shown in Figure 6.12). The water outlet temperature variation also has similar trends, at the rate of 1.1℃ per 100 W/m^2 increased solar radiation.

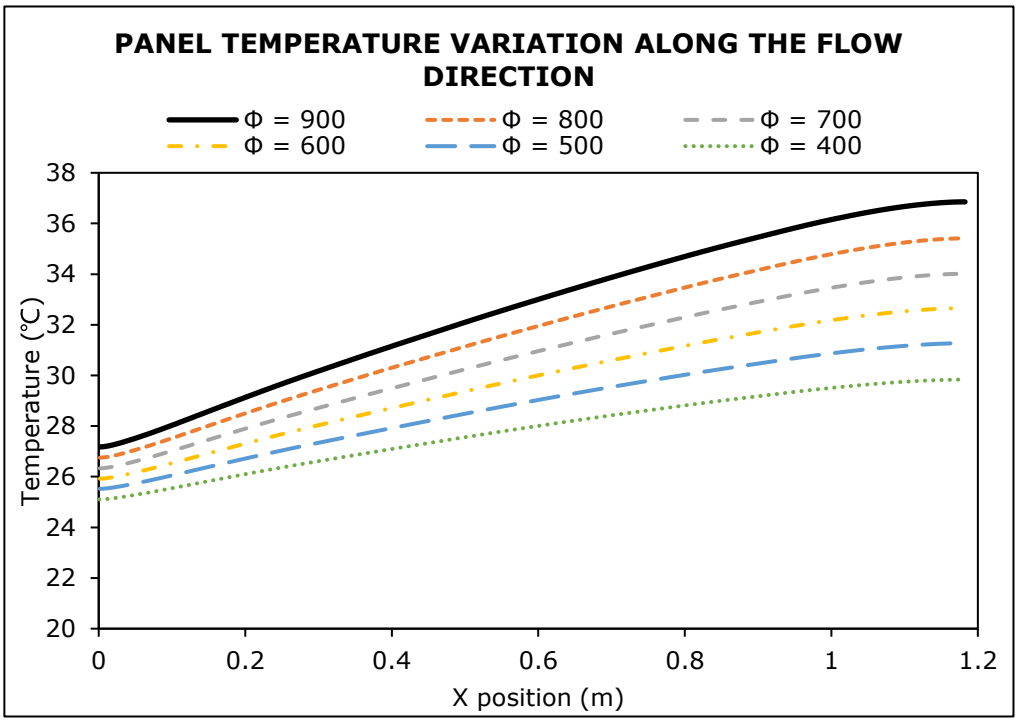


Figure 6.11 X-Y Plot of PV cell temperature against X position in different solar radiation conditions (Φ, W/m²) at flow velocity of 0.05m/s

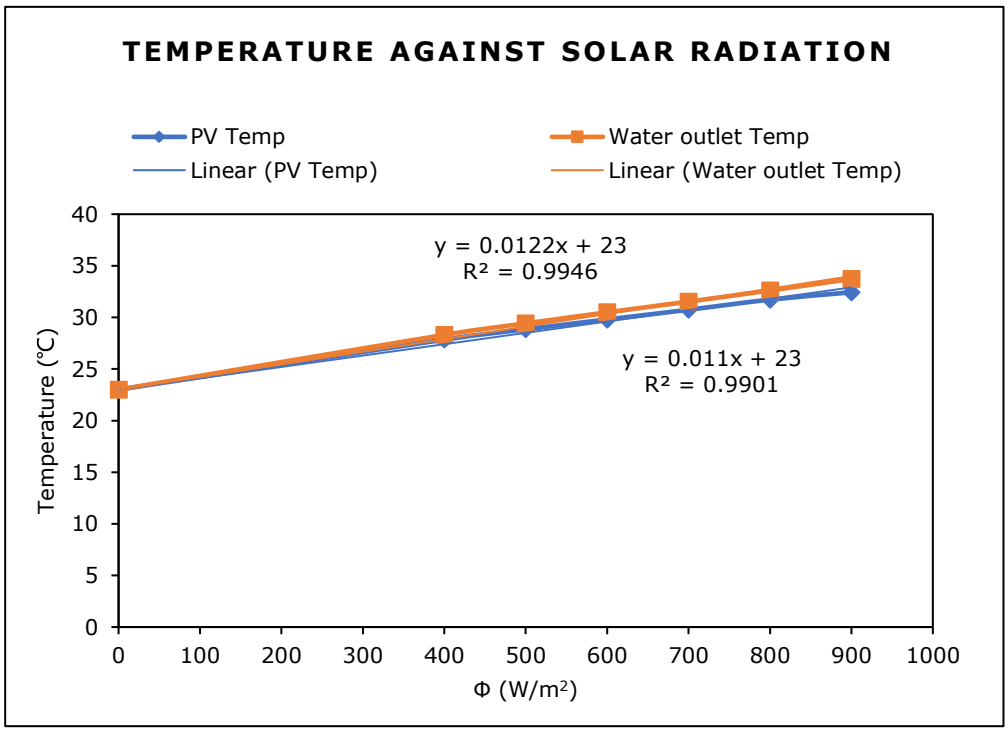


Figure 6.12 Average temperature of panel and outlet water in different solar radiation conditions (Φ, W/m²) at flow velocity of 0.05m/s

- *Effect of inlet water temperature*

Figure 6.13 shows the PV cell temperature difference along the X position at different inlet water temperatures. It can be seen from the figure that for every 2℃ of inlet water temperature rise, the overall panel temperature is raised for 2℃. The temperature increase profiles of different inlet temperature settings are parallel to each other, which means the heat transfer efficiency is not changed. The maximum temperature difference of the panel surface keeps constant at 9.66℃ as shown in Figure 6.14. Similarly, the temperature increase of outlet water is also constant at around 10.67℃.

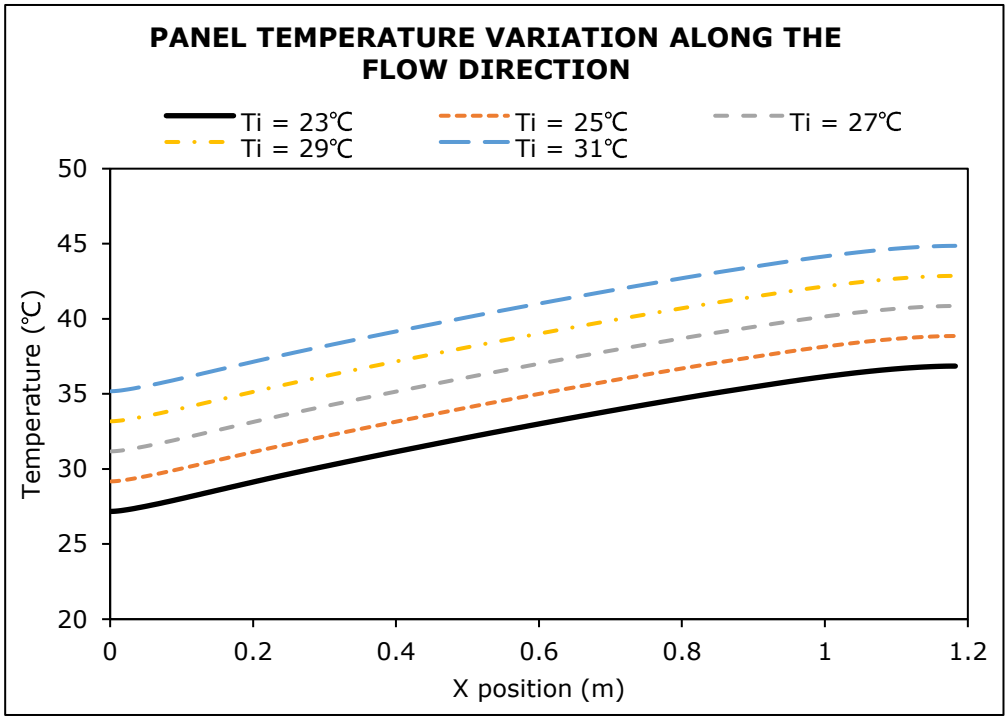


Figure 6.13 X-Y Plot of PV cell temperature rise against X position in different water inlet temperatures

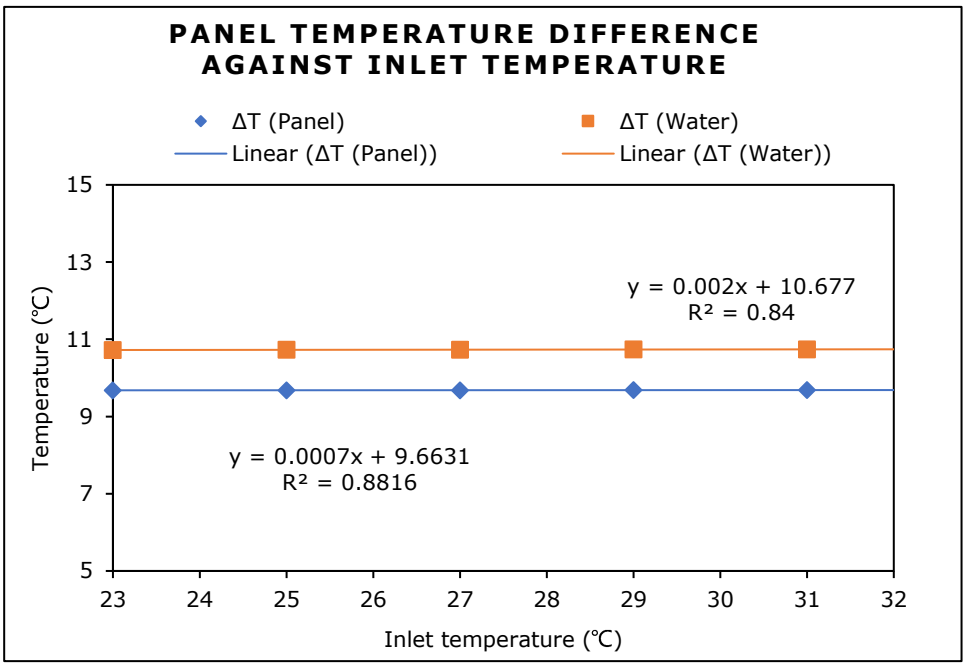


Figure 6.14 Outlet and inlet temperature difference under different ambient temperatures

- *Parallel flow against counter flow*

In addition to the parallel flow pattern, the PVT-PCM system could also be configured to have counter flow pattern, which means each 6mm pipe has opposite flow direction against the pipes nearby. In order to study the effects of counter water flow against parallel flow, three of the sliced sections are combined together with the middle pipe flowing at opposite direction. The results are shown in Figure 6.15 below. It can be seen that by using counter flow, the temperature difference across the PV panel has been reduced by 3.32℃. However, the average panel temperature has also increased from 31.72℃ to 34.66℃. Meanwhile, the outlet water temperature is also significantly reduced compared to the parallel flow configuration. The reason of that is because counter flow introduces heat transfer within the water domain, hence reduces the cooling capacity of

the absorber. In this study, the parallel flow configuration is used as it has higher outlet water temperature and lower average PV panel temperature.

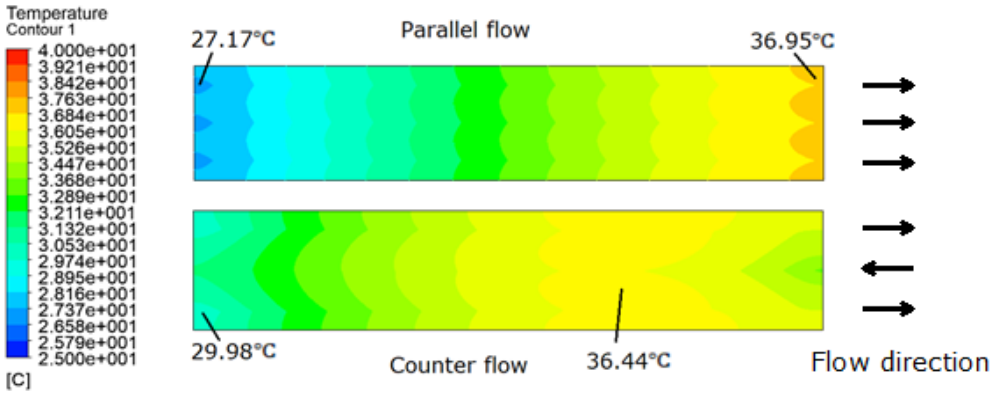


Figure 6.15 Temperature contour comparison of parallel and counter flow.

From the parametric analysis of the water-cooled PV panel, it can be seen that the water cooling solution can effectively reduce PV cell temperature. The performance difference is significant compared to the natural air cooling which were presented in Section 5.2.

6.3.3 Parametric analysis on PCM side

The size and shape of PCM storage panel could vary significantly depends on the system configuration, climate, and energy utilization requirements. Thus, for the purpose of parametric study, only a certain amount of PCM surrounded by the 1183mm length, 6mm diameter pipe is considered. In this case, the thickness of the surrounded PCM is set to 10mm, as further increase thickness will only increase total charging and

discharging time. Figure 6.16 below shows the 3d geometry of the PCM model. The model could be further simplified to 2D geometry to reduce calculation loads.



Figure 6.16 3D geometry and 2D slice of the PCM model

Geometry, mesh, and materials

The meshing profile contains 40244 mesh elements along with two adapted meshes. Results generated by all three meshes are compared to ensure the final result is independent against element size. The mesh element counts and the relative RMS errors of each mesh profile is shown in Table 6.5 below. The material used in this case is liquid water and PCM-HS22P.

Table 6.5 Mesh element and RMS error of the PCM parametrical analysis model

Mesh Case	Element count	RMS Error
Original	40244	
1st Adaption	68617	0.14%
2nd Adaption	91699	0.12%

Boundary and initial conditions

There are 2 specified boundaries, water inlet, and water outlet, as shown in Figure 6.17 below. The inlet is set as velocity inlet with given velocity and temperature value, and the outlet is set to pressure outlet. The other walls are set to adiabatic condition.

Other than the varying parameter, the initial conditions are set with PCM initial temperature of 20℃, flow speed of 0.05m/s and inlet temperature of 25℃ for charging process, and PCM initial temperature of 25℃, flow speed of 0.05m/s and inlet temperature of 20℃ for discharging process.

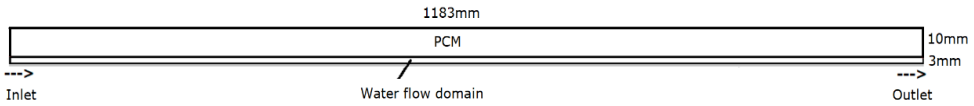


Figure 6.17 Schematic diagram and boundaries of the PCM model

Parametric analysis setups

The model has been simulated with different parameter adjustments. The effect of flow velocity and water inlet temperature against PCM thermal performance has been studied. Table 6.6 below shows the parameter sets used in this analysis

Table 6.6 Parameter sets of the PCM side analysis

Set parameter	**Phase change temperature Tp (℃)**	**Inlet water temperature Ti (℃)**	**Flow speed v (m/s)**
Charging	23	25	0.05
Discharging	22	20	0.05
Parameter Variations			
	Ti (Charging)	**Ti (Discharging)**	**v**
	25	20	0.01
	27	18	0.03
	29	16	0.05
	31	14	0.07
	33	12	0.09

- *Effect of flow velocity*

Figure 6.18 below shows the PCM temperature contour of the charging process. It can be seen that the PCM gets heated up slowly while higher temperature water is running from the left to the right. The whole charging process is finished around 5 hours. It is noted that at t = 4 hours, portions of PCM on the left side is fully melted, and there is a transition boundary which could be observed in the middle section. This is due to the temperature change of water flowing from left to the right side, which reduces the heat transfer along the flow direction. Same observation could also be seen during the discharging process, which is the reverse of the charging process.

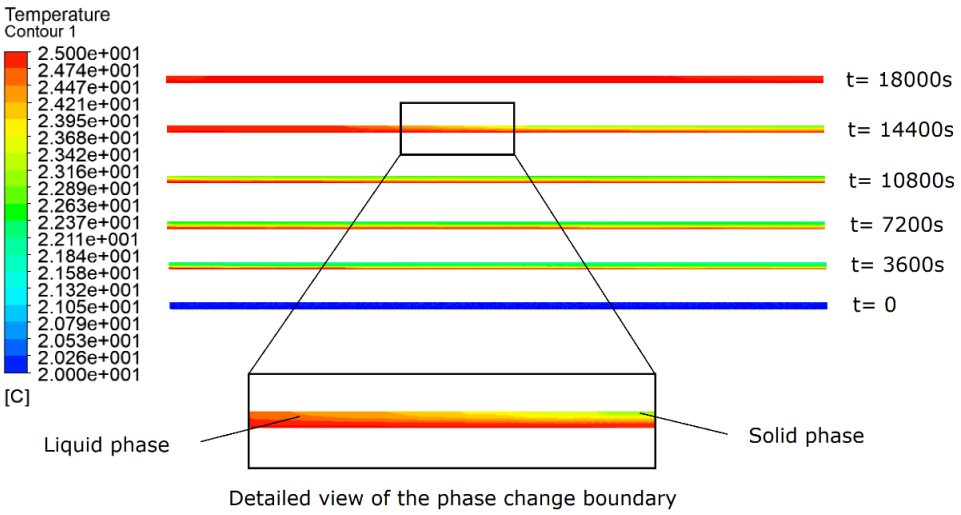


Figure 6.18 PCM temperature contour of the charging process at flow velocity of 0.05m/s

Figure 6.19 shows the average PCM temperature change during charging and discharging process at different water inlet velocities. It can be seen from the figure that by increasing flow speed from 0.01m/s to 0.03m/s, the time needed for

completing both charging and discharging process is greatly reduced. However, the difference becomes smaller when flow speed is further increased to 0.05m/s. For flow speed above 0.05m/s, the resulted time changes are further reduced and become minimal. Same pattern could also be found in Figure 6.20, which shows the PCM liquid fraction against time. The limiting factor of the charging and discharging performance is the low thermal conductivity of PCM, which limits the maximum rate of energy transfer. Figure 6.21 shows the correlation between charging and discharging time against different flow velocity, which again shows the fact that further increasing flow speed has no effects on time reduction.

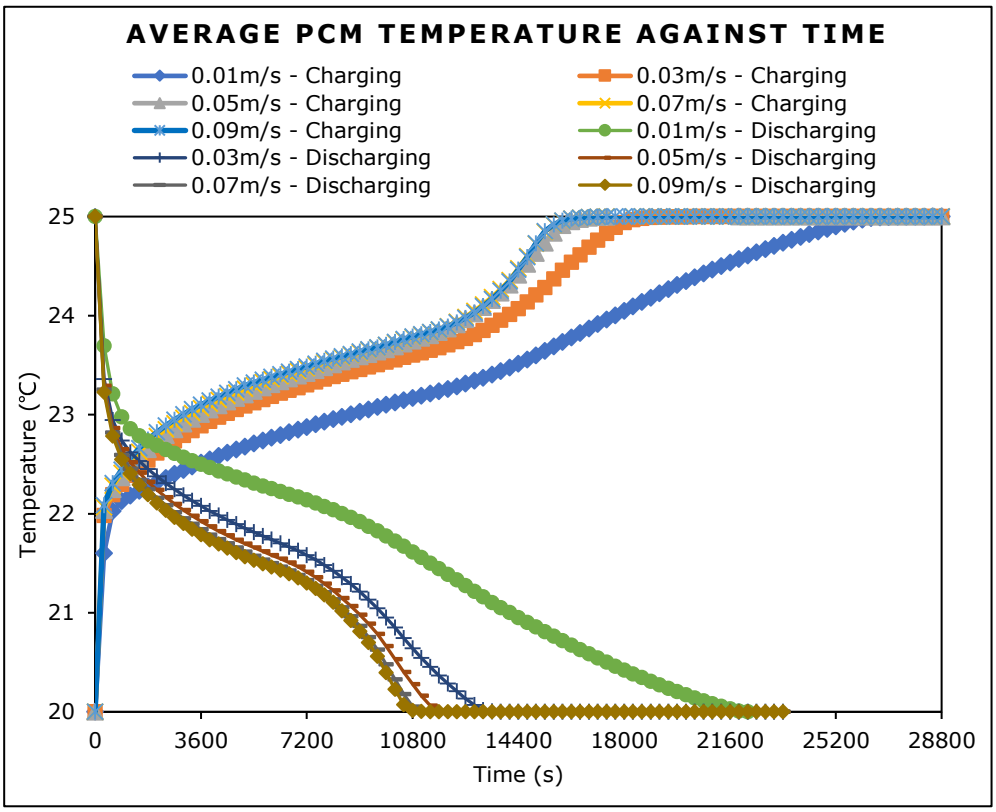


Figure 6.19 Average PCM temperature against time during charging period under different inlet water velocities

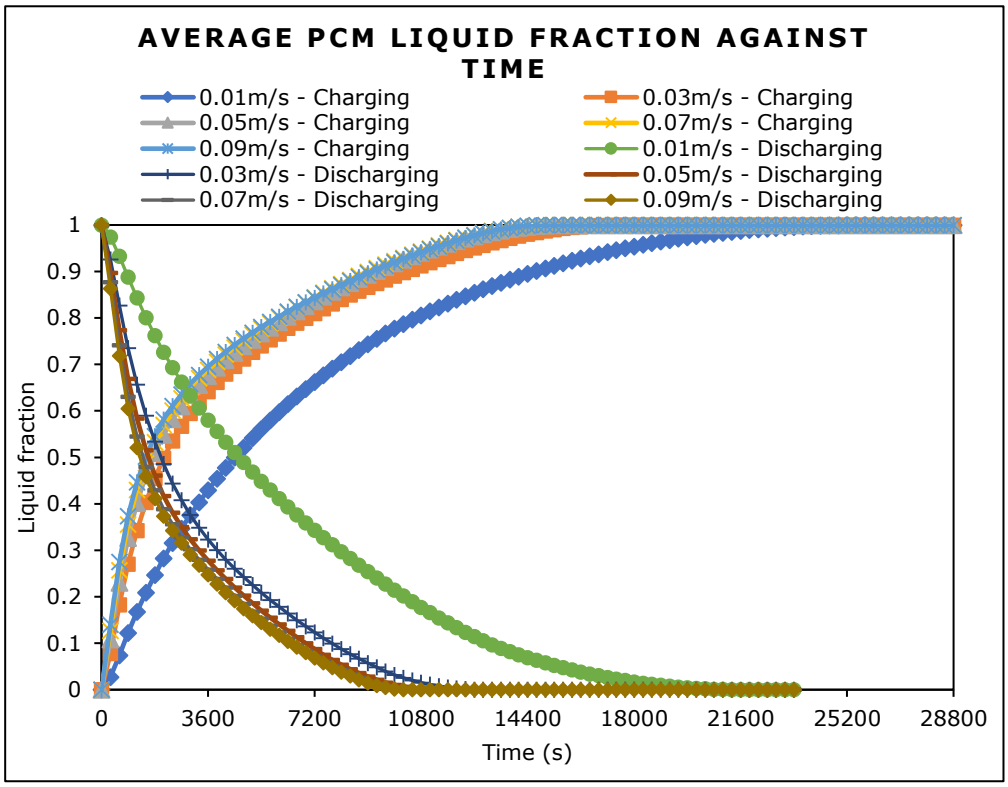


Figure 6.20 PCM liquid fraction against time of different flow velocities.

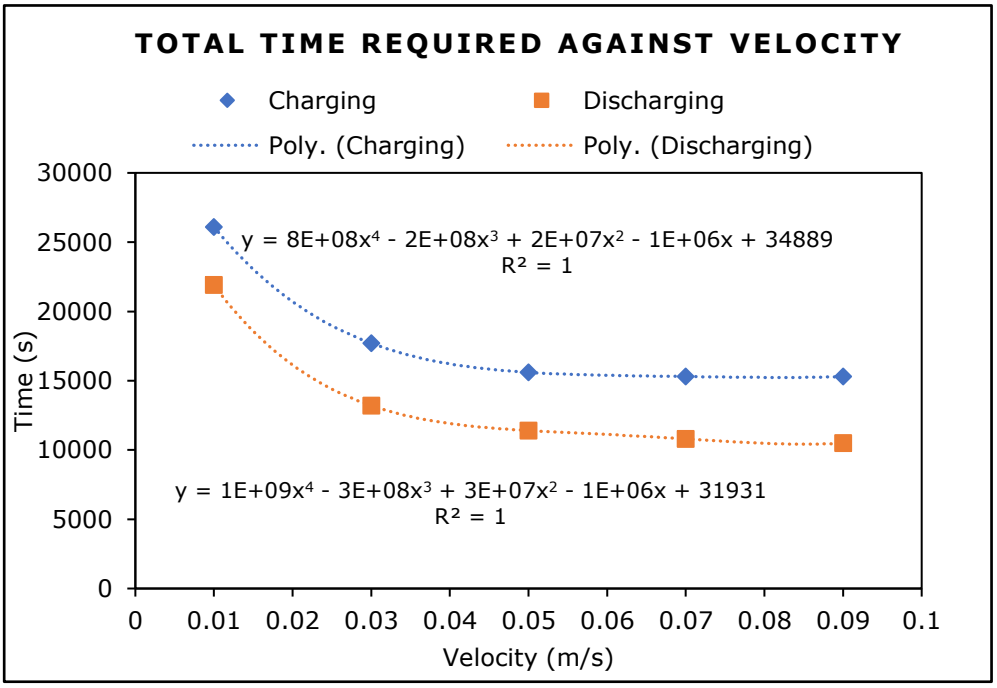


Figure 6.21 Total charging and discharging time required against different flow velocities.

Figure 6.22 shows the average water outlet temperature against time under different flow velocities. It can be seen from the figure that at lower inlet velocity, the increase rate of water outlet temperature is slower compared to higher inlet velocities. Similar to the change pattern of PCM temperature, the most significant difference is between flow velocity of 0.01m/s to 0.03m/s. The outlet temperature differences become closer as flow speed increases. It is noticed that at higher flow velocities, the outlet temperature rises (drops) soon after the charging (discharging) process starts, with less than 1℃ difference compared to the inlet temperature which is 25℃ (20℃). The limitation of PCM's low thermal conductivity restricts the heat transfer process between water and PCM.

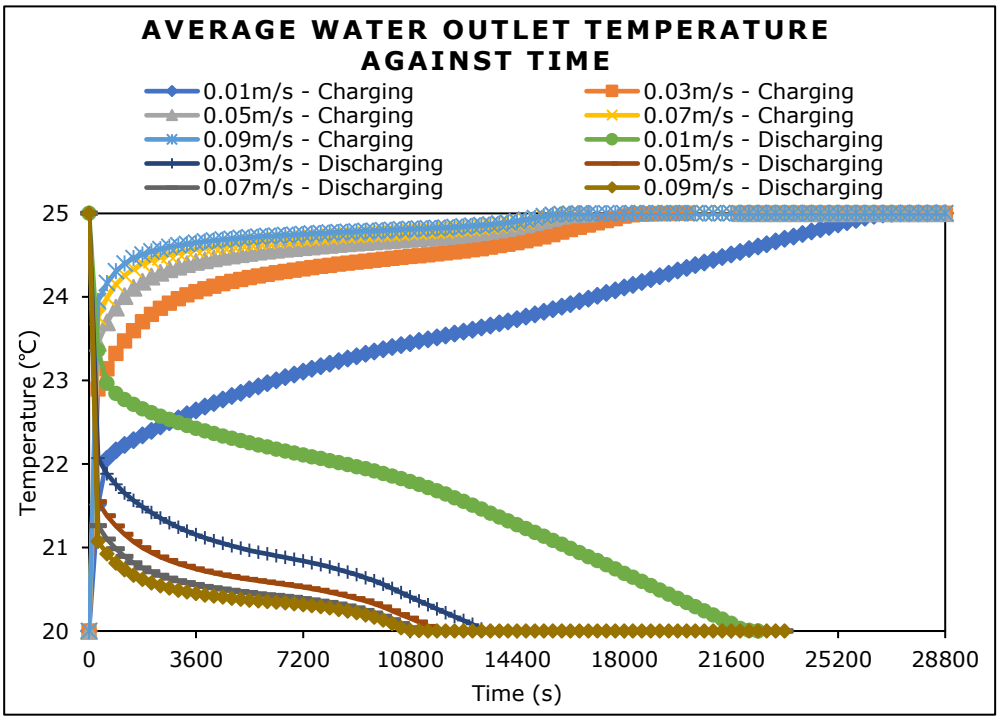


Figure 6.22 Average water outlet temperature against time during under different inlet water velocities

- *Effect of inlet water temperature*

Figure 6.23 and 6.24 shows the average PCM temperature and liquid fraction at different water inlet temperatures. It can be seen from the figure that the increased (decreased) water inlet temperature reduces the time needed for completing charging (discharging) process. Similar to the pattern observed from changing flow velocity, the effective time reduction becomes smaller when temperature difference is further increased for both charging and discharging process. The correlation of time needed for charging and discharging process against the temperature difference between inlet water and PCM's phase change temperature is given in Figure 6.25. It can be seen that the further increase the temperature difference will have very little effects on the reduction of both charge and discharge time. The limitation here is due to the solidification and melting speed within the PCM, which is another result due to PCM's low thermal conductivity.

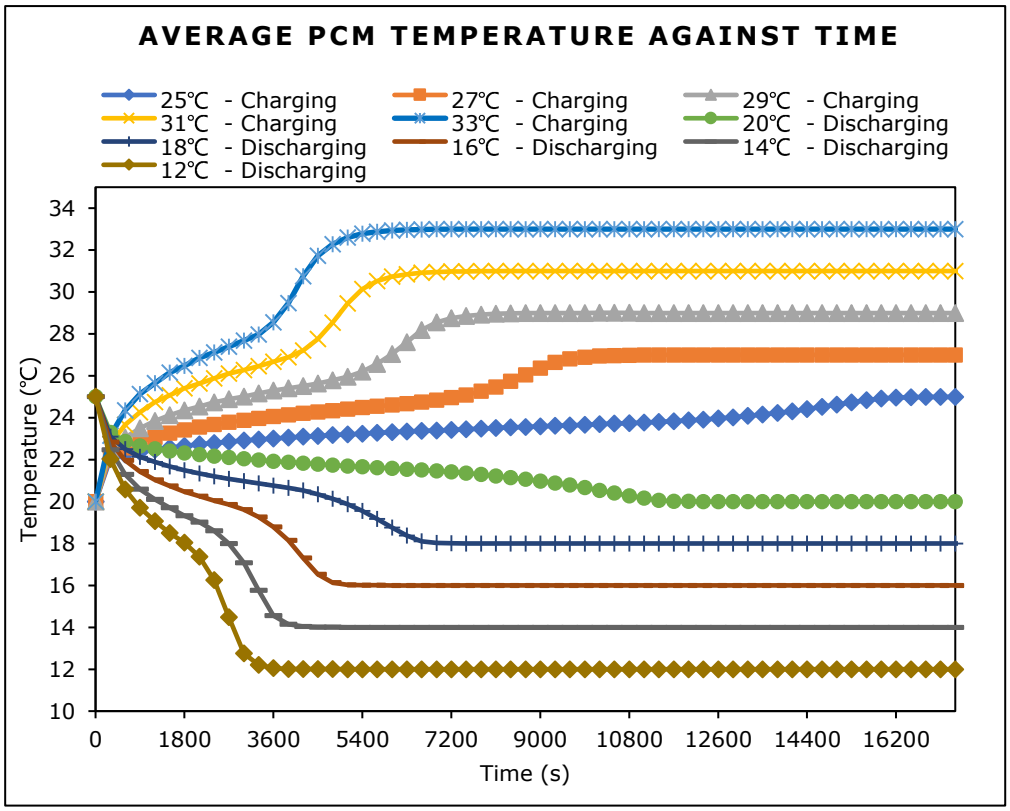


Figure 6.23 Average PCM temperature against time under different inlet water temperatures

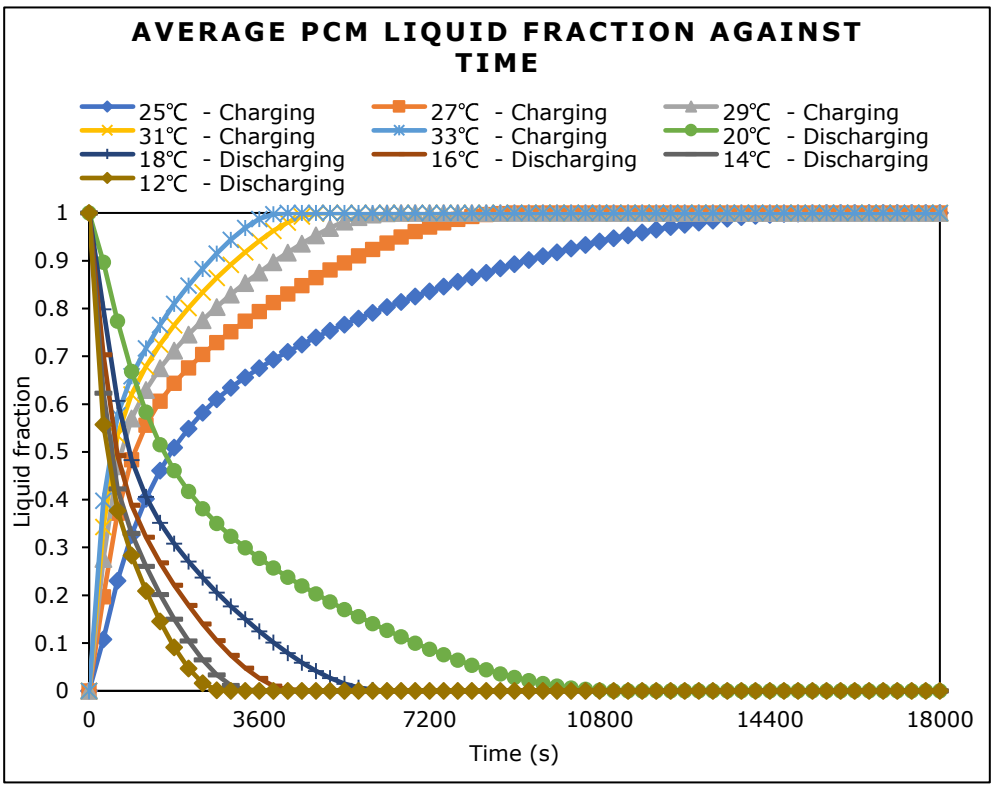


Figure 6.24 PCM liquid fraction against flow time during discharging process under different inlet water temperatures

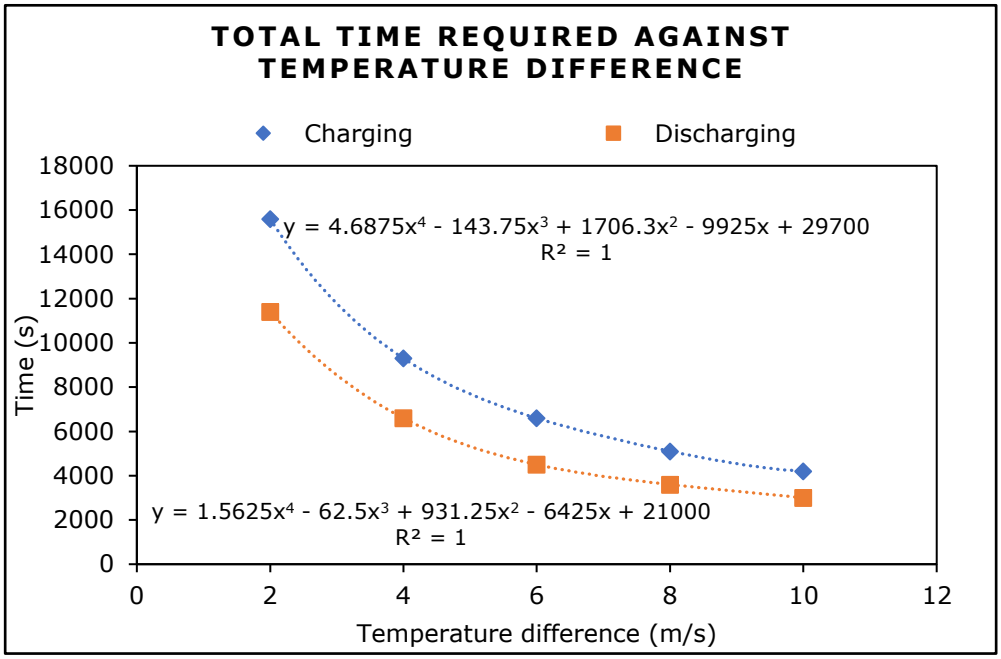


Figure 6.25 Total charging and discharging time required against different inlet temperature

Figure 6.26 shows the average water outlet temperature against time at different inlet temperature settings. It can be seen from the figure that the overall change pattern is similar compared to the change of PCM temperature. During charging (discharging) process, the higher (lower) the inlet temperature is, the sooner the outlet water will rise (fall) to the same temperature of the water inlet.

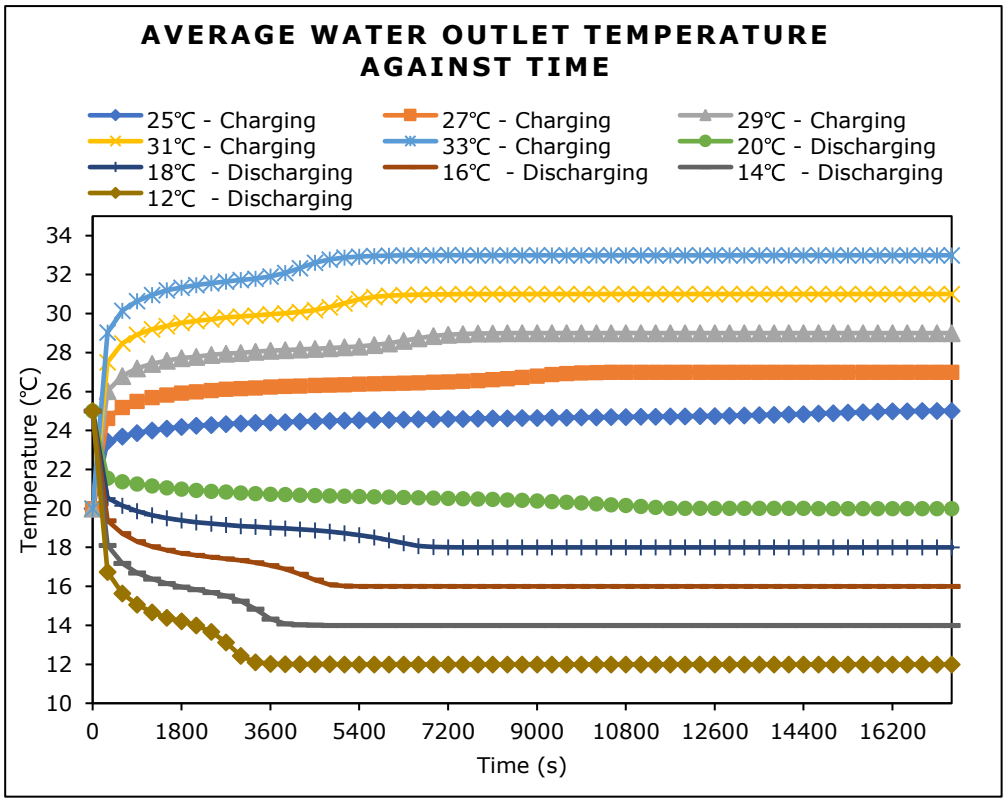


Figure 6.26 Average water outlet temperature against time under different inlet water temperature

In order to effectively cool the PV panel during daytime operation, the outlet water temperature must be kept relatively low for a long period of time. The above analysis indicates that only using bare pipe is not effective from both PV cooling and heat utilization's perspective due to the low thermal conductivity of the PCM. In order to improve the heat transfer between water and PCM, additional fins should be added to increase the surface area of contact, hence enhance the heat transfer process.

6.3.4 Fin analysis for PCM storage system

In many common heat transfer designs, fins are widely used as an extension of surface area in order to increase the rate of heat transfer. In recent years, researchers have studied the feasibility and the degree of thermal performance enhancement of added fins in PCM latent heat storage system. However, most of the studies are based on paraffin PCMs, and there is no clear correlation available at the moment to help with fin sizing of this work's design. Hence it is decided to study the effect of added fins to the overall heat transfer enhancement to the Salt-Hydrate based PCM storage systems. There are many types of fins with different structures, the fins to be discussed is the most common type of longitudinal fins, which is commonly used in terms of PCM heat transfer enhancement. The longitudinal fins could either be square or round according to the usage (as illustrated in Figure 6.27), with the same 2D cross-sectional geometry.

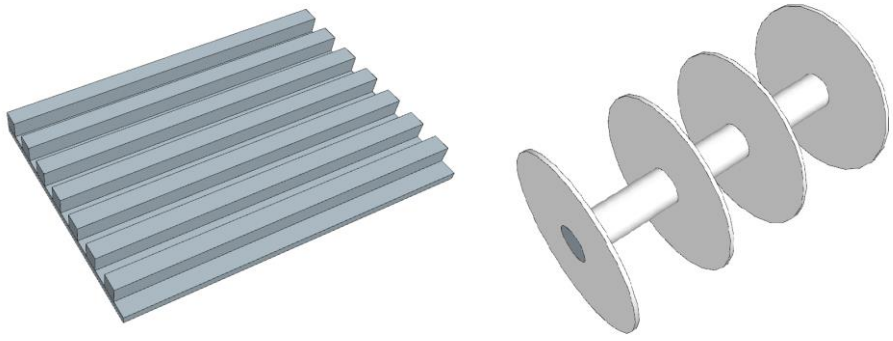


Figure 6.27 Common designs of longitudinal fins

- *Effect of fin interval*

Due to the low thermal conductivity of PCM, even when added with additional fins, the temperature variation inside PCM storage tank is still uneven across the whole body. In order to investigate the effect of fin density and its enhancement on heat transfer perspective, several models have been built with different fin intervals. The model is simulated and compared with reference value where there's no fin been added.

Model setup

This model is a two-dimensional cross-sectional plane consists of two fins with a certain interval and a section of PCM domain placed in between. The fin is 1mm thick and 10mm long (same as the thickness of PCM), with one of four interval values of 5mm, 10mm, 25mm, and 50mm (shown in Figure 6.28). As an example, the meshing profile with fin interval of 25mm has an element count of 46253. The mesh has been adapted twice (element count of 66076 and 92506 respectively), and the benchmark result of all three meshes have been compared to ensure the result is independent of element size level (RMS error of 0.15% and 0.04% respectively). The material used in this model is aluminium (for fins) and PCM-HS22P. Aluminum is chosen to be the fin material instead of copper because while aluminium could achieve around 60% of copper's heat transfer ability, the weight and cost of aluminium are significantly less than copper, hence it is more practical to be used in applications.

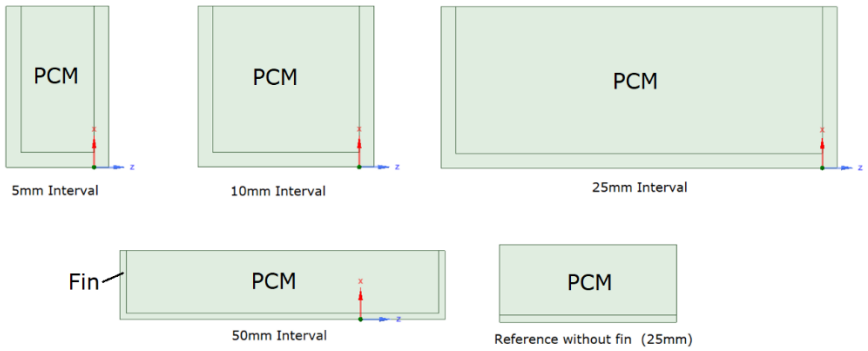


Figure 6.28 model geometry used for interval analysis (not to scale)

Boundary and initial conditions

There are only one specified boundary conditions, the heated surface, is at the bottom of the aluminium plate. The model is simulated in both charging and discharging conditions. The initial temperature of heated surface and PCM in charging process is 25 ℃ and 20 ℃ respectively, and the initial temperature of heat surface and PCM in discharging process is 20℃ and 25℃ respectively. The average temperature of the PCM is monitored and recorded every 5 minutes.

Results and discussion

Figure 6.29 shows the comparison of time-related PCM temperature contour between the case with 25mm fin interval and reference case in charging process. It can be seen from the figure that the PCM temperature of the model with fins is generally higher than the model without fins. It takes less than 3 hours for the PCM in model with fins to complete its charging process, while the reference model needs an extra hour. The temperature gradient in reference model is evenly along the

horizontal axis, while in model with fins the gradient is U shaped due to the existence of two extra hot surface on both sides. It can also be seen that the general temperature distribution of discharging process is similar to the temperature gradient in charging process. Both reference model and model with fins finishes discharge in less than 2 hours. However, the time needed for model with fins is still less than the reference model (could be found in Figure 6.32).

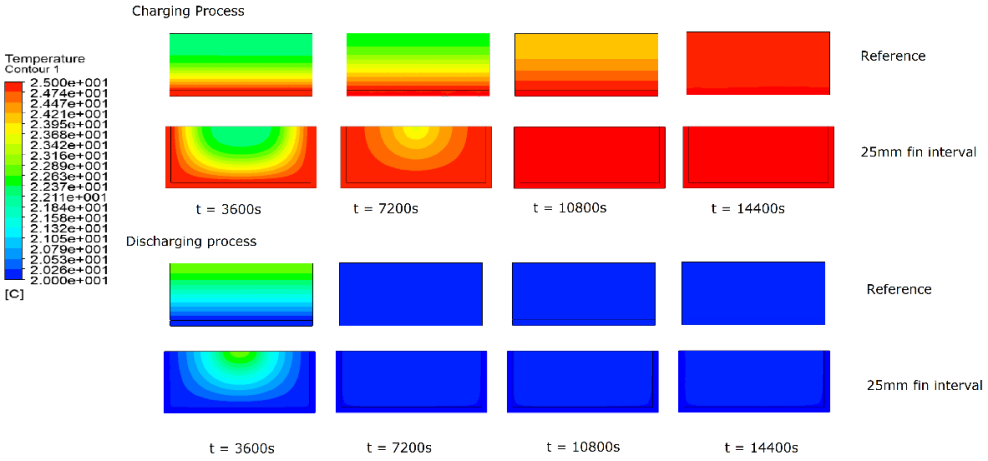


Figure 6.29 Comparison of time-related PCM temperature contour between case with 25mm fin interval and reference case in charging process

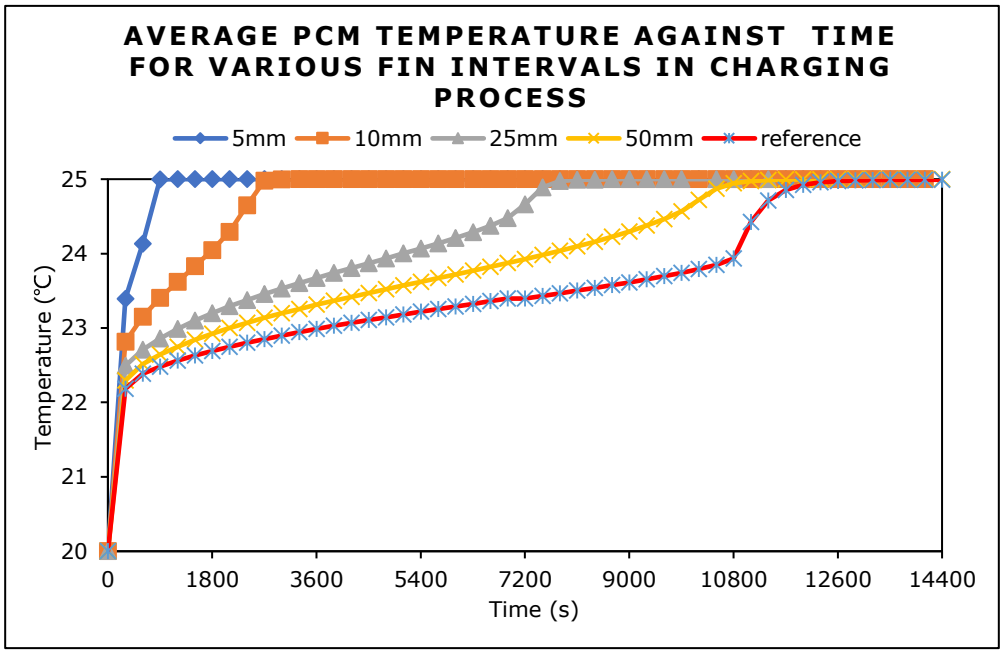


Figure 6.30 Average PCM temperature against flow time for various fin intervals in charging process

Figure 6.30 shows the PCM temperature variation along with time for different model settings in charging process. The temperature rise of the reference model is the slowest among all other models and is the one that needs the most time to complete charging process. There is not much difference at the beginning of the charging process when comparing the 50mm interval model with 25mm interval model, however, when entering the melting phase, the difference starts to become noticeable. The model with 25mm fin interval finishes charging process around t = 7800s (120min) while the model with 50mm fin interval finishes around t =11100s (185min). By further reducing fin interval, the time needed for charging process is significantly reduced. It can be seen that the model with 10mm interval finishes charging process around t = 3000s (50min) and the model with 5mm interval finishes at t = 900s (15min). Thus, it can be concluded that reducing fin intervals can significantly enhance the rate of heat transferred into PCM,

the shorter the interval is, the soonest the PCM will finish its charging process.

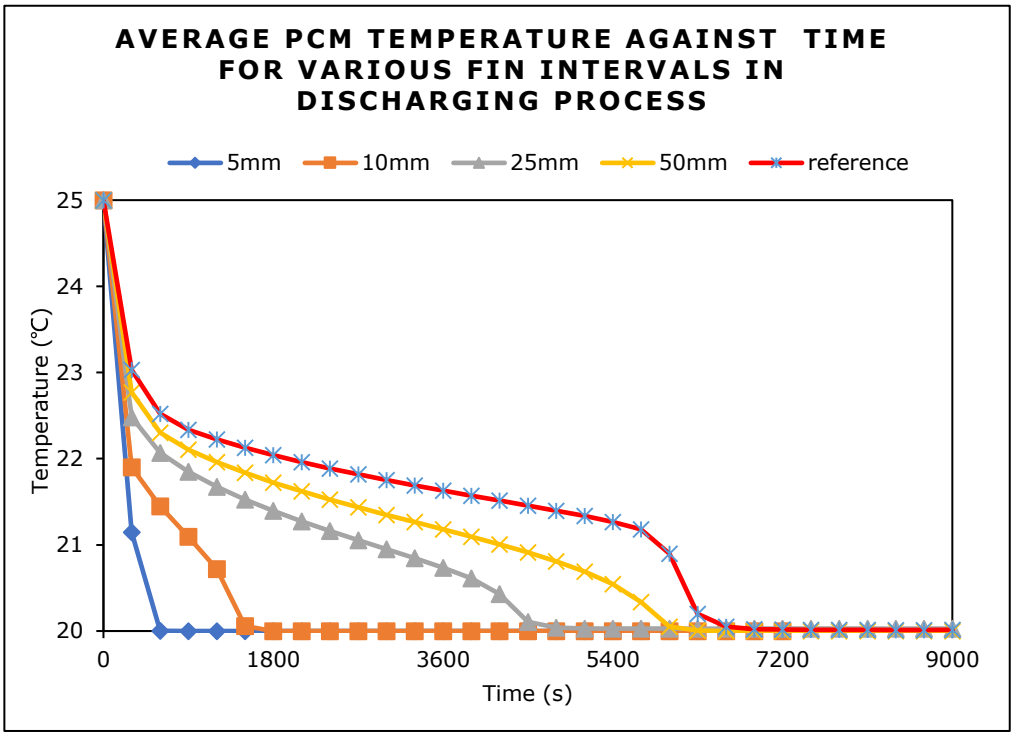


Figure 6.31 Average PCM temperature against flow time for various fin intervals in discharging process

Figure 6.31 shows the PCM temperature variation along with time for different model settings in discharging process. The temperature drop of the reference model is the slowest among all other models and is the one that needs the most time to complete discharging process. All models perform similar trends compared with charging process, with the only difference is that the time required to complete discharging process is less due to the thermal physical properties of PCM-HS22P. The reference model is the slowest that finishes at t = 6900s (115min), while the other four models of 50mm, 25mm, 10mm and 5mm finish their process at t = 6300s (105min), 4800s (80min), 1500s (25min) and 300s (5min) respectively.

Similar conclusion could be drawn that reducing fin interval can significantly reduce the time needed to complete discharging process. One thing should be noted, however, is that the as the fin density increases, the volume portion of PCM is reduced. With fin interval of 5mm, PCM melts or solidifies so quickly, which makes one of the big advantages of PCM – the characteristic of offset temperature hardly noticeable. Another thing should be noted is that for a given volume, higher fin density means less volume for PCM, which results in reduced heat storage capacity. Thus, it is important to consider such effect when calculating the required PCM volume.

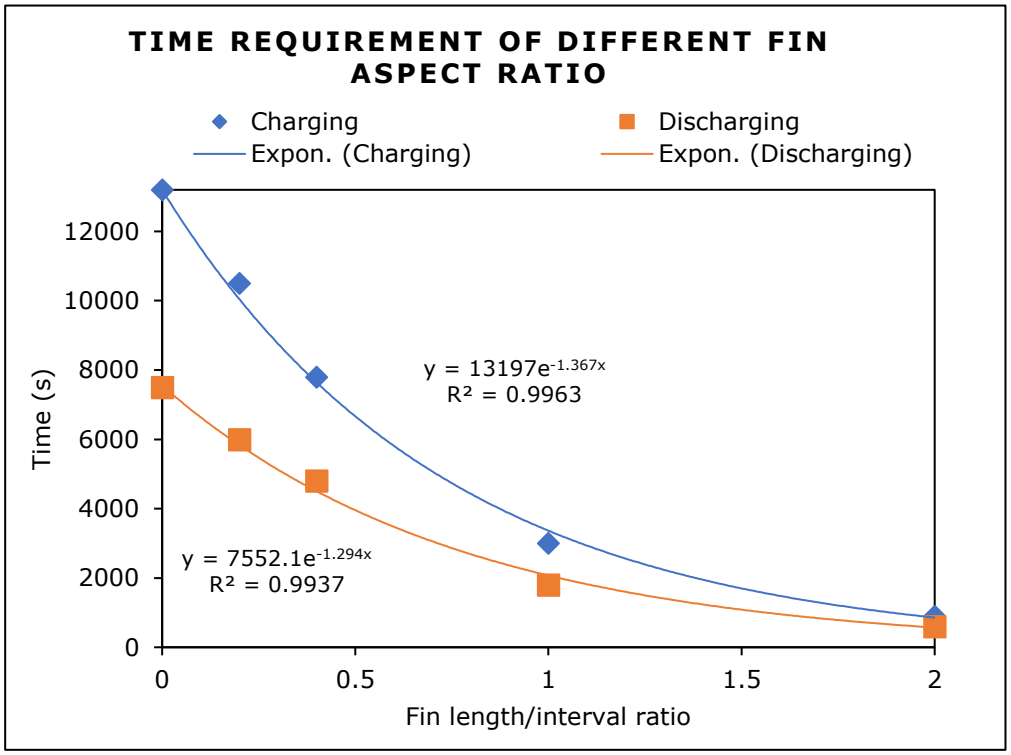


Figure 6.32 Charging and discharging time requirement of fins with different length/interval ratio

Figure 6.32 shows the charging and discharging time required for fins with different length/interval ratio. It can be seen from the figure that assuming the temperature at fin surface is

uniform and constant, exponential correlations could be used to describe the relationship of time and length/interval ratio.

- *Effect of fin length*

Fins are most commonly made by highly conductive metals such as copper or aluminium. Those metals have very high thermal conductivity, but at the same time, they also have low specific heat capacity. This leads to a fact that the longer the fins are, the greater the temperature drop/increase at the fin tip will be. The amount of temperature drop per unit length of the fin depends on the thickness and the thermal conductivity of its surrounding materials.

Model setup

This model is a a two-dimensional geometry of a 20mm long, 1mm thick aluminum plate with a 1mm thick fin attached at the middle of the plate. The length of the fin varies from 10mm to 40mm (see Figure 6.33 below) with aspect ratios (length : thickness) of 10, 20, 30 and 40. The thickness of PCM is set to 50mm. All meshes have been adjusted to have acceptable mesh independency, for example, the meshing profile of 40mm fin length model contains 18500 elements, and has been adapted twice (element count of 23250 and 31600 respectively) with an acceptable difference (RMS error of 0.12% and 0.05% respectively). The material used in this model is aluminium and PCM-HS22P.

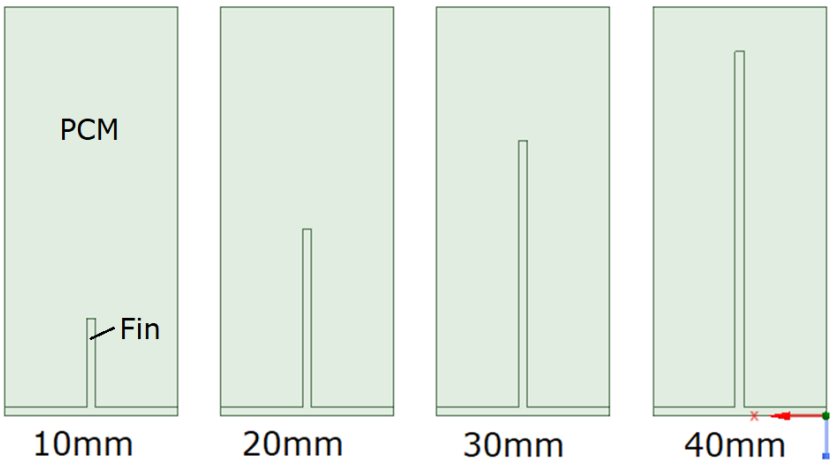


Figure 6.33 Geometries of the Fin length analysis models

Boundary and initial conditions

There are only one specified boundary conditions, the heated surface, is at the bottom of the aluminium plate. The model is simulated twice in both charging and discharging conditions. The initial temperature of heated surface and PCM in charging and discharging process is 25℃ and 20℃ respectively, and the initial temperature of heat surface and PCM in discharging process is 20℃ and 25℃ respectively.

Results and discussion

Figure 6.34 and 6.35 shows the temperature (color scale) and liquid fraction (grey scale) contour of all the fin length analysis models at the time of 1hr, 2hr, 3hr and 4hr during charging and discharging process. It can be seen from the figure that after 4 hours of charging, most part of PCM melted with 40mm length fin while only small amount of PCM melted with 10mm length of fin. The difference is minimal at the beginning of

charging process, and becomes more obvious with time. It can also be observed from the figure that the temperature drop along the fin is more noticeable with longer fin lengths. On the other hand, the discharging process shares similar observations as charging process other than the fact that the temperature drop along the fins are generally more significant compared to the temperature drop in charging process.

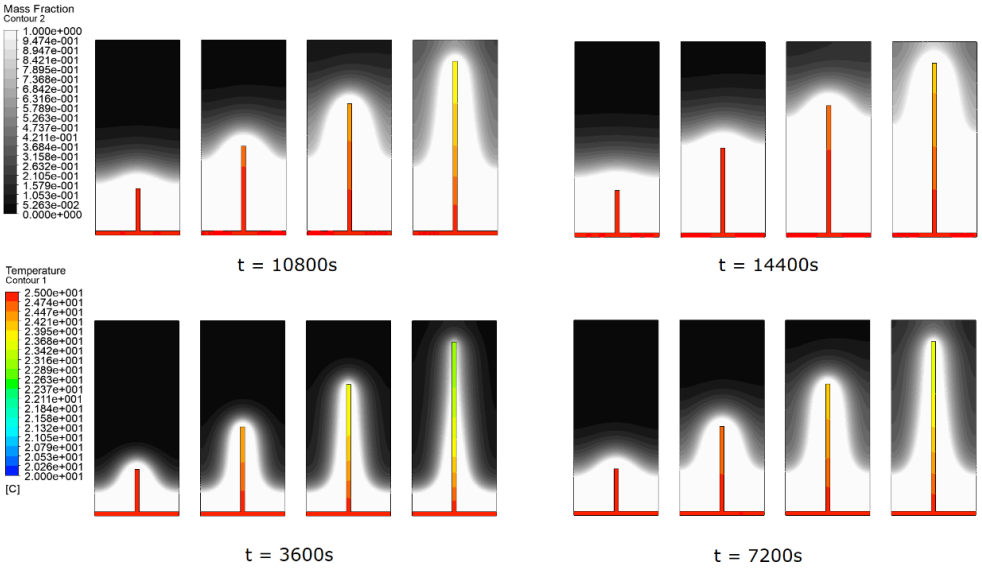


Figure 6.34 Temperature and liquid fraction contour of the fin length analysis models at time of 1hr, 2hr, 3hr and 4hr during charging process

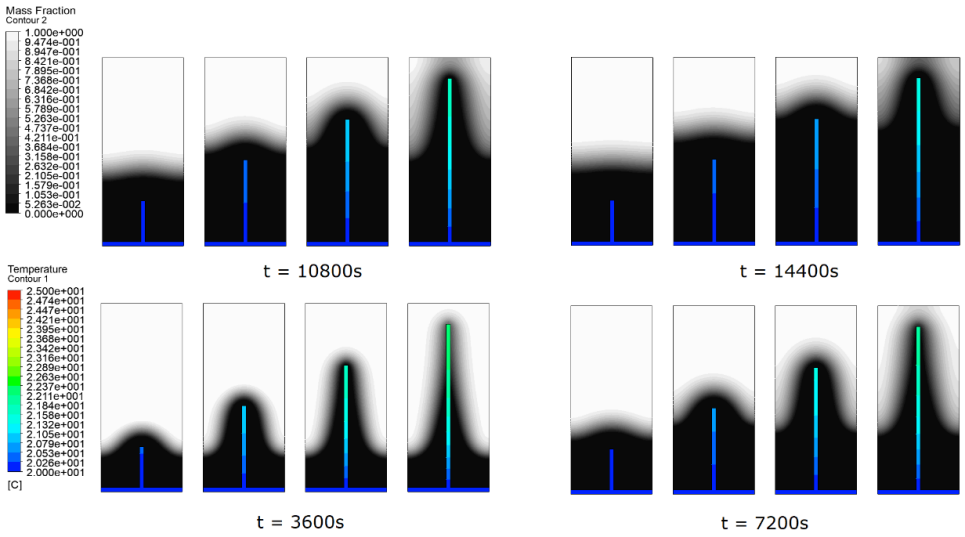


Figure 6.35 Temperature and liquid fraction contour of the fin length analysis models at time of 1hr, 2hr, 3hr and 4hr during discharging process

Figure 6.36 and 6.37 shows the maximum temperature drop from the fin tip to the bottom plate with different fin lengths during charging and discharging process. It can be seen from the figure that in charging process, although at t = 0, all fins have the same temperature drop of 5℃, soon after the charging process starts, the temperature drop of 10mm fin length reduces significantly, and is trending to 0. The temperature drop reduction of fins with longer length are slower. After 5 hours of charging, the temperature drops of 10mm, 20mm, and 30mm fin lengths are reduced within less than 1℃, while the fin length of 40mm still needs more time to achieve that. On the other hand, the discharging process shows similar trend other than one fact that the temperature drop along the fin becomes more consistent with reduced decreasing rate compared to the charging process. This is due to the higher solid phase thermal conductivity of PCM.

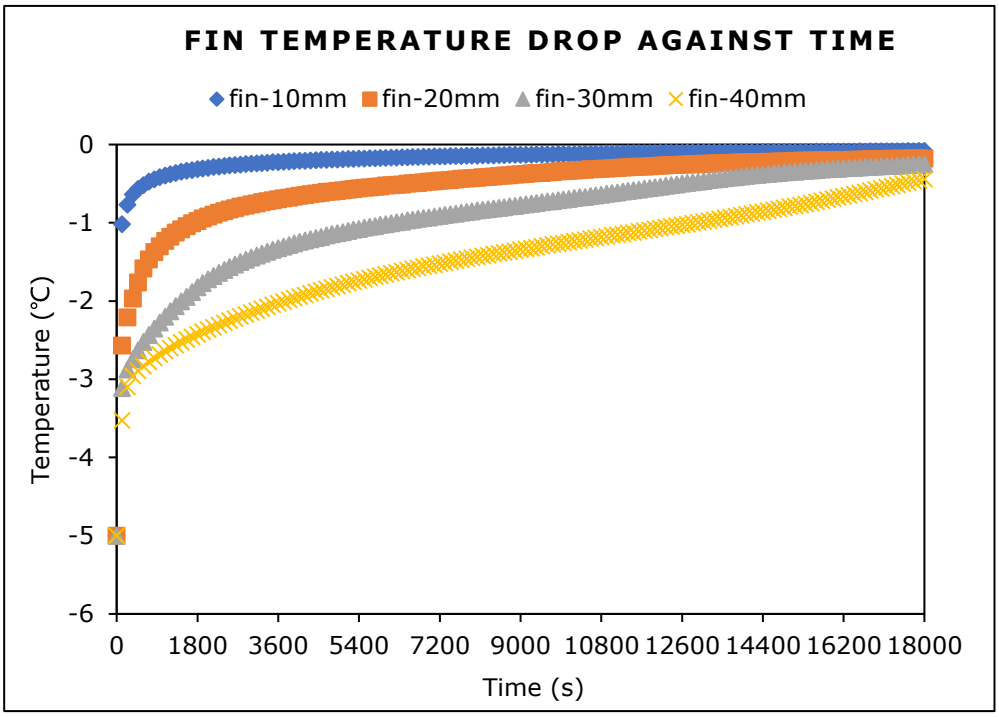


Figure 6.36 Fin temperature drop against times during charging process

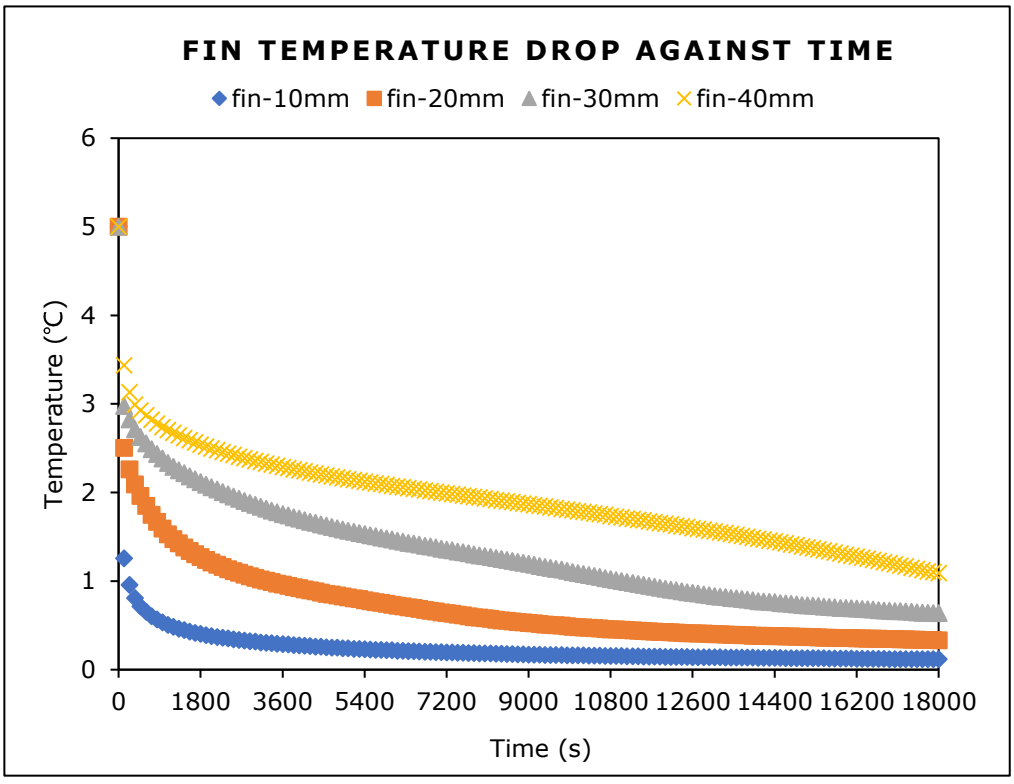


Figure 6.37 Fin temperature drop against times during discharging process

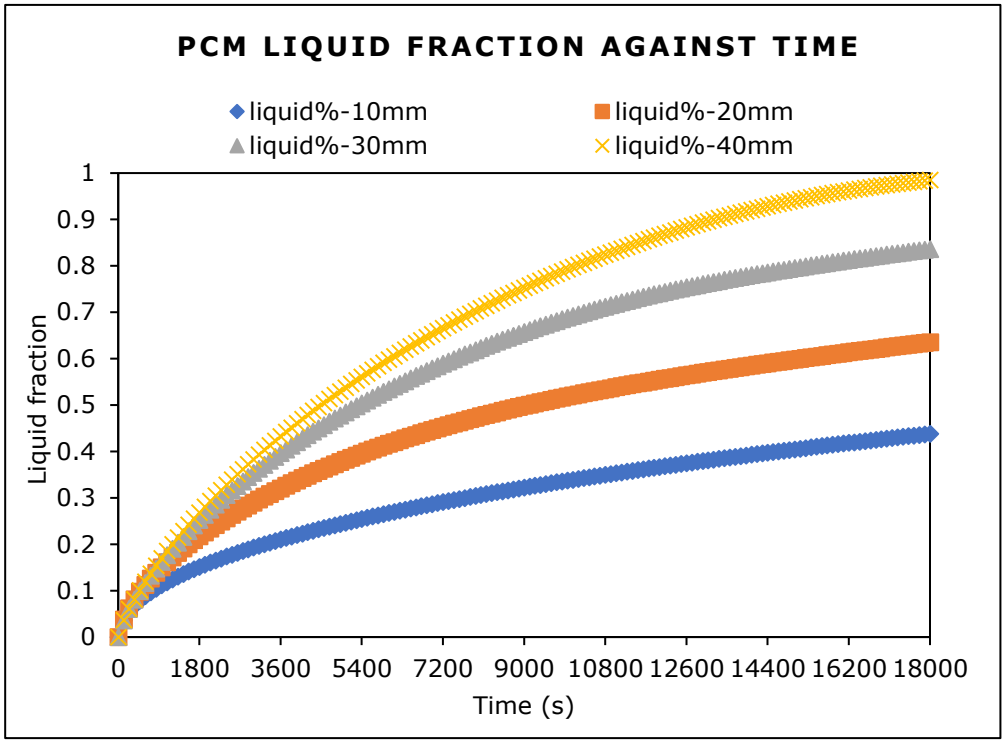


Figure 6.38 PCM liquid fraction against time during charging process

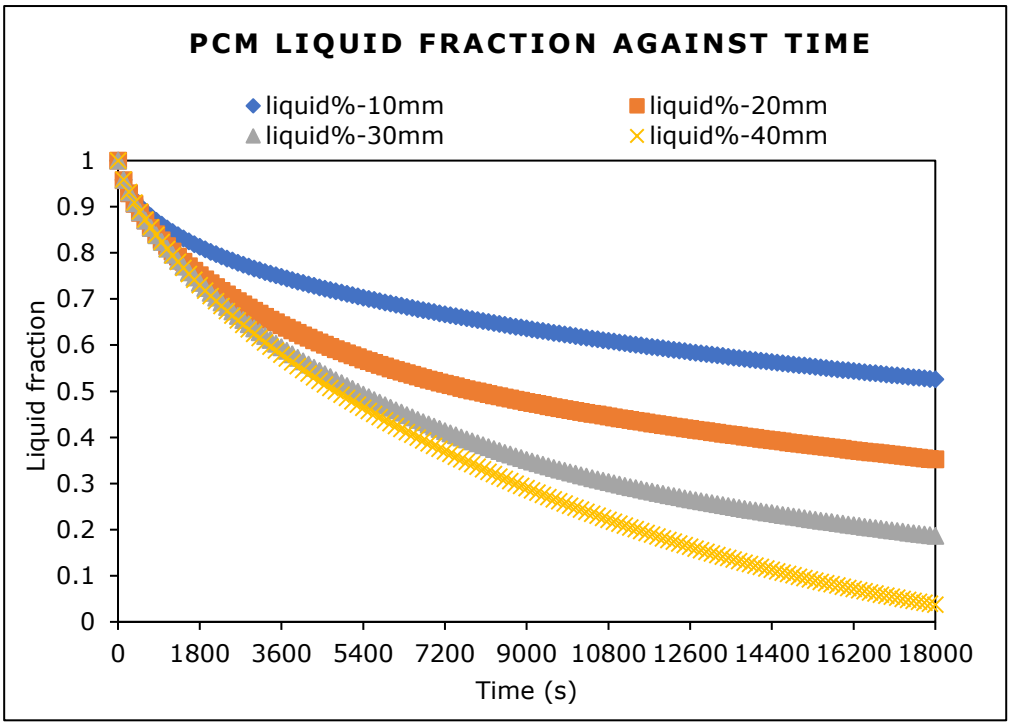


Figure 6.39 PCM liquid fraction against time during discharging process

Figure 6.38 and 6.39 shows the PCM liquid fraction against time during charging and discharging process. It can be seen from figure that in charging process, after 5 hours of heating, the PCM with 40mm fin length is almost fully melted with liquid fraction of 98.5%, while the liquid fraction of PCM with 30mm, 20mm and 10mm fin length is at 83.3%, 63.5%, and 43.6% respectively. For all fin lengths, the fastest PCM melting rate occurs at the start of the charging process, and is reduced gradually along increased time. The model with longer fin length could maintain higher melting rate for a longer time, while the melting rate of model with shorter fin length drop in sequence to the same melting speed. The discharging process also shows similar trends, with liquid fraction of 3.76%, 18.79%, 35.22% and 52.68% for fin length of 40mm, 30mm, 20mm and 100 respectively.

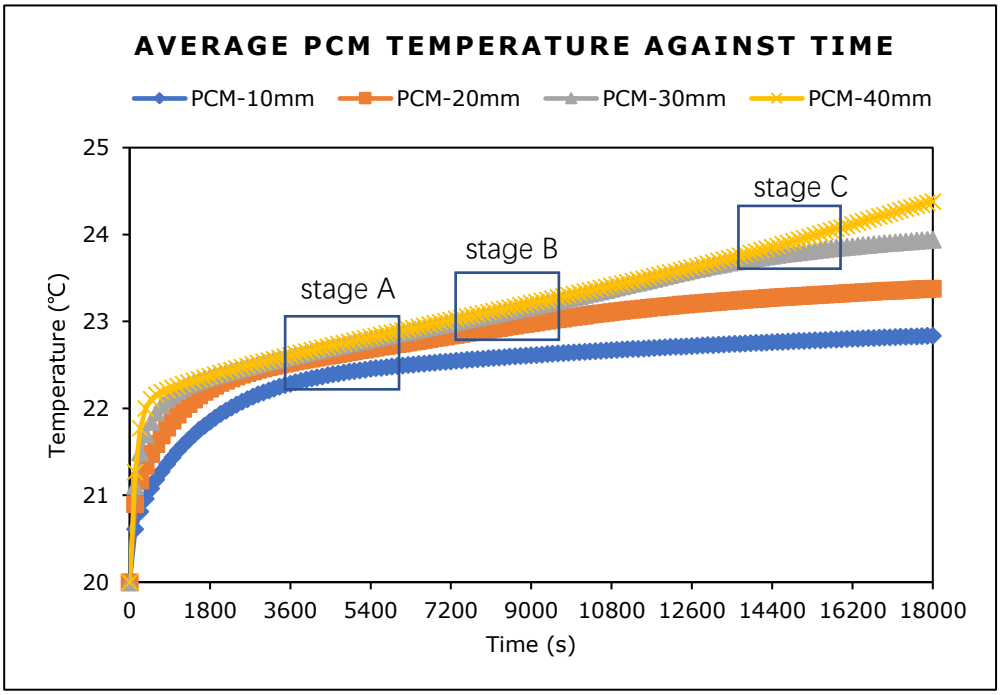


Figure 6.40 Average PCM temperature against time for charging process

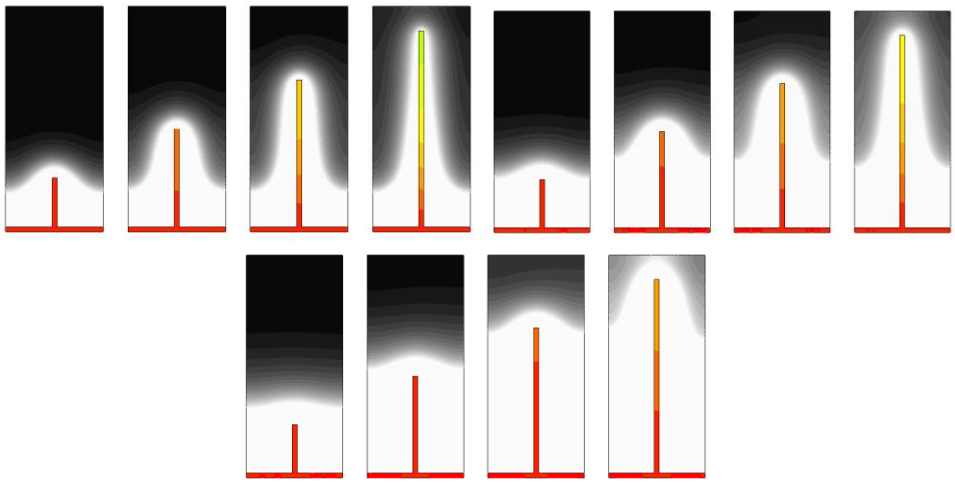


Figure 6.41 PCM melt fraction contour at stage A(top left), B(top right), C(bottom)

Figure 6.40 shows the average PCM temperature against time for charging process with all fin lengths. The temperature profile could be categorized into three stages, where at each stage, the PCM is fully melted around one of the shorter fins (as illustrated in Figure 6.41). It can be seen that although 10mm fin could maintain highest temperature, it has the least effect in reducing charging time. The benefit of 10mm fin diminishes at stage A, where the whole fin is submerged into the fully charged PCM layer. On the other hand, the 20mm, 30mm and 40mm fin lengths have similar time-reduction benefits during the first 2 hours until stage B, where the fully charged PCM layer rises above 20mm length fin. Similarly, at stage C, the benefit of 30mm fin diminishes as submerged into the fully charged PCM layer. The square box of stage A,B and C shown in Figure 6.41 and 6.42 are marked as indication only, showing that the time reduction effect of the shorter fin diminishes within the marked period.

On the other hand, the average PCM temperature against time for discharging process is shown in Figure 6.42. The temperature profile of all fin models has similar three different stages as the charging process. The three stages are marked in the figure. It is noted that the transition into the next stage is less noticeable, and the overall enhancement of added fins are smaller compared to the charging process. This is due to the larger solid state thermal conductivity. In order to match the same degree of performance enhancement of the charging process, thicker (smaller aspect ratio) fins should be used instead.

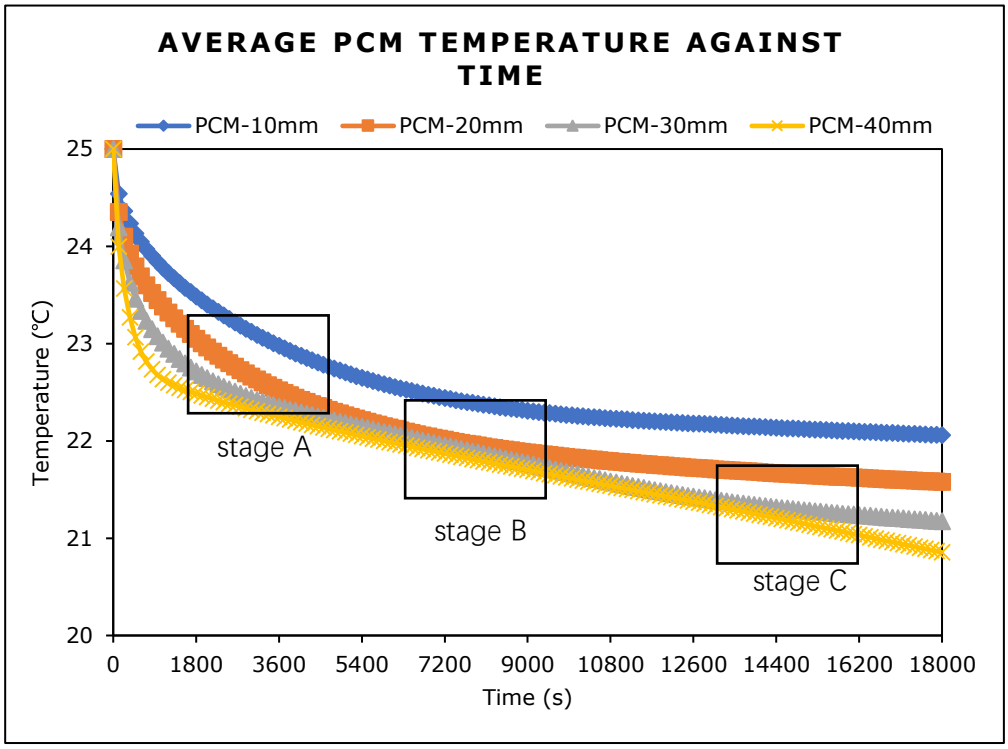


Figure 6.42 Average PCM temperature against time for discharging process

From above fin length analysis, it is considered that despite of fin temperature drop, longer fins (larger aspect ratio) will have

better thermal performance enhancement compared to the fins with shorter length (small aspect ratio).

6.4 Summary

The proposed PVT-PCM system has been presented and the component selection as well as related working principles have been briefly discussed.

The parametric analysis of PV panel reveals that using water cooling could effectively lower the PV cell temperature, by increasing flow speed, the temperature gradience on the panel surface will be smaller, hence better thermal performance. However, the degree of performance gain is significantly reduced with increased velocity larger than 0.05m/s.

The parametric analysis of PCM storage tank shows that the PCM has great potential to be used under various environmental situations if the limitation due to PCM's low thermal conductivity could be lifted. Again, the performance gain of PCM is minimal after increase water velocity over 0.05m/s.

The fin analysis for PCM storage system reveals the correlation between different fin length and intervals against the melting and solidification conditions of PCM. It is found that the heat transfer rate could be greatly enhanced by adding additional fins into the storage tank. The fin with shorter intervals and longer length is preferred as it can further accelerate the phase change process for a longer period of time.

The results of this chapter are used for the initial design and optimizations for the whole system analysis in transient weather conditions in the following chapters.

CHAPTER 7. PVT-PCM OPTIMIZATION FOR UK WEATHER.

7.1 Introduction

Having completed the parametric analysis of the individual system components under the effects such as water flow speed, solar radiation level and ambient temperature. The whole system is put into a transient simulation with real weather conditions. The weather profile of Nottingham has first been chosen as it is located in the middle part of England. The weather and solar radiation data of Nottingham for summer and winter design days are shown in Table 7.1 below (CIBSE, 2015). The hourly thermal and electrical performance of the whole system will be investigated, at the same time, the performance of the PVT-PCM system is then compared with the conventional flat plate PV only setup in terms of energy saving potentials as well as cost.

Table 7.1 Hourly ambient temperature and solar radiation of summer and winter design days of Nottingham, UK

	Summer design day (21st July)		**Winter design day (21st Jan)**	
Hour	Temperature (℃)	Solar radiation (W/m^2)	Temperature (℃)	Solar radiation (W/m^2)
1:00	14	0	0	0
2:00	13	0	0	0
3:00	13	0	0	0
4:00	12	16	-1	0
5:00	12	103	0	0
6:00	13	241	0	0
7:00	15	389	0	0
8:00	16	532	0	17
9:00	17	655	1	110

10:00	18	757	1	203
11:00	19	824	2	261
12:00	20	845	3	282
13:00	21	811	2	261
14:00	21	736	2	191
15:00	22	614	1	96
16:00	21	467	0	12
17:00	21	312	0	0
18:00	20	176	0	0
19:00	20	53	0	0
20:00	19	0	0	0
21:00	18	0	0	0
22:00	17	0	0	0
23:00	15	0	0	0
0:00	14	0	0	0

In order to study the maximum latent heat storage performance of the PCM panel, it is considered in this case that the enclosure of PCM panel is free from natural convection in order to store energy with minimal heat loss. However, due to the fact that heat utilization from PCM is not a fixed rate and is heavily affected by demand, in some extremely hot situations, additional natural or forced air convection is sometimes necessary to prevent overheating of the system if stored latent heat is not utilized during the previous day. There are many ways to introduce natural or forced convection to the PCM panel, this study provides an example of utilizing natural ventilation without additional power requirement. In order to achieve that, the PCM panel can be placed at a well-ventilated area with an additional enclosure which has self-controlled dampers installed (as illustrated in Figure 7.1 below).

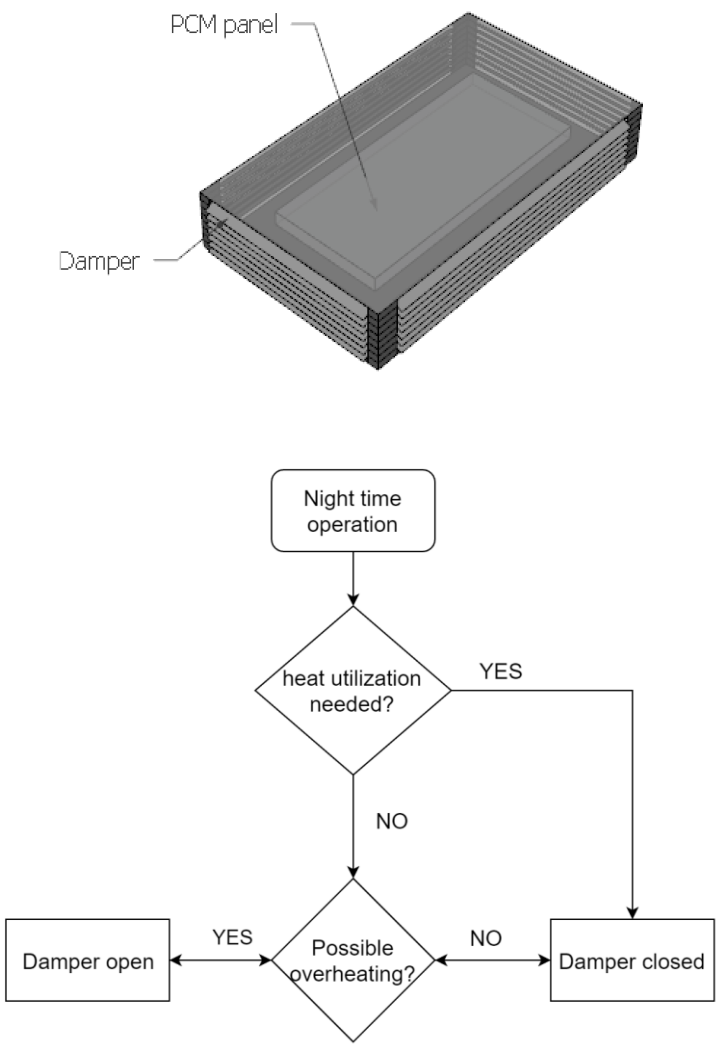


Figure 7.1 Sample illustration of additional PCM enclosure with dampers and a simple damper contol algroism

7.2 Performance evaluation for PV only system

In order to set design parameters to the PVT-PCM system, the transient thermal performance of a conventional flat plate PV panel is studied first. This performance evaluation sets a benchmark for the newly designed system to evaluate the degree of performance enhancement.

The model used in PV only evaluation is the same model used in Section 5.2. The hourly temperature and solar radiation data are considered to be accurate enough for such PV performance evaluation due to the uncertain nature of real weather conditions. To simulate the real time PV panel temperature under hourly environmental conditions, the model is simulated in transient solver with input data updated hourly. At each hourly interval, new boundary conditions of air temperature and PV panel heat flux will be input to represent real time environmental conditions. The whole model is simulated for 24 hours, and the average temperature of the PV panel is calculated hourly.

There are two types of weather which will be discussed, windy day condition and calm day condition. Windy day is generally more performance friendly for PV panels as additional cooling is provided by forced convection. However, in some situations there might be little or no wind, or there might be obstacles blocking the air movement, i.e., building facades. Considering the fact that serious overheating issue often occurs during calm day, it is also important to evaluate the PV performance under such extreme conditions with minimal wind. In this case, the wind speed of windy day is set to 5m/s which is the average wind speed of Nottingham, and the wind speed in calm day is set to 0.1m/s.

7.2.1 Summer design day

Figure 7.2 shows the hourly temperature profile of the conventional back plate PV system in summer design day with moderate wind along with environmental conditions. It can be seen from the figure that PV temperature stays the same to the ambient when there's no solar radiation. The cell temperature starts to rise at 5:00 at about 15.6℃, and the peak cell temperature is recorded at 13:00 with cell temperature of 43.3℃. The cell temperature starts to drop gradually after 13:00, and reaches ambient temperature after 20:00.

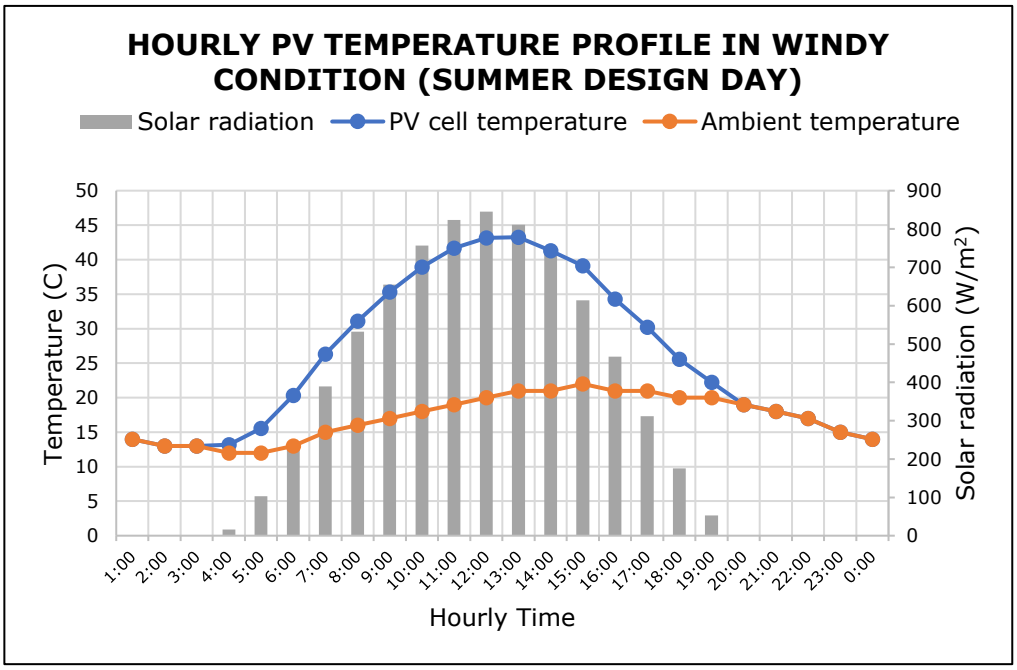


Figure 7.2 Hourly PV temperature profile in windy condition (Summer Design day)

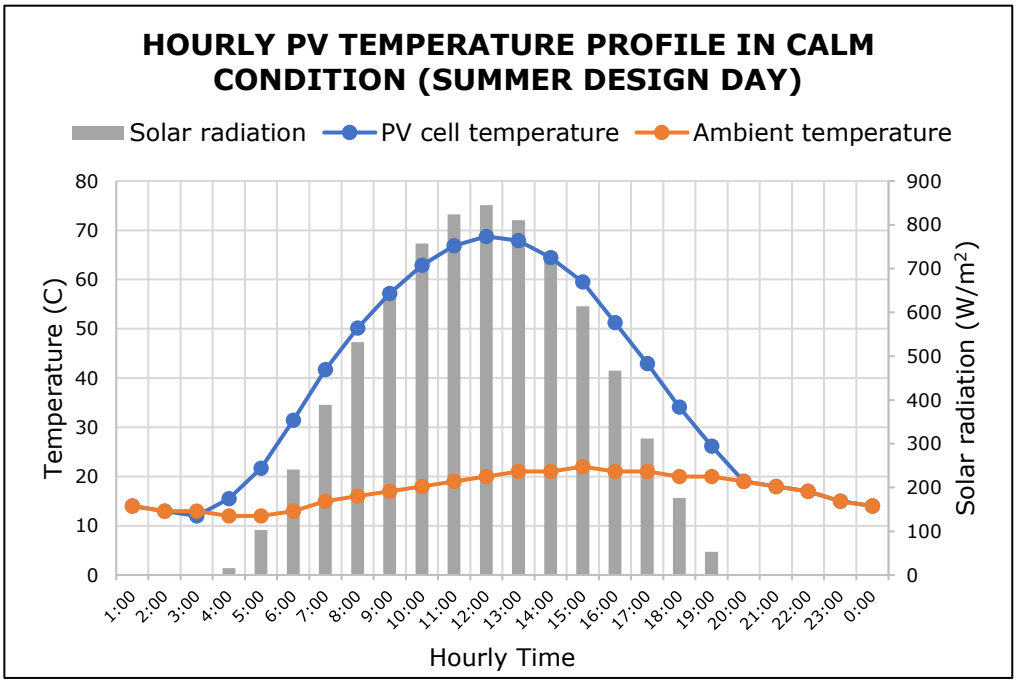


Figure 7.3 Hourly PV temperature profile in calm condition (Summer Design day)

Figure 7.3 shows the hourly temperature profile of the conventional back plate PV system in summer design day with minimal wind along with environmental conditions. It can be seen that due to the lack of cooling provided by natural convection, the PV cell temperature rises significantly when compared to the windy day condition. The PV cell temperature increases rapidly with the time, and the maximum cell temperature is 68.8℃ at 12:00, which is too hot as the electrical efficiency of PV cells is significantly reduced under that temperature. Moreover, the structural stability will also be affected at such high temperature. Although this is not an average daily situation, it is important that a proper PV system design should also consider those extreme weather conditions.

7.2.2 Winter design day

Figure 7.4 shows the hourly temperature profile of the conventional back plate PV system in the winter design day with wind or without wind along with other environmental conditions. It can be seen from the figure that at conditions where there is no wind, the maximum cell temperature can reach 24.6℃ at 12:00, while on the other hand, the maximum cell temperature is only 12℃ in windy situations. Considering the fact that although the photovoltaic efficiency will be improved by further reducing cell temperature, not much power gain can be obtained using additional cooling method during winter time. As a result, both temperatures are considered to be acceptable without additional cooling. However, considering the fact that PV panel could also be used as a reasonably good solar collector, the PVT-PCM system could also be used only for the purpose of collecting solar thermal energy, which is equivalent up to 1.1kWh/m^2 per day without considering any potential energy loss.

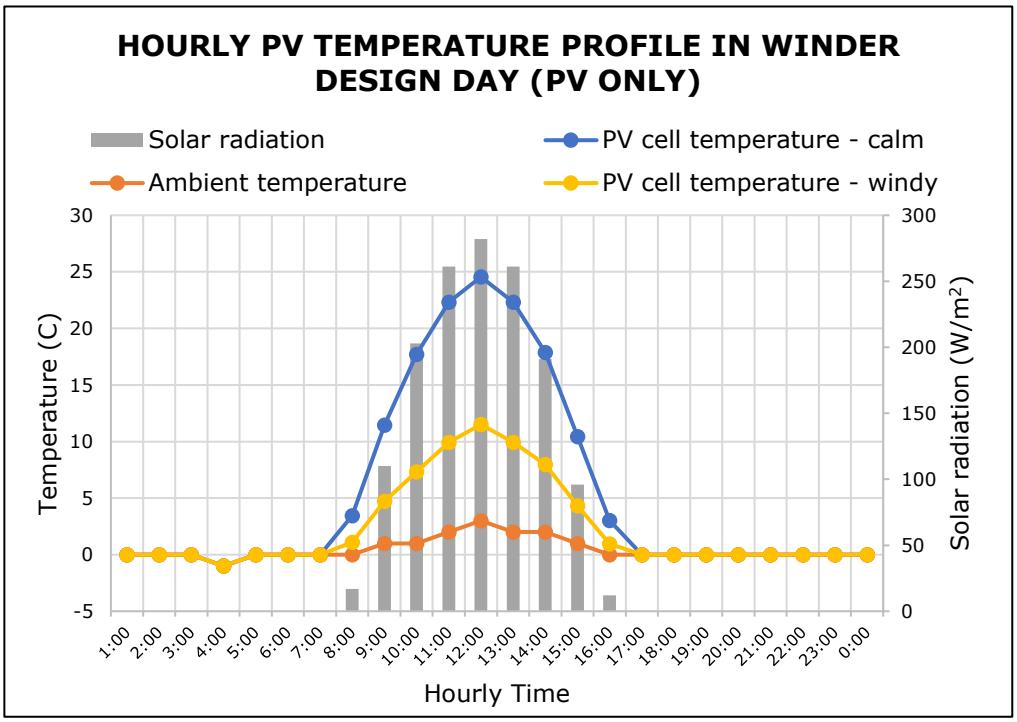


Figure 7.4 Hourly PV temperature profile in winter design day for both calm and windy conditions

7.3 PVT-PCM system design and optimization

7.3.1 PCM storage panel sizing

The size of the PCM storage tank depends on the amount of heat that can be stored during the daytime period. The daily energy delivered by solar radiation is calculated to be 5.8kWh/m^2, with the absorbance ratio of 0.71 and the surface area of 0.621m^2, the maximum amount of energy that can be stored in the PCM is calculated to be 3.4kWh/day. The energy loss due to natural ventilation in PV only system is not considered here as this PVT system utilizes water cooling as its only method of convection heat transfer (built into the building envelope). At the same time, the energy loss via long wave

radiation is negligible due to the small temperature difference between water cooled PV panel temperature and surrounding temperature. Table 7.2 below shows the calculation process required to acquire the amount of PCM storage needed for the maximum daily load. It is calculated that approximately 0.036m^3 of PCM is needed in order to fully utilize the energy.

Table 7.2 Sizing of required PCM material

Daily load	**Total energy**	**PCM fusion heat**	**Required PCM Volume**
3.4kWh	12240kJ	185kJ/kg	0.036m^3

7.3.2 System specification

The 1183mm x 525mm x4mm PV panel is cooled by a 1mm thick copper absorber plate with a series of circular water pipe evenly distributed below the plate. The water pipe is assumed to have perfect contact with the copper plate. The number and diameter of the water channels are customizable under different maximum working loads. In this study, the number of pipes is chosen to be seven and pipe diameter is set to 6mm, this combination is proved to be sufficient for cooling PV panel in previous parametric analysis.

The Shape of PCM storage panel is also customizable as long as the volume and heat transfer design is sufficient for the types of usage. In this case, the dimension of the PCM panel is set to have similar foot print of the PV panel. The thickness of the storage tank is set at 61mm so that the total volume of PCM panel is 0.038m^3 (allowing some headroom for extra fin

installation). A series of seven 6mm diameter water pipe is evenly distributed along the horizontal axis in the middle of the storage tank. The position of the water pipe is evenly distributed across the width of the PCM panel.

The PV and PCM parts are connected with each other using additional water pipes, so that they can be placed separated to in order to suit different physical restrictions while installing. The cross-sectional view of the PV and PCM parts are shown in Figure 7.5 below.

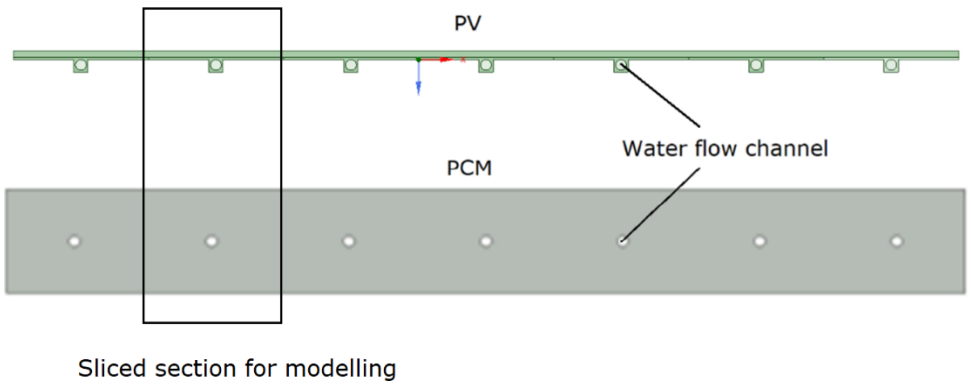


Figure 7.5 Cross sectional view of the PV and PCM parts

7.4 System performance evaluation and optimization

Before conducting a whole day simulation, a capacity analysis will be conducted to study the performance on a steady state setting with peak temperature and solar radiation levels of the day. This is to ensure the preliminary design can withstand extreme situations, in this case, a maximum solar radiation and temperature of 845Wh/m^2 and 22℃ respectively, for 5 hours.

In order to reduce the complexity of simulation process, the model is simplified by dividing the whole model vertically into 7 equal parts; each part has exact same geometry. It is expected that each individual part will perform very similarly to the whole unit.

7.4.1 PV performance under maximum loads

The 3D model of the divided PV part has been illustrated in section 6.3.2. Figure 7.6 below shows the geometry and meshing of the model. The material of heatsink has been set to copper, and the flow domain has been set to water. There are three specified boundary types in this model, water inlet, water outlet and panel surface. The panel surface is set to have a constant heat flux of 600W/m^2 after considering the panel absorbance ratio, and have thermal physical properties of PV with 0.004m thickness. The water inlet has been set to have velocity values range from 0.01m/s to of 0.1m/s with inlet water temperature of 23℃ which equals to the fully melted PCM temperature. The initial temperature of the model is also set to 23℃.

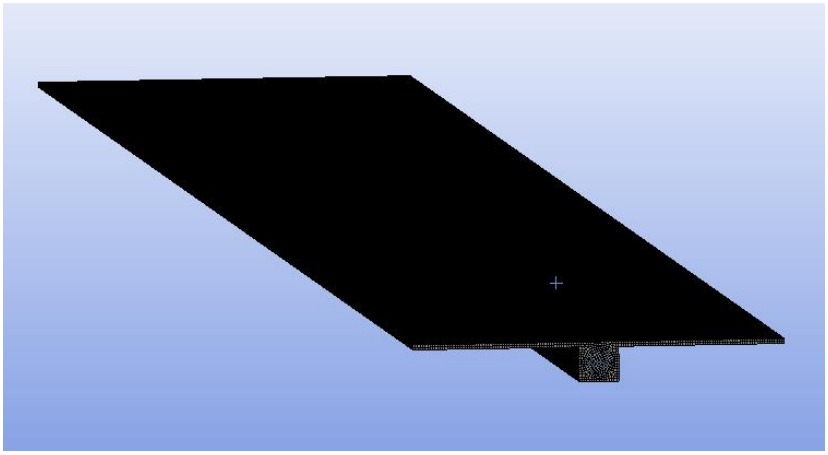


Figure 7.6 Meshing of the sliced PV absorber unit

Results and discussion

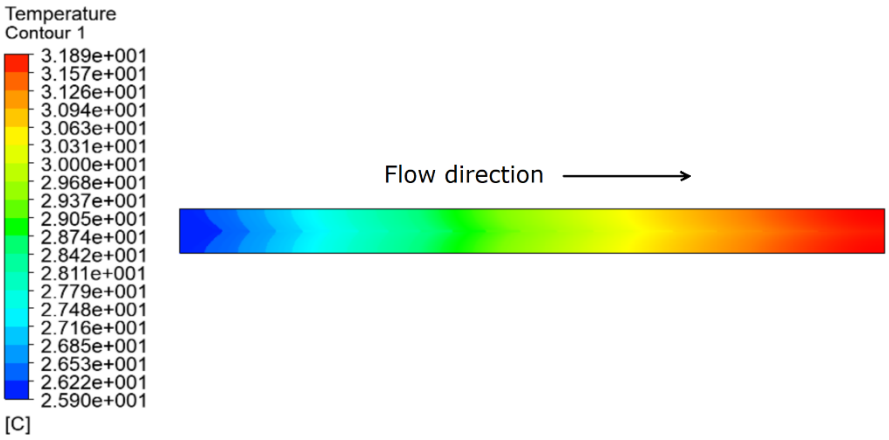


Figure 7.7 Temperature contour of the PV surface on the heatsink

Figure 7.7 shows the temperature contour of the PV surface. It can be seen from the figure that the temperature increases along the water flow direction. The maximum panel temperature is 31.8℃ near the outlet and the average PV temperature is 28.25℃. There is a 5℃ temperature rise along the flow direction, which is relevantly small. Considering the fact that PV panel without cooling will reach near 80℃ under the same condition, the thermal management of PV panel is significantly improved by using water cooling. Another transient simulation of the same initial condition indicates the PV temperature becomes steady in less than 1 hour, which means the water flow is more than sufficient to maintain PV at cooler temperature during maximum solar loads. Another three runs of the model with lower inlet velocity value of 0.05m/s, 0.02m/s and 0.01m/s shows

different results of PV temperature. The comparison is presented in Figure 7.8 below.

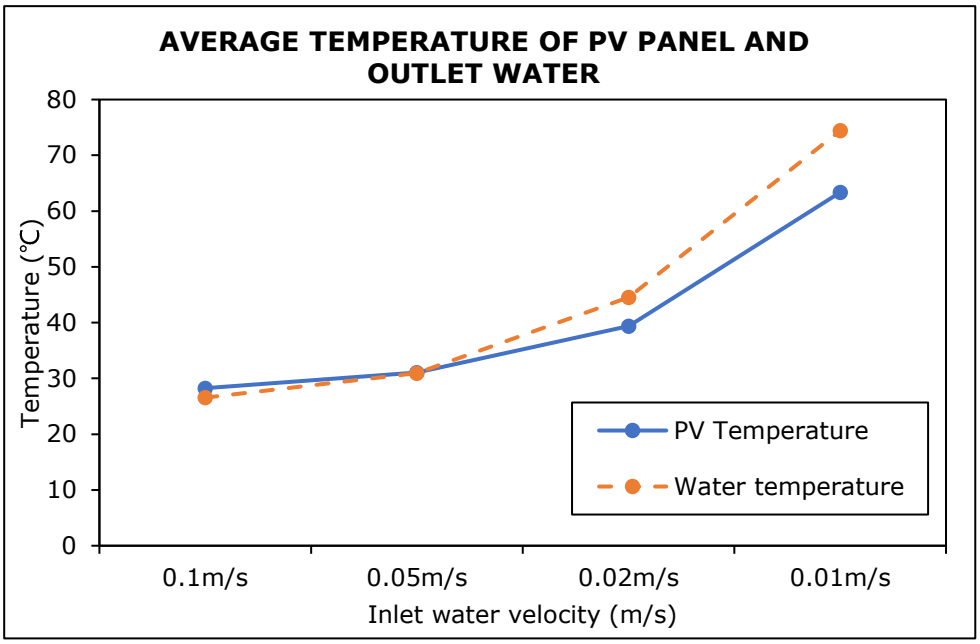


Figure 7.8 Average temperature of PV panel and outlet water

From the figure, it can be seen that by changing inlet water speed from 0.1m/s to 0.05m/s, there's a 2.8℃ rise in average PV temperature. However, if the inlet velocity is further reduced to 0.02m/s, the temperature increase of PV panels will become greater, at 8.56℃ after 5 hours. Results show that inlet velocities of 0.1m/s are 0.05m/s are adequate for cooling PV panel under maximum load, while on the other hand, there is a significant PV temperature increase at flow speed of 0.02 and 0.01m/s, which show the sign of accumulated heat stored on the PV panel. All the water outlet temperatures are higher than the melting temperature of PCM-HS22P which is 22℃, and hence can successfully trigger the phase change process.

7.4.2 PCM performance under maximum load

The 3D model of the divided PCM part has been built according to Figure 7.5 with dimension of 1183mm x 75mm x 61mm. The meshing contains 682028 elements and is adapted and examined to eliminate the effect of mesh element size against final results (RMSE <1%). The materials used in this case are PCM-HS22P and liquid water. The material of PCM storage panel has been set to PCM-HS22P, and the flow domain has been set to water. There are two specified boundary conditions in this model, water inlet, water outlet. The water inlet has been set to have an initial velocity of 0.1m/s at a constant temperature of 31℃, The initial temperature of the PCM is set to 20℃. At this stage, no additional fin is added.

Results and discussion

Figure 7.9 shows the temperature contour at the outlet end of PCM storage tank. It can be seen from the figure that even after 5 hours of maximum load, there is only a small fraction of PCM melted around the water pipe. At the same time, the outlet water temperature still stays relatively high, at range from 29.7℃ to 30.9℃. Considering the fact that the inlet temperature is only 31℃, which means most of the thermal energy carried along with the water flow is not efficiently stored in the PCM. In this case, fins must be added in order to enhance heat transfer between water and PCM.

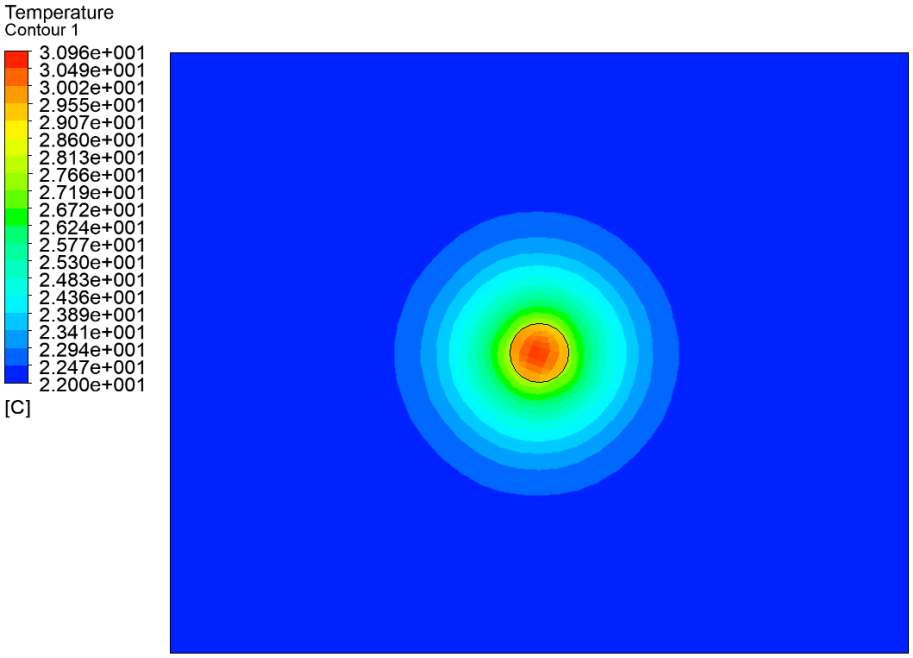


Figure 7.9 Temperature contour at the outlet end of PCM storage tank

7.4.3 Additional fin design

In order to increase contact surface area inside the PCM tank, an additional fin array has been added on the surface of the water pipe as shown in Figure 7.10 below. The fin surface is measured to be 61mm X 61mm and the thickness of the fins is 1.5mm with 15mm fin spacing based on the analysis presented earlier. In order to enhance heat discharging rate during nighttime using natural convection, the fin is also connected with the outer enclosure of the PCM panel, which is made by 3.5mm thick aluminium. In addition, an extra 1.5mm thick pipe wall has been added to the model, where in previous models there is only a surface acting as an interface between fluid domain and PCM. The results with/without additional pipe wall are still comparable by considering the fact that the boundary

interface without additional pipe wall acts like a surface with very high thermal conductivity.

Due to the fact that the sliced PCM panel section has wider width (75mm) compared to the height (61mm), there will be a small gap of 14mm without fins between two fin arrays. Such small un-finned volume is essential to prevent any uneven thermal expansion of PCM in real situations, as well as allow PCM to be poured into the PCM panel much more easily.

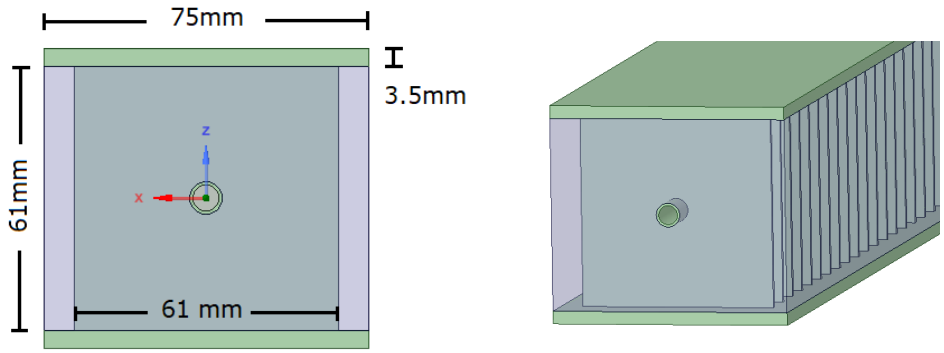


Figure 7.10 Dimension and placement of the added fin

The modified model has a total number of 3318566 mesh elements, and is adapted and examined to ensure mesh independency. The fin material is set to aluminium. The total volume of the fins is less than 0.003m^3 which replaces 7.8% of the PCM in the panel, however, the amount of PCM reduced could be neglected considering the fact that the preliminary PCM sizing is only a rough estimation. In addition, hourly simulation study presented in section 7.4.5 indicates that the reduced amount of PCM is still enough even under the hottest summer design day. All the other model setting criteria is the

same as previous model without fins, and the total simulation time is also set to 18000s.

Results and discussion

Figure 7.11 shows the temperature contour at the outlet end of PCM storage tank. It can be seen from the figure that although PCM temperature near the outlet section is much lower compared to the model without added fins, the outlet water temperature has dropped significantly compared to the previous model without fins, at around 25℃ which is 5℃ less. It is also noticed that there is only a little temperature difference between the centre position of the water pipe and the near wall position, which indicates that a more complete heat exchange has taken place.

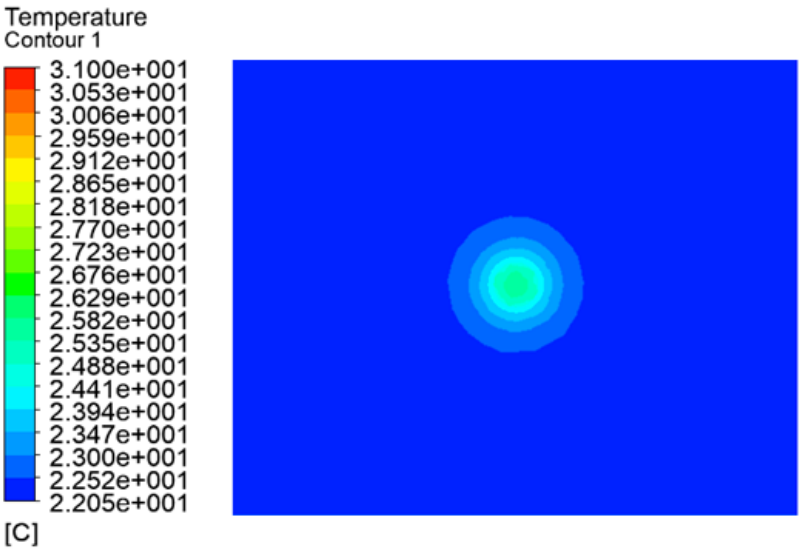


Figure 7.11 Temperature contour at the outlet end of PCM storage tank with added fin

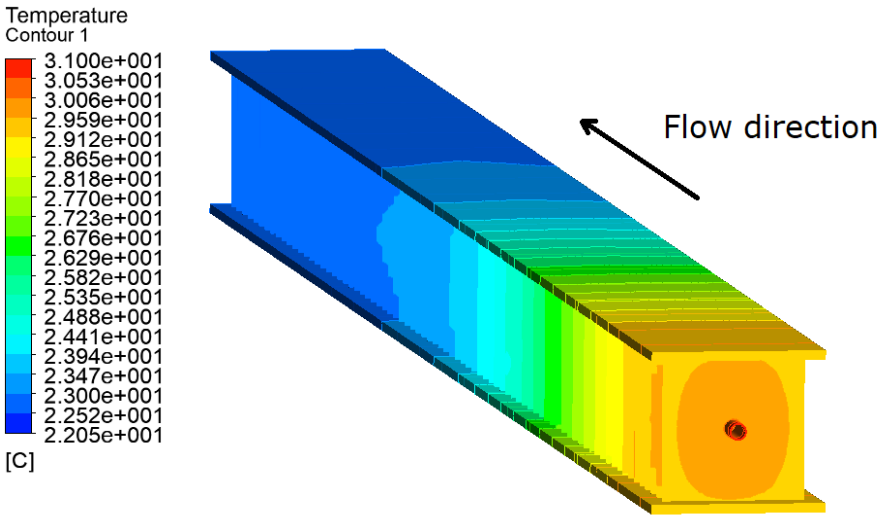


Figure 7.12 Temperature contour of added fins

Figure 7.12 shows the temperature contour of the added fin surface with flow speed of 0.1m/s at t = 18000s. It can be seen that the fin temperature drops gradually along the flow direction. The fin temperature near the rear portion is around 22℃, which indicates that a complete heat exchange process has taken place. The added fin allows the PCM to melt in a more desirable pattern (front portion melt first, and slowly spread towards rear portion). The melting pattern could be clearly seen in Figure 7.13 below.

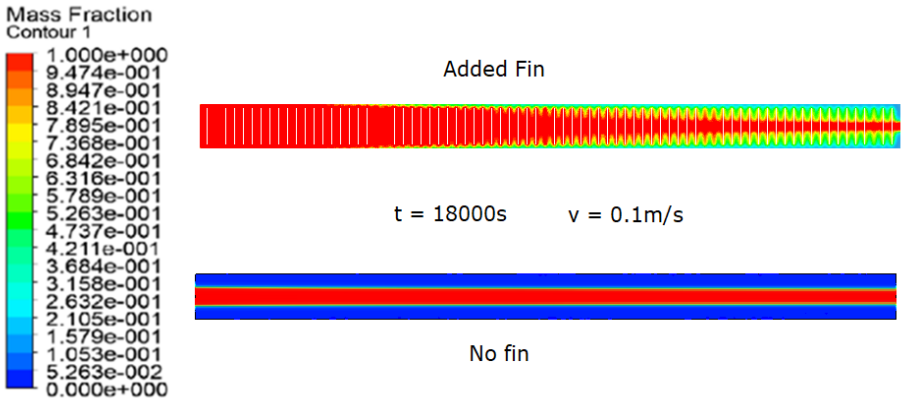


Figure 7.13 Comparison of melt fraction contour of the cross-sectional area of the PCM panel at time = 18000s

Figure 7.13 shows the PCM melt fraction contour of the cross-sectional area of the PCM tank at flow time = 18000s. It can be seen from the figure that the fraction of PCM melted in the model with added fins is significantly larger than the model without added fins. Without fins, the melted PCM is surrounding the water pipe, which further reduces the heat transfer process due to the low liquid phase thermal conductivity of PCM. As a result, the outlet water temperature is not reduced by much, which will cause the reduction of cooling efficiency if recirculated as inlet water for PV cooling. On the other hand, for model with added fins, the most part of melted PCM is located at the front portion near the inlet, while at the rear portion, despite of much lower water temperature, PCM around the fins is still melting slowly. The outlet water temperature is reduced significantly when compared to the inlet temperature which can be seen in Figure 7.11, which can be effectively reused for PV cooling. By comparison, the added fin is a significant improvement in heat transfer efficiency.

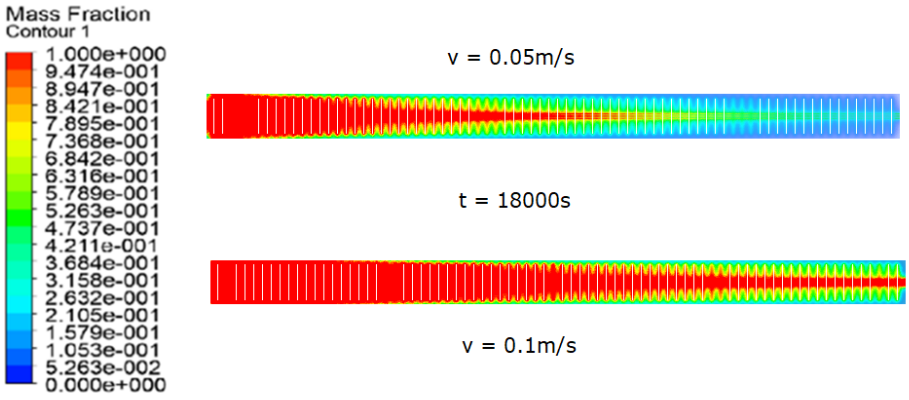


Figure 7.14 PCM melt faction contour comparison between two different inlet velocity settings

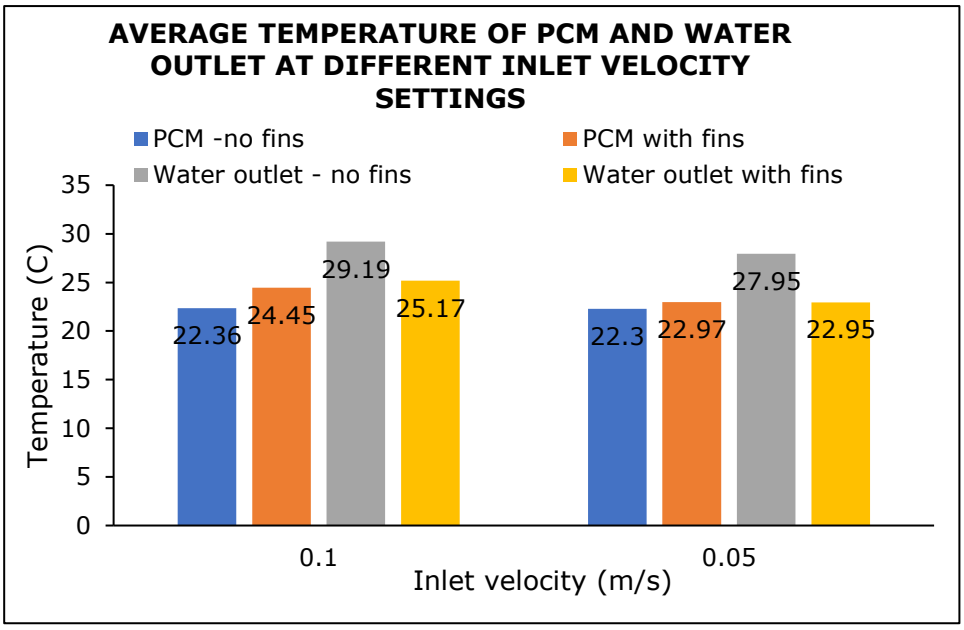


Figure 7.15 Comparison of average PCM temperature and water outlet temperature between model with fins and model without fins

Figure 7.14 shows the comparison of PCM melting fractions between two different inlet velocity settings. It can be seen from the figure that by changing the flow to 0.05m/s, there's less PCM melted during the 5-hour period, however, the water outlet temperature is dropped significantly, which is better when reused for PV cooling. Figure 7.15 shows the comparison of average PCM temperature and water outlet temperature between model with fins and model without fins. The result shows that there is a 1.48℃ decrease in PCM average temperature with added fins when flow speed is reduced to 0.05m/s, while the PCM temperature of model without fins is only decreased by 0.03℃. In both velocities, the model with added fins shows a more complete phase change process. it is obvious that the PCM stored far more amount of energy with added fin than without fins. While the average outlet temperature of the model without fin decreases about 1.24℃ with reduced speed, both values are still considered to

be significantly higher than the average outlet temperature of the model with added fins. Considered the fact that PCM is not only used to store latent energy, but is also used as heat sink to cool recirculated water in the closed loop PVT-PCM system, hence the water flow speed of 0.05m/s has the best performance balance between PV and PCM side, and will be used in the hourly analysis in section 7.4.5.

7.4.4 PVT-PCM pump sizing

In order to effectively circulate the water within the water pipes, additional pump is needed. It can be calculated that at optimum flow velocity of 0.05m/s, there is a total water volume flow rate requirement of 35l/h. Due to the fact that the PVT system uses closed loop water cooling, the hydraulic head is small enough to be neglected, and the minimum pumping power needed was calculated at 0.002W per module (0.62m^2 PV panel with associated PCM storage). The detailed pump power calculation has been presented in section 6.3.1.

7.4.5 Hourly analysis – daytime

Simulation procedure

To simulate the whole PVT-PCM system under hourly load and evaluate the end of the day performance, both PV and PCM models will be run in sequence. For each hour, the predicted PV

outlet temperature is transferred as PCM water inlet temperature, and the PCM water outlet temperature is the PV water inlet temperature at the following second (as Figure 7.16 shown below). The water velocity is set to 0.05m/s. The simulation starts 4:00 in the morning in summer condition and 9:00 in winter condition, and is run throughout the day. The initial temperature of PCM is set to be the same as the ambient temperature at 4:00 in summer and 9:00 in winter. The ambient temperature and solar radiation data are updated hourly, as preliminary simulations indicate that using smaller timestep sizes has negligible improvements on final results due to the very consistent temperature of PCM outlet water under a given load (shown in Figure 7.17).

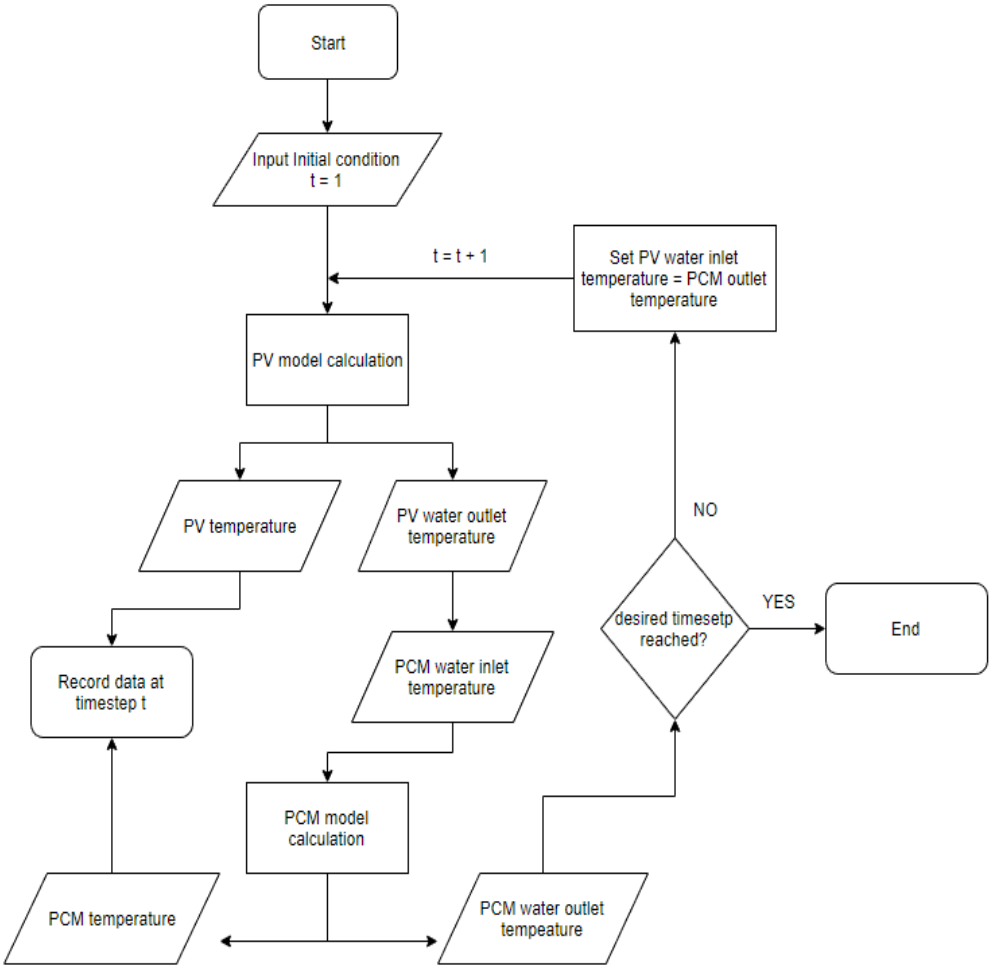


Figure 7.16 Flow chart of the hourly simulation process

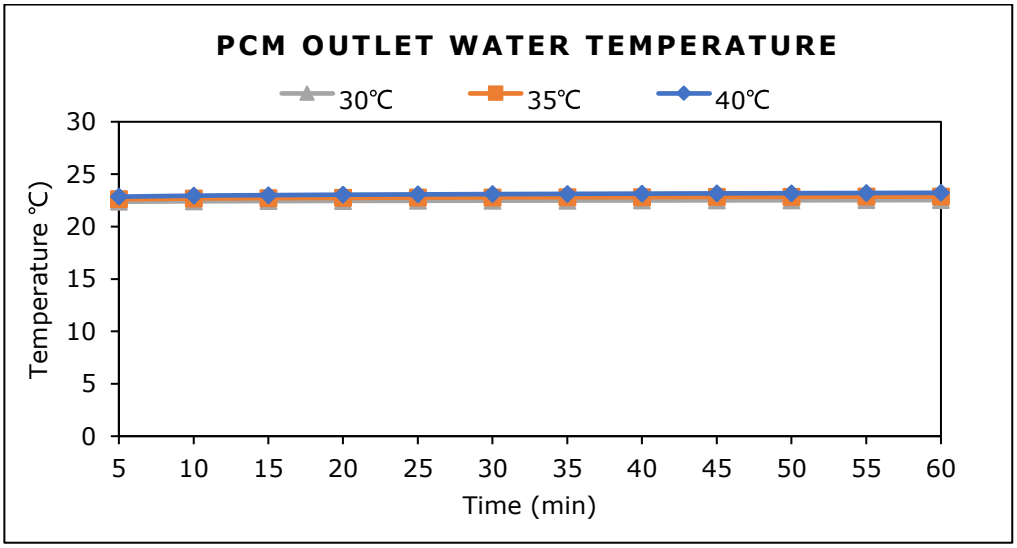


Figure 7.17 PCM outlet water temperature under different inlet temperature settings.

- Summer design day

Figure 7.18 shows the daily maximum temperature contour of PV temperature at 12:00. The average temperature of the panel is 32.09℃ with peak cell temperature measured at 35.72℃. There is 9℃ temperature variation along the flow direction as the water temperature increased during the flow. However, considering that the PV only system reaches 68.76℃ under the same environmental condition, there is a massive 36.67℃ reduction in PV cell temperature. Due to the fact that the PVT system is working as a closed loop system, there is no heat exchange to the outside environment, hence the panel temperature is independent with the variation of ambient temperature.

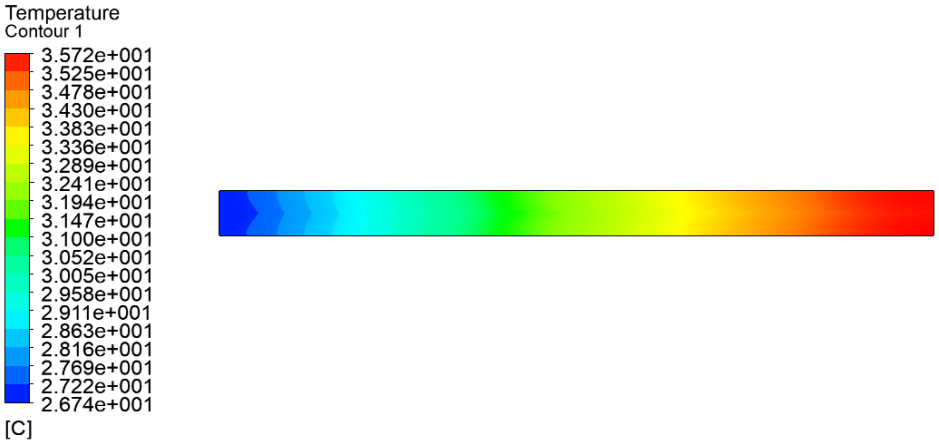


Figure 7.18 Daily maximum temperature contour of PV temperature at 12:00 (summer)

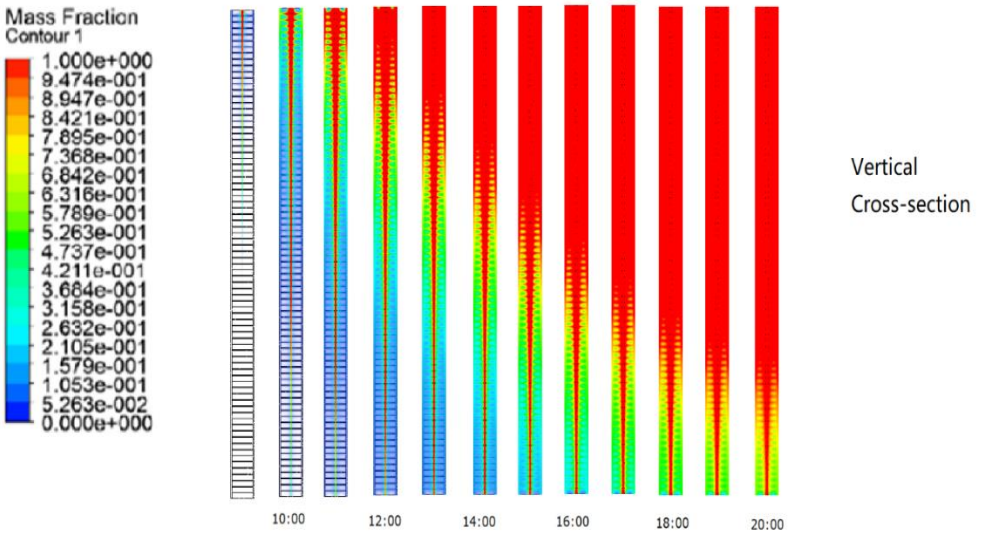


Figure 7.19 Hourly liquid fraction contour of the vertical and horizontal cross-sectional area of the PCM storage panel (summer)

Figure 7.19 shows the hourly temperature contour of the cross-sectional area of the PCM storage tank during the daytime charging period. It can be seen from the figure that the PCM gets heated up slowly and stays in solid phase during early morning. The first part of PCM starts to melt at temperature over 22℃ near the water inlet section between 8:00 – 9:00. The melting process is slowly spreading along the flow direction to the rear section after that. The first portion of fully liquified PCM appears around 11:00, and the liquid phase PCM is spreading along the flow direction with increased time. It can also be seen that the melting speed of PCM is the fastest during the midday while solar insolation level is high (> 800W/m^2). Towards the end of the day, the PCM melting speed is reduced after 16:00 due to the reduced solar insolation level. By the time of 20:00, most of the PCM are fully melt, with a small portion of PCM near the water outlet still in phase change process, and the phase change process is towards the liquid phase (liquid fraction >50%).

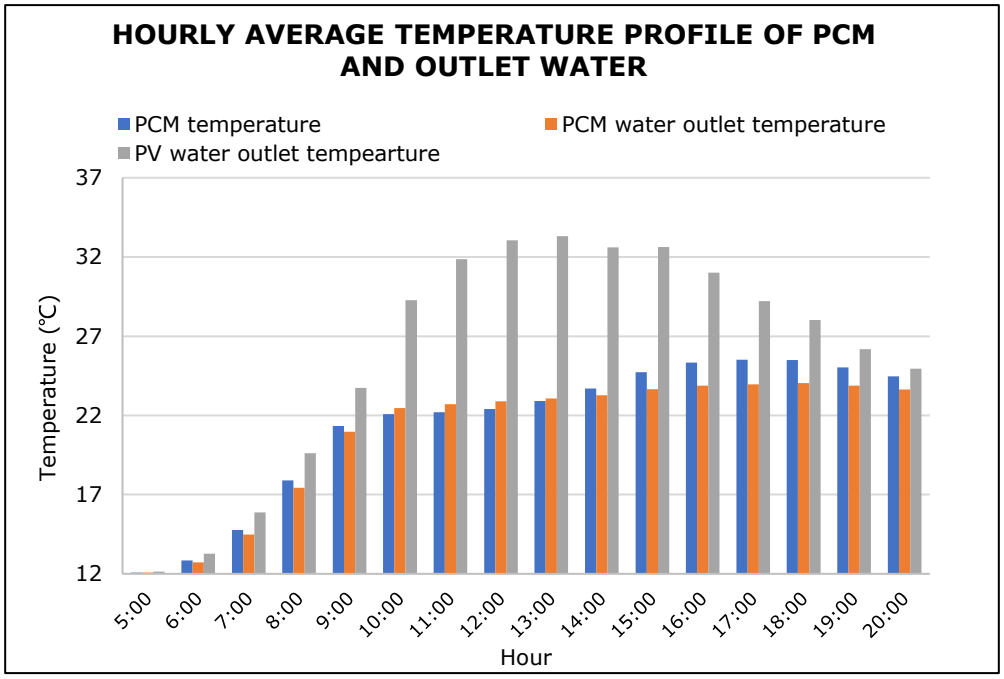


Figure 7.20 Hourly average temperature profile of PCM and the outlet water (summer)

Figure 7.20 shows the hourly average temperature profile of PCM and the outlet water during daytime charging period. It can be seen from figure that the temperatures of both PCM and PCM water outlet start to rise rapidly in early morning, and are both reached over 22℃ at 10:00. After that, the temperature change becomes very stable and the relative temperature difference in the rest of the day is less than 3℃. On the other hand, the outlet water temperature from PV panel rises significantly with increased solar insolation level. However, the water outlet temperature from PCM panel during the day is able to be kept below 24℃, which indicates the adequate thermal performance of PCM as a heat sink. It is also noticed that from 18:00 to 20:00, the average temperature of both PCM and outlet water start to decrease slightly, this is due to the reason that as the water inlet temperature decreases, the high

temperature (super-heated) portion of PCM near water inlet is disappearing as sensible energy is taken away by water to the PCM with lower temperature at the rear portion and is stored there as latent heat, which lowers average temperature slightly.

- Winter design day

Figure 7.21 shows the temperature contour of the PV panel temperature at 16:00. The average panel temperature is observed to be 16.21℃. It can be seen that the temperature difference along the flow direction is much smaller when compared to the summer design day, at 1.69℃. This is due to the lower solar insolation level during winter period.

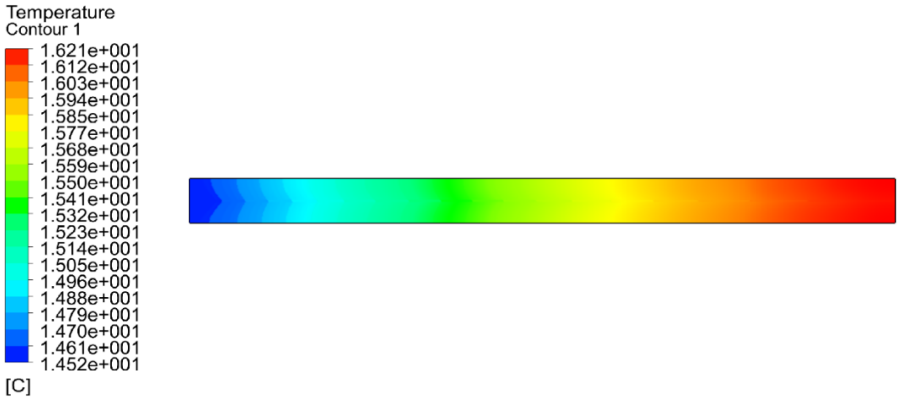


Figure 7.21 Daily maximum temperature contour of PV temperature at 16:00 (winter)

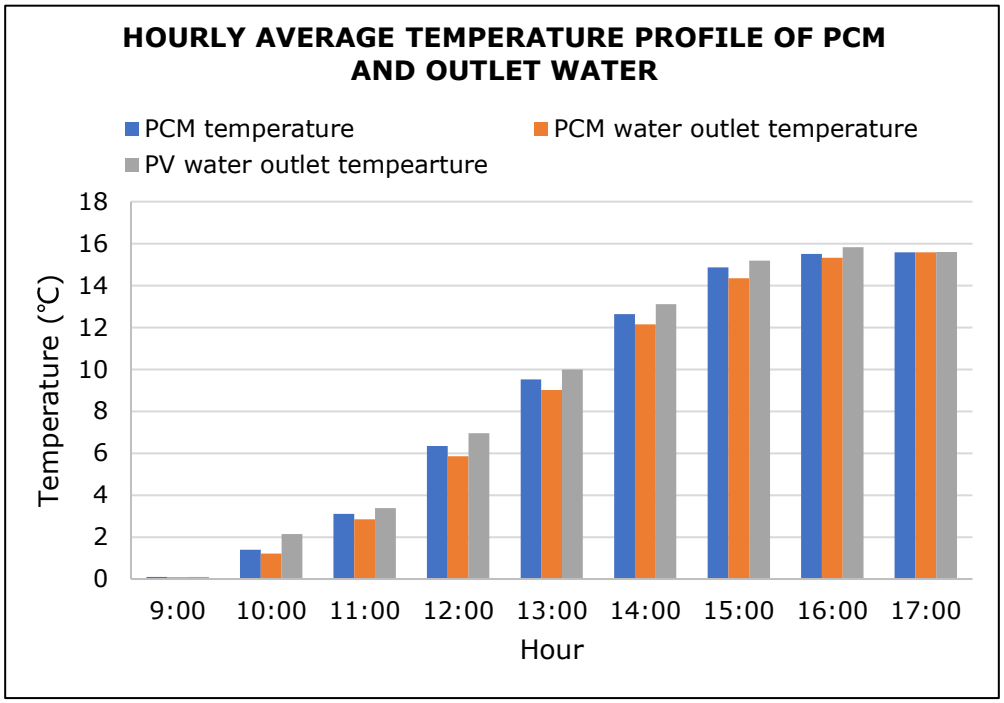


Figure 7.22 Hourly average temperature profile of PCM and the outlet water (Winter)

Figure 7.22 shows the hourly temperature profile of PCM and outlet water during the daytime charging period. It can be seen that the PCM temperature rises from 0℃ to 15.6℃ during the daytime. The difference between PV outlet water temperature and PCM temperature is small due to the low solar insolation level in winter time. The PCM is not melt and the heat is stored as sensible heat.

7.4.6 Ability of PCM self-heat dissipation

The latent heat stored during the daytime can be utilized by multiple ways during night, however, in extreme situations while heat utilization is not possible, it is essential that the system itself could dissipate enough heat using natural convection in order to prevent PV panels from overheating during the next daytime cycle. In this case, it is assumed that

no heat is utilized during the night, hence the PCM storage panel needs to be cooled by natural ventilation only after 20:00. The PCM is assumed to be fully melted with temperature of 23℃. The average wind speed is set to 5m/s according to the Nottingham's climate data.

Results and discussion

Figure 7.23 shows the liquid fraction contour of the horizontal and vertical cross-sectional area of the PCM panel. It can be seen from figure that at 5:00 in the morning, the PCM is still not fully solidified. However, as another daytime working cycle starts, the damper is still opened so that the natural convection continues to cool the PCM panel due to the low ambient temperature in the early morning. By comparing with Figure 7.18, it can be seen that at time of 11:00, the comparison of two melting contours of PCM is identical, which means the excess amount of heat is successfully dissipated and hence there is no overheating possibility. The damper on the enclosure of the PCM panel could be closed and the whole PVT-PCM system is resumed to the normal working condition.

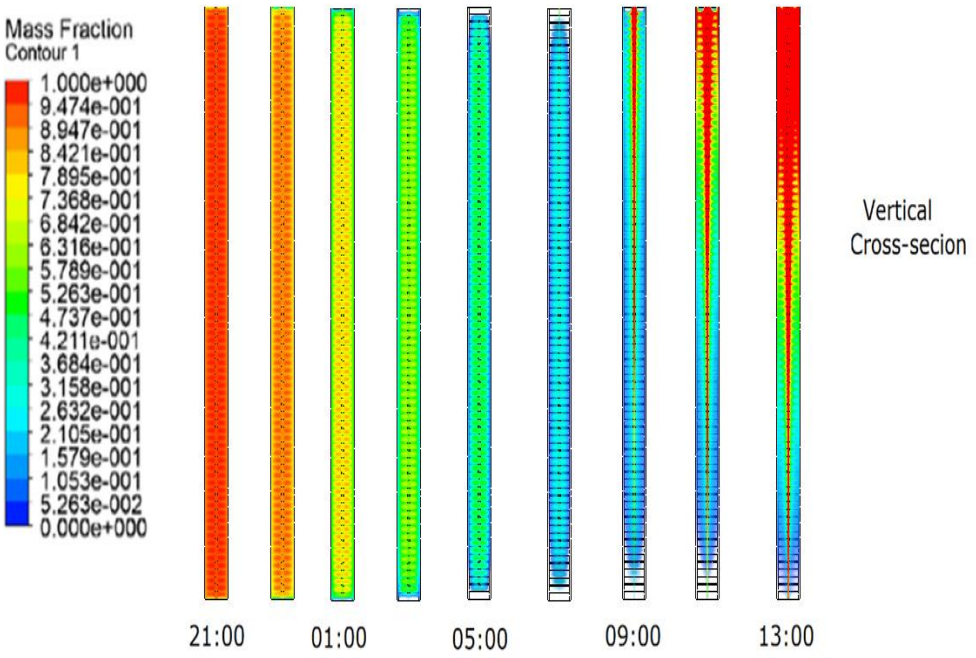


Figure 7.23 Hourly liquid fraction contour of the cross-sectional area of the PCM storage panel during summer night time.

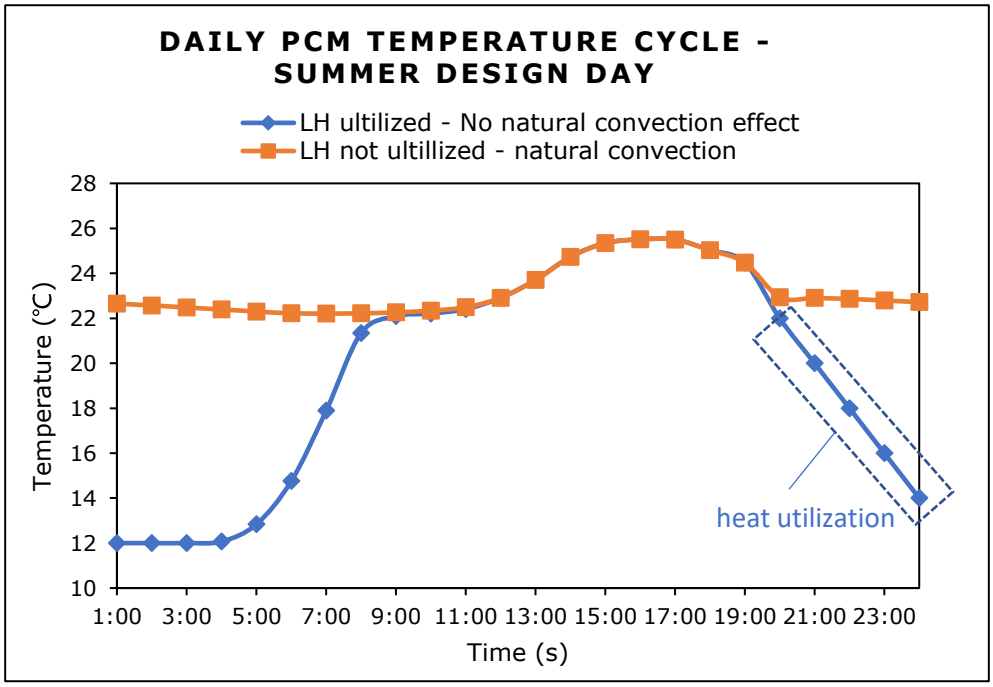


Figure 7.24 PCM temperature comparison of the two working modes with/without latent heat utilization

Figure 7.24 shows the PCM temperature comparison of the two working modes where latent heat is dissipated either by utilization or natural convection. It can be seen that although the solidification process of PCM by natural convection is extremely slow, the whole system is still managed to perform the normal daytime working cycle. The PCM temperature difference between two situations becomes minimal at 08:00, thus the overall PV performance during the day will not be affected by much. It should be noted that the marked heat utilization rate is just for illustration only, as actual heat utilization rate is heavily dependent on actual system configuration which will be discussed in Chapter 8. It is certain that no matter how slow the heat utilization rate is, the temperature of PCM at the start of next working day is lower than the yellow line (no utilization at all), which means no potential overheating will happen on the next working day no matter whether the stored heat is utilized or not, and how fast the heat is utilized.

Considering the fact that the summer design day represents the maximum solar load and the highest ambient temperature profile, thus it can be proved that the proposed PVT-PCM system can work effectively without overheating issues in the UK.

7.5 Performance comparison

7.5.1 PV panel thermal management

Summer design day

Figure 7.25 shows the comparison of panel temperature between PV only and PVT-PCM system under windy conditions. The PVT-PCM system enters daytime working cycle as water circulation pump switched on at sunrise. The daytime working cycle stops at 20:00 when water pump stop circulating at sunset. It can be seen from the figure that despite the 5m/s wind provides good amount of cooling for the PV only system, with a maximum panel temperature of 43.3℃ at 13:00, the PVT-PCM system still has better thermal performance, with a significantly reduced peak panel temperature of 32.3℃ at 13:00 under the same condition. It is noticed that at 19:00, the PV cell temperature of PVT/PCM system is higher than the PV only setup, this is due to the fact that while the circulation pump is still on, the PV panel has been kept at same temperature as PCM, and the PCM is nearly fully charged at the end of the daytime (water temperature~24℃). On the other hand, the PV only system doesn't have active circulation, and the temperature drops closely to ambient as the solar insolation level is low at 19:00. The PV cell temperature of PVT-PCM and PV only setup both drops to the same as ambient temperature after sunset at 20:00.

The cell temperature sensitivity to the environmental condition of the PVT system is much lower compared to the PV only setup, which results in the steadier temperature profile across the day. The maximum temperature difference between PV only and

PVT set up occurs at 13:00, at around 11.6℃. The advantage of lower cell temperature is the improved conversion efficiency from solar energy to electricity, as well as the reduced degradation of crystalline silicon modules and hence the extended life cycle.

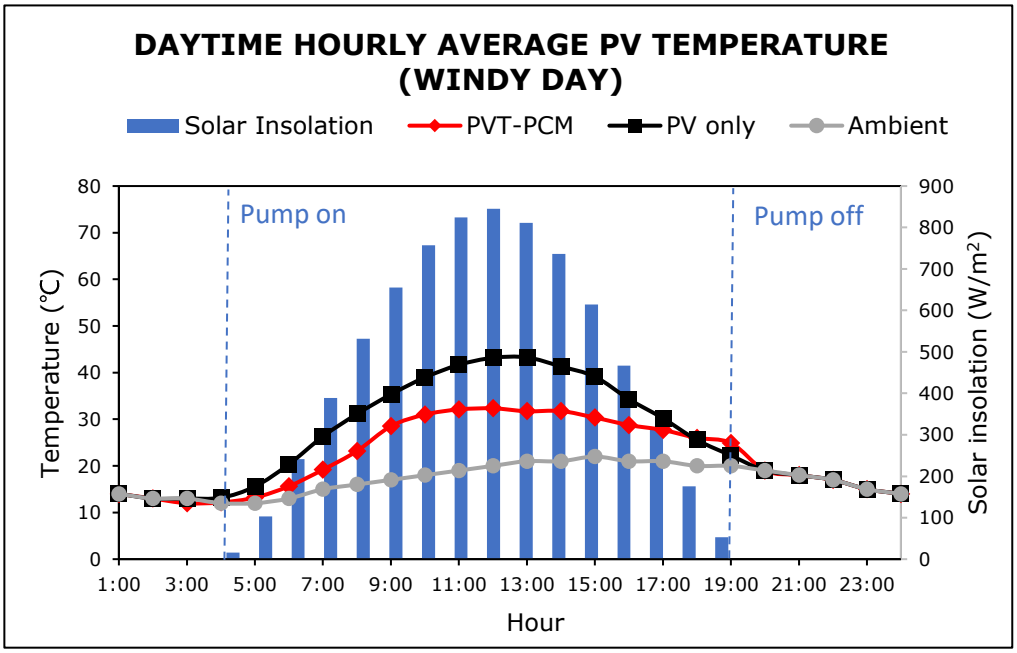


Figure 7.25 Summer time hourly average PV temperature comparison (Windy day)

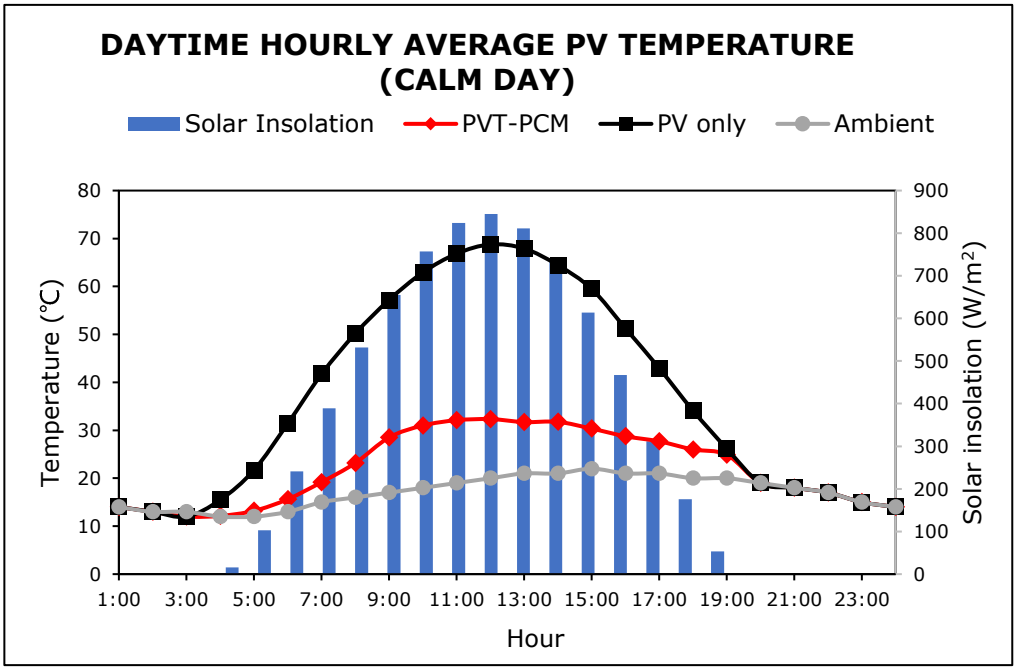


Figure 7.26 Summer time hourly average PV temperature comparison (Calm day)

Figure 7.26 shows the comparison between PV only and PVT-PCM system under minimal wind conditions. It can be seen that the PV only setup suffers from significant overheat issue with a peak cell temperature at 7838℃ at 13:00. On the other hand, the PVT-PCM system solves the overheating problem related with the lack of natural convection completely, with a significantly reduced peak cell temperature of 32.3℃. The maximum temperature difference is 36.5℃ between two systems. The serious overheat problem of PV only setup will not only significantly lower the photovoltaic efficiency and shorten the panel's life cycle, but also cause potential damage to frameworks and surrounding building structures. It should also be noted that the performance of PVT-PCM system is independent of the ambient temperature fluctuation during daytime due to the use of water circulation and PCM heat sink. As a result, the daily system performance is very stable under various climate conditions. It is considered that the PVT-PCM

system is significantly superior regarding to the ability of regulating PV cell temperature, in both windy and calm weather conditions.

Winter design day

Figure 7.27 shows the winter design day temperature comparison of the PV only setup against PVT-PCM system in windy condition. Similarly, the PVT-PCM system enters daytime working cycle as water circulation pump switched on at sunrise. The daytime working cycle stops at 16:00 when water pump stop circulating at sunset. It can be seen from the figure that the temperature rise of PVT-PCM is slower than the PV only setup due to the low PCM temperature. The peak panel temperature of PV only setup occurs at 12:00 with the temperature value of 11.5℃, while the peak panel temperature of PVT-PCM system occurs at 16:00 with the temperature value of 15.5℃. It is noticed that the PV only setup shows lower PV cell temperature after 13:00, this is due to the nature of closed loop system as PCM is still in charging process, while PV only setup uses passive cooling and is kept cooler under low solar insolation level and low ambient temperature. Although the PV only setup up shows lower panel temperature in the afternoon, the overall electrical performance difference of the two setup is nearly identical. The detail electrical performance comparison of will be presented in section 7.5.2.

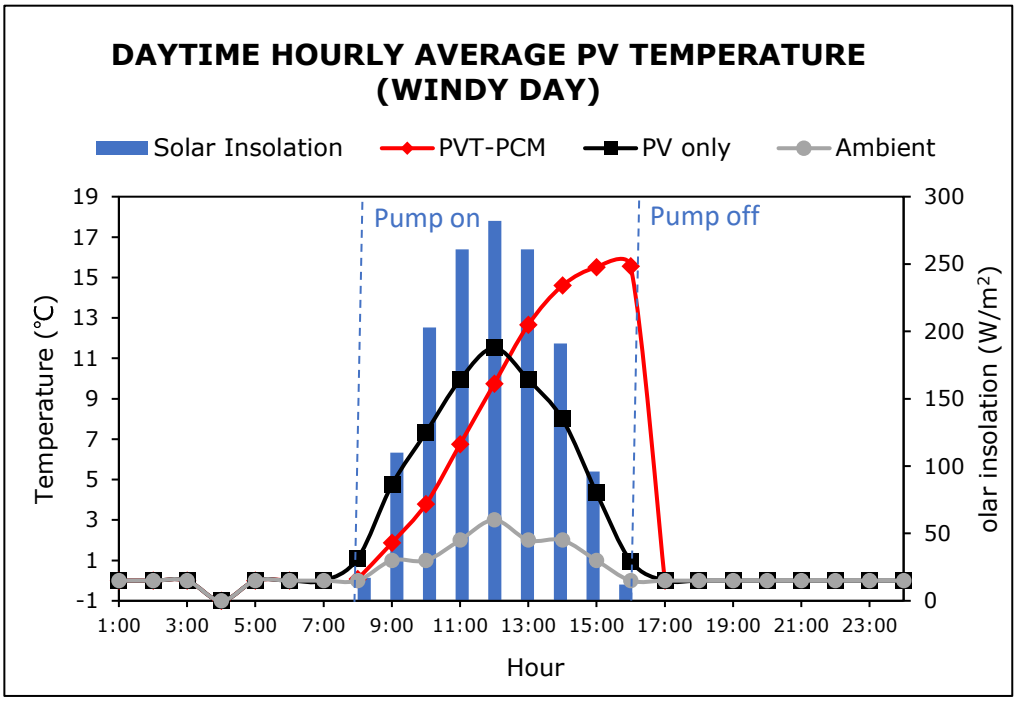


Figure 7.27 Winter time hourly average PV temperature comparison (Windy day)

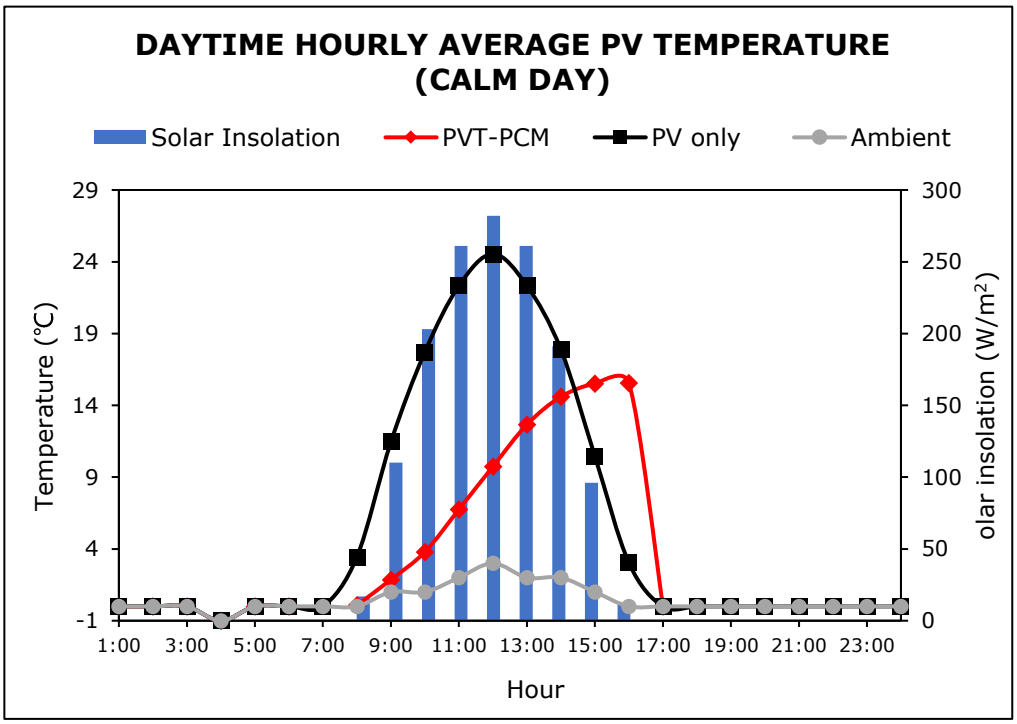


Figure 7.28 Winter time hourly average PV temperature comparison (Calm day)

Figure 7.28 shows the winter design day temperature comparison of the PV only setup against PVT-PCM system in

minimal wind condition. It can be seen that without the aid of natural convection, the peak panel temperature of PV only setup reaches 24.6℃ at 12:00, while the PVT-PCM system could maintain a lower panel temperature with a peak value of 15.5℃ at 16:00.

7.5.2 PV electrical performance

Summer design day

The electrical efficiency of PV panel is affected by cell temperature, and the correlation used to calculate temperature dependent electrical output is presented and discussed in chapter 4. The temperature dependent power rating of both system in summer design day condition is shown in Figure 7.29 and 7.30 below.

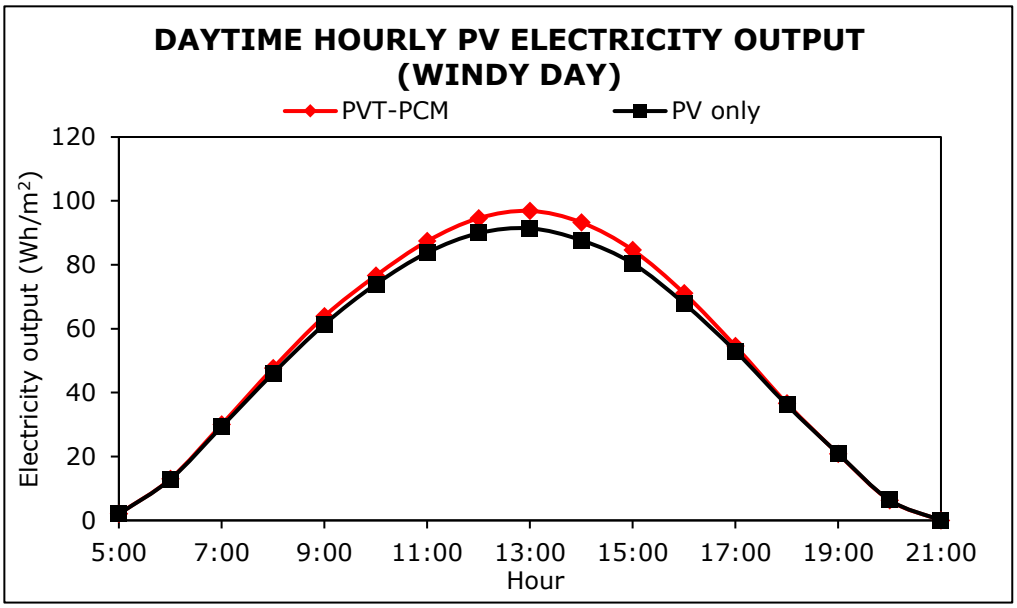


Figure 7.29 Summer time hourly PV electricity output comparison (Windy day)

Figure 7.29 shows the hourly electrical output ratings of the PV panel used in PVT-PCM and PV only setup in windy conditions. It can be seen that the electrical performance of PVT-PCM system is more efficient when compared to the PV only model. The peak power output of PV only setup is observed at 91.41Wh/m^2 at 13:00, while the peak power output of PVT-PCM system is 96.87Wh/m^2 at 13:00. The difference is small during early morning and late afternoon, but is increased to about 7% during the mid of the day where the ambient temperature and solar radiation are both at maximum level. The PVT-PCM system can have 4.3% increased power output at the end of the day compared to the PV only setup (879.26Wh/m^2 versus 843.05Wh/m^2) in windy days.

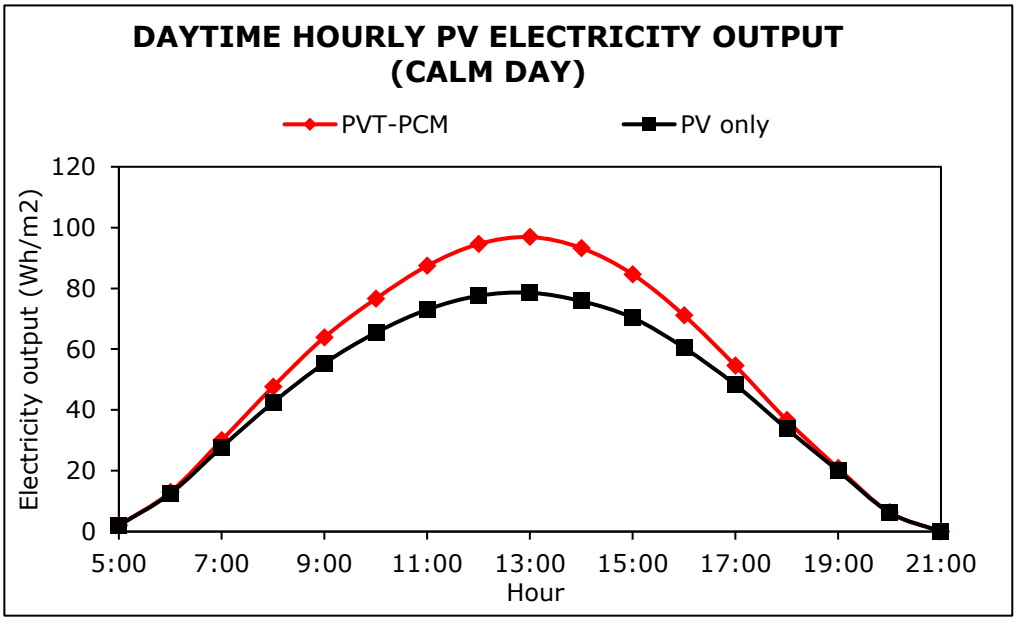


Figure 7.30 Summer time hourly PV electricity output comparison (Calm day)

Figure 7.30 shows the hourly electrical output ratings of the panel in minimal wind conditions. The electrical performance of

PV only setup is significantly reduced due to excess amount of accumulated heat on the surface of the Panel. The maximum performance dip happens at 12:00, at 86% compared the windy conditions for the PV only setup. The peak electrical output of PV only setup is observed at 78.55Wh/m^2 at 13:00, while the peak power output of PVT-PCM system is 96.87Wh/m^2 at 13:00. The PVT-PCM system can have 17.4% more power output at the end of the day compared to the PV only setup (879.26Wh/m^2 versus 749.40 Wh/m^2) in calm days.

It is hence to be concluded that the PVT system has much higher electricity output efficiency compared to conventional PV only setups and can withstand extreme hot weather conditions without affecting electrical performance.

Winter design day

On the other hand, the hourly PV electricity output comparison in winter design day condition is shown in figure 7.31 and 7.32 below. It can be seen from figure 7.30 that in windy conditions, the electrical performance of PVT-PCM system and PV only setup is very similar. The peak performance of PVT-CPM system can be obtained at 13:00 with an electricity output of 36.12Wh/m^2, while the peak performance of PV only system is 35.82 Wh/m^2. The PVT-PCM system has 0.5Wh/m^2 lower power output compared to the PV only setup at the end of the day, however, the reduction in electrical power output is negligible (less than 0.5%) compared to the total power output of the day (184.45Wh/m^2)

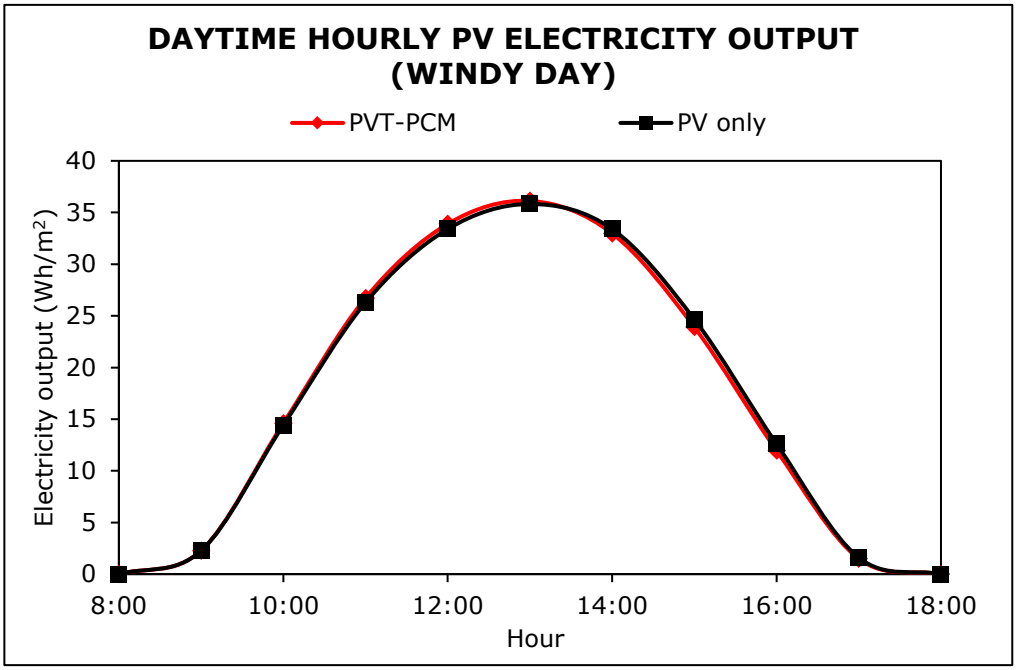


Figure 7.31 Winter time hourly PV electricity output comparison (Windy day)

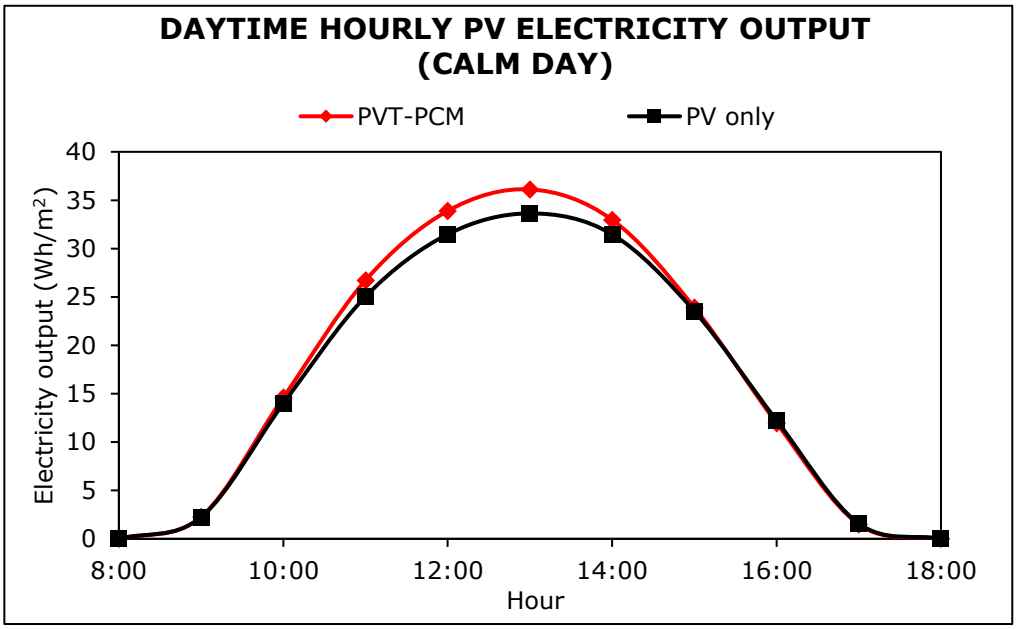


Figure 7.32 Winter time hourly PV electricity output comparison (Calm day)

In conditions where there is minimal wind, the advantage of PVT-PCM system becomes more obvious. The peak electrical performance of PV only setup drops to 34Wh/m^2 at 13:00 due to the increased panel temperature, while the PVT-PCM system could achieve 36.12Wh/m^2. The PVT-PCM system can have 5%

more power output at the end of the day compared to the PV only setup (183.96Wh/m^2 versus 175.21W/m^2) in calm days.

Considering the fact that the additional power required for the pump is very small (<0.1W per module), the performance comparison of two system in winter design day shows that the PVT-PCM system still has its advantage over traditional PV only setup even in extremely cold conditions.

7.6 Energy saving potential of PVT system

Table 7.3 below shows the energy saving potentials of the PVT-PCM system compared with conventional PV only system. It can be seen that in summer design day, every 1m^2 PVT-PCM module can output 152.92Wh more electricity compared to the PV only setup in minimal wind conditions, after considering the additional pump energy consumption. In windy conditions, the difference in electricity output is smaller, at 44.92Wh per day, but it still proves that the PVT-PCM system has superior performance over PV only setup even in windy conditions. After taking into account the potential latent energy stored by the PCM system, the difference becomes significantly larger, at 5499.92Wh/day and 5391.92Wh/day depending on weather conditions.

On the other hand, when operating in winter design day conditions, the electrical performance gain of every 1m^2 PVT-PCM system is much smaller, at 10.35Wh/day in minimal wind condition and -0.15Wh/day in windy condition. However, after

considering the thermal energy stored in PCM, the difference becomes 1027.35Wh/day in minimal wind condition and 1016.75Wh/day in windy condition.

Table 7.3 Energy saving potentials of the PVT-PCM system compared with PV only system

Summer design day	**Calm**			**Windy**		
(Wh/m^2.day)	PVT	PV	Difference	PVT	PV	Difference
Electricity output	879	749	130	879	843	36
Pump energy	-0.08	0	-0.08	-0.08	0	-0.08
Net electricity gain			129.92			35.92
Thermal energy	5347	0	5347	5347	0	5347
Total energy gain			5476.92			5382.92
Winter design day	**Calm**			**Windy**		
(Wh/m^2.day)	PVT	PV	Difference	PVT	PV	Difference
Electricity output	184	175.2	8.8	184	184.5	-0.5
Pump energy	-0.05	0	-0.05	-0.05	0	-0.05
Net electricity gain			8.75			-0.55
Thermal energy	1017	0	1017	1017	0	1017
Total energy gain			1025.75			1016.45

Table 7.4 Overall daily electrical and thermal efficiency

Summer	**Calm**		**Windy**	
	PVT-PCM	PV Only	PVT-PCM	PV Only
Electrical efficiency	**11.6%**	9.9%	**11.6%**	11.2%
Thermal efficiency	**71%**	0%	**71%**	0%
Winter	**Calm**		**Windy**	
	PVT-PCM	PV Only	PVT-PCM	PV Only
Electrical efficiency	**12.8%**	12.8%	**12.8%**	12.2%
Thermal efficiency	**71%**	0%	**71%**	0%

Table 7.4 shows the overall daily electrical and thermal efficiency for summer and winter design day. It can be seen that the PVT-PCM system could achieve daily electrical efficiency of 11.6% - 12.8% throughout a year, which is about the same as PV panel's nominal efficiency (11.9%), while the

PV only setup has reduced electrical efficiency range from 9.9% to 12.8%. The thermal efficiency of PVT-PCM system is 71% year-round, the limitation here is the thermal absorbance of PV panel.

From above analysis, it is considered that the PVT-PCM system has superior performance over conventional PV only setup throughout the year. The performance advantage increases with increased solar insolation level.

7.7 Cost analysis

In order to estimate the cost and benefit of the PVT-PCM system, a simple cost analysis is presented in this section. The total cost of the system could be divided into material cost, installation cost and maintenance cost.

- *Material cost*

The material cost of PCM could be determined as table 7.5 below. The price of PCM-HS22P can only be disclosed to bulk buyers at the moment according to the manufacture, hence the unit price is determined from an alternate source (Mickpeterson.org, 2017).

Table 7.5 Material cost of PCM

PCM-HS22P	Unit price	quantity	total price
	£/kg	unit	£
	3.7	70	259

The material cost of copper plate and copper pipe can be determined as table 7.6 below. The prices of the copper plate and pipe are acquired from current copper market value as well as from JTM Plumbing (JTM Plumbing, 2017).

Table 7.6 Material cost of Copper plate and pipe

Copper plate	Unit price	Density	Volume	Weight	Total price
	£/kg	kg/m^3	m^3	kg	£
	4.5	8960	0.00621	5.56	25.02
Copper pipe	**Unit price**	**Quantity**	**Total price**		
	£/m	unit	£		
	1.06	8.2	8.692		

The material costs of aluminium pipe and aluminium sheet can be determined as table 7.7 below. The price of aluminium pipe and sheet are acquired from MW Profiles (MW Profiles, 2017) and Rapid Lab (Rapid Fab, 2017).

Table 7.7 Material cost of aluminium pipe and sheet

Aluminium pipe	Unit price	Quantity	Total price
	£/m	unit	£
	0.99	8.2	8.118
Aluminium sheet 1.5mm	**Unit price**	**Total fin area**	**total price**
	£/m^2	m^2	£
	25	2	50
Aluminium sheet 3.5mm	**Unit price**	**Area**	**total price**
	£/m^2	m^2	£
	75	1.24	93

The material cost of water pump is based on a 2W pump acquired from Alibaba (Alibaba, 2017), as pump with power

rating smaller than 2W could not be found on the internet. The price of the pump is shown as table 7.8 below.

Table 7.8 Material cost of water pump

Water pump	Unit price	Quantity	Total price
	£	unit	£
	3	1	3

By knowing the material cost of each system component, the total additional material cost per m^2 could hence be determined as table 7.9 below.

Table 7.9 Total additional material cost of PVT-PCM (apart from PV)

PCM (£)	259
Copper plate (£)	25.02
Copper pipe (£)	8.69
Aluminium plate (£)	8.12
Aluminium sheet 1.5mm (£)	50
Aluminium sheet 3.00mm (£)	93
water pump (£)	3
Total (£)	443.83
Total cost per m^2 (£)	**714.61**

- *Yearly saving estimation*

The average performance of PVT-PCM system is assumed to be the average between maximum (summer design day) and minimum (winter design day) throughout a year. The average PV only performance is assumed to be the average of maximum (windy condition) and minimum (calm day condition) throughout a year. Assuming electricity is the only energy source, the yearly energy saving beneficial from

upgrading PV only to PVT-PCM system could be determined as table 7.10 below. It should be noted that if hot water or space heating is provided by alternate sources such as gas, the yearly cost beneficial will be affected accordingly.

Table 7.10 Yearly saving estimation

Average daily energy saving (kWh/m^2)	3.23
Number of days	365
Utility price (£/kWh)	0.13
Yearly saving (£/m^2)	**153.27**

- *Installation/maintenance cost and discounted payback period*

The installation and maintenance cost is assumed to be 50% of the total material cost. The annual discount rate and inflation rate is assumed to be 5% and 3% respectively. As a result, the yearly discounted cash flow could be calculated from table 7.11 below.

Table 7.11 Discounted payback period calculation

Year	**Cash flow (£)**	**Present value factor**	**Discounted cash flow (£)**	**Cumulative discounted cash flow (£)**
n	CF	PV=(1/1+0.08)^n	CF X PV	
0	-1071.92	1.00	-1071.92	-1071.92
1	153.27	0.93	141.92	-930.00
2	153.27	0.86	131.40	-798.59
3	153.27	0.79	121.67	-676.92
4	153.27	0.74	112.66	-564.27
5	153.27	0.68	104.31	-459.95
6	153.27	0.63	96.59	-363.37
7	153.27	0.58	89.43	-273.93
8	153.27	0.54	82.81	-191.13

9	153.27	0.50	76.67	-114.45
10	153.27	0.46	70.99	-43.46
11	153.27	0.43	65.73	22.27
Total payback period (year)			**10.67**	

From the cost analysis, the calculated total payback period is 10.67 years. However, in real life the payback period may vary significantly due to various reasons such as different location, different installation and different method of latent heat utilization.

Considering the fact that the material costs of most system components are based on individual order price, the future cost could be reduced if parts are ordered in larger quantities. Moreover, since the cost of PCM takes the most significant part of the overall cost, the payback period could also be significantly reduced by the future mass production price drop of PCM as currently PCM is only prepared on demand by a few manufacturers.

7.8 Summary

In this chapter, the performance of the proposed PVT-PCM system is analysed and compared with conventional flat plate PV panels. From the analysis, it can be seen that the PCM can effectively manage the PV cell temperature without any additional cooling. The added fins inside PCM panel has significantly enhanced the whole system performance, hence it is a vital part to ensure sufficient heat transfer rate to and from the PCM.

The results are clear from the comparison that the PVT-PCM system has superior performances from both electricity generation and thermal storage perspective. During summer design day conditions, the cell temperature of PV panel is 1.8 times lower compared to the PV only setup, and in extreme weather conditions where there is minimal wind, the cell temperature difference is increased to 3 times. The reduction of cell temperature results to an increased photovoltaic performance of 44.93Wh/m^2 (5.38% improvement) per day in windy conditions and 152.93Wh/m^2 (21.06% improvement) per day in minimal wind conditions. Even during the coldest winter day, the PVT-PCM system still managed to have better overall performance. The thermal efficiency of PVT-PCM is consistent at 71% throughout a year while PV only setup is 0. The additional cost of the PVT-PCM solution compared to PV only setup could be recovered in an estimated payback period of 10.67 years. The payback period of the proposed PVT-PCM system could be much less in mass production.

CHAPTER 8. POTENTIAL HEAT UTILIZATION – CASE STUDY

8.1 Introduction

As one of several advantages of PVT-PCM system, the amount of latent heat stored by PCM panels is quite significant, thus it is worth studying the potential ways to utilize this amount of energy. The biggest problem of PCM thermal storage solution, compared to conventional PVT solution, is that the temperature of charged PCM is much lower compared to the heated water using additional solar collector, hence it is insufficient to provide direct heating from the PCM material. Thus, the idea of the latent heat recovery is to introduce two-stage heating rather than conventional single stage heating. The concept of two stage heating is to add preheating stage provided by PCM before conventional boiler or air-con unit, and hence offset the heating energy consumption.

Figure 8.1 shows the PVT-PCM configuration used for this case study. The example house is located in Nottingham, UK, and is installed with a 1.5kW rated solar panel array. The whole system contains 20 individual modules of 75W unit which was studied in previous chapters. The PCM modules could be configured either as a series of modular panel or a combined panel. Figure 8.2 shows some sample configurations of 20 PCM panels. In this study, the combined panel option will be used.

Instead of 20 separate PCM storage panels, they are combined into a single PCM storage panel which has the dimension of 5915mm x 2100mm x 61mm (5 x 4 array of the single unit). The reason to combine the separate PCM panel into one large panel is to reduce material and installation cost in practical situations. The PCM panel is placed above ceiling inside a ventilation channel in order to ensure sufficient natural convection when needed (as shown in Figure 8.3). The PCM panel is charged during the daytime, and can thus be used for air and water preheating.

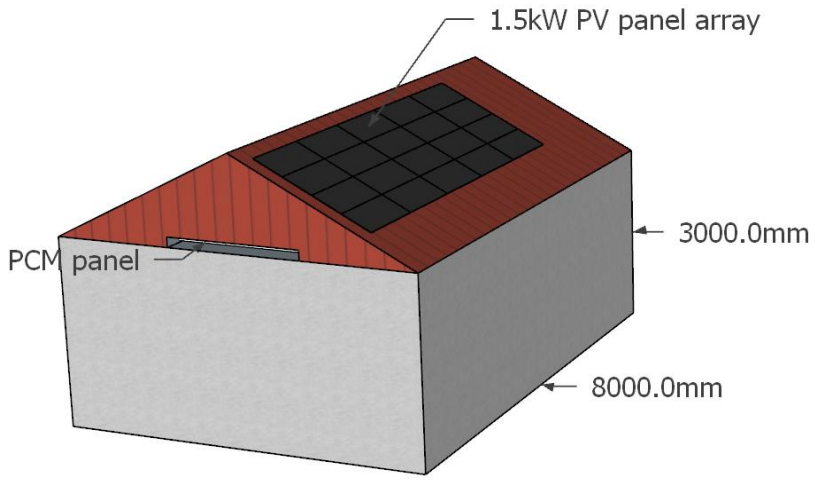


Figure 8.1 A sample configuration of PVT-PCM system used for the case study

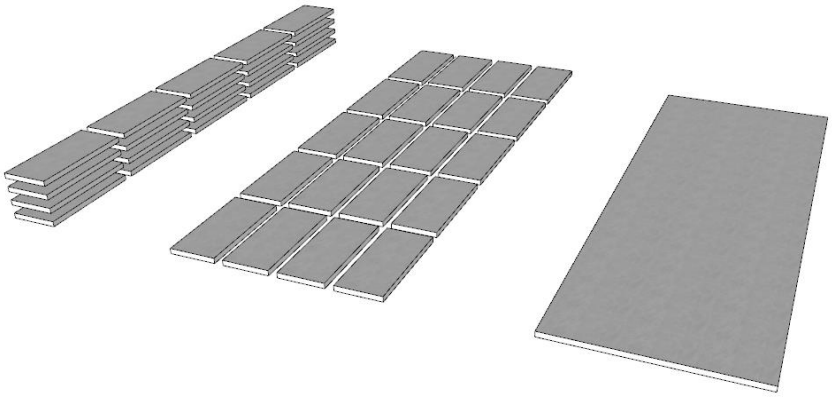


Figure 8.2 Sample configurations of PCM modules (stacked modular panel, 4 x 5 modular panel and 4 x 5 combined panel)

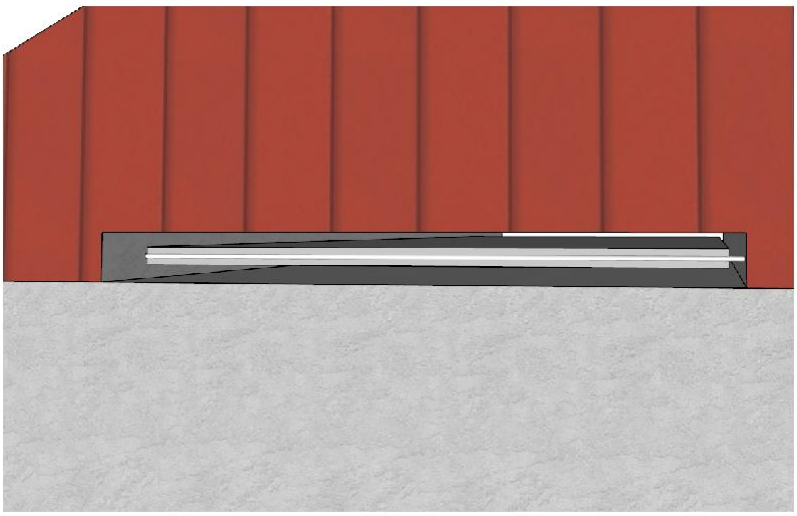


Figure 8.3 Detailed vie of PCM panel inside the ventilation channel

Additionally, in situations where air preheating is not required, the PCM panels could be combined as a thin layer and placed under the floor. By doing so, the PCM panels could act as an additional insulation, while at the same time provide moderate underfloor heating.

8.2 PCM melting condition prediction

In order to know whether the PCM is able to melt after the daytime, below equation is used to estimate whether the amount of solar insolation of a particular month is able to let PCM reach melting temperature.

$$Q_{sensible} = \sum_1^n m_n C_{p.n}(22 - T_a) \quad \textbf{8.1}$$

And

$$Q_{heat} = \emptyset_{total} \times 0.71 \times 3600 \quad \textbf{8.2}$$

Where $Q_{sensible}$ is the total amount of energy needed for the PVT-PCM system to reach PCM melting temperature (22℃). m_n is the mass of each system components (kg), $C_{p.n}$ is the specific heat capacity of each system component (J/kgK), and T_a is the minimum ambient temperature (℃). On the other hand, Q_{heat} is the heat absorbed by PV panel during the day, and $\emptyset_{total}$ is the daily total solar insolation.

If $Q_{sensible} > Q_{heat}$, PCM is not melted (no latent energy stored), if $Q_{sensible} < Q_{heat}$, PCM is (full/partially) melted.

The result of the monthly PCM melting ability is calculated and presented in table 8.1 below. The monthly temperature is determined from BBC weather (BBC weather, 2017) and the monthly average solar insolation level is determined from CIBSE guild A (CIBSE, 2014). It can be seen that PCM is able to melt during February to October, while the solar insolation

level during November to January is too low to trigger the phase change process of PCM.

Table 8.1 Monthly PCM melting ability estimation

Month	Energy absorbed	Ambient temperature	Energy required	PCM>22℃
	(kJ)	(℃)	(kJ)	(Yes/No)
Jan	3662.75	0	4760.97	N
Feb	7057.12	1	4760.97	Y
Mar	11241.29	3	4307.54	Y
Apr	14242.03	4	4080.83	Y
May	16596.11	6	3627.40	Y
Jun	17258.11	10	2720.55	Y
Jul	15952	12	2267.13	Y
Aug	13280.98	11	2493.84	Y
Sep	10249.56	7	3400.69	Y
Oct	8179.2	5	3854.12	Y
Nov	3624.41	2	4534.26	N
Dec	2660.80	3	4307.54	N

8.3 Air preheating

8.3.1 System description

The concept of air preheating mode is to use charged PCM storage panel to preheat outside fresh air before entering the room. Figure 8.4 below shows the detailed view of the proposed air preheat system. There are 4 dampers that can direct air into different paths. While air preheat mode is in operation, the damper 2 and 3 are closed and damper 1 is open, and the fan

is turned on to suck air into the room. By doing this, fresh air is forced into the ventilation channel where PCM panel is located. The air gets heated up while passing through the PCM panel and enters the room with a warmer temperature. On the other hand, when additional heating is not required, damper 1 is closed and dampers 2,3 are open, the fan is turned on and suck the air out of the room. By doing that the air bypasses the preheating air chamber and enters directly to the room.

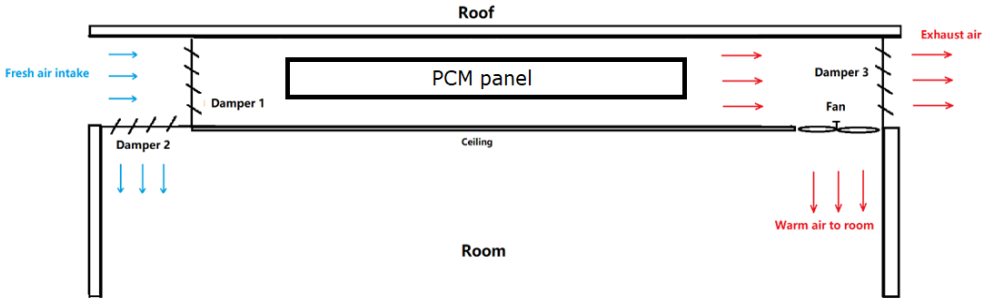


Figure 8.4 Schematic diagram of the designed air preheating system

8.3.2 Case model setup

Figure 8.5 shows the cross-sectional dimension of the ventilation channel. The PCM panel is located at the middle of the channel, with 50mm gap between each side. The total cross-sectional area could be calculated as 0.354m^2, and the cavity area for air to pass through can be calculated as 0.226m^2.

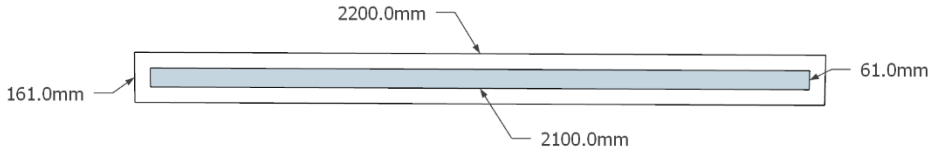


Figure 8.5 Cross sectional view of the ventilation channel.

Because the air gaps at the sides are much smaller compared to the size of PCM panel, a simplified two-dimensional model is

set up to evaluate the air preheating ability of the PCM panel. The geometry and dimension of the model is shown in Figure 8.6 below.

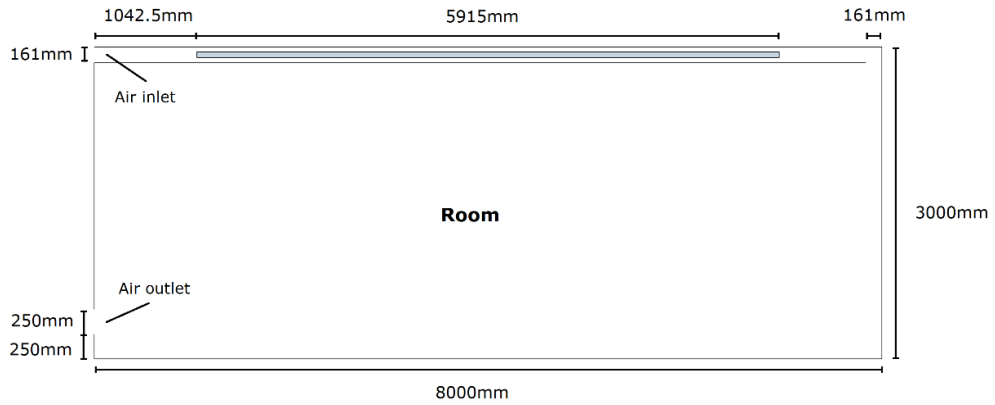


Figure 8.6 Geometry and dimension of air pre-heating model

The mesh profile of this model has 206496 elements, and has been adapted twice to ensure its mesh independency. The initial temperature of PCM panel enclosure is set to 22.5℃, which is the average temperature during the discharge process. The inlet air temperature is set to have different values range from 2℃ to 12℃, which represents the air temperature at night time throughout a year. The insulated walls of the model are set to have zero heat flux with outside environment. The initial room temperature is set to the same as ambient temperature.

According to CIBSIE guide of occupancy fresh air requirement (CIBSE, 2014), the minimum fresh air supply rate must be above 10l/s per person. A typical UK household will have 4 occupants during night time (2 adults, 2 children), thus the required air is 40l/s and hence the corresponding air flow speed can be calculated as 0.12m/s. Due to the large amount of latent heat stored in the PCM and the lower convection heat transfer

rate at low air velocity, it is considered that the PCM panel could stays above 22℃ for an extended period of time based on the convection heat dissipation performance studied in section

8.3.3 Results and discussion

Figure 8.7 shows the temperature contour of air from t = 5min to t = 30min. It can be seen that the warm air drops down from the ceiling to the bottom right of the room, and starts to fill up the whole room as cold air is vented through outlet located at the lower left corner. The air flow pattern could be obtained in Figure 8.8, it can be seen that the maximum air velocity is observed when passing through the opening on the ceiling. After the warm air left the opening, it circulates within the room while mixing with existing room air. The velocity magnitude of air is gradually decreased from the right side of the room to the left side. The air flow pattern is unsteady and changes with time. It is considered that the room air temperature becomes relatively steady at t = 30min. There is no hot or cold spot inside the room, and there is no place with insufficient air movement, thus the ventilation design of this case study is considered to be effective.

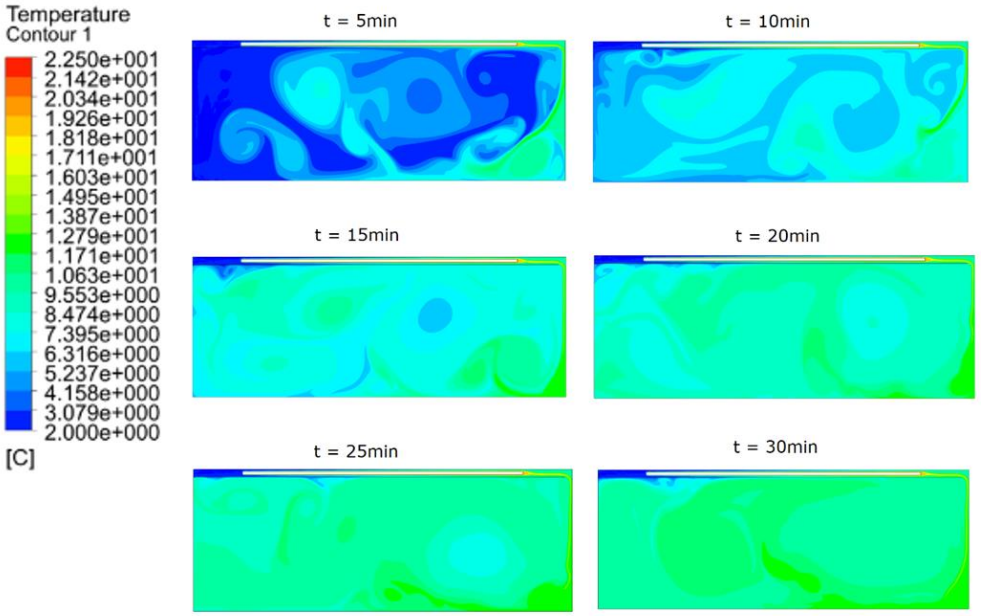


Figure 8.7 Room air temperature contours with 2℃ inlet temperature

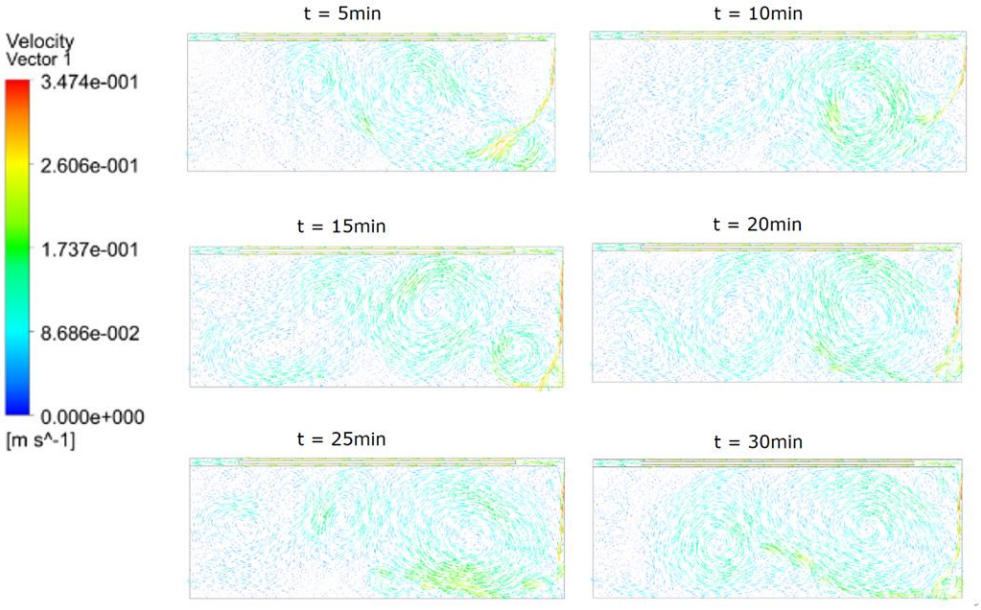


Figure 8.8 Room air velocity vectors with 2℃ inlet temperature

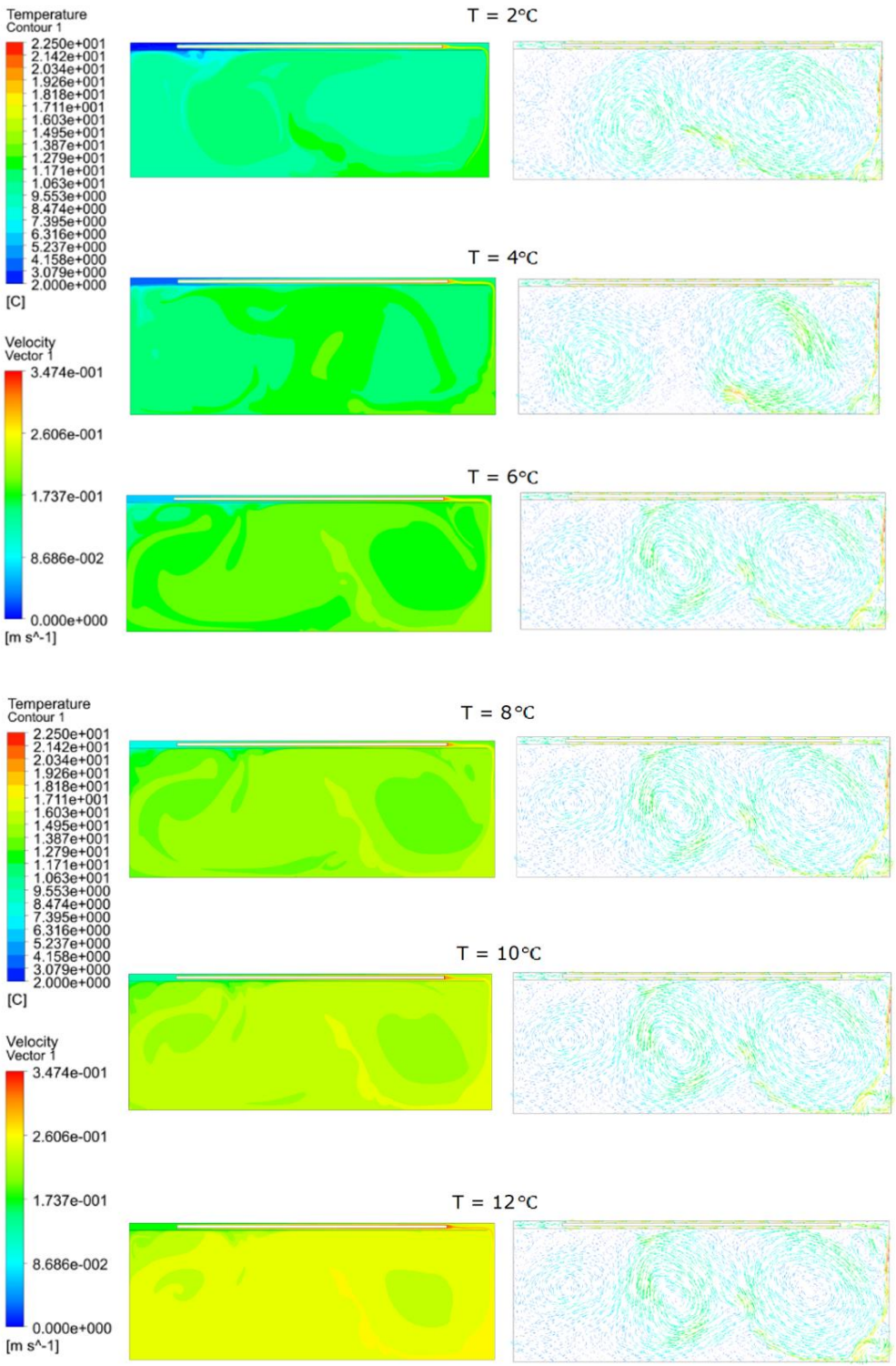


Figure 8.9 Temperature and velocity at different inlet temperature

Figure 8.9 shows the air temperature contour and velocity magnitude at different inlet temperature conditions from 2℃ to

12℃ at t = 30min. It can be seen that the room temperature rises with increased inlet temperature. The air flow pattern at inlet temperature of 2℃ and 4℃ are different from the air flow pattern at higher inlet temperatures, which is probably due to the increased air temperature difference when initial room temperature is low at lower inlet temperature settings. Again, no hot or cold spot are found in all inlet temperature settings after 30 minutes, and the air movement within the room is sufficient for ventilation purposes. The average room temperature obtained from the results shows a linear correlation with corresponding inlet temperature, and the correlation is shown in Figure 8.10 below. For every 1 ℃ increase of inlet air temperature, the corresponding room temperature is increased by 0.55℃.

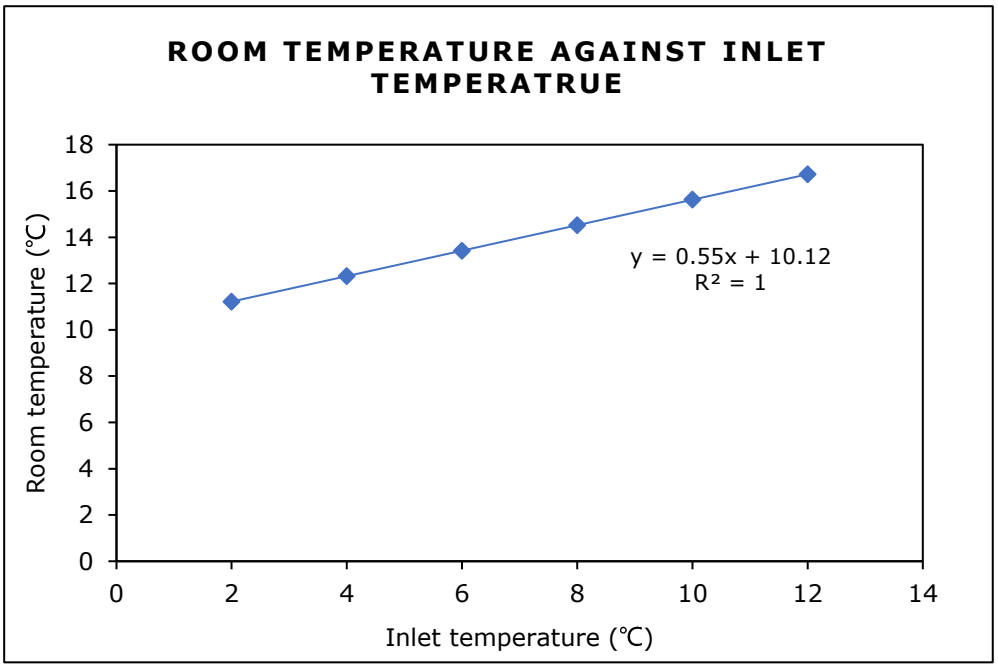


Figure 8.10 Correlation between room temperature and inlet temperature

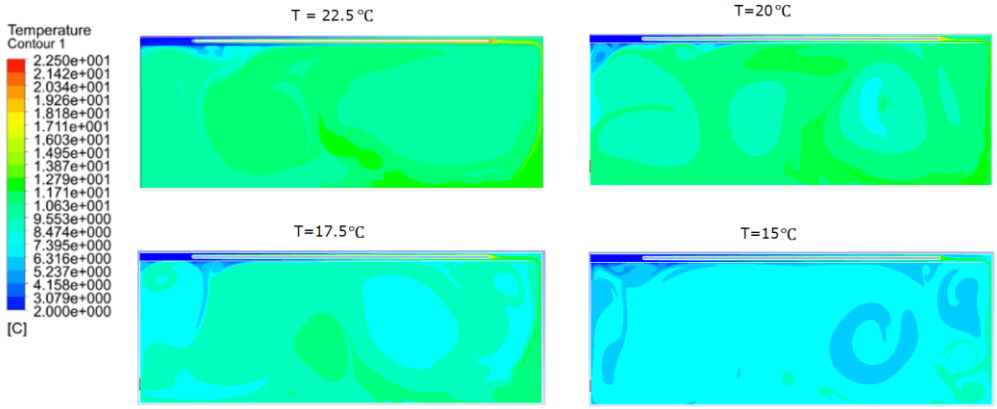


Figure 8.11 Room temperature under different PCM storage surface temperature

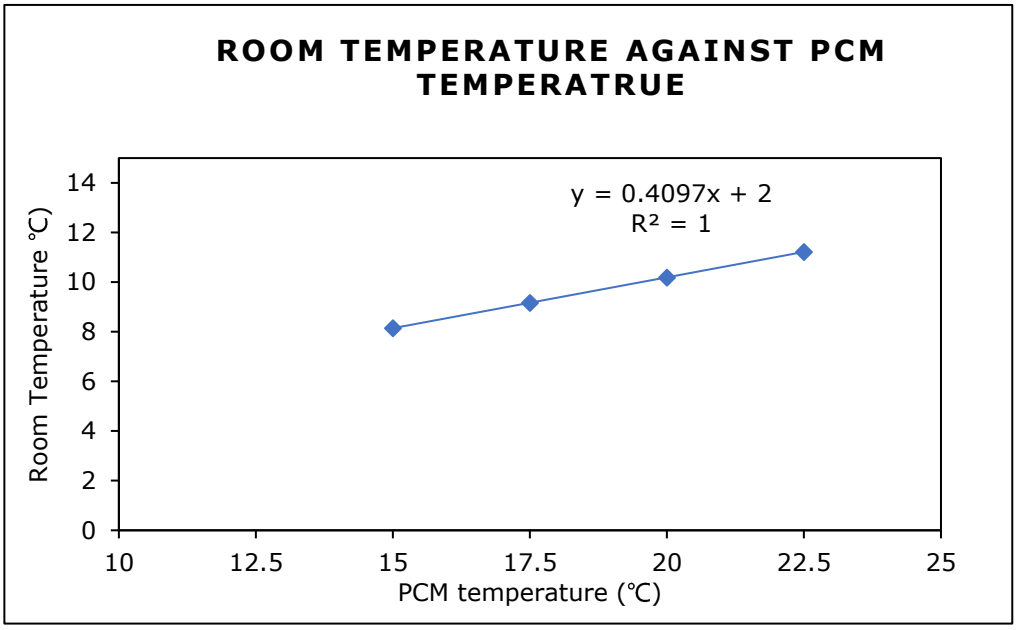


Figure 8.12 Correlation between room temperature and PCM storage surface temperature

Figure 8.11 shows the temperature contour of room temperature at t= 30min under different surface temperature of PCM storage when the inlet temperature remains constant at 2℃. It can be seen that despite of the fact that the condition of warm air distribution is not changed by much, the reduced surface temperature will result in the reduction of room temperature. The linear correlation is shown in Figure 8.12. It

can be seen that for every 1℃ of reduced surface temperature of PCM storage panel, the room temperature is reduced by approximately 0.41℃.

By knowing the correlation shown in Figure 8.10 and 8.12, the air preheating performance of such configuration can be predicted under different environmental conditions by knowing both the inlet air temperature and the surface temperature of PCM storage tank.

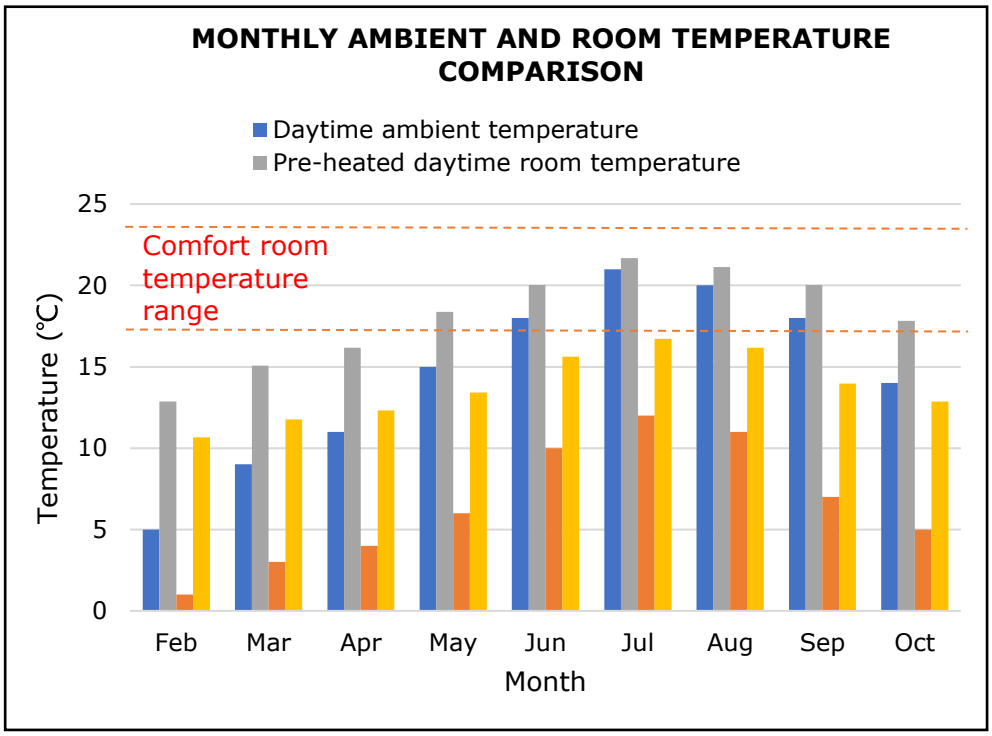


Figure 8.13 Monthly comparison between ambient temperature and predicted preheated room temperature

Figure 8.13 shows the monthly daytime and night time comparison of the ambient temperature and maximum preheated room temperature predicted by the correlation shown in Figure 8.10. The indoor comfort room temperature range is normally between 18℃ – 24℃ depending on local

climate condition (CIBSE, 2014). It can be seen that with the preheating of air by utilizing latent energy stored in PCM panel, the room temperature could be maintained at a much higher degree compared to the ambient temperature. As a result, the additional heating demand during cold time will be greatly reduced. Moreover, in months of April, May, September and October, the additional space heating demand may be fully substituted by only using PCM for air preheating when adding additional sources of heat gain (i.e. internal/fabric heat gain) into consideration.

8.4 Water preheating

8.4.1 System description

The purpose of this heat recovery mode is to save energy consumed for boilers by preheating the cold water coming from the main before entering the boiler. A simple schematic diagram showing the principle of water preheating configuration is illustrated in Figure 8.14 below. It is recommended by UK Energy Saving Trust (Energy saving trust, 2008) that for a domestic high pressure system, the minimum water flow rate requirement is 14l/min($2.3x10^{-4}m^3/s$). The single large PCM panel used in this case study has a total number of twenty-eight individual 6mm pipes, each pipe has the same length of 5195mm. In order to provide 14l/min water

through the system, each parallel pipe should have a minimum flow speed of 0.29m/s.

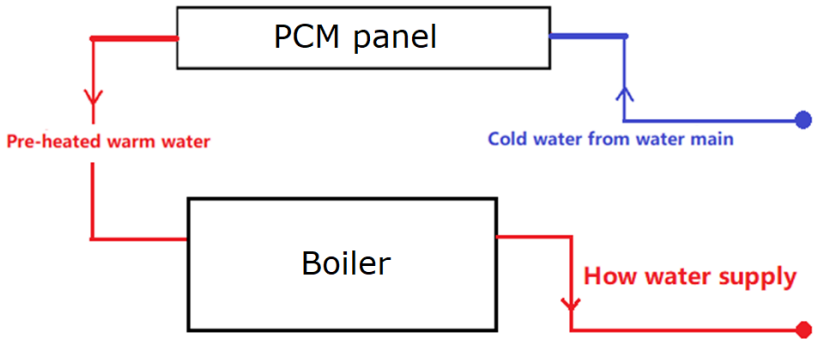


Figure 8.14 Schematic diagram of the water preheating configuration

8.4.2 Case model setup

The model built for study uses the horizontal cross-section area of five individual PCM modules (used in section 7.4.5) connected in series with a total length of 5195mm (shown in Figure 8.15 below).

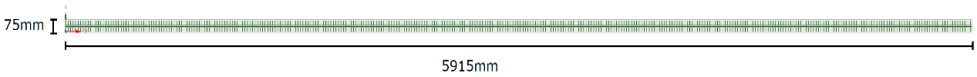


Figure 8.15 Geometry of the water preheating model

The meshing profile has 271364 elements, and is adapted twice to ensure mesh independence. The inlet water temperature from the main water supply is considered to be around 10℃ with small variations of several degrees year-round (Anglian water, 2015). In this case, the inlet water temperature is fixed to be 10℃. The initial temperature of PCM is set to be 23℃.

8.4.3 Results and discussion

Figure 8.16 shows the liquid fraction contour of the PCM panel cross-sectional area. It can be seen that the most part of PCM solidifies after 1 hour of cold water flow. The PCM near inlet is fully solidified at t = 1h as seen in figure, and there is still some liquid phase PCM left near the water outlet. The fast solidification process proves that water preheating mode could also be used to dissipate unwanted heat from the PCM panel. Considering that hot water is needed every day for shower or other usage in domestic homes, by using cold water supply to dissipate unwanted heat from PCM panel during summer period, the requirement of occasional natural convection cooling to prevent overheating is no longer necessary.

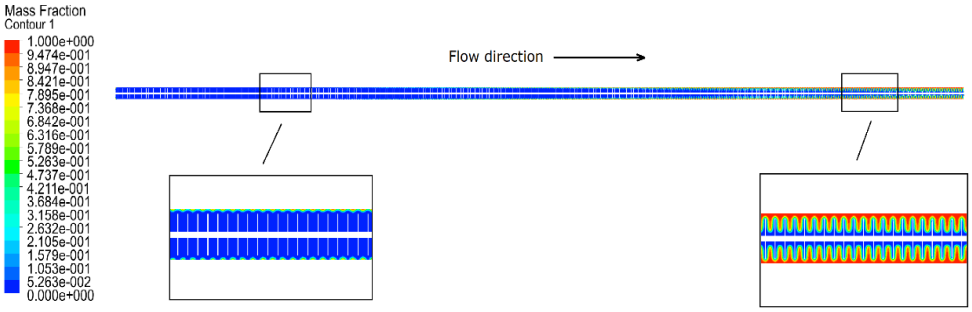


Figure 8.16 Liquid fraction contour of PCM panel cross-section after 1 hour.

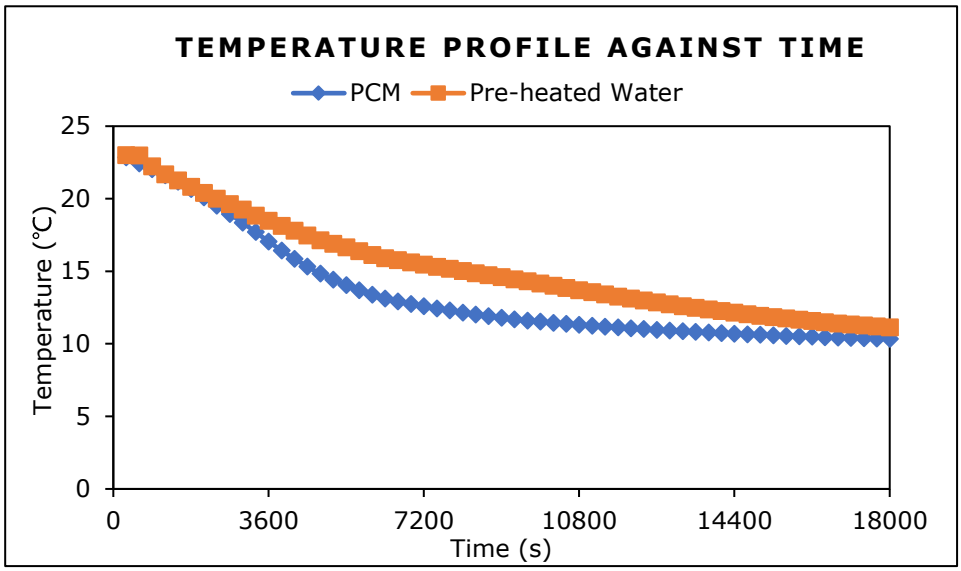


Figure 8.17 Temperature profile of pre-heated water and PCM against time.

Figure 8.17 shows the temperature profile of PCM and preheated water temperature. It can be seen that even most of the PCM solidifies within two hours, the preheated water temperature could still be kept at a relevant high degree. For 1 hour of hot water usage, the PCM panel could provide pre-heated warm water with 8.5℃ to 13℃ temperature rise. Consider that a normal boiler heats water up to around 60℃ (Energy saving trust, 2008), a 10℃ preheating can thus represent a 20% energy saving from the boiler. For 2 hours of hot water usage, the preheating temperature rise drops to 5.5℃, and for 3 hours of usage, the temperature rise drops to 3.7℃.

It should be noted that using both air preheating and water preheating at the same time will affect both performances. However, both air and water preheating shows great potential of latent heat utilization.

8.5 Summary

This chapter demonstrates the potential of PCM latent heat utilization via a case study. From the study, it can be seen that the stored latent thermal energy is capable of providing fresh air preheating at more comfortable temperature for a long lasting period when the ambient temperature is low. On the other hand, it can also reduce hot water load by around 20% during the first hour of water preheating. By combining both heat recovery method, it is clear that the latent heat stored within PCM could be effectively utilized even in the hottest day (by water preheating) without additional heat dissipation by natural convection.

CHAPTER 9. PVT-PCM SYSTEM IN SUBTROPICAL CLIMATE

9.1 Introduction

As discussed in Chapter 7 and 8, the proposed PVT-PCM system shows great advantages over conventional PV only setup under UK (temperate) climate. In order to further study the potential performance difference under different climate conditions, the PVT-PCM system is simulated again under a different climate zone. In this case, the temperature profile of Shanghai, China is chosen due to the fact that Shanghai is part of 'hot summer cold winter' region which has extreme weather conditions both in summer and in winter (JCJ,2001). The weather data of summer and winter design day is shown in Table 9.1 below (NASA, 2015).

Table 9.1 Hourly ambient temperature and solar radiation of summer and winter design days of Shanghai, China

	Summer design day (21st July)		**Winter design day (21st Jan)**	
Hour	Temperature (℃)	Solar radiation (W/m^2)	Temperature (℃)	Solar radiation (W/m^2)
1:00	30	0	-1.6	0
2:00	30	0	-2	0
3:00	30	0	-2.5	0
4:00	29	0	-2.9	0
5:00	29	22	-2.7	0
6:00	30	178	-2.5	0
7:00	31	395	-2.3	33
8:00	33	608	-1.1	181
9:00	34	786	0.1	359
10:00	36	915	1.3	500
11:00	37	975	1.6	581
12:00	38	975	1.8	587

13:00	38	911	2.1	518
14:00	38	786	1.7	385
15:00	38	612	1.4	209
16:00	37	399	1	50
17:00	36	181	0.6	0
18:00	36	23	0.3	0
19:00	34	0	-0.1	0
20:00	33	0	-0.4	0
21:00	31	0	-0.7	0
22:00	31	0	-1	0
23:00	31	0	-1.3	0
0:00	31	0	-1.3	0

9.2 Thermal Performance analysis

Due to the fact that the summer ambient temperature in Shanghai is much higher than Nottingham, the PCM-HS22P is considered not suitable for such high temperature. In this case, another PCM from PlusICE is chosen which has a higher melting temperature of 32℃ as the temperature range of Shanghai is higher than the working temperature range of PCM-HS2P . The properties of PCM-S32 is shown in Table 9.2 below. A simple PCM capacity sizing (Table 9.3) shows that the minimal required PCM volume is 0.042m^3, as a result, compared to the size chosen under UK climate, the new PCM panel size is increased by 15% according to the increased solar insolation to allocate the extra amount of PCM.

Table 9.2 PlusICE PCM-S32 properties (PlusICE, 2013).

Phase Change Temp (℃)	**Density (kg/m^3)**	**Latent Heat (kJ/kg)**	**Conductivity (W/mK)**	**Specific heat (kJ/kgK)**
32	1460	200	0.51	1910

Table 9.3 Sizing of required PCM material

Daily load	Total energy	PCM fusion heat	PCM Volume
3.43kWh	12330kJ	200kJ/kg	0.042m^3

The hourly simulation process used in this chapter is the same in chapter 8. The PCM and PV initial temperature are set to the ambient temperature at the start of the daytime circle.

9.2.1 Summer design day

Figure 9.1 shows the hourly PV temperature comparison between PVT-PCM and PV only setup in windy (5m/s wind) conditions. It can be seen that even with moderate natural convection, the peak PV cell temperature of PV only setup still reaches at 59.92℃ at 13:00, which is significantly higher than the PV panel's suggested normal working cell temperature (NOCT) of 47.5℃. On the other hand, the peak PV cell temperature of PVT-PCM system only reaches 43.71℃, which is 37% lower than the PV only setup.

The performance of PV only setup where there is minimal wind (0.1m/s wind) is much worse than the windy condition. Figure 9.2 illustrates that the peak cell temperature under minimal wind condition can reach 82℃, which is 36.8% higher than the peak temperature under windy condition. Compared with the temperature profile of PVT-PCM, the difference is almost doubled.

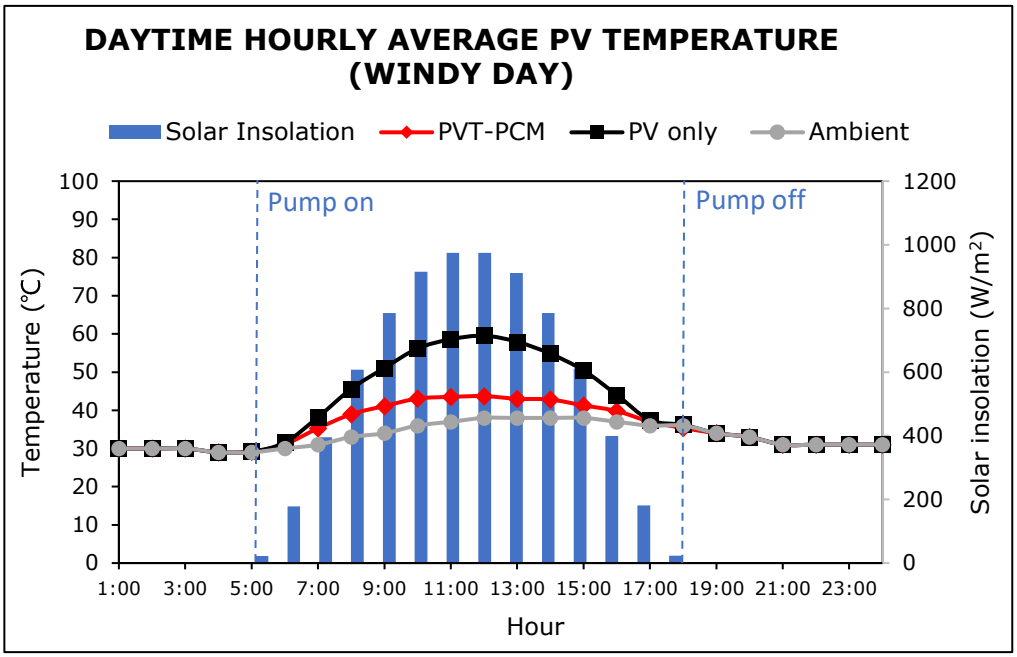


Figure 9.1 Summer design day PV panel temperature comparison of PVT-PCM and PV only setup in windy condition.

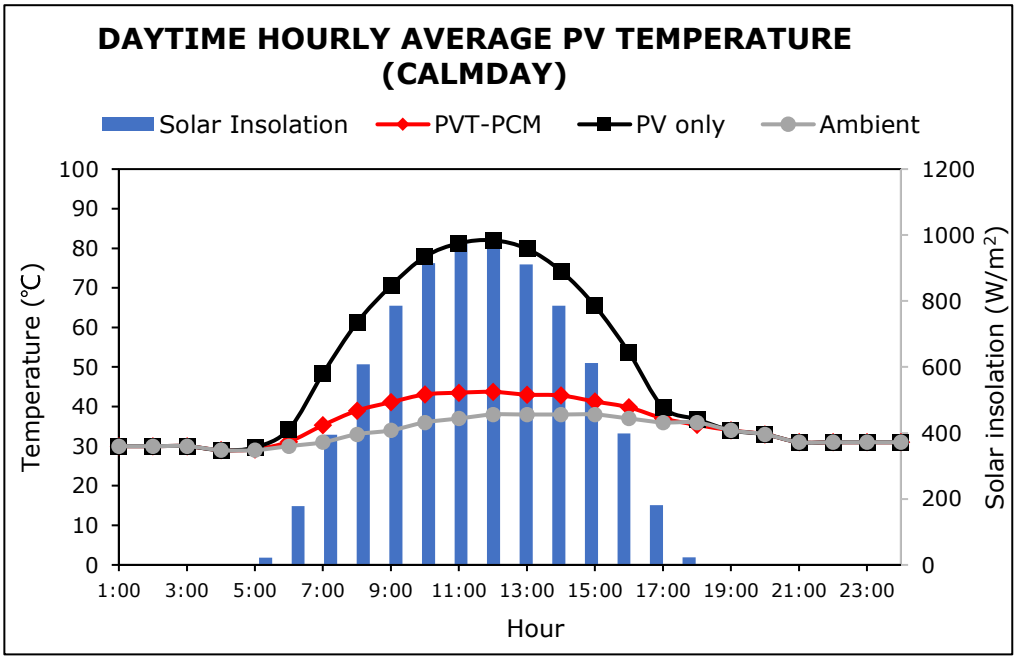


Figure 9.2 Summer design day PV panel temperature comparison of PVT-PCM and PV only setup in calm condition.

Figure 9.3 shows the melt fraction contour of PCM-S32 during the summer daytime cycle. It can be seen that by the time of

18:00, most majority of PCM is melted. Figure 9.4 shows the temperature profiles of PCM, PCM outlet and PV outlet. It can be seen from the figure that the PCM shows adequate ability of cooling down the hot water circulated from PV panel. The PCM outlet temperature stays relatively low during the midday, results in much reduced PV temperature. The rate of PCM temperature rise tends to increase towards the end of the day as PCM melt fraction increases, however, due to the faster decrease rate of solar radiation, the overall temperature within the system keeps stable with no overheating throughout the day. During the night the stored latent heat is released and the PCM temperature is lowered back to ambient before next morning.

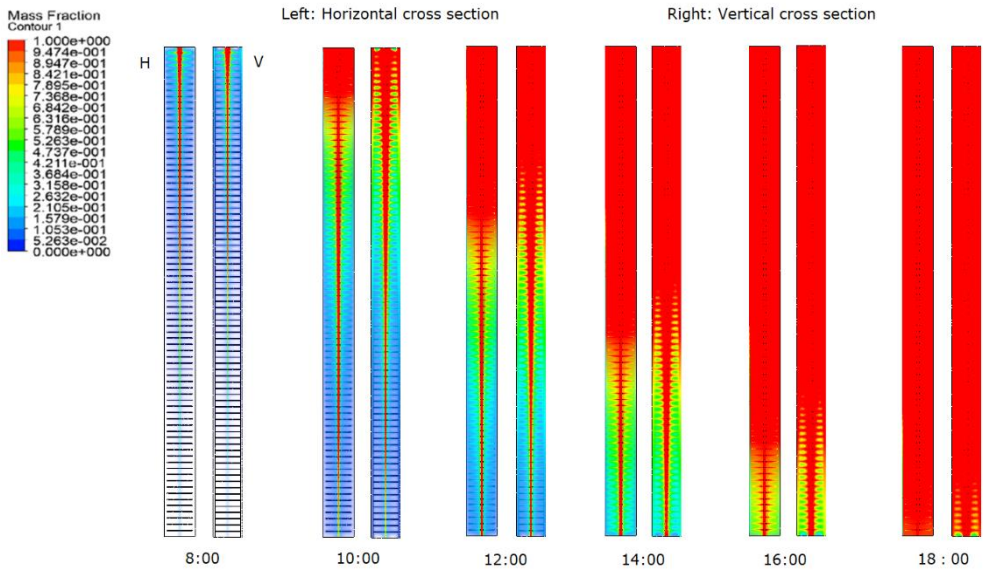


Figure 9.3 Melt fraction contour of PCM-S32

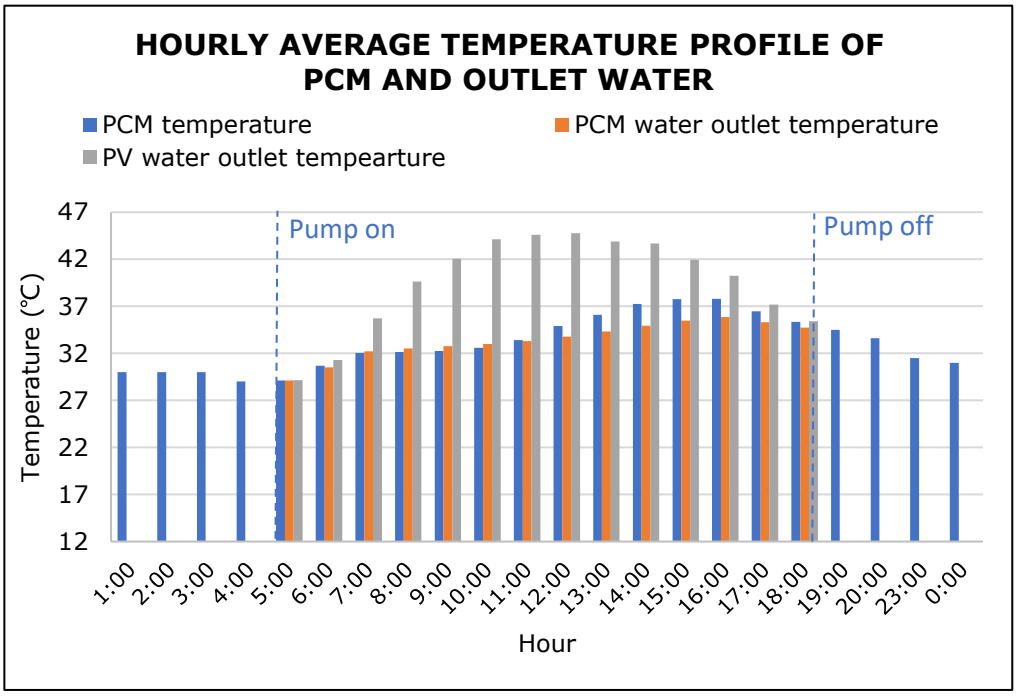


Figure 9.4 Temperature profile comparison of PCM, PCM outlet and PV outlet (Summer).

9.2.2 Winter design day

The PV cell temperature during winter period is much lower for both systems compare to the summer time. Figure 9.5 shows the temperature comparison in windy condition. The PVT-PCM could manage a lower PV temperature until 12:00, after which the PV only setup has lower cell temperature due to reduced solar insolation level. The peak cell temperature of PV only setup is 18.69℃ at 12:00, while the peak cell temperature of PVT-PCM system is 27.78 ℃ at 16:00. Similar as the in Nottingham, the PV cell temperature of PVT-PCM system is higher than PV only setup in the afternoon, and this is due to the continues charging of PCM. The water circulation pump could always be switched off anytime in the afternoon to reduce PV cell temperature if electricity output is the priority.

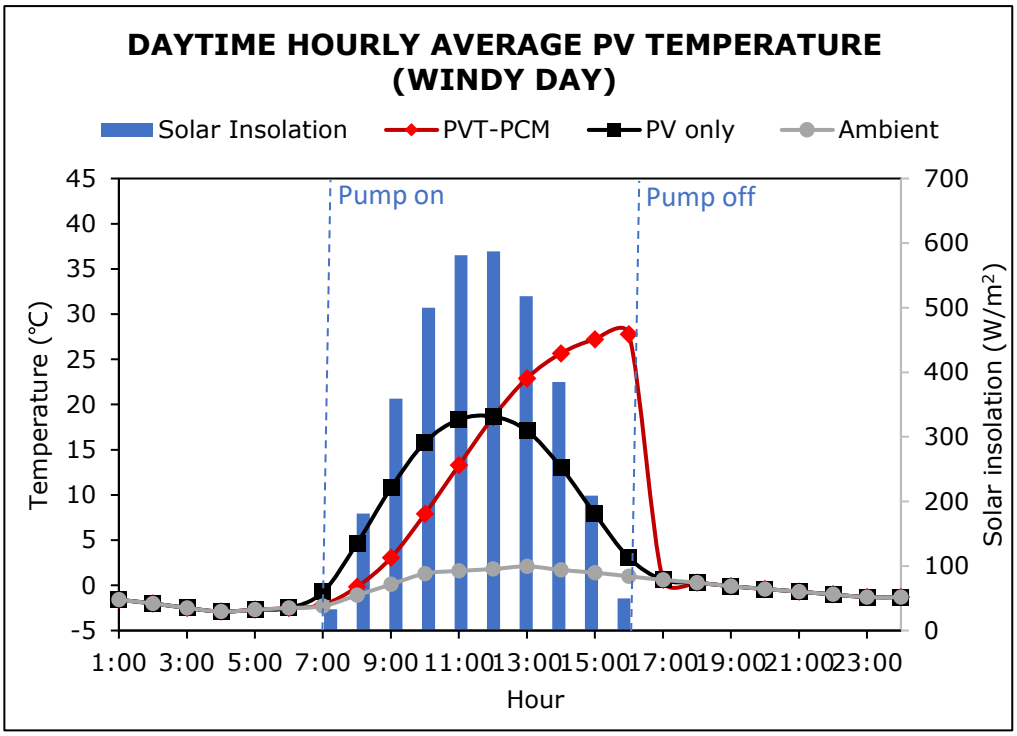


Figure 9.5 Winter design day PV panel temperature comparison of PVT-PCM and PV only setup in windy condition.

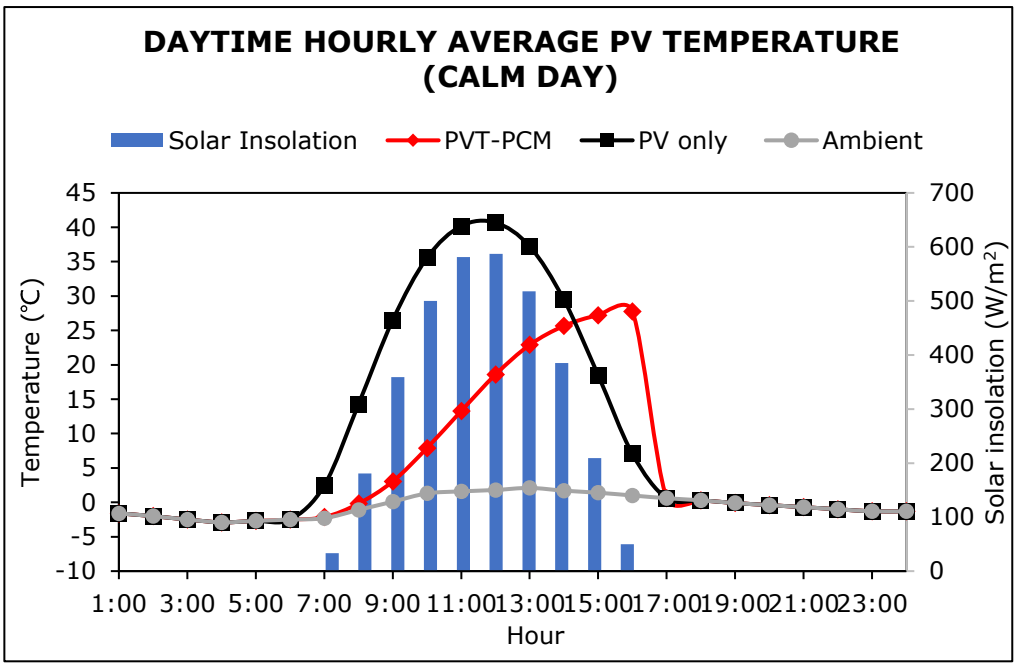


Figure 9.6 Winter design day PV panel temperature comparison of PVT-PCM and PV only setup in calm condition.

Figure 9.6 shows the PV temperature comparison under minimal wind conditions. Without natural ventilation, the peak

cell temperature of PV only setup increases significantly to 40.68℃, hence the advantage of PVT-PCM system is more noticeable.

Figure 9.7 shows the temperature profile comparison of PCM, PCM outlet and PV outlet during the daytime cycle in winter period. It can be seen that by the end of the day, the PCM temperature increases from -0.65℃ to 27.64℃. The PCM did not melt due to the low solar radiation and ambient temperature at winter design day. During the night the stored latent heat is released and the PCM temperature is lowered back to ambient before next morning.

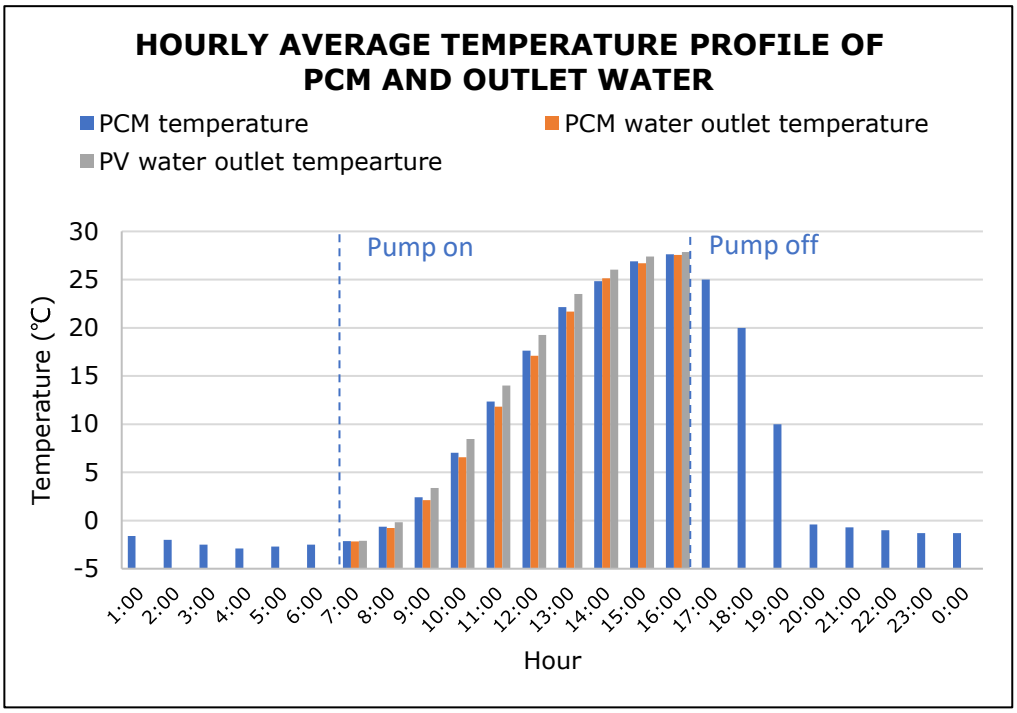


Figure 9.7 Temperature profile comparison of PCM, PCM outlet and PV outlet (Winter).

9.3 Electrical performance analysis

9.3.1 Summer design day

Figure 9.8 shows the hourly electrical output ratings of the PV panel used in PVT-PCM and PV only setup in windy conditions. It can be seen that the electrical performance of PVT-PCM system is more efficient when compared to the PV only model. The peak power output of PV only setup is observed at 96.53Wh/m^2 at 12:00, while the peak power output of PVT-PCM system is 105.28Wh/m^2 at 12:00. The PVT-PCM system has 9% higher peak power output. Similar to the performance difference under UK weather, the difference is small during early morning and late afternoon, but is obvious during the mid of the day where the ambient temperature and solar insolation are both at maximum level.

The electricity output power difference under summer minimal wind condition, on the other hand, is much more significant. Due to the extreme high PV cell temperature of PV only setup at midday, the peak electricity output drops by a further 11.58% to 83.38Wh/m^2 compared to the windy condition. The peak electricity output enhancement of the PVT-PCM system increased to 26.3% under minimal wind condition.

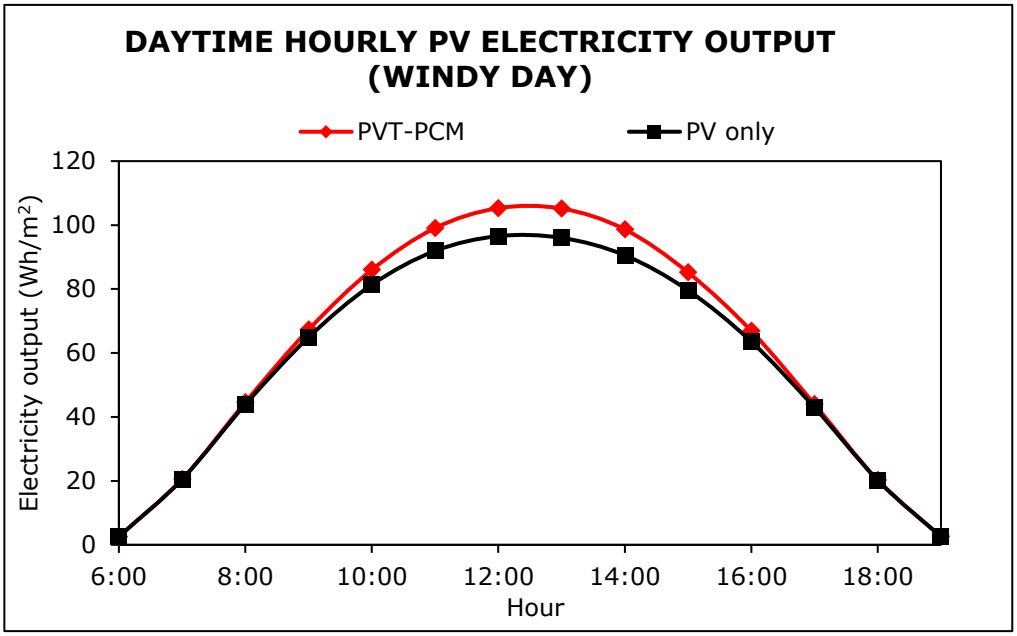


Figure 9.8 Summer time hourly electricity output comparison (Windy condition)

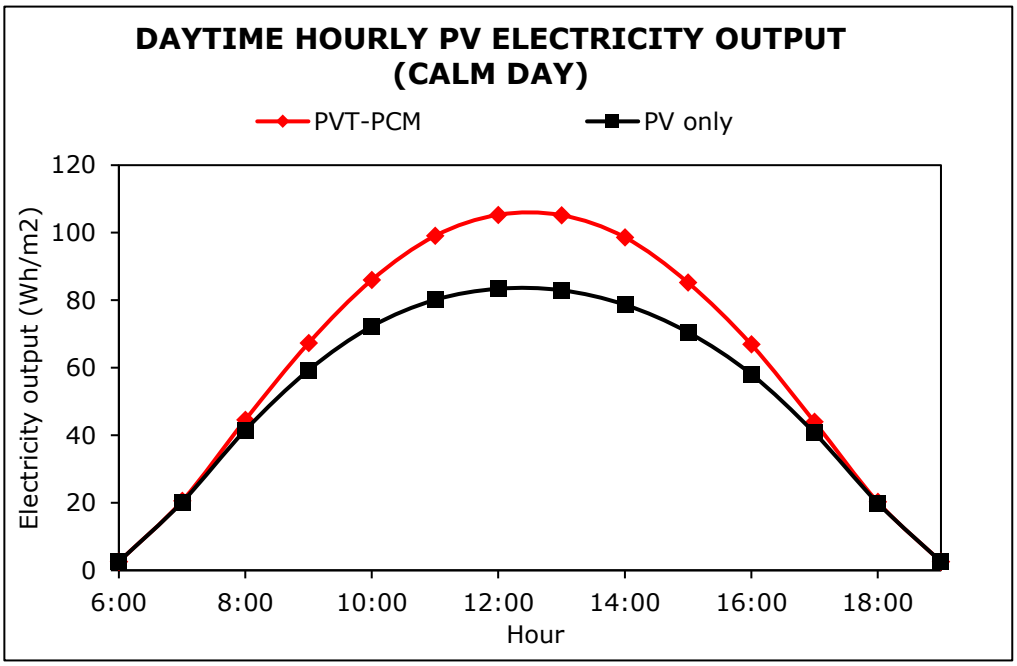


Figure 9.9 Summer time hourly electricity output comparison (Calm condition)

9.3.2 Winter design day

The electrical performance of the two systems during coldest winter design day with moderate wind is barely noticeable. As

Figure 9.10 shown below, the PVT-PCM system has slightly higher electricity output during the first half of the day. After 14:00, the electricity output drops below the PV only setup due to the increasing PV and PCM temperature. It can be seen from the figure that despite the difference is barely noticeable, the PVT-PCM system still has slightly better overall performance.

On the other hand, under minimal wind condition, the overall electrical performance of PV only setup drops significantly due to the lack of natural convection cooling. The peak electricity output of PV only setup is observed at 64.37Wh/m^2 at 13:00, while the PVT-PCM has a much higher peak output of 73.18Wh/m^2 (13.7% increase) at 12:00.

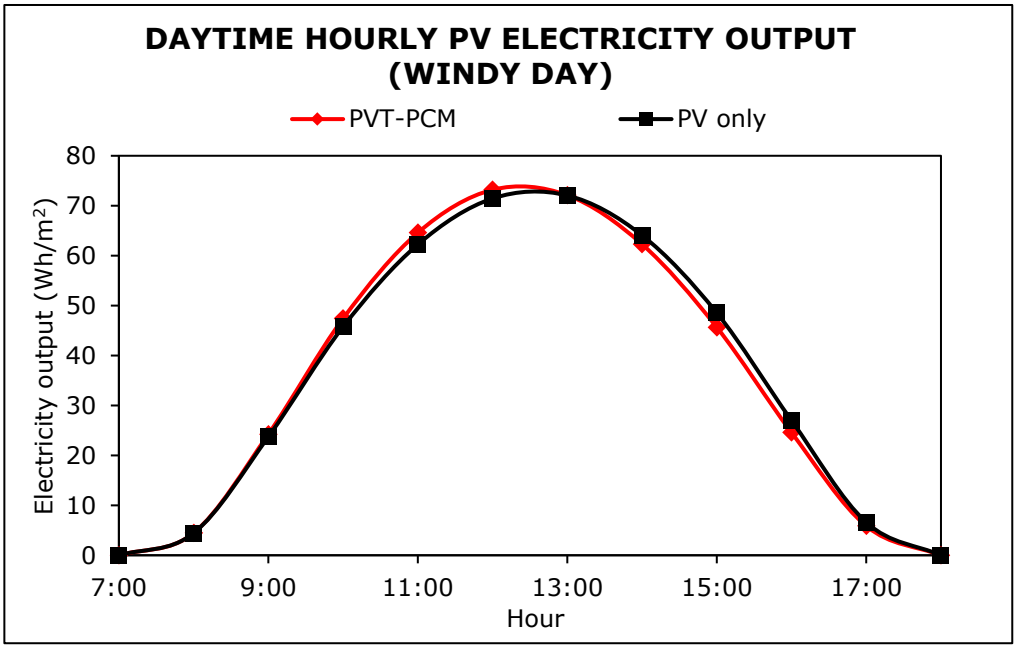


Figure 9.10 Winter time hourly electricity output comparison (Windy condition)

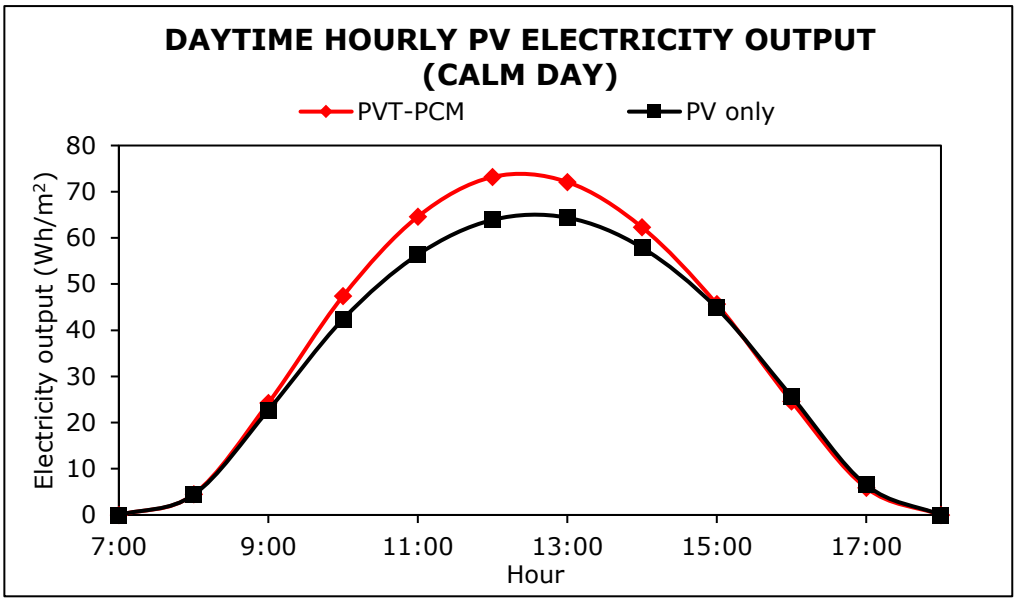


Figure 9.11 Winter time hourly electricity output comparison (Calm condition)

9.4 Energy saving potential

Table 9.4 below shows the energy saving potentials of the PVT-PCM system compared with conventional PV only system. It can be seen that in summer design day, every 1m^2 PVT-PCM module can output 135.92Wh more electricity compared to the PV only setup in minimal wind conditions, after considering the additional pump energy consumption. In windy conditions, the difference in electricity output is smaller, at 51Wh per day. After taking into account the potential latent energy stored by the PCM system, the difference becomes significantly larger, at 5649.92Wh/day and 5563.92Wh/day depending on wind conditions.

On the other hand, when operating in winter design day conditions, the electrical performance gain of every 1m^2 PVT-PCM system is much smaller, at 35.95Wh/day in minimal

wind condition and -1Wh/day in windy condition. Similarly, after considering the thermal energy stored in PCM, the difference becomes 2451.95Wh/day in minimal wind condition and 2415.95Wh/day in windy condition.

Table 9.4 Energy saving potentials of the PVT-PCM system

Summer design day	**Calm**			**Windy**		
(Wh/m^2.day)	PVT	PV	Difference	PVT	PV	Difference
Electricity output	848	712	136	848	797	51
Pump energy	-0.08	0	-0.08	-0.08	0	-0.08
Net electricity gain			135.92			50.92
Thermal energy	5513	0	5513	5513	0	5513
Total energy gain			5649.92			5563.92
Winter design day	**Calm**			**Windy**		
(Wh/m^2.day)	PVT	PV	Difference	PVT	PV	Difference
Electricity output	424	388	36	424	425	-1
Pump energy	-0.05	0	-0.05	-0.05	0	-0.05
Net electricity gain			35.95			-1.05
Thermal energy	2416	0	2416	2416	0	2416
Total energy gain			2451.95			2415.95

Table 9.5 Overall daily electrical and thermal efficiency

Summer	**Calm**		**Windy**	
	PVT-PCM	PV Only	PVT-PCM	PV Only
Electrical efficiency	**10.9%**	8.5%	**10.9%**	10.8%
Thermal efficiency	**71%**	0%	**71%**	0%
Winter	**Calm**		**Windy**	
	PVT-PCM	PV Only	PVT-PCM	PV Only
Electrical efficiency	**12.4%**	11.4%	**12.4%**	12.4%
Thermal efficiency	**71%**	0%	**71%**	0%

Table 9.5 shows the overall daily electrical and thermal efficiency for summer and winter design day. It can be seen

that the PVT-PCM system could achieve daily electrical efficiency of 10.9% - 12.4% throughout a year, while the PV only setup has reduced electrical efficiency range from 8.5% to 12.4%. The serious overheating issue of PV only setup during summer time can be solved completely if replaced by the PVT-PCM system.

9.5 Cost analysis

Considering the fact that labour and manufacturing costs in China are generally much lower when compared to the UK, the overall initial cost estimation is reduced by 30% according to the average price difference between China and UK (70% of the material cost in UK with another 20% additional installation and maintenance cost). In addition, the utility price in Shanghai is also much lower, at the rate equivalent to £0.06/kWh in the British pound.

Following the same procedure of the cost analysis presented in section 7.7, the discounted payback period can then be determined by using Table 9.6 – 9.8 below. The calculated discounted payback period if the upgrade took place in Shanghai is 12.83 years.

Table 9.6 Adjusted additional cost of PVT-PCM

Initial material cost (£/m^2)	Adjustment factor	Adjusted material cost (£/m^2)
714.61	1.15 x 0.7	**575.26**

Table 9.7 Yearly saving estimation for Shanghai

Average daily energy saving (kWh/m^2)	4.02
Number of days	365

Utility price (£/kWh)	0.06
Yearly saving (£/m^2)	**88.04**

Table 9.8 Discounted payback period calculation for Shanghai

Year	**Cash flow (£)**	**Present value factor**	**Discounted cash flow (£)**	**Cumulative discounted cash flow (£)**
n	CF	PV=(1/1+0.08)^n	CF X PV	
0	-690.31	1.00	-690.31	-690.31
1	88.04	0.93	81.52	-608.79
2	88.04	0.86	75.48	-533.31
3	88.04	0.79	69.89	-463.42
4	88.04	0.74	64.71	-398.71
5	88.04	0.68	59.92	-338.79
6	88.04	0.63	55.48	-283.31
7	88.04	0.58	51.37	-231.94
8	88.04	0.54	47.57	-184.38
9	88.04	0.50	44.04	-140.33
10	88.04	0.46	40.78	-99.55
11	88.04	0.43	37.76	-61.80
12	88.04	0.40	34.96	-26.83
13	88.04	0.37	32.37	5.54
Total payback period (year)			**12.83**	

9.6 Latent heat utilization

Due to the nature of 'hot summer cold winter' climate condition in Shanghai, there's no space heating requirement most of the year except winter period. As a result, the benefit from a dedicated fresh air supply system with PCM air preheating is likely to be unjustified to the additional investment. On the other hand, in some cases where air preheating is required, the PCM-S32 can achieve better performance compared to PCM-HS22P due to its much higher phase change temperature.

In this study, only water preheating is considered as the heat utilization which is more practical as hot water is needed everyday regardless the geographical location.

According to an experimental observation (Xue, 1991), the average water supply temperature in Shanghai is around 14℃. Assuming the PCM is fully charged with an average temperature of 33℃, the water preheating performance could be evaluated using the same method presented in section 8.4.

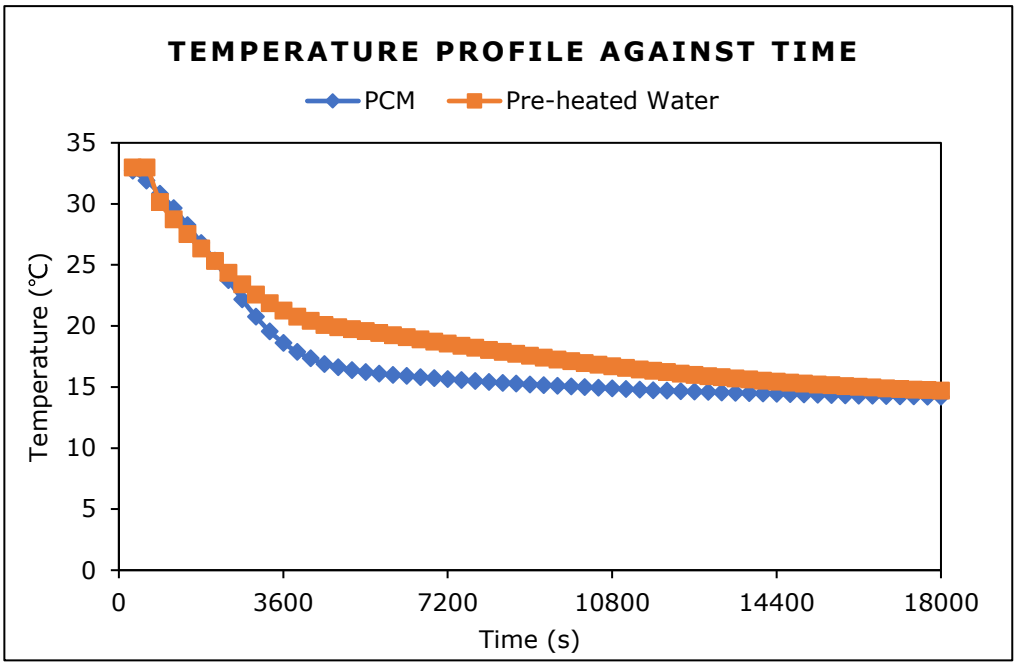


Figure 9.12 Temperature profile of PCM and pre-heated water temperature.

Figure 9.12 shows the temperature profile of PCM and preheated water temperature. It can be seen that most PCM solidifies within 1 hour, which is faster than the Solidification speed of 2 hours estimated in section 8.4.3. For 1 hour of hot water usage, the PCM panel could provide pre-heated warm water with 7.3℃ to 19℃ temperature rise. Consider that a normal boiler heats water up to around 60℃ (Energy saving

trust, 2008), a 19℃ preheating can result in 41% less boiler energy consumption. For 2 hours of hot water usage, the preheating temperature rise drops to 4.55℃, and for 3 hours of usage, the temperature rise drops to 2.7℃. It can be seen that the water preheating could effectively discharge the PCM during night time, and the effect is greater compared to colder climate conditions due to the higher temperature difference between PCM and water supply.

9.7 Performance comparison under two climate conditions

Table 9.9 below shows the comparison of some key factors regarding to the PVT-PCM performance under different climate conditions of Nottingham and Shanghai. From the electrical performance's perspective, it can be concluded that in hotter climates, the proposed PVT-PCM system could achieve better thermal management over PV cell temperature, which leads to a further increase in electrical performance gain when compared to colder climates. From the thermal storage perspective, the overall efficiency is still restricted by the PV panel absorbance ratio. However, due to the fact that higher melting point PCM is used for hotter climates, the overall thermal utilization could have better performance compared to colder climates. However, from the economical perspective, due to the geographical and economic difference between two countries, the payback period if used in Shanghai is about 2 years longer than Nottingham. The increased payback period in Shanghai is mainly due to the much lower utility price in the

local region. Thus, it is important to consider both energy and economic performance when designing such system for a specific location.

Table 9.9 Comparison of some key factors under two climates

	Nottingham	**Shanghai**
Max. PCM temp	24.5℃	34.7℃
Max. boiler energy saving	20%	41%
Max. cell temp reduction	36.5℃	38.3℃
Max. PV efficiency increase	1.7%	2.4%
Daily energy saving	3.23kWh/m^2	4.02 kWh/m^2
Payback period	10.67 years	12.83 years

9.8 Summary

In this chapter, the performance of the proposed PVT-PCM system is evaluated again under a hotter climate condition of Shanghai. The thermal, electrical and cost analysis, as well as latent heat utilization are presented. By comparing the system performance under both climates, it is found that the energy saving potential of the PVT-PCM system is greater in hotter subtropical climate conditions. However, the cost comparison shows that the increased energy performance might not result in increased economic performance if used in different climate conditions due to the difference in local utility rates.

CHAPTER 10. CONCLUSION AND RECOMMENDATIONS

10.1 Introduction

Overheating of PV panel under intense sunlight has been an issue affecting its electrical performance. The dilemma between photovoltaic and thermal performance can be eased with properly designed PVT systems. This study brought up a new concept of a PCM based PVT system which is superior from both photovoltaic and thermal performance' perspective.

During the research process, an extensive literature review has been done to study the state of the art of PV, PVT and PCM as well as their applications. Several analytical and numerical models were built for individual components to assess the feasibility of the proposed BIPVT design. Due to the lack of related study, the effect of PCM thermal properties was firstly studied via computational modelling prior to the parametric analysis for each system components. The effect such as solar radiation level, ambient temperature, wind speed and water flow rate have been analysed and discussed. The results from parametric analysis were then used to size the PVT-PCM system. The energy and economic performance of the PVT-PCM are evaluated under two different climate conditions. The results show that the system has superior performance over conventional PV systems under both climate conditions. In addition, two ways of latent heat utilization were also presented and discussed; both were showing great potentials.

10.2 Achievements and Findings

This research involves a novel PVT-PCM system which has better overall performance compared with many existing PVT systems. During the research process, several important findings have been revealed and are listed below:

- The conventional PV panel temperature may be acceptable in windy conditions in UK climate (43℃ in Nottingham with 5m/s wind), but when there is little wind, it will rise significantly (up to 69℃) which will result in overheating. The situation is worse in Subtropical areas like Shanghai, where the temperature could reach from 59℃ to 82 ℃ even if there's wind;

- Based on literature review, the most significant factor that affects the PV cell temperature is the unpredictable ambient conditions. Passive cooling can reduce maximum cell temperature effectively, however, by providing additional active cooling, effectiveness is usually much greater;

- Active water cooling of the PV panel can greatly improve photovoltaic efficiency, while only consuming small amount of extra energy (0.002W per module in this case). The performance boost is most significant in extreme weather conditions (hot with little wind), even during windy conditions, there is still a slight performance increase;

- The PCM thermal storage solution is superior to conventional water based storage solution as PCM could store up to 14

times more energy than water for the same volume, and can maintain a moderately cool temperature during the working hours of PV panel;

- The PCM with higher solid phase thermal conductivity has significantly shorter discharging time compared to the charging time, and Vice versa;

- The PCM thermal performance is greatly affected by fin designs, thus it is essential to integrate properly designed fins while using PCM as latent heat storage solutions;

- By careful design of the PVT-PCM system, the PCM can effectively regulate the PV panel temperature for an extended period of time without any additional cooling;

- Due to the fact that the PV cell temperature of the PVT-PCM system is less dependent on ambient conditions, the system can be used in hotter climates and the proportion of performance enhancement will be greater, as long as the thermal capacity of PCM system is effectively managed;

- The PVT-PCM system could achieve a maximum PV cell temperature reduction of 36.5℃ (38.3℃) when compared with conventional PV only setups in Nottingham (Shanghai) area, which leads to a maximum of 1.7% (2.4%) electrical efficiency enhancement;

- The PVT-PCM system could provide up to 5.4kWh (and 5.7kWh) more energy per unit module during the summer design day of Nottingham (and Shanghai) compared to the

conventional PV only setup of same size; The yearly average daily energy saving of the PVT-PCM system in Nottingham (Shanghai) is estimated at 3.23kWh (4.02kWh) per unit module;

- The additional cost other than the PV panel could be recovered after an estimated payback period of 10.67 years if used in Nottingham (12.83 years if used in Shanghai). The payback period could be significantly shortened in the future if the system is mass produced;

- Better energy performance does not always represent better economic performance; the economic performance will be greatly affected by the regional economic differences, in this case, the Payback period in Shanghai is longer than Nottingham despite of the lower initial and maintenance cost due to the much lower utility rate;

- The charged PCM could effectively provide warm air when space heating is required. In Nottingham, the required space heating energy could be solely provided by PCM air preheating during April to October;

- The amount of latent heat stored in the PCM during the summer design day is capable of saving up to 20% of boiler heating energy for Nottingham (41% if used in Shanghai) climate condition.

10.3 Limitations

Although this research has achieved its objectives, there are still some unavoidable limitations. First, due to the nature that utilization of CFD software requires a significant amount of time as well as computational resources, the proposed PVT-PCM system is only evaluated in two specific design conditions of Nottingham, UK and Shanghai, China. Second, due to the recent change in laboratory regulations, re-using existing experimental rig that doesn't meet new regulation is no longer permitted, thus, carrying out experimental work is hardly possible within the given timeframe. As a result, the experimental performance evaluation of the designed system in real environmental conditions cannot be carried out.

10.4 Future work

It is recommended for future work to continuing study the system's performance under other climate conditions in order to have a generalized sizing guide. The monthly and yearly performance could also be detailly investigated. At the same time, experimental works could be carried out to further evaluate the system's realistic energy saving potential. Moreover, it is recommended to study the performance of multiple system configurations in a real case study, by mounting the system in different angles and orientations.

BIBLIOGRAPHY

Aaditya, G., Pillai, R., & Mani, M. (2013). An insight into real-time performance assessment of a building integrated photovoltaic (BIPV) installation in Bangalore (India). *Energy for Sustainable Development, 17*(5), 431-437.

Aelenei, L., Rereira, R., Gonçalves, H., & Athienitis, A. (2014). Thermal performance of a hybrid BIPV-PCM: modeling, design and experimental investigation. *Energy Procedia, 48*, 474-483.

Affolter, P., Eisenmann, W., Fechner, H., Rommel, S. M., Serensen, H., Tripanagnostopoulos, Y., & Zondag, Y. (2006). *PVT Roadmap: a European Guide for the Development and Market Introduction of PV-Thermal Technology.* Netherlands: ECN Editor.

Agrawal, B., & Tiwari, G. N. (2010). Optimizing the energy and exergy of building integrated photovoltaic thermal (BIPVT) systems under cold climatic conditions. *Applied Energy, 87*(2), 417-726.

Ahn, J.-G., Kim, J.-H., & Kim, J.-T. (2015). A Study on Experimental Performance of Air-Type PVT Collector with HRV. *Energy Procedia, 78*, 3007-3012.

Alami, A. H. (2014). Effects of evaporative cooling on efficiency of photovoltaic modules. *Energy Conversion and Management, 77*, 668-679.

Alfegi, M. E., Sopian, K., Othman, M. Y., & Yatim, B. B. (2008). Experimental Investigation of Single Pass, Double Duct Photovoltaic Thermal (PVT) Air Collector with CPC and Fins. *American Journal of Applied Sciences*, 866-871.

Alibaba. (2017). Retrieved from Taobao.com: https://item.taobao.com/item.htm?spm=a230r.1.14.65.ebb2eb2VE3Ufh&id=523394622919&ns=1&abbucket=18#detail

Anderson, T. N., Duke, M., Morrison, G. L., & Carson, J. K. (2009). Performance of a building integrated photovoltaic/thermal (BIPVT) solar collector. *Solar Energy, 83*(4), 445-455.

Anglian water. (2015). *Design Considerations for water supplies in apartment buildings and flats.* Retrieved 04 13, 2017, from http://www.anglianwater.co.uk/_assets/media/Design_Considerations_for_water_supplies_in_apartment_buildings_and_flats_LED.pdf

Ansys, I. (2013). *ANSYS Fluent User's Guide.* Southpointe, PA 15317: Ansys, Inc.

Bahaidarah, H., Sybhan, A., Gandhidasan, P., & Rehman, S. (2013). Performance evaluation of a PV (photovoltaic) module by back surface water cooling for hot climatic conditions. *Energy, 59*, 445-453.

Baloch, A. A., Bahaidarah, M. S., Gandhidasan, P., & Al-Sulaiman, F. A. (2015). Experimental and numerical performance analysis of a converging channel heat exchanger for PV cooling. *Energy Conversion and Management, 103*, 14-27.

BBC weather. (2017). *Weather Nottingham.* Retrieved from www.bbc.co.uk: http://www.bbc.co.uk/weather/2641170

Bejan, A. K. (2003). *Heat Transfer Handbook.* Wiley: IEEE.

Bergene, T., & Lovvik, O. M. (1995). Model calculations on a flat-plate solar heat collector with integrated solar cells. *Solar Energy, 55*(6), 453-462.

Biswas, K., Lu, J., Shroushian, P., & Shrestha, S. (2014). Combined experimental and numerical evaluation of a prototype nano-PCM enhanced wallboard. *Applied Energy*, 517-529.

BP Solar. (2001). *Solar modules BP280F & BP275F.* Retrieved 07 22, 2014, from http://www.posharp.com/bp275f-solar-panel-from-bp-solar_p166512668d.aspx

Brideau, S., & Collins, M. (2014). Development and validation of a hybrid PVThermal air based collector model with impinging jets. *Solar Energy, 102*, 243-246.

Brinkworth, B. J. (2006). Optimum depth for PV cooling ducts. *Solar Energy, 80*(9), 1131-1134.

Chandel, S. S., & Agarwal, T. (2017). Review of cooling techniques using phase change materials for enhancing efficiency of photovoltaic power systems. *Renewable and Sustainable Energy Reviews, 73*, 1342-1351.

Chandrasekar, M., & Senthilkumar, T. (2015). Experimental demonstration of enhanced solar energy utilization in flat PV (photovoltaic) modules cooled by heat spreaders in conjunction with cotton wick structures. *Energy, 90*, 1401-1410.

Chandrasekar, M., Suresh, S., Senthilkumar, T., & Karthikeyan, M. G. (2013). Passive cooling of standalone flat PV module with cotton wick structures. *Energy Conversion and Management, 71*, 3-50.

Chaplin, D., Fuller, C., & Pearson, G. (1954). A new silicon p-n junction photocell for converting solar radiation into electrical power. *Applied Physics, 25*(5), 676.

Chow, T. (2010). A review on photovoltaic/thermal hybrid solar technology. *Applied Energy*, 365-379.

Chow, T., Fong, K., He, W., Lin, Z., & Chan, A. (2007). Performance evaluation of a PV ventilated window applying to office building of Hong Kong. *Energy and Buildings*, 643-650.

Chow, T., Pei, G., Fong, K., Lin, Z., Chan, A., & Ji, J. (2008). Energy and exergy analysis of photovoltaic–thermal collector with and without glass cover. *Applied Energy, 86*(3), 310-316.

CIBSE. (2014). *Module 69: Delivering ventilation to occupied spaces.* Retrieved 03 31, 2015, from https://www.cibsejournal.com/cpd/modules/2014-10/

CIBSE. (2015). *CIBSIE Guide A: Environmental Design.* London: CIBSIE.

Ciulla, G., BranoLo, V., Cellura, M., Franzitta, V., & Milone, D. (2012). A finite difference model of a PV-PCM system. *Energy Procedia, 30*, 198-206.

Daghigh, R., Ruslan, M., & Sopian, K. (2011). Advances in liquid based photovoltaic/thermal (PVT) collectors. *Renewable and Sustainable Energy Reviews*, 4156-4170.

Darzi, R. A., Afrouzi, H. H., Khaki, M., & Abbasi, M. (2015). UNCONSTRAINED MELTING AND SOLIDIFICATION INSIDE RECTANGULAR ENCLOSURE. *Journal of Fundamental and Applied Science*, 436-451.

Department for Business, Energy & Industrial Strategy. (2016). *Electricity: Chapter 5, Digest of United Kingdom Energy Statistics (DUKES).* London: National Statistics.

Department of Business, Energy & Industrial Strategy. (2016). *UK Energy Statistics, Q3 2016.* London: National Statistics.

Dhaidan, N. S. (2017). Nanostructures assisted melting of phase change materials in various cavities. *Applied Thermal Engineering*, 193-212.

Duffie, J. A., & Beckman, W. A. (1991). *Solar Engineering of Thermal Process (2nd edition).* Hoboken, New Jersy: John Wiley & Sons, Inc.

Ebrahimi, M., Rahimi, M., & Rahimi, A. (2015). An experimental study on using natural vaporization for cooling of a photovoltaic solar cell. *International Communications in Heat and Mass Transfer, 65*, 22-30.

Edwards, D., Denny, V., & Mills, A. (1970). *Transfer Processes an Introduction to Diffusion, Convection, and Radiation.* New York: Holt, Rinehart and Winston.

Elarga, H., Goia, F., Zarrella, A., Monte, A. D., & Benini, E. (2016). Thermal and electrical performance of an

integrated PV-PCM system in double skin façades: A numerical study. *Solar Energy, 136*, 112-124.

Elsafi, A., & Gandhidasan, P. (2015). Performance of a Photovoltaic or Thermal Double-Pass Solar Air Heater with Different Fin Configurations. *Journal of Clean Energy Technologies*, 28-33.

Energy saving trust. (2008). *Domestic heating by gas boiler systems - guidance for installers and specifiers.* London: E&OE.

Evans, J. (2012). *Centrifugal Pump Efficiency—What Is Efficiency?.* Retrieved from https://www.pumpsandsystems.com/topics/pumps/pumps/centrifugal-pump-efficiency-what-efficiency

Farshchimonfared, M., Bilbao, J. I., & Sproul, A. B. (2015). Channel depth, air mass flow rate and air distribution duct diameter optimization of photovoltaic thermal (PVT) air collectors linked to residential buildings. *Renewable Energy, 76*, 27-35.

Fu, K., Kanou, M., Kodama, Y., & Miyatake, O. (2000). Thermal conductivity enhancement of energy storage media using carbon fibers. *Energy Conversion & Management, 41*(14), 1543-1556.

Fundholi, A., Ibrahim, A., Othman, M. Y., Ruslan, M. H., Kazem, H. A., Zaharim, A., & Sopian, K. (2014). Energy and Exergy Analyses on Water based Photovoltaic Thermal (PVT) Collector with Spiral Flow Absorber. *Recent Advances in Energy, Environment and Geology*, 70-74.

Gardas, B. B., & Tendolkar, V. M. (2013). HYBRID PHOTOVOLTAIC THERMAL SYSTEM: A STATE- OF THE-ART LITERATURE REVIEW. *International Journal of Mechanical and Production Engineering, 2*(1), 44-51.

Garg, H., & Adhikari, R. (1999). System performance studies on a photovoltaic/thermal (PVT) air heating collector. *Renewable Energy*, 725-730.

Goetzberger, C. H. (2003). Photovoltaic materials, history, status and outlook. *Material Science and Engineering, 40*(1), 1-46.

Gokmen, N., Hu, W., Hou, P., Chen, Z., Sera, D., & Spataru, S. (2016). Investigation of wind speed cooling effect on PV panels in windy locations. *Renewable Energy, 90*, 283-390.

Guo, C., & Zhang, W. (2008). Numerical simulation and parametric study on new type of high temperature latent heat thermal energy storage system. *Energy Conversion & Management, 49*(5), 919-927.

Hao, G., Yu, X., Huang, Y., Xu, Y., Zhao, X., Li, H., & Chen, M. (2007). Application and Development of Building-Integrated Photovoltaics(BIPV) System in China. *Proceedings of ISES World Congress*, 1685-1689.

Hasan, A., Sarwar, J., Alnoman, H., & Abdelbaqi, S. (2017). Yearly energy performance of a photovoltaic-phase change material (PV-PCM) system in hot climate. *Solar Energy, 146*, 417-429.

Haurant, P., Christophe, M., & Dupeyrat, P. (2014). The PHOTOTHERM project: full scale experimentation and modelling of a photovoltaic - thermal (PV-T) hybrid system for domestic hot water applications. *Energy Procedia, 48*, 581-587.

Hazi, A., Hazi, G., Grigore, R., & Vernica, o. (2014). Opportunity to use PVT systems for water heating in industry. *pplied Thermal Engineering, 63*(1), 151-157.

Ho, C. J., Tanuwijava, A. O., & Lai, C. (2012). Thermal and electrical performance of a BIPV integrated with a microencapsulated phase change material layer. *Energy and Buildings, 50*, 331-338.

Ho, C. J., Jo, B. T., & Lai, C. (2013). Performance assessment of a BIPV integrated with a layer of water –saturated MEPCM. *Energy Build, 67*, 322-333.

Huang, B. J., Yang, P. E., Lin, Y. P., Chen, H. J., Lai, R. C., & Cheng, J. S. (2011). Solar cell junction temperature measurement of PV module. *Solar Energy, 85*(2), 388-392.

Huang, B., Lin, T., Hung, W., & Sun, F. (2001). Performance evaluation of solar photovoltaic/thermal systems. *Solar Energy, 70*(5), 443-448.

Huang, J. M. (2011). The effect of using two PCMs on the thermal regulation performance of BIPV systems. *Solar Energy Materials and Solar Cells, 95*(3), 957-963.

Huang, M. J., Eames, P. C., Norton, B., & Hewitt, N. J. (2011). Natural convection in an internally finned phase change material heat sink for the thermal management of photovoltaics. *Solar Energy Materials and Solar Cells, 95*(7), 1598-1603.

Huang, M., Eames, P., & Norton, B. (2004). Thermal regulation of building-integrated photovoltaics using phase change materials. *International Journal of Heat and Mass Transfer*, 2715-2733.

Huang, M., Eames, P., & Norton, B. (2006). Comparison of a small-scale 3D PCM thermal control model with a validated 2D PCM thermal control model. *Solar Energy Materials and Solar Cells, 90*(13), 1961-1972.

Ibrahim, A. (2009). Performance of photovoltaic thermal collector (PVT) with different. *WSEAS Transactions on Environment and Development*, 321-330.

Ibrahim, A., Fudhol, A., Kamaruzzaman, S., & Othmanb, Y. (2014). Efficiencies and improvement potential of building integrated photovoltaic thermal (BIPVT) system. *Energy Conversion and Management, 77*, 527-534.

Incropera, F. P. (2007). *Fundamentals of Heat and Mass Transfer.* Canada: John Wiley.

Iten, M., Liu, S., Shukla, A., & Silva, P. (2017). Investigating the impact of Cp-T values determined by DSC on the PCM-CFD model. *Applied Thermal Engineering*, 65-75.

JCJ. (2001). *Design Standard for Energy Efficiency of Residential Buildings in Hot Summer and Cold Winter Zone.*

Jean, P. (2013). *Turbulent Flows: Models and Physics.* London: Springer Science & Business Media.

Jegadheeswaran, S., & Pohekar, S. D. (2009). Performance enhancement in latent heat thermal storage system: A review. *Renewable and Sustainable Energy Reviews, 13*(9), 2225-2244.

Joanna, Costello. (2015). Solar Society marks new milestone. *Renewable Energy Focus, 16*, 40-41.

José, T. V., Timo, L., & Kai, S. (2014). Multi-objective optimization of hybrid photovoltaic–thermal collectors integrated in a DHW heating system. *Energy and Buildings, 74*, 78-90.

JTM Plumbing. (2017). *Yorkshire/Lawton/Cubralco Copper Pipe Coils.* Retrieved from http://www.jtmplumbing.co.uk: http://www.jtmplumbing.co.uk/pipe-fittings-c433/copper-pipe-6mm-219mm-c174/yorkshire-lawton-cubralco-copper-pipe-coils-pp10984?utm_source=google&utm_medium=cpc&utm_term=yorkshire-lawton-cubralco-copper-pipe-coils-copper-pipe-8mm-x-1mtr-copper-pipe-8mm-x-1

Kacira, M., Simsek, M., Babur, Y., & Demirkol, S. (2004). Determining optimum tilt angles and orientations of photovoltaic panels in Sanliurfa, Turkey *Renew Energy, 29*, 1265-1275

Kalogirou, S. (2009). *Solar energy engineering: processes and systems.* Oxford: Elsevier.

Kalogirou, S. (2009). Solar energy engineering: processes and systems: chapter 9. *Academic Press*, 469–517.

Kalogirou, S. A. (2009). *Solar Energy Engineering: Processes and Systems.* Oxford: Elsevier.

Kamthania, D., Nayak, S., & Tiwari, G. N. (2011). Performance evaluation of a hybrid photovoltaic thermal double pass facade for space heating. *Energy and Buildings*, 2274-2281.

Kant, K., Shukla, A., Sharma, A., & Biwolec, P. H. (2016). Heat transfer studies of photovoltaic panel coupled with phase change material. *Solar Energy, 140*, 151-161.

Karatepe, E., Boztept, M., & Colak, M. (2007). Development of a suitable model for characterizing photovoltaic arrays with shaded solar cells. *Solar Energy*, 977-992.

Kasaeian, A., Khanjari, Y., Golzari, S., Mahian, O., & Wongwises, S. (2017). Effects of forced convection on the performance of a photovoltaic thermal system: An experimental study. *Experimental Thermal and Fluid Science, 85*, 13-21.

Kenisarin, M., & Mahkamov, K. (2016). Salt hydrates as latent heat storage materials:Thermophysical properties and costs. *Solar Energy Materials and Solar Cells, 145*(3), 255-286.

Khanna, S., Reddy, K. S., & Mallick, T. K. (2017). Performance analysis of tilted photovoltaic system integrated with phase change material under varying operating conditions. *Energy, 133*, 887-899.

Kiijarvi, J. (2011). Darcy Friction Factor Formulae in Turbulent Pipe Flow. *Lunowa Fluid Mechanics Paper*, 1-11.

Kim, J.-H., Park, S.-H., & Kim, J.-T. (2014). Experimental Performance of a Photovoltaic-thermal Air Collector. *Energy Procedia*, 888-894.

Kim, J.-H., Park, S.-H., Kang, J.-G., & Kim, J.-T. (2014). Experimental performance of heating system with building - integrated PVT (BIPVT) collector. *Energy Procedia, 48*, 1374-1384.

Koller, M., Walter, H., & Hameter, M. (2016). Transient Numerical Simulation of the Melting and Solidification Behavior of NaNO3 Using a Wire Matrix for Enhancing the Heat Transfer. *MDPI Energies*, 188-206.

Kosny, J., Biswas, K., Miller, W., & Kriner, S. (2012). Field thermal performance of naturally ventilated solar roof with PCM heat sink. *Solar Energy, 86*(9), 2504-2514.

Krauter, S. (2004). Increased electrical yield via water flow over the front of photovoltaic panels. *Solar Energy Materials and Solar Cells, 82*(1-2), 131-137.

Krauter, S., Araujo, R., Schroer, S., Hanitsch, R., Salhi, M., Triebel, C., & Lemoine, R. (1999). Combined photovoltaic and solar thermal systems for facade integration and building insulation. *Solar Energy*, 239-248.

Kumar, R., & Rosen, M. (2011). A critical review of photovoltaic-thermal solar collectors for air heating. *Applied Energy*, 3603-3614.

Launder, B., & Spalding, D. (1972). *Mathematical Models of Turbulence.* London: Academic Press.

Lee, K., Medina, M. A., & Sun, X. (2015). On the use of plug-and-play walls (PPW) for evaluating thermal enhancement technologies for building enclosures: Evaluation of a thin phase change material (PCM) layer. *Energy and Buildings*, 86-92.

Li, D., Zheng, Y., Liu, C., & Wu, G. (2015). Numerical analysis on thermal performance of roof contained PCM of a single residential building. *Energy Conversion and Management*, 147-156.

Lin, K., Zhang, Y., Xu, X., Di, H., Yang, R., & Qin, P. (2004). Modeling and simulation of under-floor electric heating system with shape-stabilized PCM plates. *Building and Environment*, 1427-1434.

Ling, Z., Zhang, Z., Shi, G., Fang, X., Wang, L., Gao, X., & Liu, X. (2014). Review on thermal management systems using phase change materials for electronic components,

Li-ion batteries and photovoltaic modules. *Renewable and Sustainable Energy Reviews, 31*, 427-438.

Liu, B., & Jordan, R. (1963). The long term average performance of flat-plate solar energy collectors. *Solar Energy, 7*(2), 53-73.

Mailuha, J. T., Murase, H., & Inoti, I. K. (1994). Knowledge engineering-based studies on solar energy utilization in Kenya. *Agriculture Mechanization in Asia, Africa, and Latin America*, 13-16.

Meng, Z., & Zhang, P. (2017). Experimental and numerical investigation of a tube-in-tank latent thermal energy storage unit using composite PCM. *Applied Energy, 190*(1), 524-539.

Merrigan, U. P. (1982). *Sunlight to Electricity.* Cambridge, Massachusetts: MIT Press.

Mickpeterson.org. (2017, 02 05). *PCMSelection.* Retrieved from http://www.mickpeterson.org: http://www.mickpeterson.org/Classes/Design/2011_12/comfort/dec_images_x/PCMSelection.pdf

Mojiri, A., Stanley, C., & Rosengarten, G. (2014). Spectrally splitting hybrid photovoltaic/thermal receiver design for a linear concentrator. *Energy Procedia, 48*, 618-627.

Mojumder, J. C., Chong, W. T., Ong, H. C., Leong, K. Y., & Mamoom, A. A. (2016). An experimental investigation on performance analysis of air type photovoltaic thermal collector system integrated with cooling fins design. *Energy and Buildings, 130*, 272-285.

MW Profiles. (2017). *Aluminium Round Tube / Pipe - VARIOUS SIZES - 1 METER LONG.* Retrieved from ebay.co.uk: http://www.ebay.co.uk/itm/Aluminium-Round-Tube-Pipe-VARIOUS-SIZES-1-METER-LONG-/282093115539?var=&hash=item41ae0f5893:m:mb9QeqM8wI00qCytlkOF5OA

NASA. (2015). *Navier-Stokes Equations, 3 Dimensional-Unsteady*. (NASA) Retrieved 03 01, 2017, from

https://www.grc.nasa.gov/www/k-12/airplane/nseqs.html

NEF. (2017). *Types of Photovoltaic (PV) Cells*. Retrieved from National Energy Foundation: http://www.nef.org.uk/knowledge-hub/solar-energy/types-of-photovoltaic-pv-cells

Nithyanandam, K., Pitchumani, R., & Mathur, A. (2014). Analysis of a latent thermocline storage system with encapsulated phase change materials for concentrating solar power. *Applied Energy, 113*, 1446-1460.

Oliver, M., & Jackson, T. (2001). Energy and economic evaluation of building-integrated photovoltaics. *Energy, 26*(4), 431-439.

Othman, M. Y., Hamid, S. A., Tabook, M. A., Sopian, K., Rosian, M., & Ibarahim, Z. (2016). Performance analysis of PVT Combi with water and air heating system: An experimental study. *Renewable Energy, 86*, 716-722.

OXY. (2016). *Calcium Chloride - A Guide to Physical Properties.* Retrieved from http://www.oxy.com: http://www.oxy.com/OurBusinesses/Chemicals/Products/Documents/CalciumChloride/173-01791.pdf

Pasupathy, A., Velraj, R., & Seeniraj, R. (2008). Phase change material-based building architecture for thermal management in residential and commercial establishments. *Renewable and Sustainable Energy Reviews, 12*(1), 39-64.

PlusICE. (2013). *PlusICE PCM (HYDRATED SALT) (S) RANGE.* Retrieved from pcmproducts.net: http://www.pcmproducts.net/files/PlusICE%20Range-2013.pdf

Poirier, D., & Salcudean, M. (1988). On numerical methods used in mathematical modelling of phase change in liquid metals. *ASME J. Heat Transfer*, 562-570.

Preet, S., Bhushan, B., & Mahajan, T. (2017). Experimental investigation of water based photovoltaic/thermal (PV/T)

system with and without phase change material (PCM). *Solar Energy*, 155, 1104-1120.

Puertas, A. M., Romero-Cano, M. S., Javier De Las Nieves, F., Rosiek , S., & Batlles, F. (2017). Simulations of Melting of Encapsulated CaCl2·6H2O for Thermal Energy Storage Technologies. *MDPI Energies*, 10,568.

Qiu, Z., Ma, M. X., Zhao, X, Li, P., & Ali, S. (2016). Experimental investigation of the energy performance of a novel Micro-encapsulated Phase Change Material (MPCM) slurry based PV/T system. *Applied Energy*, 260-271.

Radziemska, E. (2003). The effect of temperature on the power drop in crystalline silicon solar cells. *Renewable Energy*, 1-12.

Radziemska, E. K. (2015). Degradation of electrical performance of a crystalline photovoltaic module due to dust deposition in northern Poland. *Renewable Energy*, 418-426.

Rapid Fab. (2017). *Rapid Fab Aluminium Prices.* Retrieved from http://www.fab.net.au: http://www.fab.net.au/rapidfab/Aluminium%20Prices.pdf

Renno, C. (2014). Optimization of a concentrating photovoltaic thermal (CPVT) system. *Applied Thermal Engineering, 67*(1-2), 396-408.

Rockendorf, G., Sillmann, R., Podlowski, L., & Lizenburger, B. (1999). PV-hybrid and thermoelectric collectors. *Solar Energy, 67*(4-6), 227-237.

RubiTherm. (2017, 04 05). *Data Sheet- RT25*. Retrieved from https://www.rubitherm.eu/

Sahoo, S. K., Das, M. K., & Rath, P. (2016). Application of TCE-PCM based heat sinks for cooling of electronic components: A review. *Renewable and Sustainable Energy Reviews*, 550-582.

Sattari, H., Mohebbi, A., Afsahi, M. M., & Yancheshme, A. A. (2017). CFD simulation of melting process of phase change materials (PCMs) in a spherical capsule. *International Journal of Refrigeration*, 209-218.

savENRG. (2015). *Technical Data Sheet HS22P.* Retrieved from https://savenrg-pcm-pouch.com/

Schiro, F., Benato, A., Stoppato, A., & Destro, N. (2017). Improving photovoltaics efficiency by water cooling: Modelling and experimental approach. *Energy*, In press.

Schott, T. (1985). Operational temperatures of PV modules. *International 6th PV Solar Energy Conference*, 392-396.

Sebti, S. S., Mastiani, M., Mirzaei, H., Dadvand, A., Kashani, S., & Hosseini, S. A. (2013). Numerical study of the melting of nano-enhanced phase change material in a square cavity. *Applied Physics and Energy*, 307-316.

Sendy, A. (2017). *Pros and Cons of Monocrystalline vs. Polycrystalline Solar Panels*. Retrieved from Solarreviews: http://www.solarreviews.com/solar-energy/pros-and-cons-of-monocrystalline-vs-polycrystalline-solar-panels/

Sharma, A., Tyagi, V. V., Chen, C., & Buddhi, D. (2009). Review on thermal energy storage with phase change materials and applications. *Renewable and Sustainable Energy Reviews*, 318-345.

Shatikian, V., Ziskind, G., & Letan, R. (2008). Numerical investigation of a PCM-based heat sink with internal fins: Constant heat flux. *International Journal of Heat and Mass Transfer, 51*(5-6), 1488-1493.

Singh, P., Singh, S., Lal, M., & Husain, M. (2008). Temperature dependence of I–V characteristics and performance parameters of silicon solar cell. *Solar Energy Materials and Solar Cells*, 1611-1616.

Sobhnamayan, F., Sarhaddi, F., Alavi, M., Farahat, S., & Yazdanpanahi, J. (2014). Optimization of a solar photovoltaic thermal (PVT) water collector based on exergy concept. *Renewable Energy, 68*, 356-365.

Solanki, S., Dubey, S., & Tiwari, A. (2009). Indoor simulation and testing of photovoltaic thermal (PVT) air collectors. *Applied Energy, 86*(11), 2421-2428.

SOLAR, B. (2014). *Solar modules BP280F & BP275F.* Retrieved 07 22, 2014, from http://www.posharp.com/bp275f-solar-panel-from-bp-solar_p166512668d.aspx

Sopian, K., Yigit, K. S., Liu, H. T., Kakac, S., & Veziroglu, T. N. (1996). PERFORMANCE ANALYSIS OF PHOTOVOLTAIC THERMAL AIR HEATERS. *Energy Conversion and Management, 37*(11), 1657-1670.

Sparrow, E. M., & Tian, K. K. (1977). Forced Convection Heat Transfer at an Inclined and Yawed Square Plate—Application to Solar Collectors. *Heat Transfer, 99*(4), 507-512.

Srinivas, M., & Jayaraj, S. (2013). Performance Study of a Double Pass, Hybrid -Type Solar Air Heater with Slats. *International Journal of Energy Engineering*, 112-121.

Stropnik, R., & Stritih, U. (2016). Increasing the efficiency of PV panel with the use of PCM. *Renewable Energy, 97*, 671-679.

Stropnik, R., & Stritih, U. (2016). Increasing the efficiency of PV panel with the use of PCM. *Renewable Energy*, 671-679.

Su , D., Jia, Y., Huang, X., Alva, G., Tang, Y., & Fang, G. (2016). Dynamic performance analysis of photovoltaic–thermal solar collector with dual channels for different fluids. *Energy Conversion and Management, 120*(15), 13-24.

Subramanian, R. (2014). *Heat transfer to or from a fluid flowing through a tube.* Retrieved 07 28, 2016, from semanticscholar.org: https://pdfs.semanticscholar.org/809a/b85fce9fb51afe436231072631149d15179a.pdf

Teo, H. G., Lee, P. S., & Hawlader, M. N. (2012). An active cooling system for photovoltaic modules. *Applied Energy, 90*(1), 309-315.

The Engineering Tool Box. (2016). *Convective Heat transfer*. (www.EngineeringToolBox.com) Retrieved 07 24, 2016, from http://www.engineeringtoolbox.com: http://www.engineeringtoolbox.com/convective-heat-transfer-d_430.html

Theodore, L. (2011). *Heat Transfer Applications for the Practicing Engineer.* New York: Wiley.

Tripanagnostopoulos, Y., Souliotis, M., Yianoulis, P., & Nousia, T. (2002). Hybrid photovoltaic/thermal solar systems. *Solar Energy, 72*(3), 217-234.

U.S. EIA. (2016). *International Energy Outlook 2016.* New York: eia.

Vasel, A., & Lakovidis, F. (2017). The effect of wind direction on the performance of solar PV plants. *Energy Conversion and Management, 153*, 455-461.

Vats, K., Tomar, V., & Tiwari, G. (2012). Effect of packing factor on the performance of a building integrated semitransparent photovoltaic thermal (BISPVT) system with air duct. *Energy and Buildings, 53*, 159-165.

Versteeg, H., & Malalasekera, W. (1995). *An Introduction To Computational Fluid Dynamics.* Essex: Longman Scientific& Technical.

Vikas, Yadav, A., & Soni, S. K. (2017). Simulation of Melting Process of a Phase Change Material (PCM) using ANSYS (Fluent). *International Research Journal of Engineering and Technology (IRJET)*, 3289-3294.

Wang, P., Yao, H., Lan, Z., Peng, Z., Huang, Y., & Ding, Y. (2016). Numerical investigation of PCM melting process in sleeve tube with internal fins. *Energy Conversion and Management*, 428-435.

Warhaft, Z. (1997). *The Engine and the Atmosphere: An Introduction to Engineering.* Cambridge: Cambridge University Press.

Wu, Y., Tang, Y., Li, Z., Ding, X., Yuan, W., Zhao, X., & Yu, B. (2016). Experimental investigation of a PCM-HP heat sink on its thermal performance and anti-thermal-shock capacity for high-power LEDs. *Applied Thermal Engineering*, 192-203.

Xu, X., Meyers, M., Sammakia, B., & Murray, B. (2012). Thermal modeling of hybrid concentrating PVT collectors with tree-shaped channel networks cooling system. *Thermal and Thermomechanical Phenomena in Electronic Systems*, 1131-1139.

Xu, Y., Kong, X., Zeng, Y., Tao, S., & Xiao, X. (2014). A modeling method for photovoltaic cells using explicit equations and optimization algorithm. *International Journal of Electrical Power & Energy Systems, 59*, 23-28.

Xue, D. (1991). *Air Conditioning (1st Edition).* Beijing: Tsing Hua University.

Zakharchenko, R., Licea-Jimenez, L., Perez-Garcıa, S., Vorobiev, P., Dehesa-Carrasco, U., Perez-Robles, J., & Vorobiev, Y. (2004). Photovoltaic solar panel for a hybrid PVThermal system. *Solar Energy Materials and Solar Cells, 82*(1-2), 253-261.

Zhang, X., Zhao, X., Smith, S., Xi, J., & Yu, X. (2012). Review of R&D progress and practical application of the solar photovoltaic/thermal (PVT) technologies. *Renewable and Sustainable Energy Reviews, 16*(1), 599-617.

APPENDIX

1. Data of PV model validation

Air temp=20℃		Radiation=450W/m^2	
Wind speed	Analytical	CFD	RMSE
0.1	70.72	70.17	6.05E-05
0.5	60.77	60.22	8.19E-05
1	52.15	51.75	5.88E-05
2	43.70	43.45	3.38E-05
3	39.54	39.38	1.58E-05
4	36.98	36.99	7.31E-08
5	35.21	35.23	3.23E-07
			0.0059914

wind speed=5 m/s		radiation=450 W/m^2	
Air temp	Analytical	CFD	RMSE
10	25.22	25.01	6.93E-05
15	30.22	30.01	4.83E-05
20	35.21	35.23	3.23E-07
25	40.21	40.24	5.57E-07
30	45.21	45.25	7.83E-07
			0.004884

wind speed=5 m/s		air temp=20℃	
Solar Radiation	Analytical	CFD	RMSE
300	30.15	30.05	1.1E-05
400	33.52	33.35	2.57E-05
500	36.89	36.72	2.12E-05
600	40.26	40.07	2.23E-05
700	43.63	43.41	2.54E-05
			0.004597

2. Sample of steady state PV temperature calculation

Solar radiation	Ambient Temp	Short Wave	long wave	Tfilm	cell temp	Rayleigh	Ψ	Nufree	hfree	Re	hforce	Nuforce	Nuconv	hconv	qconv	q total	Cell temp+1
600.00	20.00	264.55	0.00	17.50	15.00	4442407.23	0.35	24.29	3.43	49979.27	20.93	148.19	148.41	20.96	65.07	329.62	15.59
600.00	20.00	264.55	0.00	17.79	15.59	3920342.76	0.35	23.56	3.33	49979.27	20.93	148.19	148.39	20.95	57.42	321.96	16.16
600.00	20.00	264.55	0.00	18.08	16.16	3410402.14	0.35	22.78	3.22	49979.27	20.93	148.19	148.37	20.95	49.94	314.49	16.72
600.00	20.00	264.55	0.00	18.36	16.72	2912301.24	0.35	21.92	3.10	49979.27	20.93	148.19	148.35	20.95	42.64	307.19	17.27
600.00	20.00	264.55	0.00	18.63	17.27	2425762.63	0.35	20.97	2.96	49979.27	20.93	148.19	148.33	20.95	35.51	300.06	17.80
600.00	20.00	264.55	0.00	18.90	17.80	1950515.37	0.35	19.90	2.81	49979.27	20.93	148.19	148.31	20.94	28.55	293.09	18.33
600.00	20.00	264.55	0.00	19.16	18.33	1486294.88	0.35	18.64	2.63	49979.27	20.93	148.19	148.29	20.94	21.75	286.30	18.84
600.00	20.00	264.55	0.00	19.42	18.84	1032842.75	0.35	17.07	2.41	49979.27	20.93	148.19	148.27	20.94	15.11	279.66	19.34
600.00	20.00	264.55	0.00	19.67	19.34	589906.56	0.35	14.93	2.11	49979.27	20.93	148.19	148.24	20.93	8.63	273.17	19.82
600.00	20.00	264.55	0.00	19.91	19.82	157239.64	0.35	10.92	1.54	49979.27	20.93	148.19	148.21	20.93	2.30	266.84	20.30
600.00	20.00	264.55	-0.01	20.15	20.30	265399.22	0.35	12.35	1.74	49979.27	20.93	148.19	148.22	20.93	-3.88	260.66	20.76
600.00	20.00	264.55	-0.01	20.38	20.76	678244.80	0.35	15.44	2.18	49979.27	20.93	148.19	148.25	20.93	-9.92	254.62	21.22
600.00	20.00	264.55	-0.01	20.61	21.22	1081520.87	0.35	17.26	2.44	49979.27	20.93	148.19	148.27	20.94	-15.83	248.71	21.66
600.00	20.00	264.55	-0.01	20.83	21.66	1475446.54	0.35	18.60	2.63	49979.27	20.93	148.19	148.29	20.94	-21.59	242.94	22.09
600.00	20.00	264.55	-0.01	21.05	22.09	1860236.33	0.35	19.67	2.78	49979.27	20.93	148.19	148.31	20.94	-27.23	237.31	22.52
600.00	20.00	264.55	-0.01	21.26	22.52	2236100.14	0.35	20.57	2.90	49979.27	20.93	148.19	148.33	20.94	-32.73	231.80	22.93
600.00	20.00	264.55	-0.01	21.46	22.93	2603243.22	0.35	21.34	3.01	49979.27	20.93	148.19	148.34	20.95	-38.11	226.42	23.33
600.00	20.00	264.55	-0.01	21.67	23.33	2961866.27	0.35	22.01	3.11	49979.27	20.93	148.19	148.36	20.95	-43.37	221.17	23.73
600.00	20.00	264.55	-0.01	21.86	23.73	3312165.51	0.35	22.62	3.19	49979.27	20.93	148.19	148.37	20.95	-48.50	216.03	24.11
600.00	20.00	264.55	-0.01	22.06	24.11	3654332.77	0.35	23.16	3.27	49979.27	20.93	148.19	148.38	20.95	-53.52	211.02	24.49
600.00	20.00	264.55	-0.01	22.24	24.49	3988555.52	0.35	23.66	3.34	49979.27	20.93	148.19	148.39	20.95	-58.42	206.12	24.86
600.00	20.00	264.55	-0.01	22.43	24.86	4315017.03	0.35	24.12	3.41	49979.27	20.93	148.19	148.41	20.96	-63.20	201.33	25.22
600.00	20.00	264.55	-0.01	22.61	25.22	4633896.41	0.35	24.54	3.47	49979.27	20.93	148.19	148.42	20.96	-67.88	196.65	25.57
600.00	20.00	264.55	-0.01	22.78	25.57	4945368.70	0.35	24.93	3.52	49979.27	20.93	148.19	148.43	20.96	-72.45	192.09	25.91
600.00	20.00	264.55	-0.01	22.95	25.91	5249604.98	0.35	25.30	3.57	49979.27	20.93	148.19	148.44	20.96	-76.91	187.62	26.24
600.00	20.00	264.55	-0.02	23.12	26.24	5546772.43	0.35	25.64	3.62	49979.27	20.93	148.19	148.45	20.96	-81.27	183.26	26.57
600.00	20.00	264.55	-0.02	23.28	26.57	5837034.41	0.35	25.96	3.67	49979.27	20.93	148.19	148.46	20.96	-85.53	179.00	26.89
600.00	20.00	264.55	-0.02	23.44	26.89	6120550.58	0.35	26.26	3.71	49979.27	20.93	148.19	148.47	20.96	-89.69	174.84	27.20
600.00	20.00	264.55	-0.02	23.60	27.20	6397476.93	0.35	26.54	3.75	49979.27	20.93	148.19	148.48	20.97	-93.75	170.78	27.50
600.00	20.00	264.55	-0.02	23.75	27.50	6667965.91	0.35	26.81	3.79	49979.27	20.93	148.19	148.49	20.97	-97.72	166.81	27.80
600.00	20.00	264.55	-0.02	23.90	27.80	6932166.46	0.35	27.07	3.82	49979.27	20.93	148.19	148.49	20.97	-101.60	162.93	28.09
600.00	20.00	264.55	-0.02	24.05	28.09	7190224.13	0.35	27.31	3.86	49979.27	20.93	148.19	148.50	20.97	-105.39	159.14	28.38

3. Calculation of PV material properties

Elements of module	Density	Specific heat	Thickness	Surface area	Heat capacity	Weight	Thermal conductivity
	(kg/m^3)	(J/kgK)	(m)	(m^2)	(J/K)	(kg)	(W/mK)
Toughened glass cover	3000	500	0.003	0.621	2794.50	5.59	0.8
Monocrystalline silicon PV cell	2330	677	0.0005	0.621	489.79	0.72	148
Tri-laminated Polyester	1200	1250	0.0005	0.621	465.75	0.37	0.17
Whole Panel	2691.25	560.96	0.004	0.621	3750.04	6.69	0.59

4. Data of Heat transfer validation

Velocity	Mass flow rate	Re	Pr	Nu	Numerical h_{conv}	CFD h_{conv}	RMSE
m/s	Kg/s				W/m^2K	W/m^2K	
0.004	0.000451256	48	5.3	3.755997	187.7998	181.85	0.001004
0.008	0.000902511	96	5.3	3.899674	194.9837	184.82	0.002717
0.01	0.001128139	120	5.3	3.968288	198.4144	187.08	0.003263
0.02	0.002256278	240	5.3	4.287417	214.3709	200.96	0.003914
0.04	0.004512557	480	5.3	4.843133	242.1566	229.98	0.002528
0.06	0.006768835	720	5.3	5.326017	266.3009	254.38	0.002004
0.08	0.009025114	960	5.3	5.758096	287.9048	278.8	0.001
0.1	0.011281392	1200	5.3	6.151631	307.5816	301.27	0.000421
0.15	0.016922088	1800	5.3	7.012749	350.6375	353.6618	7.44E-05

Velocity	Mass flow rate	Re	Pr	Nu	Numerical h_{conv}	CFD h_{conv}	RMSE
m/s	Kg/s				W/m^2K	W/m^2K	
0.35	0.039484872	4200	5.43	35.83003	1791.502	1613.28	0.009897
0.4	0.045125568	4800	5.43	39.8695	1993.475	1804.33	0.009003
0.45	0.050766264	5400	5.43	43.80894	2190.447	1987.03	0.008624
0.5	0.05640696	6000	5.43	47.66162	2383.081	2174	0.007698
0.55	0.062047656	6600	5.43	51.43786	2571.893	2370.7	0.00612
0.6	0.067688352	7200	5.43	55.14597	2757.298	2557.68	0.005241
0.65	0.073329048	7800	5.43	58.79271	2939.635	2747.43	0.004275

5. Data of PCM RT-25 validation

Charging Process			
Time Step (h)	PCM-RT25 (℃)	Iten et al. (℃)	Numerical (℃)
0	16	16	16
0.5	19.9	20	20.5
1	22.18	22	22.5
1.5	23.38	23	23.2
2	24.4	24	24.5
2.3	26.05	25	26
2.4	29.78	33	30
2.5	32.24	33.7	32.5
2.7	33.17	34.8	34
2.8	33.58	35.2	34.5
3	34.07	35.5	35
RMS		0.04522	0.01768

Discharging Process			
Time Step (h)	PCM-RT25 (℃)	Iten et al. (℃)	Numerical (℃)
0	30	30	30
0.1	25.61	26	26.3
0.2	25.54	25.5	25.7
0.3	25.498	25.4	25.5
0.5	25.46	25.3	25.3
1	25.196	25	25
1.5	24.5478	24.5	24.7
2	23.013	23.3	23.6
2.5	20.66	21	21.8
RMS		0.0093	0.0226

6. Data of PCM HS22P validation – Timestep

Charging				
	0.05s	0.1s	1s	10s
Time	Temperature			
s	℃	℃	℃	℃
0	20	20	20	20
1800	22.50	22.50	22.50	22.48
3600	22.71	22.72	22.72	22.70
5400	22.86	22.88	22.88	22.87
7200	23.00	23.02	23.02	23.02
9000	23.11	23.16	23.16	23.15
10800	23.23	23.28	23.28	23.28
12600	23.34	23.41	23.41	23.40
14400	23.47	23.56	23.56	23.54
16200	23.61	23.75	23.75	23.71
18000	24.24	24.88	24.87	24.75
19800	25	25	25	25

Discharging				
	0.05s	0.1s	1s	10s
Time	Temperature			
s	℃	℃	℃	℃
0	25	25	25	25
1800	22.30	22.30	22.30	22.31
3600	22.00	22.00	22.00	22.00
5400	21.75	21.76	21.76	21.77
7200	21.53	21.55	21.55	21.56
9000	21.22	21.27	21.27	21.29
10800	20.01	20	20	20.03
12600	20	20	20	20

7. Data of PCM HS22P validation – Solid vs. Solidification & Melting

Charging		
	Solid	Solidification & Melting
Time	Temperature	Temperature
s	℃	℃
0	20	20
1800	22.50	22.48
3600	22.71	22.68
5400	22.86	22.85
7200	23.00	22.99
9000	23.11	23.11
10800	23.23	23.24
12600	23.34	23.35
14400	23.47	23.49
16200	23.61	23.64
18000	24.24	24.32
19800	25	25

Discharging		
	Solid	Solidification & Melting
Time	Temperature	Temperature
s	℃	℃
0	25	25
1800	22.30	22.30
3600	22.00	22.00
5400	21.75	21.76
7200	21.53	21.55
9000	21.22	21.28
10800	20.01	20
12600	20	20

8. Data of PV temperature - PV only – Summer - Nottingham

Time	PV Temp windy (℃)	PV Temp calm (℃)	Air Temp(℃)	Solar rad(W/m^2)
4:00	13.17	15.48	12	16
5:00	15.57	21.69	12	103
6:00	20.34	31.41	13	241
7:00	26.31	41.71	15	389
8:00	31.11	50.17	16	532
9:00	35.32	57.18	17	655
10:00	38.96	62.91	18	757
11:00	41.66	66.83	19	824
12:00	43.17	68.76	20	845
13:00	43.26	67.91	21	811
14:00	41.32	64.44	21	736
15:00	39.12	59.49	22	614
16:00	34.3	51.26	21	467
17:00	30.2	42.96	21	312
18:00	25.56	34.11	20	176
19:00	22.23	26.18	20	53
20:00	19	19	19	0

9. Data of PV temperature - PV only – Winter - Nottingham

PV only	PV Temp windy (℃)	PV Temp calm (℃)	Air Temp(℃)	Solar rad(W/m^2)
8:00	1.1	3.44	0	17
9:00	4.73	11.45	1	110
10:00	7.33	17.72	1	203
11:00	9.94	22.33	2	261
12:00	11.51	24.55	3	282
13:00	9.94	22.33	2	261
14:00	7.99	17.89	2	191
15:00	4.34	10.45	1	96
16:00	0.97	3.03	0	12

10. Data of PVT-PCM design - Summer – Nottingham

Time	PV water outlet Temp(℃)	PCM water outlet Temp(℃)	PV Temp(℃)	PCM Temp(℃)	Air Temp(℃)	Solar rad(W/m^2)
4:00	12.13	12.08	12.16	12.07	12	16
5:00	13.27	12.73	13.2	12.84	12	103
6:00	15.88	14.48	15.63	14.76	13	241
7:00	19.62	17.43	19.18	17.89	15	389
8:00	23.73	20.96	23.17	21.34	16	532
9:00	29.28	22.46	28.51	22.09	17	655
10:00	31.87	22.71	30.99	22.21	18	757
11:00	33.06	22.89	32.1	22.41	19	824
12:00	33.31	23.08	32.33	22.91	20	845
13:00	32.61	23.28	31.72	23.7	21	811
14:00	32.63	23.65	31.76	24.73	21	736
15:00	31.02	23.87	30.35	25.34	22	614
16:00	29.21	23.96	28.76	25.51	21	467
17:00	28.03	24.04	27.69	25.5	21	312
18:00	26.18	23.87	26	25.03	20	176
19:00	24.95	23.64	24.89	24.47	20	53

11. Data of PVT-PCM design - Winter – Nottingham

Time	PV water outlet Temp(℃)	PCM water outlet Temp(℃)	PV Temp(℃)	PCM Temp(℃)	Air Temp(℃)	Solar rad(W/m^2)
8:00	0.1	0.08	0.08	0.1	0	17
9:00	2.14	1.21	1.86	1.39	1	110
10:00	3.38	2.85	3.79	3.1	1	203
11:00	6.95	5.86	6.75	6.34	2	261
12:00	9.99	9.02	9.74	9.52	3	282
13:00	13.11	12.15	12.66	12.64	2	261
14:00	15.19	14.346	14.6	14.86	2	191
15:00	15.83	15.33	15.51	15.51	1	96
16:00	15.6	15.58	15.56	15.59	0	12

12. Data of PV temperature - PV only – Summer – Shanghai

Time	PV Temp windy (℃)	PV Temp calm (℃)	Air Temp(℃)	Solar rad(W/m^2)
5:00	30.47	33.056	29	22
6:00	35.61	43.81	30	178
7:00	42.27	56.56	31	395
8:00	49.7	68.75	33	608
9:00	55.16	77.66	34	786
10:00	60.31	84.85	36	915
11:00	62.75	88.16	37	975
12:00	63.71	88.97	38	975
13:00	62.12	86.33	38	911
14:00	59.03	81.02	38	786
15:00	54.68	73.29	38	612
16:00	48.3	62.23	37	399
17:00	41.69	49.74	36	181
18:00	37.56	40.18	36	23

13. Data of PV temperature - PV only – Winter - Shanghai

PV only	PV Temp windy (℃)	PV Temp calm (℃)	Air Temp(℃)	Solar rad(W/m^2)
7:00	-0.75	2.45	-2.3	33
8:00	4.62	14.28	-1.1	181
9:00	10.76	26.51	0.1	359
10:00	15.82	35.56	1.3	500
11:00	18.33	40.19	1.6	581
12:00	18.69	40.68	1.8	587
13:00	17.11	37.23	2.1	518
14:00	13.07	29.46	1.7	385
15:00	7.89	18.49	1.4	209
16:00	3.04	7.05	1	50

14. Data of PVT-PCM design - Summer – Shanghai

Time	PV water outlet Temp(℃)	PCM water outlet Temp(℃)	PV Temp(℃)	PCM Temp(℃)	Air Temp(℃)	Solar rad(W/m^2)
5:00	29.16	29.11	29.2	29.12	29	22
6:00	31.30	30.5	31.13	30.68	30	178
7:00	35.73	32.22	35.29	32.04	31	395
8:00	39.63	32.52	38.97	32.13	33	608
9:00	42.05	32.75	41.11	32.26	34	786
10:00	44.11	33.01	43.06	32.58	36	915
11:00	44.59	33.29	43.51	33.39	37	975
12:00	44.78	33.79	43.71	34.91	38	975
13:00	43.88	34.31	43.02	36.1	38	911
14:00	43.69	34.95	42.81	37.25	38	786
15:00	41.94	35.48	41.28	37.77	38	612
16:00	40.24	35.85	39.81	37.79	37	399
17:00	37.19	35.32	37.02	36.48	36	181
18:00	35.41	34.72	35.37	35.34	36	23

15. Data of PVT-PCM design - Winter – Shanghai

Time	PV water outlet Temp(℃)	PCM water outlet Temp(℃)	PV Temp(℃)	PCM Temp(℃)	Air Temp(℃)	Solar rad(W/m^2)
7:00	-2.11	-2.16	-2.15	-2.15	-2.3	33
8:00	-0.17	-0.79	-0.18	-0.65	-1.1	181
9:00	3.38	2.12	3.04	2.42	0.1	359
10:00	8.46	6.56	7.9	7.03	1.3	500
11:00	14	11.82	13.29	12.36	1.6	581
12:00	19.24	17.1	18.58	17.63	1.8	587
13:00	23.5	21.69	22.9	22.15	2.1	518
14:00	26.02	25.14	25.66	24.84	1.7	385
15:00	27.38	26.71	27.21	26.88	1.4	209
16:00	27.84	27.56	27.78	27.64	1	50

16. Manufacturer datasheet of BP275 PV panel

BP SOLAR

SOLAR MODULES

BP280F & BP275F

SOLAR MODULES

PRODUCT FEATURES

- High efficiency monocrystalline silicon cells.
- Designed for maximum reliability and minimum maintenance.
- Produced using in-house technology in cell manufacturing and encapsulation.
- Highly resistant to water, abrasion, hail impact and other environmental factors.
- Lightweight anodised aluminium frame or laminate version only.
- All proven products. Only materials with extensive field experience used.
- Designed and manufactured to comply with European and International standards. European specification ESTI503.
- 20 year product warranty



APPLICATIONS

GRID-CONNECT

Rain-screen Façades
Sun-shade & Balcony Products
Roofing Products
Domestic/Residential Roof Products
Multi-Kilowatt and Megawatt Power Stations
Generator-type Power for centralised locations.

TELECOMS

Microwave Repeaters and Terminals.
VHF/UHF Radio Systems and Repeaters.
Mobile Radio Systems.
HF/SSB Radio Transceivers
TV Translators
Radio Telephones & Telemetry.
Radio Navigational Aids
Fibre Optic Repeaters
Miscellaneous Packages DC Loads

RURAL INFRASTRUCTURE

Community/Village Water Pumping
Community/Village Water Purification
Community/Village Refrigeration, Medical and Domestic
Community/Village Lighting
Community/Village Television & Video
Individual House Power
Community/Village Power

SPECIALIST

Cathodic Protection
Aircraft Obstruction Lighting
Lighthouse Lighting Systems
Racon Systems
Beacon Buoy Lighting Systems
Fog Warning Systems



CELL SPECIFICATIONS

36 series connected, 125 mm monocrystalline silicon pseudo square cells.

TECHNICAL SPECIFICATIONS

Module Catalogue Number	BP280	BP275
Nominal Peak Power (Pmax)	80.00W	75.00W
Voltage @ maximum power (V mp)	17.00V	17.00V
Current @ maximum power (I mp)	4.70A	4.45A
Short-circuit current (I sc)	5.0A	4.75A
Open-circuit Voltage (V oc)	21.8V	21.40V

Dimensions F=Framed L=Laminate

BP275/280F	Length 1188 mm	Width 530 mm
	Depth 43.5 mm	Weight 7.5 kg
BP275/280L	Length 1183 mm	Width 525 mm
	Depth 4 mm (±1 mm)	Weight 5.5 kg

17. Manufacturer datasheet of PCM-HS22P

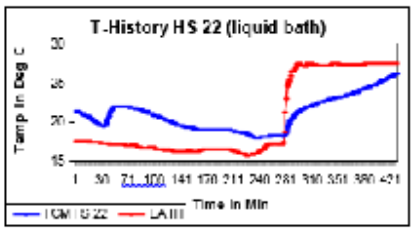
savENRG

Technical Data Sheet

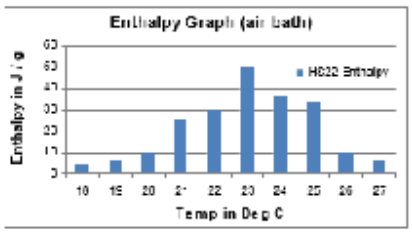
Product : HS22P

Description : Inorganic material

Appearance : Brown / gray colored liquid above 25 °C



T History graph for HS22P



Enthalpy Vs Temp for HS22P

Fig1: T-History graph for HS22 done in liquid & air bath

A 30 g sample is taken in a test tube in molten condition and placed in a temperature-controlled bath. A temperature sensor is placed in the test tube and bath to record the temperatures using a data logger. The bath is maintained at around 12 °C during the freezing cycle and at around 32 °C during the melting cycle.

Property	Value*	Test Method	Test Conditions (if any)
Melting Temp (°C)	23.0	T-History	@ 32 °C Liquid Bath
Freezing Temp (°C)	22.0	T-History	@ 12 °C Liquid Bath
Latent Heat (kJ/kg)	185	T-History	@ 20 to 23 °C
Liquid Density (kg/m^3)	1540	ASTM D891-95	@ 30 °C
Solid Density (kg/m^3)	1840	Internal	@ 0 °C
Liquid Specific Heat (kJ/kgK)	3.04	Calorimeter	@ 31 °C
Solid Specific Heat (kJ/kgK)	2.2	Calorimeter	@ 0 °C
Liquid Thermal Conductivity (W/mK)	0.56	KD2Pro	@ 30 °C
Solid Thermal Conductivity (W/mK)	1.13	KD2Pro	@ 15 °C
Base Material	Inorganic		
Congruent Melting	YES		
Flammability	NO		
Thermal Stability (Cycles)	~2000	Internal	
Maximum Operating Temperature (°C)	~80		
Flash Point (°C)	NA		

* Nominal Values. Actual values mentioned in Test Certificate

WWW.RGEES.COM
© 2015 RGEES LLC. ALL RIGHTS RESERVED

18. Manufacturer datasheet of PCM-S32

PCM — *PlusICE PCM (HYDRATED SALT) (S) RANGE* — 2013-1

PCM Type	Phase Change Temperature (°C)	Phase Change Temperature (°F)	Density (kg/m3)	Density (lb / ft3)	Latent Heat Capacity (kJ/kg)	Latent Heat Capacity (Btu / lb)	Volumetric Heat Capacity (MJ/m3)	Volumetric Heat Capacity (Btu / ft3)	Specific Heat Capacity (kJ/kg K)	Specific Heat Capacity (Btu / lb °F)	Thermal Conductivity (W/m K)	Thermal Conductivity (Btu / ft2h°F)	Max Operating Temp (°C)	Max Operating Temp (°F)
HYDRATED SALT BASED PCM SOLUTIONS														
S117	117	243	1,450	90.5	160	69	232	6,227	2.61	0.618	0.700	0.405	140	284
S89	89	192	1,550	96.8	151	65	234	6,282	2.48	0.588	0.670	0.387	120	248
S83	83	181	1,600	99.9	141	61	226	6,055	2.31	0.547	0.620	0.358	120	248
S72	72	162	1,666	104.0	127	55	212	5,679	2.13	0.505	0.580	0.335	120	248
S70	70	158	1,680	104.9	110	47	185	4,960	2.10	0.497	0.570	0.329	120	248
S58	58	136	1,505	94.0	145	62	218	5,857	2.55	0.604	0.690	0.399	120	248
S50	50	122	1,601	99.9	100	43	160	4,297	1.59	0.377	0.430	0.249	120	248
S46	46	115	1,587	99.1	210	90	333	8,945	2.41	0.571	0.450	0.260	56	133
S44	44	111	1,584	98.9	100	43	158	4,251	1.61	0.381	0.430	0.249	120	248
S34	34	93	2,100	131.1	115	49	242	6,482	2.10	0.497	0.520	0.301	70	158
S32	32	90	1,460	91.1	200	86	292	7,837	1.91	0.452	0.510	0.295	60	140
S30	30	86	1,304	81.4	190	82	248	6,650	1.90	0.450	0.480	0.277	60	140
S27	27	81	1,530	95.5	183	79	280	7,515	2.20	0.521	0.540	0.312	60	140
S25	25	77	1,530	95.5	180	77	275	7,392	2.20	0.521	0.540	0.312	60	140
S23	23	73	1,530	95.5	175	75	268	7,186	2.20	0.521	0.540	0.312	60	140
S21	22	72	1,530	95.5	170	73	260	6,981	2.20	0.521	0.540	0.312	60	140
S19	19	66	1,520	94.9	160	69	243	6,527	1.90	0.450	0.430	0.249	60	140
S17	17	63	1,525	95.2	160	69	244	6,549	1.90	0.450	0.430	0.249	60	140
S15	15	59	1,510	94.3	160	69	242	6,485	1.90	0.450	0.430	0.249	60	140
S13	13	55	1,515	94.6	160	69	242	6,506	1.90	0.450	0.430	0.249	60	140
S10	10	50	1,470	91.8	155	67	228	6,115	1.90	0.450	0.430	0.249	60	140
S8	8	46	1,475	92.1	150	65	221	5,938	1.90	0.450	0.440	0.254	60	140
S7	7	45	1,700	106.1	150	65	255	6,844	1.85	0.438	0.400	0.231	60	140

PCM Products has a policy of continues product and product data improvement and reserves the right to change design and specifications without notice